目次

所長挨拶

2020 年度は、新型コロナウイルス感染拡大の影響により、前期は全て遠隔授業（オンライン）、後期は十分な感染症対策のもと頑張って約５割の対面授業を実施しました。このような厳しい状況下において、慣れないオンライン講義をこなしながら学問への情熱を持ち続けた教員と、研究を続けた大学院生の熱意と努力により、分子生体膜研究所（分生研）はかろうじて研究教育活動を継続することができました。今回の新型コロナウイルスの性質を考えますと、完全に 2020 年以前の生活環境に戻るには、少し先のことになります。ワクチンや特効薬が市場に充足し、あるいは集団免疫が形成されるなどして、感染爆発や重症化リスクが十分抑制された状態になることが重要だと考えています。そのためには、最低でも 1～2 年の時間がかかると言われています。したがって、それまでの間、With コロナの状態が続くことを覚悟し、3 密（密閉・密集・密接）の対策などを通して感染を防ぎながら、分生研が本来の機能を発揮できるようにしていかねばなりません。

一方、この 1 年の経験のなかで、皆さんも対面で人と接する活動は、人間の生活にとって不可欠のものであることを再確認されたのではないでしょうか。実空間での対面がかなわない状況で、オンライン講義・会議、テレワークなどの活用は、その不便をある程度補ってくれました。しかしながら、研究活動や教育あるいは仕事を進める上で不可欠な人との信頼関係や共感を、リモートの環境だけで醸成するのは難しいことも実感しました。With コロナを経て新たに到来する Post コロナ社会では、対面での接触がより貴重で価値あるものとして重視され、大切なものとして追求されるべきでしょう。

2020 年に分生研としては大変悲しいことが起こりました。東北薬科大学附属癌研究所時代から分生研にいたる今日まで、長きにわたり顧問・名誉所長としてご指導いただいてきました箱守仙一郎先生は 2020 年 11 月 11 日、91 歳で逝去されました（細野教授の

追悼文をご参照）。分生研の一同を代表し、先生のご指導に感謝し、心よりご冥福をお祈り申し上げます。

また、今年度は 2006 年に分生研が設立されたと同時に赴任してきた生体膜情報部門の東秀好教授が御退職を迎えられました（写真は最終講義にて、東教授と司会の生化学教室の関教授）。長い間本当にお疲れ様でした。今後のご健勝とご活躍を心よりお祈り致します。

今回の年報では、各研究部門の研究活動報告および第４回箱守仙一郎賞の奨励賞および優秀論文賞、および東教授が主催した第 14 回東北糖鎖研究会（詳細は東教授の紹介文）をご紹介致します。

皆様からのご指導ご鞭撻のほど心よりお願い申しあげます。

令和３年３月吉日

東北医科薬科大学　分子生体膜研究所･所長

顧　建国

追悼　箱守仙一郎先生―サイホウそして、Glycosynapse―

分子認識学部門　細野雅祐

本学 元評議員・名誉分子生体膜研究所長　箱守仙一郎先生におかれましては、2020年 11 月 10 日、米国シアトルにて逝去されました。享年 91 歳。現地との時差など細かいことを除けば、奇しくも 2017 年のこの日、先生の米寿をお祝いして当研究所において開催された「箱守仙一郎糖鎖科学シンポジウム」および記念祝賀会から、ちょうど 3 年を経て旅立たれたことになります。その前年、定例の生化学特別講義では、100 分超の口演を起立のまま全うされていたことを思えば、ややお元気がなくなった印象はありましたが、それでも 50 名を超える内外のお弟子さん達に囲まれ、皆様からの祝福を和やかな笑顔で受けておられました。先生は帰国後体調を崩されたものの、ご令室光子さまをはじめご家族の献身的な介護により小康を得ていると伺っておりました。筆者としても何とか理由をつくってシアトルへお見舞いに行かねばと思案しているうちに今般のコロナ禍が顕著となり、結局渡航の機会を見いだせないまま先生とお別れせねばならなくなりました。まことに痛恨の極みであります。

私事で恐縮ですが、1980 年代半ば、大学院生であった筆者が箱守先生の生化学特別講義を拝聴してまず驚いたのは、先生が「細胞」を”サイホウ”と発音されていたことです。同胞や胞子を読むときにはホウと発音するにもかかわらず、細胞は当たり前のようにサイボウと読んでいた。もちろん以前からそう教わっていたからに相違ないのですが、その一点に加え、ある学生が質問に起立して「愚問かもしれませんが」と前置きしたとたん、「あーたたちが質問しようとするときに、愚問などというものはありません！」（だから、遠慮せずにお聞きなさい）と一喝されたこと。その 2 点をもって箱守先生に「他の先生とはちがう」スケールの大きさを感じ、魅了されてしまいました。恥ずかしながら、そのときの講義の内容はほとんど記憶しておりませんが、確か当時筆者らが勉強した「コーン・スタンプの生化学」ではほんの数行しか触れられていなかった糖脂質および糖タンパク質に関するお話であり、その後毎年の講義を拝聴するなかで、如何に先生が当時から最先端の知識を披露して下さっていたか、次第に分かるようになりました。

箱守先生ご逝去の報せがネットワーク間を広がるにつれ（発信源はおそらく Dr. Laine？）、なかば自然発生的に”Hakomori Lab. Alumini”という字句が生まれ、次第に箱守研ゆかりの研究者に寄稿を呼び掛けて memorial e-book をつくろうという話が進みました。ムコ多糖（こんにちのグリコサミノグリカン）の生化学的研究で世界的に知られた正宗一先生門下の箱守先生は、1959 年（昭和 34 年）に当研究所の前身である東北薬科大学附属癌研究所第一部を立ち上げられてから、実に 60 年という年月を常に第一線で先導してこられ、しかも本拠地は米国シアトルです。その間に箱守先生とリ

サーチの面で関わった方がいったいどのくらいおられるのか、我々には調べようもありません。そんなとき、箱守先生の高弟である Dr. Roger Laine の後押しに加え、箱守先生のもとで長く秘書兼ライターをしておられた Dr. Stephen Anderson がお持ちの膨大なメーリングリストをもとに全面的に協力して下さるとのお話があって、前所長井ノ口仁一先生を中心に昨年末から本格的にプロジェクトが動きはじめ、先ごろデジタル追悼文集”Fond Memories of Professor Sen-itiroh Hakomori”を完成いたしました。Dr. Laine は同時に、箱守先生の広範な業績リストを作成し、送ってくださいました。これは（例えばタンパク質・核酸・酵素のような）邦文雑誌に掲載された論文も含む詳細なもので、1952 年の第一報（*J. Biochem.*）[1)] から直近の第 737 報（2019 年、*Glycoconj. J.*）[2)] まで記載されています（うち peer-reviewed original paper は 585 報）。論文の種類を問わずに単純計算すると、実に 68 年間にわたっておしなべて毎月一報論文を発表されていたことになります。報数の多さにも圧倒されますが、もちろん掲載誌の質についても Nature と Science 合わせて 10 報をはじめ、*Cell*、*PNAS*、*JBC*、*Cancer Res* など、目もくらむような内容であります。このような箱守先生のご業績については、既に多く活字（テキスト）になっており今更感がございますが、筆者なりの視点で以下いくつかのエポックを点描風に記したいと思います。

科学史をひもといてみれば明らかですが、前世紀半ば、近代生化学を牽引してきた多くの研究者は、内外を問わず基本的に”Chemical biologist”でした。医学部出身の先生方の中にも医師免許を取得しつつ、「医化学」という分野において chemistry を基盤とした研究を強力に推進された方が多くおられますが、箱守先生もそのお一人です。世代が異なるとはいえ、薬学部出身にもかかわらず「生物系」というエクスキューズに隠れて化学を疎かにしてきた筆者などにとっては、まさに汗顔の至りと下を向くばかりです。曰く、「あーたたち、ほんとにケミストリーが分かってるの？」。

もともと「がんと正常細胞（組織）の違い」に注目されていた先生は、1961 年、癌研在職中にがんの糖鎖変化に関する報告をいきなり *Nature* 誌に Letter として発表します（実際には２連報）。[3)] 同時にその違いを知る術として、先ずは化学で糖鎖構造を明らかにする戦術をとられ、1964 年、*J. Biochem* 誌 [4)] に糖の完全メチル化法に関する論文を発表。後に<u>箱守のメチル化法</u>と呼ばれるようになったこの方法は、ジメチルスルホキシドと水素化ナトリムにより生じたメチルスルフィニルカルボアニオンが糖と反応してできるナトリウムアルコキシド中間体をヨウ化メチルによってメチル化するもので、特殊な装置を必要とせず、一回の反応で難反応性の酸性糖も含め高収率で完全メチル化が可能な画期的方法であり、糖鎖構造分析に広く応用されました。次いで、1968 年に *PNAS*、*BBRC* 誌 [5, 6)] に糖脂質における<u>がんの糖鎖不全現象</u>（悪性転換細胞における長鎖糖脂質の減少とその前駆物質の蓄積）が報告されます。これは、その後木幡博士らによって拓かれた糖タンパク質糖鎖のがん性変化（多分枝性）と相俟って、来るべきがん特異抗原や腫瘍マーカー全盛期の礎となるお仕事であったと思い

ます。一方で先生は、ガラクトースオキシダーゼによって非還元末端のガラクトースあるいはガラクトサミンを酸化しつつ、トリチウムホウ素ナトリウムによって還元すると同時に放射ラベルする細胞表面標識法を開発されました（1975 年、*JBC* 誌）[7]。この手法は悪性細胞におけるパラグロボシドや Forssman 抗原などの糖脂質含量の増加や、さらには（発表年は前後するが）細胞のがん化により発現が低下する細胞表層タンパク質フィブロネクチンの発見（1973 年、*PNAS* 誌、ガラクトプロテイン a と称された）[8] に繋がったのです。1970 年代後半頃から、箱守先生は当時知られるようになって間もないモノクローナル抗体（MoAb）に着目し、がん性変化の見られる（すなわち腫瘍マーカーの候補となる）糖脂質をターゲットに、種々の MoAb を樹立しました。なかでも FH6（1984 年、*JBC* 誌）[9] は、主に肺腺がんなどのマーカーである SLX（シアリル LeX-i）を認識する MoAb で、抗体によるがんの診断に広く応用されました。前述したような悪性化細胞に特異的に発現する糖鎖抗原は、がん特異的糖鎖抗原（シアリル Tn、GM2、GD2、globo-H など）と呼ばれますが、これらを標的として、診断のみにとどまらず治療まで行おうとする試みは当時から行われ、分子標的薬を用いる現代の薬物治療戦略の基盤となりました。箱守先生は、並行して細胞表面構造のクラシカルな代表格である血液型にも精力的に関わられ、血液型研究における金字塔ともいうべき **ABO 式血液型システムの分子遺伝学的解明**に関する論文が 1990 年に発表されました（*Nature* 誌）[10]。おりしも糖転移酵素遺伝子のクローニングが急激に進んだ（日本人研究者の貢献が最も大きい）時代の先駆けとなるお仕事ですが、A 型を規定する A 遺伝子（α1-3GalNAc 転移酵素をコード）の単離を端緒に、B 型の Gal 転移酵素との違いがたった 4 個のアミノ酸残基に集約されることを見いだし、結果として長いあいだ不明であった *cis*AB 型発生のメカニズムが解明されたのです。筆者は、しばしば大学の仕事として周辺の高校に出向き、いわゆる出前講義を行っておりますが、テーマとしていつもこの話題を取り上げ、箱守先生のご紹介をしながら ABO 式血液型の不思議についてお話しています。

紙面も限られていますので、ここからは駆け足になります。後にも述べますが、箱守先生は一貫して”膜成分としての糖脂質および糖タンパク質糖鎖の構造と機能”を研究テーマとされ、そのエンドポイントは、「細胞間相互作用の詳細」および「細胞のがん化メカニズム」を明らかにすることだったと思われます。これには“細胞認識”や“細胞接着”および“シグナル伝達”というキーワードがよくあてはまります。細胞表面上のいわゆるネオラクト系のII型糖鎖（SSEA-1=Le^x など）を中心とした研究が継続して行われる中で、1990 年、リンパ球ホーミング現象における E-セレクチンの白血球側の糖鎖リガンドが、シアリル Le^x であることが明らかにされました（Science 誌）[11]。言うまでもありませんが、セレクチンはI型の膜貫通タンパク質で、細胞外の N 末端に糖結合能をもつ C 型レクチンドメインをもっています。すなわちこれは、細胞同士が carbohydrate-protein interaction （CPI）によって結合する細胞間相互作用のひとつに他

なりません。3 種ある**セレクチンのリガンド糖鎖**の同定には多くの研究者が参入し、一部で紆余曲折もあったようですが、この相互作用はがんの転移機構にも直接関係することから非常に注目を集めるテーマとなりました。タンパク質が糖鎖を直接認識し、細胞機能に影響を与える CPI の事例については、この他にもガレクチンやシグレックなどのレクチンが関与するものや、インテグリンあるいは**成長因子受容体と糖脂質との結合**など、多くのエビデンスが報告されています（箱守研では EGFR と GM3、2006 年、*PNAS* 誌）[12]。一方、細胞と細胞の結合には上記のほかに糖鎖-糖鎖間のホモフィリック（Le^x と Le^x など）あるいはヘテロフィリック（GM3 と Gg3 など）な相互作用によるものがあり、その後のシグナル伝達において重要であることも示されました（1989 年、*JBC* 誌）[13]。「**carbohydrate-carbohydrate interaction（CCI）**」は少し前まで箱守先生の口癖のようになっていたと記憶しています。そして晩年、先生が最も力を入れておられたテーマは、何といっても**細胞膜マイクロドメイン**に関するものだったと思います。1997 年に Dr. Kai Simons らによって提唱された”脂質ラフト”という細胞膜モデルは、シグナルプラットフォームとしての形態機能として注目され、すでに定説となっていた Singer-Nicolson の流動膜モザイクモデルにうまくフィットした形で、脂質の海に漂う「**動く筏**」として世界的な広がりを見せました。それに対して先生は、早くから細胞膜における糖脂質成分の集合状態（組織化）に着目され（1991 年、*Glycobiology* 誌）[14]、脂質マイクロドメインという概念を思考しておられた中で、上述した CPI や CCI の事象などを含む様々な事実（特に細胞接着に関わる）を統合され、「**動かない**マイクロドメインがある」と結論づけたのです。既に廃刊となって久しい邦文雑誌“蛋白質 核酸 酵素”（2002 年）に、五十嵐靖之先生が司会をされた座談会記録「マイクロドメイン研究の流れと将来」が掲載されています[15]。その中で箱守先生は、Simons 先生の Lipid raft の不十分さを指摘し、「ラフトは、カベオラというテーゼに対するアンチテーゼです。私たちは、新しいテーゼを求めるべきです。」と言い切っておられます。そしてここでの発言通り、同時に *PNAS* 誌（2002 年）[16]に”**The glycosynapse**”というエレガントなタイトルの単著論文を発表されました。このグライコシナプスこそ、箱守先生が長年にわたり成されてきたお仕事から得られた膨大なエビデンスをもとに構築された、まさに集大成ともいうべき細胞膜機能形態の概念であろうと思います。すなわちラフトとは異なり、「**動かずに**、細胞接着や運動・成長などをコントロールするシグナルプラットフォーム」としての細胞膜マイクロドメイン。「新しいテーゼ」です。

冒頭でも述べた箱守先生の 2016 年の生化学特別講義の終盤は、“**epithelial-to-mesenchymal transition (EMT)**”と”**cancer stem cell**”に関するお話しでした。もちろんこれらのテーマにも先生は早くから取り組んでおられます（前者は 2009 年、後者は 2013 年、いずれも *PNAS* 誌）[17,18]。EMT における糖脂質発現変化（例えば Gg4、GM2）を知ることで、これまで知られていなかった細胞のがん化プロセスへの糖鎖の

関与を明らかにすること、また乳がん幹細胞における糖脂質の発現が対応する正常組織幹細胞と異なることを見いだされましたが、特に正常幹細胞が分裂を経てがん幹細胞に変化するのには、幹細胞とその周辺に存在する niche 細胞との接触状態（CPI、CCI）が大きく影響している可能性がある、とのことでした。

繰り返しになりますが、箱守先生は「細胞間相互作用」というものを、膜の複合糖質の組織化・シグナル伝達へのかかわりと細胞機能のコントロールという点で掘り下げられた。そして研究の基盤として、一貫して鍵を握る個々の分子の構造を正確に知ることを大切に考えてこられました。もちろん、同時にその時代の”最先端の知見や技術“をいち早く取り入れ、活用するという点においても非常に巧みであられた。さらに言えば、ご自分の研究を世に知らしめる能力、とりわけ文章力とプレゼン力がずば抜けておられました。それは例えば、研究から一歩はずれた学会の懇親会における洒脱なパフォーマンスを含めて、のお話でもあります。

ここに、レクチンの大家である大沢利昭先生が編まれ、1982 年に講談社から出版された「細胞認識と動物レクチン」という成書があります。この第一章は箱守先生が執筆され、糖脂質と糖タンパク質の細胞認識への関わりについて書かれていますが、その末尾に、当時筆者がとても魅了された文章があります。先生は、“New Yorker の世界地図”という戯画（「マンハッタン島が中央に大きく描かれ、ほかのアメリカ大陸もヨーロッパも、アジアも片隅に寄せられて描かれた」もの、とかかれていますが、残念ながら筆者は実物を知りません）を引き合いに出され、さらにご自分のことを堂々と「糖屋」を称しながら、（自分たちが成そうとしているサイエンスが）『もしかすると、“New Yorker の世界地図”に等しい「糖屋」の戯画であることを恐れる』と語られました。先生が最もエネルギッシュであったご壮年期、いかにも気宇壮大、かつ科学者として真摯であろうとするお姿が見えるようです。この部分、ときどき読み返しながら筆者は先生の声を聴きます。筆者の拙い解釈ではありますが、つまり一言でいえば、「視野を広くおもちなさい」ということなのだろうな、と。

追記

本来ならば、本文中でご紹介したそれぞれの研究に貢献された先生方のお名前も併せて記載するべきところですが、紙面の関係上ここでは省略させていただきました。失礼の段、お許し下さい。

引用文献

1) Masamune H, Hakomori S (1952). Paper partition chromatography of lipid components. J Biochem 39: 5.

2) Nakamura Y, Miyata Y, Matsuo T, Shida Y, Hakariya T, Ohba K, Taima T, Ito A, Suda T, Hakomori S, Saito S, Sakai H (2019). Stage-specific embryonic antigen-4 is a histological marker reflecting themalignant behavior of prostate cancer. Glycoconj J 36(5): 409-418.
3) Hakomori S, Kawauchi H, Ishimoda T (1961). Changes of hexose and hexosamine ratio, and the degree of branching in rat urine glycoprotein during cancer development. Nature 190: 265-266.
4) Hakomori S (1964). A rapid permethylation of glycolipid and polysaccharide as catalyzed by methylsulfinylcarbanion in dimethyl sulfoxide. J Biochem 55: 205-208.
5) Hakomori S, Murakami WT (1968). Glycolipids of hamster fibroblasts and derived malignant-transformed cell lines. Proc Natl Acad Sci USA 59: 254-261.
6) Hakomori S, Teather C, Andrews H (1968). Organizational difference of cell surface "hematoside" in normal and virally transformed cells. Biochem Biophys Res Comm 33: 563-568.
7) Gahmberg CG, Hakomori S (1975). Surface carbohydrates of hamster fibroblasts. I. Chemical characterization of surface-labeled glycosphingolipids and a specific ceramide tetrasaccharide for transformants. J Biol Chem 250: 2438-2446.
8) Gahmberg CG, Hakomori S (1973). Altered growth behavior of malignant cells associated with changes in externally labeled glycoprotein and glycolipid. Proc Natl Acad Sci USA 70: 3329-3333.
9) Novel fucolipids accumulating in human adenocarcinoma: II. Selective isolation of hybridoma antibodies that differentially recognize mono-, di-, and trifucosylated type 2 chain. J Biol Chem 259: 4681-4685.
10) Yamamoto F, Clausen H, White T, Marken J, Hakomori S (1990). Molecular genetic basis of the histo-blood group ABO system. Nature 345: 229-233.
11) Phillips ML, Nudelman E, Gaeta FCA, Perez M, Singhal AK, Hakomori S, Paulson JC (1990). ELAM-1 mediates cell adhesion by recognition of a carbohydrate ligand, sialyl-Lex. Science 250: 1130-1132.
12) Yoon S, Nakayama K, Hikita T, Handa K, Hakomori S (2006). Epidermal growth factor receptortyrosine kinase is modulated by GM3 interaction with N-linked GlcNAc termini of the receptor. Proc Natl Acad Sci USA 103(50): 18987-18991.
13) Eggens I, Fenderson B, Toyokuni T, Dean B, Stroud M, Hakomori S (1989). Specific interaction between Lex and Lex determinants: A possible basis for cell recognition in preimplantation embryos and in embryonal carcinoma cells. J Biol Chem 264: 9476-9484.

14) Kojima N, Hakomori S (1991). Synergistic effect of two cell recognition systems: Glycosphingolipidglycosphingolipid interaction and integrin receptor interaction with pericellular matrix protein. Glycobiology 1: 623-630.
15)箱守仙一郎、永井克孝、鈴木明身、平林義雄、小堤保則、五十嵐靖之（2002）マイクロドメイン研究の流れと将来（座談会）、蛋白質 核酸 酵素、47，299-314.
16) Hakomori S (2002). The glycosynapse. Proc Natl Acad Sci USA 99(1): 225-232.
17) Guan F, Handa K, Hakomori S (2009). Specific glycosphingolipids mediate epithelial-to-mesenchymal transition of human and mouse epithelial cell lines. Proc Natl Acad Sci USA 106(18): 7461-7466.
18) Liang YJ, Ding Y, Levery SB, Lobaton M, Handa K, Hakomori S (2013). Differential expression profiles of glycosphingolipids in human breast cancer stem cells vs. cancer non-stem cells. Proc Natl Acad Sci USA 110(13): 4968-4973.

ご略歴

昭和 4 年(1929 年)2 月 13 日　仙台にて誕生
昭和 25 年(1950 年)3 月　東北大学医学専門部卒業
昭和 27 年(1952 年)3 月　東北大学医学部 助手（医化学）
昭和 31 年(1956 年)6 月　フルブライト留学生（ハーバード大学留学）
昭和 32 年(1957 年)12 月　東北大学医学部 助教授（医化学）
昭和 34 年(1959 年)10 月　東北薬科大学薬学部 教授（癌研究所第一部）
(～昭和 38 年(1963 年)8 月 31 日まで)
昭和 38 年(1963 年)7 月　米国ハーバード大学準教授
昭和 41 年(1966 年)7 月　米国ブランダイス大学生化学部教授
昭和 41 年(1966 年)12 月　米国ワシントン大学公衆衛生学部教授

昭和 45 年(1970 年)8 月　米国ワシントン大学医学部 終身制教授
昭和 50 年(1975 年)6 月　フレッド・ハッチンソン癌研究所生化学部・部長 兼任
昭和 51 年(1976 年)4 月　東北薬科大学附属癌研究所指導教授
昭和 61 年(1986 年)9 月　バイオメンブレン研究所所長 兼任
平成 8 年 (1996 年)　パシフィック・ノースウエスト研究所
生体膜研究部門長 兼任
平成 12 年(2000 年)　米国科学アカデミー　正会員
平成 17 年(2005 年)　米国ワシントン大学　名誉教授
平成 18 年(2006 年)4 月　東北薬科大学附属分子生体膜研究所顧問及び指導教授
平成 26 年(2014 年)1 月　東北薬科大学附属分子生体膜研究所　名誉所長

受賞歴
昭和 59 年(1984 年)3 月　米国病理学会　フィリップ・レヴィン賞
昭和 61 年(1986 年)7 月　国立医学・衛生研究所（NIH）より
Outstanding Investigator Award
昭和 61 年(1986 年)9 月　米国・公衆衛生　National Merit Award
平成 2 年 (1990 年)5 月　フィンランド科学学士院名誉会員
平成 3 年 (1991 年)1 月　朝日賞
平成 3 年 (1991 年)5 月　イギリス・生化学会　モルトン賞　(Morton Award)
平成 4 年 (1992 年)1 月　日本癌学会　名誉会員
平成 5 年 (1993 年)2 月　第 2 回 Outstanding Investigator Award
平成 6 年 (1994 年)6 月　ヘルシンキ大学名誉博士
平成 7 年 (1995 年)8 月　カール・マイヤー賞
平成 23 年 (2011 年)　ロザリンド・コーンフェルド賞

第 14 回東北糖鎖研究会 Web 開催の報告

2020 年度の第 14 回東北糖鎖研究会は、東が世話人代表となり当研究室の黒田助教が運営を担当して行いました。

当初 8 月 28 日午後から 29 日午前の開催を予定していましたが、新型コロナ流行のため例年どおりの開催は難しいと考えられたので、井ノ口会長と相談の結果、Zoom を用いたオンライン開催とすることにしました。この Zoom 会議は、8 月 29 日（土）に開催しました。オンライン開催は初めてのことなので、会の順調な運営・進行が心配されましたが、お陰様で、参加者 60 名と例年並の規模で無事盛会のうちに終了することができました。

通常の研究集会では一般講演、ポスター発表に加え、糖質科学の分野で多数の業績を持つ研究者を招いた招待講演を行っていますが、今回はパソコンのモニターを注視する時間を削減すべく、一般講演と箱守仙一郎賞受賞講演のみのオンラインリアルタイム配信とし、ポスターについては、発表動画のオンデマンド配信にしました。
以下のようなスケジュールで行いました。

一般講演、箱守仙一郎賞受賞講演の動画配信
　　2020 年 8 月 29 日（土）9:30〜12:45
ポスター発表動画視聴期間
　　2020 年 8 月 27 日（木）9:00〜2020 年 8 月 29 日（土）21:00

通信のトラブルなどを回避するため、各講演は事前に動画として登録してもらい、東北医科薬科大学のサーバーからそれらを配信しました。質疑応答は、リアルタイムのチャットで行ってもらいました。

ポスター発表については、プレゼンテーション動画（10 分程度）を開催日の 2 日程度前からオンデマンド配信しました。したがって、例年行っているショートプレゼンテーションは省略しました。

抄録集は、事前に各世話人（研究室の必要分）、顧問の先生方と関係者（広告主等）に送付しました。

また、「みちのくポスター賞」は例年どおり審査し、優秀な発表をおこなった学部学生、大学院生を表彰しました。本会を通じて、コロナ禍により発表の機会が少なくなった学生や若手の研究者に発表の経験を積ませることができ、糖鎖科学研究を志す研究者の育成の一助になったと自負しております。

事前の準備、特に資金援助については世話人である分子生体膜研究所の諸先生方にお世話になりました。お陰様で、例年後援いただいている公益財団法人・水谷糖質科学振興財団と 5 社の協賛をいただくことができました。

例年のような懇親会もできませんし会場費もかからなかったため、黒字を計上することができました。

Zoom 会議とした講演の参加者は、60 名、ポスター当たりの視聴回数は 42.3 回と例年に劣らない盛況となりました。交通費がかからず、プレゼンテーションが見やすいなど Web 会議の利点を改めて実感しましたが、参加者間の交流という面では物足りなかったかと思われます。第 15 回の研究会は岩手医科大学において通常どおりに開催される予定ですが、より良い交流の場となることを祈っています。

東北医科薬科大学分子生体膜研究所
「箱守仙一郎賞」（Sen-itiroh Hakomori Glycoscience Award）規約

令和 2 年 4 月
東北医科薬科大学分子生体膜研究所
顧　建国

名称　　箱守仙一郎賞

授与機関　　東北医科薬科大学分子生体膜研究所

目的　　生物系化学系を問わず広く糖鎖科学を専攻し、日夜努力を続けている東北エリアの研究者を顕彰することにより、日本の糖鎖科学研究の増進を図る。

賞の種別　　奨励賞　　1~２名　顕彰楯および副賞
優秀論文賞　1~２名　顕彰楯および副賞

対象　（１）奨励賞：東北エリア（新潟県および群馬県を含む）で研究に従事する応募時 45 歳までの研究者
（２）優秀論文賞：同地域で研究に従事し，申請時点で大学院生もしくは博士研究員である者
＊ いずれも指定された期間内(各年度内)に発表（accepted でも可）された学術原著論文に対して審査・授与する。

選考方法　　自薦および他薦によるものとし、東北糖鎖研究会世話人が審査する。評価を点数化（次項参照）して決する。

授賞方法　　東北糖鎖研究会開催時に授賞および受賞講演を行う。

運用方法　　顕彰楯および副賞の購入費は、箱守賞基金を原資とし、分子生体膜研究所がこれを支弁する。

その他　　事務局は分子生体膜研究所内に置く。

応募と審査方法

（１）応募資格および応募方法
東北 6 県、新潟県および群馬県（東北糖鎖研究会エリア）で研究を行っている 45 歳以下の糖鎖科学研究者（大学院生、博士研究員は自動的に優秀論文賞へのノミネートとなる）。対象論文は、その年度内に Impact factor が付与されている英文学術雑誌（査読有）に出版、または掲載が決定されている原著論文（accepted でも可）とし、応募者が筆頭著者となっているものとする。要旨和訳と論文 PDF を添えて既定のエントリーフォームに記入してメールにて応募する。化学系・生物系は問わない。自薦および他薦どちらでも受け付ける。応募期間等についてはその都度決定し、周知する。

書類送付先：東北医科薬科大学 分子生体膜研究所　所長 顧　建国
メールアドレス：jgu@tohoku-mpu.ac.jp；　応募締め切り：5 月 31 日

（２）エントリーフォーム（別添）

（３）審査委員および審査方法
１）分子生体膜研究所所長が審査員長を務める。
２）東北糖鎖研究会世話人が審査員となる。ただし、世話人が推薦者または自薦者の所属責任者あるいは論文の共著者である場合は審査に参加しない。
３）期限内に提出された論文について事務局が一次審査（下記基礎点と推薦者の評価点の合計による）を行い、奨励賞および優秀論文賞それぞれ上位３報を選定する。
４）上位３報について審査員が下記評価項目を採点し、全員（その都度人数は異なる）の評価平均点＋基礎点＋推薦者の評価点から上位者を受賞者として決定する。
５）最高点が複数出た場合は審査員長の判断に委ねる。

基礎点

Impact factor (IF):　IF× 5 点

推薦者（自薦または他薦）の評価点（推薦書に記入、最高点 10 点）
共同研究者の貢献を考慮し、以下の項目を参考して該当研究に対する応募者の貢献度を客観的にみて公正に評価する。

１）研究の考案（最高点 2 点）
２）実験の実行（最高点 5 点）
３）論文作成（最高点 3 点）

評価最高点

独創性	10 点
インパクト（重要性）	10 点
論文構成	10 点
将来性	10 点

第 4 回箱守仙一郎賞（2019 年度）

奨励賞：ガングリオシドのアシル鎖構造による TLR4 制御メカニズム

Acyl-chain structures of ganglioside regulate TLR4 signaling

狩野　裕考（東北医科薬科大学・分子生体膜研究所・機能病態分子学）

私たちの研究室では、シアル酸を含む糖鎖とセラミドから構成されるスフィンゴ糖脂質：ガングリオシド GM3 による慢性炎症・糖尿病発症メカニズムをこれまでに明らかにしてきた。本研究では、ヒト血清およびマウス脂肪組織に含まれるガングリオシド GM3 が、どのように自然免疫応答を制御するのかについて焦点を当てた。その結果、単球・マクロファージ細胞に対する炎症促進性 GM3 分子種と炎症抑制性 GM3 分子種が存在することを見出した（*EMBO J.* 39: e101732, 2020）。GM3 分子種の生理活性は、セラミド構造中のアシル鎖の鎖長、飽和度、水酸化修飾によって制御され、炎症促進性 GM3 分子種は極長鎖飽和アシル鎖をもち、一部は α 位の水酸化（C22:0, C24:0, hC24:0）を受けた分子種であった。一方、炎症抑制性 GM3 分子種は、長鎖または不飽和アシル鎖（16:0, 18:0, 24:1）をもつ分子種であった。GM3 分子種による炎症反応の促進と抑制は、グラム陰性菌に由来する LPS や、内因性の HMGB1 といった TLR4 リガンドによる刺激に対して選択的に生じた。このことから、GM3 は TLR4 を標的とした内因性モジュレーターであると考えられた。

相互作用解析や計算シミュレーションの結果からは、GM3 が TLR4 に直接結合する可能性が得られた。その結果によれば、結合様式がアシル鎖構造によって変化するため、GM3 が TLR4 を正と負に制御できるものと推察された。ヒト血清中では、メタボリックシンドロームを発症するまでの過程において、すでに炎症促進性 GM3 分子種の増加と炎症抑制性 GM3 分子種の減少が認められた。加えて、レプチン欠損マウスおよび高脂肪食負荷マウスの内蔵脂肪組織において、炎症促進性 GM3 分子種の増加が認められた。これらの結果から、肥満に伴う GM3 のアシル鎖構造変化によって慢性炎症や疾患発症が惹起されるという、新たな分子病態像が示唆された。

今後、全身を循環する血清 GM3 分子種の発現変動パターンと、TLR4 を介する多様な疾患との関連が明らかになれば、慢性炎症性疾患の新しい診断・治療法の開発につながっていくものと期待される。

参考文献：

H. Kanoh, T. Nitta, S. Go, KI. Inamori, L. Veillon, W. Nihei, M. Fujii, K. Kabayama, A. Shimoyama, K. Fukase, U. Ohto, T. Shimizu, T. Watanabe, H. Shindo, S. Aoki, K. Sato, M. Nagasaki, Y. Yatomi, N. Komura, H Ando, H. Ishida, M. Kiso, Y. Natori, Y. Yoshimura, A. Zonca, A. Cattaneo, M. Letizia, M. Ciampa, L. Mauri, A. Prinetti, S. Sonnino, A. Suzuki, JI.

Inokuchi. “Homeostatic and pathogenic roles of GM3 ganglioside molecular species in TLR4 signaling in obesity.” ***The EMBO journal*** 39: e101732 (2020)

経歴：

2008 年： 北海道大学　薬学部　総合薬学科 卒業
2010 年： 北海道大学　大学院生命科学院　構造生物学分野　博士前期課程 修了
（溶液 NMR 法および単結晶 X 線回折法による Toll-like receptor シグナル伝達タンパク質の立体構造解析に従事）
2015 年： 東北大学　大学院薬学研究科　生命機能解析学分野　博士後期課程 修了
（ゲノムワイド RNAi スクリーニングによるショウジョウバエ Toll 受容体の新規シグナル伝達因子の網羅的同定と生理学的機能の解析に従事）
2015 年： 東北薬科大学　分子生体膜研究所　リサーチアソシエイト・博士研究員
2017 年： 東北医科薬科大学　分子生体膜研究所　機能病態分子学教室　助手
2019 年 〜 現在： 同　助教
（慢性炎症・メタボリックシンドロームにおけるスフィンゴ糖脂質の新規生理活性の探索と病態生理学的機能の解析に従事）

受賞の御礼ならびに抱負：

この度は、箱守仙一郎賞奨励賞を賜りまして、東北糖鎖研究会ならびに東北医科薬科大学・分子生体膜研究所の関係者の皆様、東北医科薬科大学・機能病態分子学教室の皆様に心より御礼申し上げます。また、本研究へのご参画・ご支援を賜りました、大阪大学理学研究科・天然物有機化学研究室、東京大学・薬学系研究科・蛋白構造生物学教室、東北医科薬科大学・薬学部・医薬情報学教室、東京大学・医学系研究科・内科学専攻 病態診断医学講座 臨床病態検査医学分野、岐阜大学・応用生物科学部・生理活性物質学研究室、東北医科薬科大学・薬学部・分子薬化学教室、ミラノ大学・医学部をはじめとする、多くの先生方に心より御礼申し上げます。

自然免疫は、植物、昆虫、マウスやヒトなどの哺乳動物に至るまでの幅広い生物種において、進化的に獲得・保存された生態防御機構です。体外から侵入する数多くの病原体や異物、そして、体内で生じる代謝・傷害・老化産物の分子構造パターンを、最低限の遺伝子数の受容体をもって認識し、恒常性維持のためのフィードバックシグナルを発すること、これが自然免疫系の機能のひとつです。自然免疫系には、生物種を大きく超えてなお共通した制御機序が備わっており、モデル生物を用いた研究や、構造生物学による普遍原理の探究が威力を発揮してきました。一方で、進化的な制約の中で、個々の生物種の生活環境や栄養応答性、病原体暴露の量的・質的変化に対応した、生物種固有のモジュレーション機構が備わっていることも、最近の研究から見えてきました。このような一種の最適化メカニズムは、受容体遺伝子の有無や重複だけでなく、進化的に変動が大きい糖鎖、脂質、糖脂質の分子種発現パターンや代謝経路の組み合わせによって構築されていることを、今回の発見は示唆しています。分子

機構の進化的普遍性と独自性の両面からアプローチすることで、僅かながらも自然免疫研究の発展に貢献したいと考えています。今後とも、ご指導ご鞭撻のほど、何卒よろしくお願い申し上げます。

優秀論文賞：Deficiency of core fucosylation activates cellular signaling dependent on FLT3 expression in a Ba/F3 cell system. Duan, C., Fukuda, T., Isaji, T., Qi, F., Yang, J., Wang, Y., Takahashi, S. and Gu, J. ***FASEB J***., 34: 3239-3252. 2020

段　程偉（Duan Chengwei、東北医科薬科大学・分子生体膜研究所・細胞制御学）

論文要旨：

Fms-Like Tyrosine Kinase 3（FLT3） はクラス III 受容体チロシンキナーゼファミリーのメンバーに属する糖タンパク質で、急性骨髄性白血病（AML）患者の約 3 分の 1 に活性化変異が認められる。FLT3 は FLT3 リガンドの結合により、二量体化・自己リン酸化が生じるが、活性化変異ではリガンド非存在下でも恒常的に活性化される。細胞は病的状態に陥ると、正常とは異なった糖鎖構造を生合成することが知られているので、本研究では FLT3 の細胞外ドメインに付加された N-型糖鎖に焦点を当てた解析を行った。FLT3 の野生型（WT）における N-型糖鎖の構造は患者に良く見られた膜貫通部位にタンデム重複挿入（ITD）とチロシンキナーゼドメイン（TKD）の活性化変異体の糖鎖と比較して、大きく異なることが見出された。また、興味深いことに、IL-3 依存性造血前駆細胞である Pro-B 細胞株 Ba/F3 細胞に WT または変異体 FLT3 遺伝子を導入したところ、細胞のコアフコシル化を大きく誘導した。 FLT3 を介したシグナル伝達におけるコアフコシル化の機能を解明するために、CRISPR/Cas9 システムを使用して、コアフコシル化酵素である Fut8 を欠損させた Ba/F3 細胞を確立した。驚くべきことに、Fut8 欠損させた造血前駆細胞では、IL-3 非依存的に細胞増殖が認められた。Fut8 を発現する通常の Ba/F3 では、増殖に IL-3 が必要であることから、コアフコシル化が細胞の増殖を制御していることが実験的に示された。Fut8 欠損細胞に発現させた野生型 FLT-3(FLT3-WT)は、下流である STAT5、AKT および ERK シグナル伝達経路を活性化させ、細胞のチロシンリン酸化レベルを大幅に増加させた。これらの活性化は、Fut8 の発現を回復させることで消失した。さらに、チロシンキナーゼ阻害剤を添加したところ、Fut8 欠損またはフコシル化阻害剤によって誘導される細胞増殖が阻害された。そこで、FLT3 リガンド非存在下でも FLT3 が二量体化・自己リン酸化にできるか検討したところ、Fut8 欠損細胞ではリガンド刺激なしで FLT3 のダイマー形成が誘導されていることを明らかにした。本研究は、コアフコシル化が FLT3 の活性化の調節機能に深くかかわっていることを示した。この知見は急性骨髄性白血病の治療に有効な薬剤の開発に価値ある方向性を示すものであり、意義のある研究である。

受賞の御礼ならびに抱負：

Amazing and happiness that is my feeling when I got the message from Prof. Gu that I received the Sen-itiroh Hakomori glycoscience award. It is a great honor for me to receive the award, which suggests an affirmation of my doctor career and encouragement of the following research job. The most important thing should be said three times. Thanks for Prof. Hakomori! Thanks for Tohoku medical and pharmaceutical university! Thanks for Prof. Gu!

First of all, I would like to express my sincere appreciation to Prof. Hakomori as well as other prize committee members. Prof. Hakomori is an outstanding scientist in the field of glycobiology. As a student, I was very lucky to listen to his academic report and admire his research spirit although he already more than eighty years old. Recently, it is regret and sad to hear his left when reading the paper “Professor Sen-itiroh Hakomori (1929-2020): A tribute to a remarkable glycobiologist, mentor and friend!”. Thanks for his contribution to the glycobiology field and his spirit will always encourage me to learn and explore.

As time goes by, I am still nostalgic for doctoral life! The inspired steering and enlightened counseling of Prof. Gu, selfless assistance of Dr. Tomohiko Fukuda, patient explanation of Dr. Tomoya Isaji, kind concern and aid of Ms. Yan Hao as well as many bits of help from other laboratory members. I miss those beautiful scenes.

Now, I was already graduated from Tohoku medical and pharmaceutical university and started adapting the society. I worked in the clinical medical research center of affiliated hospital 2 of Nantong University and still performed basic research about glycobiology. I will try my best to introduce the importance of glycans to more and more students, researchers, and clinical doctors.

研究報告

＜生体膜情報学部門＞
教授　東　秀好
助教　黒田　喜幸

生体膜情報学最終年度の報告

2006 年に分子生体膜研究所発足とともにスタートした生体膜情報学研究室は本年度が最後となった。当初は、糖鎖によるブラジキニン受容体活性化を介した神経細胞分化（突起伸展）機構の研究を行った。これは、東が三菱化学生命科学研究所時代に見出したガングリオシドや N-アセチルガラクトサミンを非還元末端にもつ糖鎖による神経細胞分化が CaMKII や PKA を介した cdc42 活性化によるという知見に端を発していた[1]。糖鎖による神経細胞分化は、ブラジキニン B2 受容体アンタゴニストで阻害されたので、外来性の糖鎖は B2 受容体に作用しているという結論である[2]。コンドロイチン硫酸も B2 受容体に作用して神経細胞分化を制御しているという結果も得ているのだが、まだ論文化していない。

東日本大震災を挟んだ時期に非神経系の細胞に対してガングリオシドやコンドロイチン硫酸がどのように振る舞うかを調べたところ、神経細胞とは異なり、B2 受容体を不応化することがわかった[3]。その後、B2 受容体が不応化された細胞では ATP 受容体の $P2Y_2$ も不応化されていることを見出した[4]。この現象を詳しく調べたところ、B2 受容体と $P2Y_2$ 受容体の間にはシグナルクロストークがあり、どちらか一方の刺激でもう一方にもアレスチンが付いて両者が不応化、さらには内在化 (endocytosis)されることがわかった。さらに、$P2Y_2$ 受容体は脂質ラフト画分に局在し、B2 受容体は小胞体滞在時から $P2Y_2$ 受容体によりラフト画分に引き込まれることを明らかにした[5, 6]。

このような B2 受容体と $P2Y_2$ 受容体の連携は両者のヘテロオリゴマー形成によるものと考えているが、$P2Y_2$ 受容体はジスルフィド架橋によってホモダイマーも形成することを見出した[7]。GPCR のホモダイマーやヘテロオリゴマー形成については当時からいくつか報告されており、その後も新たな報告が続いている。このような GPCR の性質は、GPCR 研究をますます複雑化させている。

先述の神経細胞に活性を示すガングリオシドは GT1b をはじめとする b-シリーズガングリオシドだったので、このガングリオシドが痛みに関わるかどうかを調べた。皮下に投与すると GT1b など b-シリーズガングリオシドは確かに痛みを生じさせたり、痛みを増強する効果も有していたが、その機構は B2 受容体系ではなく、グルタミン酸を皮下に蓄積させることであることを明らかにした[8]。この効果は b-シリーズガングリオシドに特異的で a-シリーズガングリオシドにはそのような効果はなく、実際、

皮下にシアリダーゼを投与すると鎮痛効果が認められた。

本年度は、アンジオテンシン II 受容体 AT1 の制御機構とアドレナリン β2 受容体 (β2AR)シグナルによるヒアルロン酸合成促進、肥満関連 GPCR である GPRC5B の機能について新たな知見を得た。

AT1 受容体は、B2 受容体とのヘテロオリゴマー形成が知られており、その活性化、不応化、内在化において B2 受容体が共存する必要がある。AT1 受容体は圧力センサーとしても働いており、特に妊娠中毒症では成長する胎児の圧力により活性化されて血圧を上げる機構が示されている。さらに、脊髄の疼痛伝達に関与することが本学薬学科の薬理学教室から報告されている。後者の研究では ATII の ACE2 による分解産物である AT(1-7)とその受容体である Mas 受容体が、AT1 受容体による疼痛反応を抑制することが示されている。Mas 受容体は AT1 受容体とヘテロダイマーを形成するという報告があったので、Mas 受容体活性化により AT1 受容体が不応化されるかどうかを調べた。Mas 受容体と AT1 受容体を共発現させ、AT(1-7)で刺激すると AT1 受容体にアレスチンがリクルートされる不応化が認められた。さらには、Mas 受容体を共発現させるだけで ATII による Gαq 系の活性化は抑制されていた（東, 黒田, 投稿準備中）。

一方、アドレナリン β2 受容体 (β2AR)をアゴニストで活性化すると AT1 受容体にアレスチンがリクルートされて不応化された。興奮すると、痛みを忘れるという現象を説明できるのではないか。ただし、Mas 受容体とは異なり、β2AR の共発現だけでは ATII による Gαq 系の活性化には影響しなかった（東, 黒田, 投稿準備中）。

β2AR の活性化は、ヒアルロン酸合成酵素の HAS2 の遺伝子発現を増強する効果を有することを見出した。ヒアルロン酸の長鎖化を促進することでガン細胞の増殖や傷の治癒といったヒアルロン酸が関与する反応を増強すると考えられる（黒田, 東, 投稿準備中）。

肥満関連 GPCR である GPRC5B はいまだリガンドが特定できていないが、インスリノーマ細胞株である MIN6 細胞に GPRC5B を発現すると、グルコース刺激なしでもインスリンの分泌量が増加することを見出した（黒田, 東, 投稿準備中）。GPRC5B 発現させると、MIN6 細胞の細胞内カルシウムイオン濃度が高く保たれていたので、その結果インスリンの分泌量が増加していたと考えられる。GPRC5B-/-マウスは空腹時の血糖値、および、血中インスリン濃度が GPRC5B+/+マウスより低いことを説明できる結果である。GPRC5B の機能の 1 つは、インスリンの基礎分泌による血糖値の保持であると考えられる。

References

1. Higashi, H. & Chen, N. H. (2004) Ganglioside/protein kinase signals triggering cytoskeletal actin reorganization, *Glycoconj J.* **20**, 49-58.

2. Kanatsu, Y., Chen, N. H., Mitoma, J., Nakagawa, T., Hirabayashi, Y. & Higashi, H. (2012) Gangliosides stimulate bradykinin B2 receptors to promote calmodulin kinase II-mediated neuronal differentiation, *J Biochem, Tokyo.* **152**, 63-72.
3. Shimazaki, A., Nakagawa, T., Mitoma, J. & Higashi, H. (2012) Gangliosides and chondroitin sulfate desensitize and internalize B2 bradykinin receptors, *Biochem Biophys Res Commun.* **420**, 193-198.
4. Yashima, S., Shimazaki, A., Mitoma, J., Nakagawa, T., Abe, M., Yamada, H. & Higashi, H. (2015) Close association of B2 bradykinin receptors with $P2Y_2$ ATP receptors, *J Biochem, Tokyo.* **158**, 155-63.
5. Nakagawa, T., Takahashi, C., Matsuzaki, H., Takeyama, S., Sato, S., Sato, A., Kuroda, Y. & Higashi, H. (2017) N-glycan-dependent cell-surface expression of the $P2Y_2$ receptor and N-glycan-independent distribution to lipid rafts, *Biochem Biophys Res Commun.* **485**, 427-431.
6. Nakagawa, T., Takahashi, C., Matsuzaki, H., Kuroda, Y. & Higashi, H. (2018) Regulation of membrane raft recruitment of the bradykinin B2 receptor by close association with the ATP/UTP receptor $P2Y_2$, *Biochem Biophys Res Commun.* **505**, 36-39.
7. Abe, M., Watanabe, K., Kuroda, Y., Nakagawa, T. & Higashi, H. (2018) Homodimer formation by the ATP/UTP receptor $P2Y_2$ via disulfide bridges, *J Biochem, Tokyo.* **163**, 475-480.
8. Watanabe, S., Tan-No, K., Tadano, T. & Higashi, H. (2011) Intraplantar injection of gangliosides produces nociceptive behavior and hyperalgesia via a glutamate signaling mechanism, *Pain.* **152**, 327-34.

＜機能病態分子部門＞
特任教授　井ノ口仁一
准教授　稲森啓一郎
講師　永福正和
助教　狩野裕考
博士研究員　新田昂大

自然免疫におけるガングリオシド GM3 の役割

近年，スフィンゴ糖脂質を介した自然免疫応答の活性化・調節機構が急速に明らかとなりつつある．セラミドへのグルコース付加によって生じるGlcCerは，抗原提示細胞である樹状細胞において，C型レクチン受容体の一つであるMincleの活性化を引き起こす．Mincleは，肥満時の脂肪組織で発現量が増加しており，さらにMincle KOマウスでは，メタボリックシンドロームの症状が緩和されることもわかってきている．続いて，GlcCerへのガラクトース付加で生成するLacCerは，好中球における自然免疫応答に関与する．LacCerは，抗酸菌細胞壁の糖脂質リポアラビノマンナンの認識に関与し，SrcファミリーチロシンキナーゼLynによるシグナル伝達を介して貪食後の食胞成熟と殺菌機構の活性化に大きく寄与する．さらに，LacCerへのガラクトース，N-アセチルガラクトサミン付加で生じるグロボ系スフィンゴ糖脂質Gb3およびGb4は，血管内皮細胞やマクロファージにおけるTLR4活性化制御に関与することが報告されている．脂肪細胞におけるGM3の発現は，組織マクロファージに由来する炎症性サイトカインTNF-α やIL-1β の刺激によって誘導される．肥満時には，脂肪組織へのマクロファージ浸潤が生じ，炎症性サイトカイン産生による慢性炎症を介して，インスリン抵抗性を呈することがよく知られている．食欲抑制ホルモンであるレプチンの欠損によって肥満・メタボリックシンドロームを呈するob/obマウスや，高脂肪食によって誘導された肥満モデルマウスの脂肪組織ではマクロファージ浸潤・慢性炎症が生じるが，内臓脂肪組織におけるGM3の発現量とGM3S遺伝子（St3gal5）の発現を調べると，それらが大幅に亢進している．GM3などのスフィンゴ糖脂質は，細胞膜上で互いに集合したクラスター，すなわち，脂質マイクロドメインと呼ばれるシグナル伝達プラットフォームを形成する3．我々は，GM3の異常な発現上昇によって，細胞膜上におけるインスリン受容体の拡散速度が影響を受け，シグナル伝達効率が大きく制限されることでインスリン抵抗性を生じることを生細胞分子イメージング法によって示した．一方，GlcCer合成酵素阻害薬であるD-PDMPやGenz-123346を用いてGM3の合成を阻害すると，脂肪細胞におけるインスリン抵抗性が解除される．興味深いのは，GM3S KOマウスにおいては，全身のインスリン感受性が改善するだけでなく，肥満による慢性炎症も大きく緩和されていることである．このことは，インスリン抵抗性よりも上流で，

GM3を介した慢性炎症メカニズムが存在することを示唆している．メタボリックシンドロームに関連するTLR4リガンドには，肥満時に脂肪組織中の発現量や血清中への分泌量が増加する特徴があり，GM3もその特徴を満たしている．そこで，実際にGM3がTLR4を介して自然免疫応答を活性化する可能性を検討することにした．

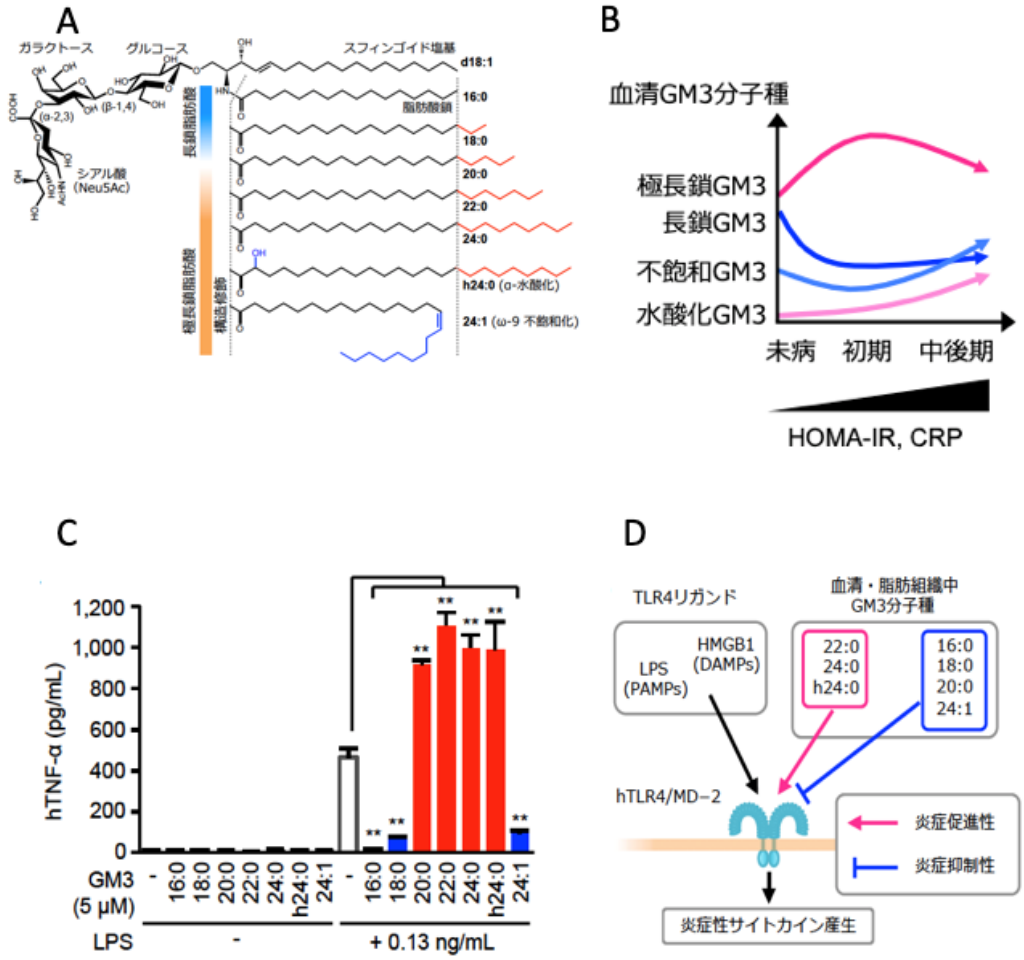

図１　GM3 分子種の自然免疫および肥満などの慢性炎症性疾患への関与
ガングリオシド GM3 の分子種多様性。 (B) GM3 分子種のメタボリックシンドローム発症過程における発現変化。(C) 極長鎖 GM3 分子種による TLR4 の活性化促進と長鎖 GM3 分子種による抑制。 (D) GM3 分子種による TLR4 活性化および抑制作用の構造活性相関。

GM3 には、異なるセラミド構造を持つ多様な分子種が存在する(図 1 A)．これらの GM3 分子種の血清中の発現パターンは，メタボリックシンドロームの発症過程で変動していた (図 1B)．これらの GM3 分子種の生理活性を検討したところ、極長鎖飽和・水酸化 GM3 分子種（C22:0,C24:0, hC24:0）は、LPS 刺激による TLR4 の活性化によるマクロファージからの TNFα や IL6 などの炎症性サイトカインの産生を著しく促進し

(図 1C)、炎症反応を増大させた．一方，長鎖 GM3 分子種（16:0, 18:0, 20:0）および不飽和 GM3 分子種（24:1, h24:1）は，炎症反応を抑制した (図 1C)．さらに、長鎖・不飽和 GM3 分子種は炎症促進性 GM3 の作用をキャンセルした．これらのことから，肥満やメタボリックシンドローム発症初期においては、GM3 分子種の炎症促進性シフトに伴って慢性炎症が生じていると考えられた(図 1B, D)．計算シミュレーションの結果からは、GM3 が TLR4 に直接結合している可能性が得られました．自然免疫に重要な役割を持っている TLR4 を介した慢性炎症は、多様な炎症性疾患やがんの発症にも深く関与しており、全身を循環する血清 GM3 分子種の発現変動パターンと，さまざまな疾患との関連性が明らかになれば、慢性炎症性疾患の新規診断・治療法の開発につながっていくものと期待さる（図 2）．

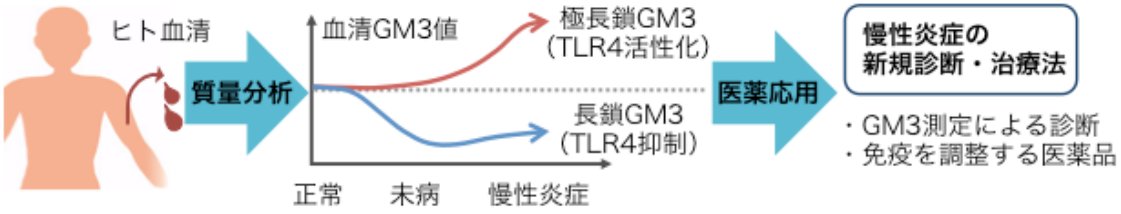

図 2　GM3 分子種にもとづく次世代の診断・治療法開発への発展性
血清中のガングリオシド GM3 の生理活性が判明したことにより、様々な医薬応用が期待できる。血清 GM3 の測定による病気の診断や、GM3 を応用した免疫抑制・活性化医薬品の開発などが挙げられる。

＜発表論文＞

１．Kanoh, H., Takahiro Nitta, T., Go, S., Inamori, K., Veillon, L., Nihei, W., Fujii, M., Kabayama, K., Shimoyama, A., Fukase, K., Ohto, U., Shimizu, T., Watanabe, T., Shindo, H., Aoki, S., Sato, K., Nagasaki, M., Yatomi, Y., Komura, N., Ando, H., Ishida, H., Kiso, M., Natori, Y., Yoshimura, Y., Cattaneo, A., Letizia, M., Zonca, A., Ciampa, M., Mauri, M., Prinetti, A., Sonnino, S., Suzuki, A. and Inokuchi, J. (2020) Homeostatic and Pathogenic Role of Ganglioside GM3 Molecular Species in TLR Signaling in Obesity. ***EMBO J*** 39: e101732 2020

２．Kato Y., Arakawa, S., Terasawa, K., Inokuchi, J., Iwata, T., Shimizu, S., Watabe, T. and Yokoyama, M-H. (2020) The ceramide analog　N-(1-hydroxy-3-morpholino-1-phenylpropan-2-yl) decaceramide induces large lipid droplet accumulation and highlights the effect of LAMP-2 deficiency on lipid droplet degradation. ***Bioorganis & medicinal chemistry letters*** DOI: 10.1016/j.bmcl.2019.126891

３． Inamori K. and InokuchiJ. (2020) Roles of Gangliosides in Hypothalamic Control of Energy Balance: New Insights. ***International journal of molecular sciences***
DOI: 10.3390/ijms21155349

４． 井ノ口仁一、稲森啓一郎、上村聡志、狩野裕考、新田昴大、二瓶弥、宍戸史、大野勲、鈴木明身　グライコリピドミクス 生化学　Vol.92, No.3, 323-335, 2020. DOI: 10.14952/SEIKAGAKU.2020.920323

＜学会発表＞

・ **潰瘍性大腸炎におけるスフィンゴ糖脂質の発現変化**
稲森啓一郎，小川仁，新田昴大，狩野裕考，遠藤克哉，佐藤賢一，中村保宏，柴田近，中川西修，丹野孝一，鈴木明身，井ノ口仁一
第 62 回日本脂質生化学会, 東京, 2020 年 5 月, 要旨集 120-121

・ **レプチンによる腎スフィンゴ糖脂質の発現誘導**
新田昂大、狩野裕考、稲森啓一郎、鈴木明身、赤井裕輝、森建文、
井ノ口仁一
第 62 回日本脂質生化学会, 東京, 2020 年 5 月, 要旨集 176-177

・**レプチンによる腎スフィンゴ糖脂質の発現誘導**
新田昂大, 狩野裕考, 稲森啓一郎, 鈴木明身, 井ノ口仁一 (東北医薬大・分生研・機能病態分子学)
第 14 回東北東鎖研究会, zoom 会議, 2020 年 8 月, 要旨集 12-13

・**Homeostatic and pathogenic roles of GM3 ganglioside molecular species in TLR4 signaling**
Jin-ichi Inokuchi
GLYCOT 2020 June 20-23, 2020 WEB conference:https://www.glycot2020.com

・ **潰瘍性大腸炎におけるスフィンゴ糖脂質の発現変化**
稲森啓一郎，小川仁，新田昴大，狩野裕考，遠藤克哉，佐藤賢一，中村保宏，柴田近，中川西修，丹野孝一，鈴木明身，井ノ口仁一
第 93 回日本生化学会大会, Web 開催, 2020 年 9 月, 要旨集 95

・**Homeostatic and pathogenic roles of GM3 ganglioside**
Jin-ichi Inokuchi
Sphingolipid Biology Oct. 5, WEB conference:
https://www.sphingolipidbiology.com/sphingoleaders/jin-ichi-inokuchi

・GM3 ガングリオシド分子種による Toll 様受容体 4 シグナルの恒常性維持と破綻の分子機構

狩野　裕考

第 14 回東北糖鎖研究会　2020 年 9 月

第 4 回箱守仙一郎賞 奨励賞受賞講演、要旨集 8-9

・ 潰瘍性大腸炎患者におけるスフィンゴ糖脂質の発現変化

稲森啓一郎，小川仁，新田昴大，狩野裕考，遠藤克哉，佐藤賢一，中村保宏，柴田近，中川西修，丹野孝一，鈴木明身，井ノ口仁一

第 39 回日本糖質学会年会，東京, 2020 年 11 月，要旨集

・ガングリオシドによる TLR4 シグナルの恒常性維持と破綻のメカニズムの解明

狩野　裕考

第 42 回東北薬学セミナー　2020 年 12 月（日本薬学会東北支部）

令和２年度東北支部奨励賞受賞講演

＜分子認識部門＞
教授　細野雅祐
講師　菅原栄紀
講師　立田岳生

レクチンの抗腫瘍メカニズムの解明と糖脂質のかかわり

１）がん細胞における Gb3 発現の抗がん剤感受性に与える影響について

スフィンゴ糖脂質の一種であるグロボトリアオシルセラミド（Gb3）は，ラクトシルセラミドを基質として α1,4-ガラクトース転移酵素（A4GALT）により合成される．最近，Gb3 が高度に蓄積しているファブリー病モデルマウスにおいて，アポトース関連分子の発現が増加しているとの報告がなされた．本年度は，Gb3 発現細胞として HeLa および A4GALT 強制発現 K562 (Gb3-K562)，Gb3 非発現細胞として A4GALT 欠損 HeLa (ΔGb3-HeLa)および K562 を用い，これらの細胞における Gb3 発現の抗がん剤感受性に対する影響について検討した．HeLa および ΔGb3-HeLa をビンクリスチン (6.25 ng/mL) およびシスプラチン (4 μM) で 48 時間処理した結果, ΔGb3-HeLa に対して HeLa の生存率はそれぞれ約 23% および約 25% 低下した．一方，K562 および Gb3-K562 では，ビンクリスチン (200 ng/mL)およびシスプラチン（25 μM）で 48 時間処理することにより，Gb3-K562 の生存率の方が K562 より約 19% および約 20% 低下した．また，ビンクリスチンおよびシスプラチン処理によるアポトーシス細胞の割合は Gb3 を発現している HeLa および Gb3-K562 の方が高いという結果が得られた．さらに，これらの抗がん剤はミトコンドリア経路を介したアポトーシスを誘導することから，この経路にかかわる Bcl-2，BcL-xL，Bax, Bim, AIF および Apaf-1 に着目し，HeLa および ΔGb3-HeLa における遺伝子発現量を調べた．その結果，アポトーシス抑制因子である Bcl-2 の発現は ΔGb3-HeLa で約 40% 高く，アポトーシス促進因子である AIF および Apaf-1 の発現量は約 30 から 40% 低かった．これらの結果から，Gb3 を発現しているがん細胞では，内因性アポトーシス制御分子の発現が変化し，抗がん剤感受性が増加する可能性が示唆された．Gb3 は細胞内膜系および細胞膜に存在することから，今後，抗がん剤感受性に直接関与する Gb3 分子の局在について詳細に検討していく．

２）がん細胞におけるナマズ卵レクチンの細胞内局在部位について

ナマズ卵レクチン（SAL）は，Gb3 の糖鎖に結合することを報告しているが，結合後の SAL の輸送形態および増殖抑制に関わる機能発現メカニズムについて検討している．昨年度，蛍光標識 SAL（HL-SAL）を用いた実験により，SAL はバーキットリンパ腫細胞株 Raji 細胞内へ取り込まれるが，この取り込みは，脂質ラフト介在型エンドサイトーシス阻害剤であるメチル-β-シクロデキストリン（MβCD）で抑制されること

を報告した．本年度は，エンドサイトーシス時に細胞膜から小胞体を分離する際に機能するダイナミンを阻害する Dyngo-4a およびクラスリン依存性エンドサイトーシス阻害剤 Pitstop2 を用い，より詳細な細胞内取り込み機構の解析を行った．その結果，Dyngo-4a 処理により HL-SAL の取り込みが阻害された．一方，クラスリン依存性エンドサイトーシス阻害剤 Pitstop2 では HL-SAL の取り込みは抑制されなかった．また，脂質ラフト介在型エンドサイトーシスには，カベオラの主要構成タンパク質であるカベオリン-1 を必要とする経路が存在する．Raji におけるカベオリン-1 および 2 の発現を調べた結果，どちらも発現していないことが示された．さらに細胞内に取り込まれた後，SAL がどのような部位に局在するのかをゴルジ体に着目して検討した．ゴルジ体のマーカータンパク質に対する抗体を用いて SAL 処理 Raji におけるゴルジ体の局在を免疫染色法により調べた結果，HL-SAL はゴルジ体の染色像と同様の局在を示すことが分かった．これらの結果から，SAL は Gb3 に結合した後，カベオラ非依存性脂質ラフトエンドサイトーシスにより細胞内に取り込まれた後，ゴルジ体に局在する可能性が示唆された（下図）．今後，取り込まれた SAL の細胞内部におけるさらに詳細な挙動および局在部位の解析を行い，SAL が Gb3 発現がん細胞に与える影響との関連を明らかにするとともに，SAL の細胞選択的キャリアーとしての可能性について検討していく．

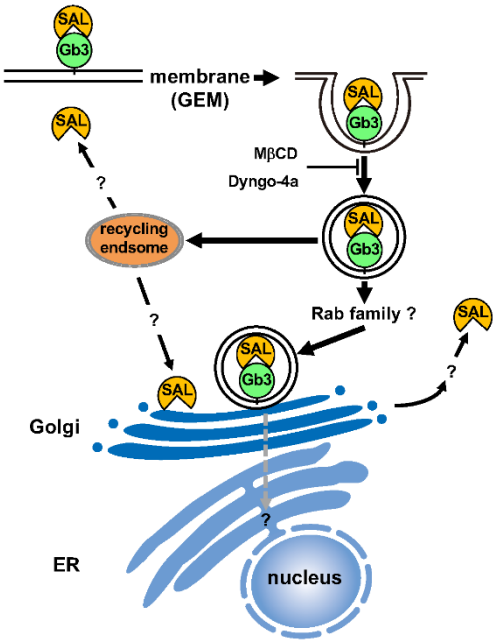

３）ウシガエルのシアル酸結合レクチン（cSBL）は，レクチンおよびリボヌクレアーゼ活性を併せ持つ多機能タンパク質である．また，正常細胞への毒性が低く，多くの種類のがん細胞に対して高い抗腫瘍活性を発揮する．cSBL による RNA 分解

は，アポトーシス誘導を実行するための重要なステップの 1 つであり，また抗がん剤の新規標的となりうる．しかし，cSBL がどのように抗腫瘍効果を発揮するのか，そのメカニズムについては未だ不明な点が多い．本研究室では，昨年度までに cSBL 耐性 (cSR) 細胞を樹立した．本年度は，その抗腫瘍メカニズムをさらに解明するため，cSR 細胞の性状解析を行った。

cSBL に対して高感受性の悪性中皮腫細胞株である H28 細胞を使用し，細胞培養の際に低用量の cSBL を添加し，継続培養することにより，cSBL 耐性（cSR）細胞を作製した．その後，限界希釈法により 5 つのクローンを得た．耐性度の高い cSR 細胞クローン (cSR-A1，-B1）の細胞増殖，形態および化学療法剤感受性および cSR-B1 における cSBL 誘導アポトーシスの解析を，細胞数測定，顕微鏡下による観察および WST-8 アッセイならびにウェスタンブロットによるカスパーゼ 3 の活性化観察によりそれぞれ行った．その結果，細胞増殖および形態に関して，H28 細胞と cSR 細胞の間に大きな差は認められなかった．cSR 細胞は他の抗腫瘍性 RNase (オンコナーゼ : ONC) に対しては耐性を示す傾向にあったが，DNA 傷害型薬剤であるドキソルビシンに対しては交差耐性を示さず，cSBL 誘導アポトーシスにおいても大きな差は認められなかった．また，これまでにマイクロアレイ解析により cSR 細胞における発現変動のあった遺伝子（differentialy expressed genes :DEGs）を多数検出しており，cSR における多面的な遺伝子発現変化が明らかになっている．cSR で発現が減少している DEGs に着目したところ，複数の Aldo-keto reductase (AKR) ファミリー遺伝子が著しく低下していることが明らかになった (Table I)．がんとの関連が報告されている AKR1B10 に注目し，その発現がタンパク質レベルでも顕著に低下していることを確認した (Fig. 1)．AKR ファミリーは，脂質，糖質その他の異物など，基質のカルボニル基を可逆的にアルコール基に還元する酵素である． AKR1B10 は，一部のがんで高発現することが報告されており，その理由としてレチノイン酸代謝に関与し，その産生を低下させることでがん細胞の増殖および生存を促進することが知られている．また CDDP，Mitomycin C，アントラサイクリン系（DOX および Idarubicin）および Docetaxel などの抗がん剤に対するがん細胞の耐性化に関与していることが示唆されている．したがって AKR1B10 は，がんのバイオマーカーとしてだけではなく，がん治療の新しい治療標的となる可能性がある．そこで，その発現低下作用を有する cSBL の機能は興味

深い．今回の知見をもとに，cSBL の抗腫瘍効果における新しい側面を明らかにし，新規の抗がん治療戦略への応用につなげていきたいと考えている．

Table 1. Gene expression changes of AKR family in cSR cells.

Gene symbol	Fold change[1]
AKR1B15	-562.0
AKR1B10	-548.5
AKR1C1	-54.0
AKR1C4	-24.7
AKR1B1	-11.4
AKR1C3	-9.1

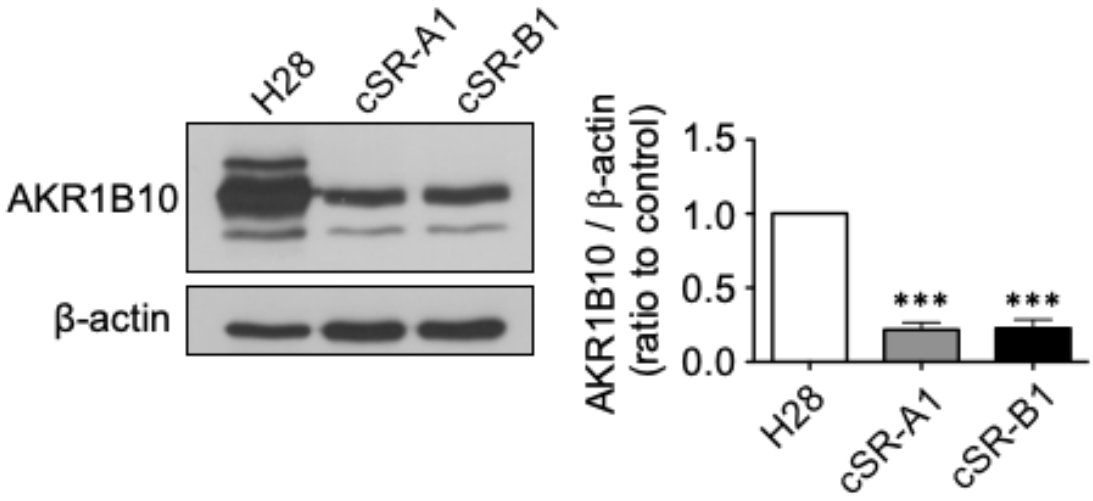

Fig. 1 AKR1B10 protein expression in H28 and cSR cells. AKR1B10 protein expression in H28 and cSR cells. The expression of AKR1B10 in each cell line was detected by western blotting. Densitometric quantification was performed using the results of three independent experiments (mean ± SD). ***P < 0.001. cSR: bullfrog sialic acid-binding lectin-resistant; SD: standard deviation

＜発表論文＞

1. Catfish egg lectin affects influx and efflux rates of sunitinib in human cervical carcinoma HeLa cells. S. Sugawara, M. Takayanagi, S. Honda, T Tatsuta, Y. Fujii, Y. Ozeki, J. Ito, M. Sato, M. Hosono, ***Glycobiology*, 30**, 802–816 (2020).
2. Bacterial Expression of Rhamnose-Binding Lectin from Catfish Eggs. S. Sugawara, T. Tatsuta, M. Hosono, *Methods in Molecular Biology* 2132, "Lectin Purification and Analysis", pp359-367, Ed. by Jun Hirabayashi, Humana Press, Springer Nature, New York, 2020.

＜学会発表＞

・がん細胞におけるナマズ卵レクチンの細胞内局在部位について
菅原栄紀，八木橋佳章，立田岳生，細野 雅祐
第 14 回東北糖鎖研究会，仙台，2020 年 8 月，要旨集 p.3

・がん細胞における Gb3 の発現量が抗がん剤感受性に与える影響について
八木橋佳章，菅原栄紀，市山遙汰，立田岳生，細野 雅祐
第 59 回日本薬学会東北支部大会，いわき，2020 年 10 月，要旨集 p.43

・尿路上皮癌におけるシアリダーゼ Neu3 の役割
伊藤淳，立田岳生，黒本 暁人，菅原栄紀，細野 雅祐，佐藤　信
第 79 回日本癌学会学術総会，広島，2020 年 10 月，OJ14-11-5

・ナマズ卵レクチンの取り込み受容体としての細胞膜 Gb3
菅原栄紀，八木橋佳章，立田岳生，細野 雅祐
第 39 回日本糖質学会年会，東京，2020 年 11 月，要旨集 p.123

・両生類由来シアル酸結合性レクチンの抗微生物活性
吉田史姫、福田百香、田中宏光、立田岳生、菅原栄紀、細野雅祐、藤井佑樹、大関泰裕、小川由起子
第 141 回日本薬学会年会，広島，2021 年 3 月，要旨 28P01-125S

・cSBL 耐性悪性中皮腫細胞の性状解析
立田岳生，中里ありす，菅原栄紀，細野 雅祐
第 141 回日本薬学会年会，広島，2021 年 3 月，要旨 28P02-180

＜細胞制御学＞
教授　　顧 建国
准教授　福田 友彦
講師　　伊左治 知弥

膵がんにおける FUT8 発現の意義と細胞接着における O-GlcNAc 修飾の機能

がんは、人口の高齢化と相俟ってその発症率が世界的に年々上昇し、日本では国民の 2 人に 1 人が生涯に一度はがんに罹患し、3 人に 1 人ががんで命を落とす時代となり、その制御が極めて大きな課題となっている。がんの治療としては、外科療法、放射線療法と化学療法の 3 大療法が長く使われてきた。その後、多くの研究者により、細胞増殖、血管新生あるいは細胞死抑制に関与する多くの成長因子やサイトカインなどの個々の働きに注目した研究が精力的に進められ、近年、第 4 のがん治療法と言われるがん細胞で異常を示すシグナル分子を標的とする分子標的療法が注目されている。

しかし、個々の分子機構が解明され、その機能を制御しても、がん治療の効果の著しい向上は見られない。実際分子標的療法が有効ながんは、がん全体の約 30%程度と考えられ、耐性腫瘍の出現による再発も多く、また残りの約 70%の腫瘍では、いまだに有効な治療法が確立されておらず、更なる抜本的な治療法の開発が待たれている。がんに対する根本的な治療法は、がん細胞の増殖•浸潤•転移に関わる多くの分子機能を同時に制御できることが必要であると私達は考えている。糖鎖はその有力な候補の一つである。細胞ががん化すると細胞表面の糖鎖が変化することは、よく知られている。実は、増殖因子、接着分子及びサイトカインの受容体の殆どは糖タンパク質であり、糖鎖修飾がそれらの機能制御に大事であることが明らかになりつつある。

糖鎖修飾の中で特に注目されるものの一つがコアフコースである。それは、コアフコースがフコース転移酵素(Fut8)により生合成され、肝がんの特異的バイオマーカーや抗体依存性細胞傷害活性(ADCC)とも深く関わる。また、T 細胞上の免疫チェックポイントである PD-1 のコアフコースの発現を下げることによって、T 細胞の活性化を介したがん細胞の排除効果が有意に高まることが明らかになった　(Okada, et al. Cell Rep. 2017)。その分子機序が PD-1 のコアフコース付加が抑制されると PD-1 のユビキチン化が有意に増強し、PD-1 の分解を促進することを、中国大連医科大学と共同研究によって明らかにした（1）。一方、私達は、コアフコースが肝がんの形成に重要な役割を果たすことを証明した(Wang et al. FASEB J., 2015)。更に、L-フコースのアナログである 2-fluorofucose (2FF, Fut8 のドナーである GDP-fucose 合成の阻害剤; Okeley, et al., PNAS. 2013)でコアフコシル化を抑えることによって、肝がん細胞の腫瘍形成能が強く抑制できることも証明した(Zhou et al Sci. Rep., s41598, 2017)。

最近、私達は膵がんにも興味を持って研究を行ってきた。膵がんは、5 年生存率が他のがんと比較して極めて低い。その理由の一つに、膵がんは、早期のうちから浸潤・転移しやすいことが挙げられる。さらに、膵臓周辺は組織が複雑に入り組んでいて、手術が難しいため、残ったがん細胞が再び増殖する可能性が高いためと考えられている。がん化に伴いがんマーカーとなる特徴的な糖鎖構造が現れるが、コアフコシル化の変化はいくつかのがんにおいて、腫瘍の増殖や転移など生理的に重要であることがわかっている。膵がんでも FUT8 の発現がアップレギュレーションされるが、膵がんの特徴である浸潤・転移しやすさとコアフコシル化の関係は未解明である。膵がんの予後不良に対する FUT8 の役割を明らかにするため、膵がんの研究に広く用いられている MIA PaCa-2 や PANC-1 細胞株に CRISPR/Cas9 を用いて FUT8 を欠損させた細胞を作成し、膵がんにおける FUT8 の機能を明らかにした（図 1）(2)。

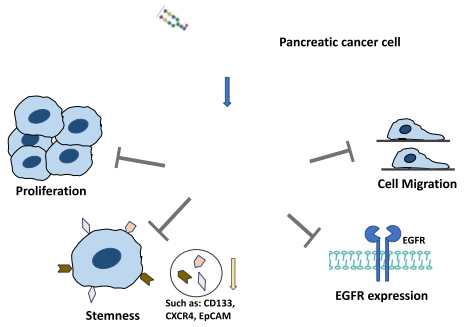

膵がん細胞におけるコアフコースの機能

トランスウェルおよびスクラッチアッセイによる細胞遊走能を検討したところ、FUT8 欠損 MIA PaCa-2 細胞は野生型に比べて、約 80%と顕著な遊走能の阻害が認められた。また、MTT およびコロニー形成による細胞増能を検討したところ、いずれの方法でも FUT8 欠損細胞は 50%以下に減少し、細胞表面における増殖因子受容体数も減少していた。さらに、2FF を添加によりコアフコシル化を阻害しても、FUT8 欠損細胞と同様に、増殖・遊走に対する抑制が確認された。FUT8 欠損により、腫瘍増殖抑制作用が期待されたため、免疫不全マウス皮下に移植したところ、生着・増殖は認められるが、有意な腫瘍増殖抑制作用が認められた。そこで、再発・転移に重要な役割を果たすと考えられているがん幹細胞性に与える影響を検討した。まず、癌幹細胞マーカーの発現を検討したところ、FUT8 欠損細胞では、CD133, CXCR4, C-Met, EpCAM などの発現が減少していた。次に、がん細胞同士の相互作用を検討するため、スフェロイドを形成させたところ、FUT8 欠損細胞では細胞間の凝集が弱く不安定であることが分かった。ヒト膵臓腺癌由来の PANC-1 細胞でも MIA PaCa-2 細胞株と同様の結果がえられた。さらに、がん幹細胞の特徴の一つである薬物耐性に対しても検討した。その結果、FUT8 の欠失は、膵がんの治療薬である Gemcitabine に対する応答性を高めた。これらの結果は、FUT8 の発現が無くなると、幹細胞性が失われることを示唆している。以上のことから、FUT8 が膵がん細胞において重要な生物学的機能を果たしていることが明らかで、実験的ではあるものの、2FF の投与でも FUT8 欠損細胞と同様の効

果が得られたことは、FUT8 の機能制御を介して、膵がん幹細胞を標的とした治療などの可能性が示された。

また、私達は、インテグリンや増殖因子受容体の下流の非受容体タンパク質チロシンキナーゼである Focal adhesion kinase(FAK)による O-GlcNAc 修飾にも注目して解析を進んでいる。一昨年、私達はドキソサイクリン(DOX)添加により、O-GlcNAc トランスフェラーゼ(OGT)ノックダウン(KD)が誘導される HeLa 細胞と 293T 細胞を樹立・解析し、1) 接着斑で複合体を形成する FAK、Paxillin、Talin に O-GlcNAc が付加している; 2) OGT-KD 細胞では異常な接着斑が形成され、かえって細胞移動が抑制され、接着斑を制御する多くのタンパク質が集積していることを明らかにした (Xu, Z., Isaji, T., et al., JBC, 2019)。しかし、FAK のどの位置に O-GlcNA c が結合するか、また、それぞれの修飾が細胞増殖や細胞伸展などの機能に与える影響など不明点が多く残されている。

これらの疑問を明らかにするため、LC-MS/MS を用いて３カ所の O-GlcNAc サイトを同定した。その３カ所の修飾は、細胞の増殖、伸展および FAK の核移行に対する影響が異なっていることを見出した。同定した３カ所の O-GlcNAc 修飾およびそれぞれの機能に関して、更なる詳細な分子機序の解析が必要である。また、主に HeLa 細胞を用いて研究を行なって来たが、他の細胞でも同じの働きをしているかを調べ、細胞間での共通性と特異性を明らかにする。さらに、O-GlcNAc 修飾された FAK を特異的に認識する抗体を作成し、がんなど様々な疾患における FAK の O-GlcNAc 修飾変化を調べることで、疾患のバイオマーカーや治療薬開発への基礎的な知見の提供を目指す。

＜論文発表＞

1. Loss of core fucosylation enhances the anticancer activity of cytotoxic T lymphocytes by increasing PD-1 degradation. Zhang, N., Li, M., Xu, X., Zhang, Y., Liu, Y., Zhao, M., Li, P., Chen, J., Fukuda, T., Gu, J., Jin, X. and Li, W. ***Eur J Immunol.*** 50, 1820-1833, 2020
2. α1,6-Fucosyltransferase contributes to cell migration and proliferation as well as to cancer stemness features in pancreatic carcinoma. Liang C., Fukuda, T., Isaji, T., Duan, C., Song, W., Wang, Y. and Gu, J. ***Biochim Biophys Acta Gen Subj.***, 1865: 3239-3252. 2021
3. Loss of core fucosylation suppressed the humoral immune response in Salmonella typhimurium infected mice. Zahid, D., Zhang, N., Fang, H., Gu, J., Li, M. and Li, W. ***J Microbiol Immunol Infect.*** pii: S1684-1182(20)30034-7. doi: 10.1016/j.jmii.2020.02.006, 2020

4. Loss of core fucosylation in both ST6GAL1 and its substrate enhances glycoprotein sialylation in mice. Huang, G., Li, Z., Li, Y., Liu, G., Sun, S., Gu, J., Kameyama, A., Li, W. and Dong, W. ***Biochem J.*** 477:1179-1201. doi: 10.1042/BCJ20190789, 2020
5. Core Fucosylation of Intestinal Epithelial Cells Protects against Salmonella Typhi Infection via Up-regulating the Biological Antagonism of Intestinal Microbiota. Hao, S., Fan, Q., Yaqiang Bai, Y., Zhou, J., Fang, H., Fukuda, T., Gu, J., Li, M. and Li, W. ***Front. Microbiol***. 11:1097. doi: 10.3389/fmicb.2020.01097, 2020.
6. A novel immunochromatographic strips assay for rapid and simple detection of systemic lupus erythematosus. Sun, Y., Li, Z., Liang, W., Zhang, Y., Song, W., Song, J., Xue, K., Wang, M., Sun, W., Gu, J., Li, M. and Li, W. ***Sci Rep.*** 10, 14178, 2020

＜学会発表＞

・**Deficiency of core fucosylation activates FLT3 signaling via induction of dimeric formation**

Chengwei Duan, Tomohiko Fukuda, Tomoya Isaji, Shinichiro Takahashi and Jianguo Gu

12th International Symposium on Glycosyltransferases (GlycoT2020), Web 開催, 2020 年 6 月

・ **FUT8 の発現は膵がん細胞の移動・増殖・がん幹細胞性に重要な役割を果たす**

梁彩霞, 福田友彦, 伊左治知弥, 顧建国

第 14 回東北糖鎖研究会, Web 開催, 2020 年 8 月, P. 27

・**接着斑キナーゼ(FAK)の O-GlcNAc 修飾による細胞機能への影響**

大山嘉順, 伊左治知弥, 福田友彦, 顧建国

第 14 回東北糖鎖研究会, Web 開催, 2020 年 8 月, P. 28

・**FLT3 を介したシグナル伝達におけるコアフコシル化の重要性**

段 程偉, 福田友彦, 伊左治知弥, 髙橋伸一郎, 顧建国

第 14 回東北糖鎖研究会, Web 開催, 2020 年 8 月, P. 10

・**シアリル化等による膜受容体の選別輸送ゾーンの特異性とその制御機構の解明**

顧建国

第 1 回オルガネラゾーン 研究会, Web 開催, 2020 年 8 月

・**インテグリンと FLT3 受容体における糖鎖機能と制御機構**

顧建国, 伊左治知弥, 福田友彦

第 93 回日本生化学会, Web 開催, 2020 年 9 月, P. 46

・**膵がん細胞の遊走・増殖・がん幹細胞的性質保持における FUT8 発現の重要性**

福田友彦, 梁彩霞, 伊左治知弥, 顧建国

第 39 回日本糖質学会年会, 誌上開催, 2020 年 11 月

・**糖鎖修飾阻害薬の急性前骨髄球性白血病細胞のレチノイン酸分化誘導に及ぼす影響に関する解析**

沖津庸子, 福田友彦, 顧建国, 髙橋伸一郎

第 67 回日本臨床検査医学会, Web 開催, 2020 年 11 月, P. 209

・**シアリル化等による膜受容体の選別輸送ゾーンの特異性とその制御について**

伊左治知弥, 顧建国

第二回オルガネラゾーンオルガネラゾーン若手の会, web 開催, 2020 年 12 月

・**糖鎖による膜受容体の選別輸送ゾーンの特異性とその制御機構の解明**

顧建国, 福田友彦, 伊左治知弥

第２回オルガネラゾーン 研究会, Web 開催, 2020 年 12 月

＜薬品物理化学部門＞
教授　山口 芳樹
講師　真鍋 法義
助手　大野 詩歩

糖鎖構造解析のための技術基盤の構築

生体分子としての糖鎖の機能を明らかにするためには，糖鎖の立体構造の特徴を理解し，レクチンや抗体など糖鎖結合分子による認識の構造基盤を解明することが重要であるとの立場で研究を進めている．本年度は分子生体膜研究所の一員となり 2 年目を迎え，昨年度に引き続き，糖鎖構造解析（実験および計算）の技術基盤の構築，および糖鎖関連の組み換え蛋白質の大量発現システムの構築を目指した．

I.　糖タンパク質の構造機能相関の解析と応用

近年構造生物学分野においてクライオ電顕に対する期待は大きく，結晶化に不向きな蛋白質（糖タンパク質，膜蛋白質，蛋白質線維，超分子複合体など）の構造解析例は今後ますます増えていくものと思われる．しかしながら，一般に糖鎖は自由度が高いため，X 線結晶構造解析やクライオ電顕の解析においても糖鎖全体の電子密度像を与えるケースは稀である．一方で，NMR 法は生体分子のダイナミクスを提供する方法として優れており，糖タンパク質糖鎖の NMR データはクライオ電顕・X 線結晶構造解析のデータを補完するものであり，相補的である．このような背景を踏まえつつ，最近の糖鎖構造解析技術をまとめた(1).

免疫グロブリンは，糖鎖の機能が最も研究された糖タンパク質の一つであるが，依然として不明な点も残されている(2)．今回我々はマウス IgG2b の Fc フラグメントを対象としたこれまでの NMR 解析データをまとめ，Fc に結合している糖鎖の切断に伴うポリペプチドの構造変化についての議論を行った(3)．近年では，バイオ医薬品・抗体-薬物複合体としての抗体の利用も増加しており，糖鎖の構造とその機能制御にますます注目が集まっている．抗体-薬物複合体の合成とがん間質をターゲットとした戦略についてまとめた(4).

糖鎖の構造機能相関を議論するにあたり，*N*-結合型糖鎖の構造決定メカニズムを知ることも重要になる．特に *N*-結合型糖鎖の分岐は標的糖タンパク質の機能を調節することがあり，*N*-結合型糖鎖の分岐構造の形成を担う糖転移酵素の立体構造に関する知見が求められている．*N*-結合型糖鎖の分岐構造を形成する糖転移酵素の構造活性相関について立体構造から議論した(5).

II. レクチン受容体の構造と機能に関する研究

レクチンは糖鎖を認識する分子として幅広く生体内で機能しているが，構造活性相関についてはいまだ不明な点が多い．例えば Siglec-7 はシアル酸に依存した免疫受容体として機能していると考えられているが，そのシアル酸結合と機能の関係は不明のままである．Siglec-7 のリガンド結合についての理解を深めるために，計算と部位特異実験を行った．その結果，従来よく知られているリガンド結合部位に加えて第２の結合サイトを見出した(6).

我々はこれまで主に C 型レクチン受容体の共通のフォールドから糖鎖結合の多様性はどのように生み出されるかという問題を設定して構造解析を行ってきた．構造解析を通じて得た知見および他グループの報告も引用しながら，C 型レクチン受容体の糖鎖認識様式をまとめて発表した(7).

C 型レクチン様受容体の一種である Dectin-1 も C 型レクチンフォールドを有するが，β グルカンの受容体として機能している．β グルカンの立体構造と Dectin-1 を含む β グルカン受容体の構造と機能の関係についてこれまでの知見を総説してまとめた(8).

III. 安定同位体利用 NMR 法による構造解析技術の構築

測定対象とする分子に安定同位体標識を施すことにより，通常では得られないユニークな情報を引き出すことが可能になる．糖鎖の水酸基は，そのコンフォメーションや分子間相互作用の決定要素として機能しているが，通常の溶液 ^{1}H-NMR では解析を行うことが困難である．本研究ではモデル化合物として 6 位が ^{17}O 標識されたグルコサミンを化学合成し(図１)，その固体 ^{17}O-NMR 測定を行った．その結果，^{17}O 化学シフトと電場勾配テンソルを見積もることに成功した(9).

β グルカンのような多糖はグルコース残基の繰り返しの構造となっており，部位特異的な情報を取り出すのは困難である．本研究では，β グルカン短鎖に ^{13}C, ^{2}H の部位特異的標識を行い，部位特異的な NMR 情報を抽出することに成功した(10)．β グルカンの鎖長・分岐とコンフォメーションの関係については不明な点が多く，問題解決の第一歩となった．

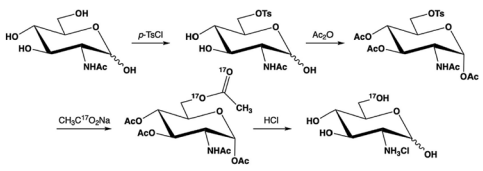

図１ [6-^{17}O]D-glucosamine ·HCl の化学合成(9)

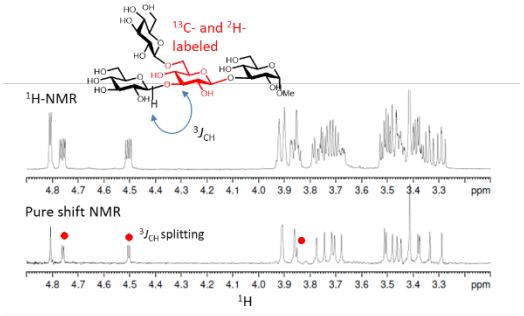

図２ ^{13}C, ^{2}H の部位特異的標識を施した β グルカン短鎖(10)の NMR スペクトル

IV. Intrinsically disordered protein のダイナミクス・相互作用の解析

神経変性疾患に関与する蛋白質の多くは特定の立体構造を形成しておらず，そのような蛋白質は intrinsically disordered protein と呼ばれている．これらの蛋白質が，どのようなメカニズムで集合し，特徴的な線維構造を形成するかは不明な点が多い．プリオンタンパク質は，外来のプリオン凝集体と遭遇することにより，種の壁を越えて凝集が誘導されることがある．しかしながら，種の壁を越えたプリオンタンパク質の凝集のメカニズムは不明であった．酵母プリオンタンパク質をモデルとして解析したところ，プリオン非常に短い領域の特定のコンフォメーションが種間の感染を制御していることが明らかになった(11).

脳内に蓄積する蛋白質線維を感度よく検出することは，神経変性疾患の発症を早期に捉えることにつながるため，様々な PET プローブが世界中で開発されている．しかしながら，PET プローブと蛋白質線維との相互作用の様式は不明な点が多い．本研究では，tau 線維と PET 化合物の相互作用様式をドッキングおよび分子動力学計算により解析した．その結果，複数の PET 化合物結合部位を提示し，各サイトにおける結合エネルギーを算出した(12,13).

V. 計算化学・データベースの基盤構築

糖鎖の立体構造・ダイナミクスの解析には NMR 法などの実験的手法に加えて，分子動力学計算などの計算化学的手法が必要になる．今回，糖鎖の分子動力学計算についての現状をまとめ，総説として発表した(14).

またデータベースから，糖鎖立体構造・相互作用の法則性を見出すことを進めており，現在は抗糖鎖抗体の立体構造データを集積し，データの分類・解析を進めている．合わせて抗体の超可変領域を含む Fv 領域のモデリングおよびドッキングの検討を引き続き行っている．

VI. その他

本年度も内外の共同研究を進め，主に生体分子の NMR 解析を行うことによって成果発表に貢献した．β-グルコセレブロシダーゼ（GBA）はグルコシルセラミド（GlcCer）を加水分解する酵素である．本論文では，GBA1 と GBA2 は，ガラクトシルセラミド（GalCer）のガラクトース残基をコレステロールに転移し β-コレステリルガラクトシド（β-GlcChol）を形成することを見出した(15).

アネキシン（ANX）はリン脂質や硫酸基を持つ糖脂質と結合することにより，知液凝固を制御することが知られていたが，その生理的や役割は部分的にしかわかっていなかった．本研究では ANX4 はスルファチドによって誘導される Factor XII の自己活性化を阻害すること，また ANX4 の後半の領域がその活性に関わっていることを明らかにした(16).

＜発表論文＞

1. 山口芳樹. (2020) 糖鎖立体構造解析技術の開発要素. *生化学* **92**, 369-377
2. Yamaguchi, Y., and Barb, A. W. (2020) A synopsis of recent developments defining how N-glycosylation impacts immunoglobulin G structure and function. *Glycobiology* **30**, 214-225
3. Yanaka, S., Yamaguchi, Y., Takizawa, T., Miyanoiri, Y., Yogo, R., Shimada, I., and Kato, K. (2021) NMR assignments of the N-glycans of the Fc fragment of mouse immunoglobulin G2b glycoprotein. *Biomol NMR Assign* **15**, 187-192
4. 眞鍋史乃, 山口芳樹, 松村保広. (2020) 有機合成化学/糖質化学は抗体-薬物複合体開発にどのように貢献できるか：糖鎖連結均一抗体-薬物複合体合成とがん間質ターゲティング療法の開拓. *有機合成化学協会誌* **78**, 485-494
5. Nagae, M., Yamaguchi, Y., Taniguchi, N., and Kizuka, Y. (2020) 3D structure and function of glycosyltransferases involved in N-glycan maturation. *Int J Mol Sci* **21**, 437
6. Yamakawa, N., Yasuda, Y., Yoshimura, A., Goshima, A., Crocker, P. R., Vergoten, G., Nishiura, Y., Takahashi, T., Hanashima, S., Matsumoto, K., Yamaguchi, Y., Tanaka, H., Kitajima, K., and Sato, C. (2020) Discovery of a new sialic acid binding region that regulates Siglec-7. *Sci Rep* **10**, 8647
7. Nagae, M., and Yamaguchi, Y. (2020) Structural aspects of carbohydrate recognition mechanisms of C-type lectins. *Curr Top Microbiol Immunol* **429**, 147-176
8. Manabe, N., and Yamaguchi, Y. (2021) 3D structural insights into b-glucans and their binding proteins. *Int J Mol Sci* **22**, 1578
9. Yamada, K., Yamaguchi, Y., Uekusa, Y., Aoki, K., Shimada, I., Yamaguchi, T., and Kato, K. (2020) Solid-state ^{17}O NMR analysis of synthetically ^{17}O-enriched D-glucosamine. *Chem. Phys. Lett.* **749**, 137455
10. Hamagami, H., Yamaguchi, Y., and Tanaka, H. (2020) Chemical synthesis of residue-selectively ^{13}C and ^{2}H double-isotope-labeled oligosaccharides as chemical probes for the NMR-based conformational analysis of oligosaccharides. *J Org Chem* **85**, 16115-16127
11. Shida, T., Kamatari, Y. O., Yoda, T., Yamaguchi, Y., Feig, M., Ohhashi, Y., Sugita, Y., Kuwata, K., and Tanaka, M. (2020) Short disordered protein segment regulates cross-species transmission of a yeast prion. *Nat Chem Biol* **16**, 756-765
12. Tagai, K., Ono, M., Kubota, M., Kitamura, S., Takahata, K., Seki, C., Takado, Y., Shinotoh, H., Sano, Y., Yamamoto, Y., Matsuoka, K., Takuwa, H., Shimojo, M., Takahashi, M., Kawamura, K., Kikuchi, T., Okada, M., Akiyama, H., Suzuki, H.,

Onaya, M., Takeda, T., Arai, K., Arai, N., Araki, N., Saito, Y., Trojanowski, J. Q., Lee, V. M. Y., Mishra, S. K., Yamaguchi, Y., Kimura, Y., Ichise, M., Tomita, Y., Zhang, M. R., Suhara, T., Shigeta, M., Sahara, N., Higuchi, M., and Shimada, H. (2021) High-contrast in vivo imaging of tau pathologies in Alzheimer's and non-Alzheimer's disease tauopathies. *Neuron* **109**, 42-58 e48

13. Mishra, S. K., Yamaguchi, Y., Higuchi, M., and Sahara, N. (2020) Pick's tau fibril shows multiple distinct PET probe binding sites: Insights from computational modelling. *Int J Mol Sci* **22**, 349
14. Re, S., Yamaguchi, Y., and Sugita, Y. (2020) Molecular dynamics simulation of glycans. *Trends Glycosci. Glycotechnol.* **32**, E113-E118, J193-J198
15. Akiyama, H., Ide, M., Nagatsuka, Y., Sayano, T., Nakanishi, E., Uemura, N., Yuyama, K., Yamaguchi, Y., Kamiguchi, H., Takahashi, R., Aerts, J., Greimel, P., and Hirabayashi, Y. (2020) Glucocerebrosidases catalyze a transgalactosylation reaction that yields a newly-identified brain sterol metabolite, galactosylated cholesterol. *J Biol Chem* **295**, 5257-5277
16. Nakayama, M., Miyagawa, H., Kuranami, Y., Tsunooka-Ota, M., Yamaguchi, Y., and Kojima-Aikawa, K. (2020) Annexin A4 inhibits sulfatide-induced activation of coagulation factor XII. *J Thromb Haemost* **18**, 1357-1369

＜学会発表＞

・**糖鎖構造の多様性の生物学的意義を求めて**

山口 芳樹

第 16 回機能性糖鎖研究会，鳥取，2020 年 1 月，16:30-18:00

・**NMR analysis of glycolipid in aqueous solution**

Yoshiki Yamaguchi

International Symposium on Glyco-lipidologue, Wako, Japan, Jan. 2020, 16:05-16:35

・**計算化学によるリビトールのコンフォメーション空間の解析**

大野 詩歩，真鍋 法義，山口 芳樹

日本薬学会第 140 年会，京都，2020 年 3 月，演題番号 27P-am103

・**紫外線照射によるトリプトファン残基の化学構造変化**

真鍋 法義，星 憲司，大野 詩歩，山口 芳樹

日本薬学会第 140 年会，京都，2020 年 3 月，演題番号 27P-am079

・**完全重水素化シクロデキストリンの酵素化学合成と糖脂質の NMR 解析への応用**

山口 芳樹，眞鍋 史乃，Peter Greimel，伊藤 幸成

日本薬学会第 140 年会，京都，2020 年 3 月，演題番号 27H-pm13

・**糖鎖認識抗体によるエピトープ認識の分子基盤**

川嵜 敏祐，中尾 広美，川嵜 伸子，築地　信，稲垣 優希，吉田 昌宏，山口 芳樹，天野 裕之，大野 詩歩，真鍋 法義

第 93 回日本生化学会大会，京都，2020 年 9 月，演題番号 P-046(2Z01-11)

・**免疫グロブリン G 結合糖鎖の立体構造データの調査**

佐藤 いずみ，大野 詩歩，真鍋 法義，山口 芳樹

第 14 回東北糖鎖研究会，仙台オンライン開催，2020 年 8 月，演題番号 O-5

・**糖鎖認識抗体の設計を目指した特異的 CDR 配列の検討**

瀬川 千夏，真鍋 法義，大野 詩歩，山口 芳樹

第 14 回東北糖鎖研究会，仙台オンライン開催，2020 年 8 月，演題番号 P-1

・**非環状糖リビトールの計算化学と NMR による動的構造解析**

大野 詩歩, 真鍋 法義, 山口 芳樹

第 14 回東北糖鎖研究会，仙台オンライン開催，2020 年 8 月，演題番号 P-2

・**コアフコース含有 N-グリカンの機能解明・制御を目指したケミカルバイオロジー**

真鍋 良幸，MARCHETTI Roberta，武部 智之，笠原 里実，高倉 陽平，長崎 政裕，二瓶 渉，田中 克典，樺山 一哉，CHIODO Fabrizio，花島 慎弥，鎌田 佳宏，三善 英知，DULAL Hari Prasad，山口 芳樹，安達 禎之，大野 尚仁，田中 浩士，SILIPO Alba，MOLINARO Antonio，深瀬 浩一

第 62 回天然有機化合物討論会，名古屋オンライン開催，2020 年 9 月，演題番号 24

・**非環状の糖鎖成分リビトールの静的および動的構造の解析**

大野 詩歩，真鍋 法義，山口 拓実，鵜澤 洵，山口 芳樹

第 59 回日本薬学会東北支部大会，紙上発表，2020 年 10 月，演題番号 PB-16

・**コアフコース含有 N-グリカン認識レクチンの探索**

真鍋 良幸，MARCHETTI Roberta，高倉 陽平，長崎 政裕，二瓶 渉，武部 智之，田中 克典，樺山 一哉，CHIODO Fabrizio，花島 慎弥，鎌田 佳宏，三善 英知，DULAL Hari Prasad，山口 芳樹，安達 禎之，大野 尚仁，田中 浩士，SILIPO Alba，MOLINARO Antonio，深瀬 浩一

第 39 回日本糖質学会年会，紙上開催，2020 年 11 月，演題番号 C66

・**抗糖鎖抗体の立体構造データベース構築と抗原結合部位の解析**

瀬川 千夏，真鍋 法義，大野 詩歩，山口 芳樹

第 39 回日本糖質学会年会，紙上開催，2020 年 11 月，演題番号 B104

・**NMR 法と分子動力学計算による非環状糖リビトールの動的構造解析**

大野 詩歩，真鍋 法義，山口 拓実，鵜澤 洵，山口 芳樹

第 39 回日本糖質学会年会，紙上開催，2020 年 11 月，演題番号 B73

・**プリオン感染における「種の壁」を解明**

志田俊信，鎌足雄司，依田隆夫，山口芳樹，Michael Feig，大橋祐美子，杉田有治，桑田一夫，田中元雅

第 59 回 NMR 討論会，群馬，2020 年 11 月，演題番号 P29

・**NMR approach to investigate glycan structure and function**

Yoshiki Yamaguchi

14th Chandigarh Science Congress-2020 (CHASCON-2020), India on line, Dec. 2020

・**N-グルカンの立体構造とその相互作用**

山口芳樹

第 4 回東北医真菌研究会，オンライン開催，2020 年 12 月，11:15-11:55

・**遠隔操作による NMR 測定の実際と生体分子の構造解析**

山口芳樹

先端研究基盤共用促進事業　新共用＆SHARE 利用報告会，オンライン開催，2021 年 3 月，16:30-18:00

・**ヒトシアル酸転移酵素 ST3Gal5 の立体構造モデリングと基質結合部位の予測**

兼瀬 鑑，大野 詩歩，真鍋 法義，山口 芳樹

日本薬学会第 141 年会，オンライン開催，2021 年 3 月，27P01-101S

・**NMR 法によるペプチド中の Asp 残基異性化の *in situ* 判別**

真鍋 法義，大野 詩歩，山口 芳樹

日本薬学会第 141 年会，オンライン開催，2021 年 3 月，28P01-085

・**非環状糖鎖成分リビトールの動的構造解析**

大野 詩歩，真鍋 法義，山口 拓実，鵜澤 洵，山口 芳樹

日本薬学会第 141 年会，オンライン開催，2021 年 3 月，29P01-079

Article

TRANSPARENT PROCESS OPEN ACCESS

THE EMBO JOURNAL

Homeostatic and pathogenic roles of GM3 ganglioside molecular species in TLR4 signaling in obesity

Hirotaka Kanoh[1,†], Takahiro Nitta[1,†], Shinji Go[1,‡], Kei-ichiro Inamori[1], Lucas Veillon[1,§], Wataru Nihei[1], Mayu Fujii[2], Kazuya Kabayama[2], Atsushi Shimoyama[2], Koichi Fukase[2], Umeharu Ohto[3], Toshiyuki Shimizu[3], Taku Watanabe[4], Hiroki Shindo[4], Sorama Aoki[4], Kenichi Sato[4], Mika Nagasaki[5,¶], Yutaka Yatomi[6], Naoko Komura[7], Hiromune Ando[7], Hideharu Ishida[7,8], Makoto Kiso[9], Yoshihiro Natori[10], Yuichi Yoshimura[10], Asia Zonca[11], Anna Cattaneo[11], Marilena Letizia[11], Maria Ciampa[11], Laura Mauri[11], Alessandro Prinetti[11], Sandro Sonnino[11], Akemi Suzuki[1] & Jin-ichi Inokuchi[1,*]

Abstract

Innate immune signaling via TLR4 plays critical roles in pathogenesis of metabolic disorders, but the contribution of different lipid species to metabolic disorders and inflammatory diseases is less clear. GM3 ganglioside in human serum is composed of a variety of fatty acids, including long-chain (LCFA) and very-long-chain (VLCFA). Analysis of circulating levels of human serum GM3 species from patients at different stages of insulin resistance and chronic inflammation reveals that levels of VLCFA-GM3 increase significantly in metabolic disorders, while LCFA-GM3 serum levels decrease. Specific GM3 species also correlates with disease symptoms. VLCFA-GM3 levels increase in the adipose tissue of obese mice, and this is blocked in TLR4-mutant mice. In cultured monocytes, GM3 by itself has no effect on TLR4 activation; however, VLCFA-GM3 synergistically and selectively enhances TLR4 activation by LPS/HMGB1, while LCFA-GM3 and unsaturated VLCFA-GM3 suppresses TLR4 activation. GM3 interacts with the extracellular region of TLR4/MD2 complex to modulate dimerization/oligomerization. Ligand-molecular docking analysis supports that VLCFA-GM3 and LCFA-GM3 act as agonist and antagonist of TLR4 activity, respectively, by differentially binding to the hydrophobic pocket of MD2. Our findings suggest that VLCFA-GM3 is a risk factor for TLR4-mediated disease progression.

Keywords chronic inflammation; ganglioside GM3; inflammation amplification loop; obesity; TLR4

Subject Categories Immunology

DOI 10.15252/embj.2019101732 | Received 7 February 2019 | Revised 13 March 2020 | Accepted 23 March 2020

The EMBO Journal (2020) e101732

Introduction

Chronic inflammation plays critical roles in pathogenesis of a variety of human diseases, including metabolic disorders (Lumeng, 2011; Hotamisligil, 2017). Prolonged and abnormal activation of pattern recognition receptors in innate immune system, such as Toll-like receptors (TLR; Kawai & Akira, 2011; Moresco *et al*, 2011), causes

1 Division of Glycopathology, Institute of Molecular Biomembrane and Glycobiology, Tohoku Medical and Pharmaceutical University, Sendai, Japan
2 Department of Chemistry, Graduate School of Science, Osaka University, Osaka, Japan
3 Graduate School of Pharmaceutical Sciences, University of Tokyo, Tokyo, Japan
4 Medical and Pharmaceutical Information Science, Tohoku Medical and Pharmaceutical University, Sendai, Japan
5 Department of Cardiovascular Medicine and Computational Diagnostic Radiology & Preventive Medicine, Graduate School of Medicine, The University of Tokyo, Tokyo, Japan
6 Department of Clinical Laboratory Medicine, Graduate School of Medicine, The University of Tokyo, Tokyo, Japan
7 Center for Highly Advanced Integration of Nano and Life Sciences (G-CHAIN), Gifu University, Gifu, Japan
8 Department of Applied Bio-organic Chemistry, Faculty of Applied Biological Sciences, Gifu University, Gifu, Japan
9 Organization for Research and Community Development, Gifu University, Gifu, Japan
10 Division of Organic and Pharmaceutical Chemistry, Tohoku Medical and Pharmaceutical University, Sendai, Japan
11 Department of Medical Biotechnology and Translational Medicine, University of Milan, Milano, Italy
*Corresponding author. Tel: +81 22 727 0117; E-mail: jin@tohoku-mpu.ac.jp
†These authors contributed equally to this work
‡Present address: Department of Pathophysiology and Metabolism, Kawasaki Medical School, Okayama, Japan
§Present address: Department of Bioinformatics and Computational Biology, The University of Texas MD Anderson Cancer Center, Houston, TX, USA
¶Present address: Nagasaki Clinic, Tokyo, Japan

chronic inflammation. In metabolic disorders, various ligands activate TLR4: (i) exogenous lipopolysaccharides elevated in serum (Cani *et al*, 2007), (ii) endogenous damage-associated molecular patterns (DAMPs), *e.g.*, high-mobility group box-1 protein (HMGB1; Harris *et al*, 2012; Guzmán-Ruiz *et al*, 2014), free fatty acids (FFAs; Shi *et al*, 2006), and fetuin-A protein (Pal *et al*, 2012), which are released from macrophages and adipose tissue. LPS and endogenous ligands induce production of various effector molecules including proinflammatory cytokines (*e.g.*, tumor necrosis factor-α [TNF-α], interleukin-6 [IL-6]), which contributes to insulin resistance and dysregulation of lipid and energy metabolisms (Lumeng, 2011; Hotamisligil, 2017).

Gangliosides are important downstream metabolites of ceramide, a sphingolipid formed by an amide linkage between the sphingoid base and fatty acid (Bikman & Summers, 2011), and involved in a variety of cellular events (Inokuchi *et al*, 2018). Glycosyltransferases, UGCG and B4GALT5/6, convert ceramide into glucosylceramide (GlcCer) and lactosylceramide (LacCer), precursor glycosphingolipids (GSLs) for GM3 ganglioside. Consecutively, ST3GAL5, a GM3 synthase (GM3S), converts LacCer into GM3 by conjugating a sialic acid (N-acetylneuraminic acid) (Fig 1A), which is followed by biosynthesis of complex gangliosides.

GM3 is secreted abundantly into human serum (Fig 1B), with concentration 10–15 μg/ml (~10 μM) (Fig 1C), and is circulated to all parts of the body, including insulin-sensitive organs (*e.g.*, liver, muscle, adipose; Senn *et al*, 1989; Veillon *et al*, 2015). Fatty acids of serum GM3 are composed of long-chain fatty acid (LCFA), 16:0, 18:0, and 20:0; very-long-chain fatty acid (VLCFA), 22:0, 23:0, and 24:0; unsaturated VLCFA, 22:1 and 24:1; and α-hydroxy VLCFA including h24:0 and h24:1 (Fig 1D), in almost same abundances of LCFA, VLCFA, and unsaturated VLCFA species, and a small amount of α-hydroxy species (Fig 1E). Altered expression of various GM3 species has been observed in patients with metabolic disorders (Veillon *et al*, 2015); however, specific biological functions of these species are poorly understood.

On the other hand, it has been suggested that GM3 on the plasma membrane plays important roles in pathogenesis of metabolic disorders (Inokuchi *et al*, 2018). GM3 is also a major ganglioside in adipocytes, and its expression is induced by proinflammatory cytokines derived from adipose tissue macrophages (Tagami *et al*, 2002; Nagafuku *et al*, 2015; Wentworth *et al*, 2016). GM3 biosynthesis occurs in Golgi, and it subsequently becomes secreted into extracellular compartment or localized in plasma membrane as a component of membrane microdomains (also called "rafts"), which are signaling platforms comprised of sphingolipids (Lingwood & Simons, 2010). GM3 on plasma membrane affects diffusion kinetics of insulin receptors and regulates signal transduction (Kabayama

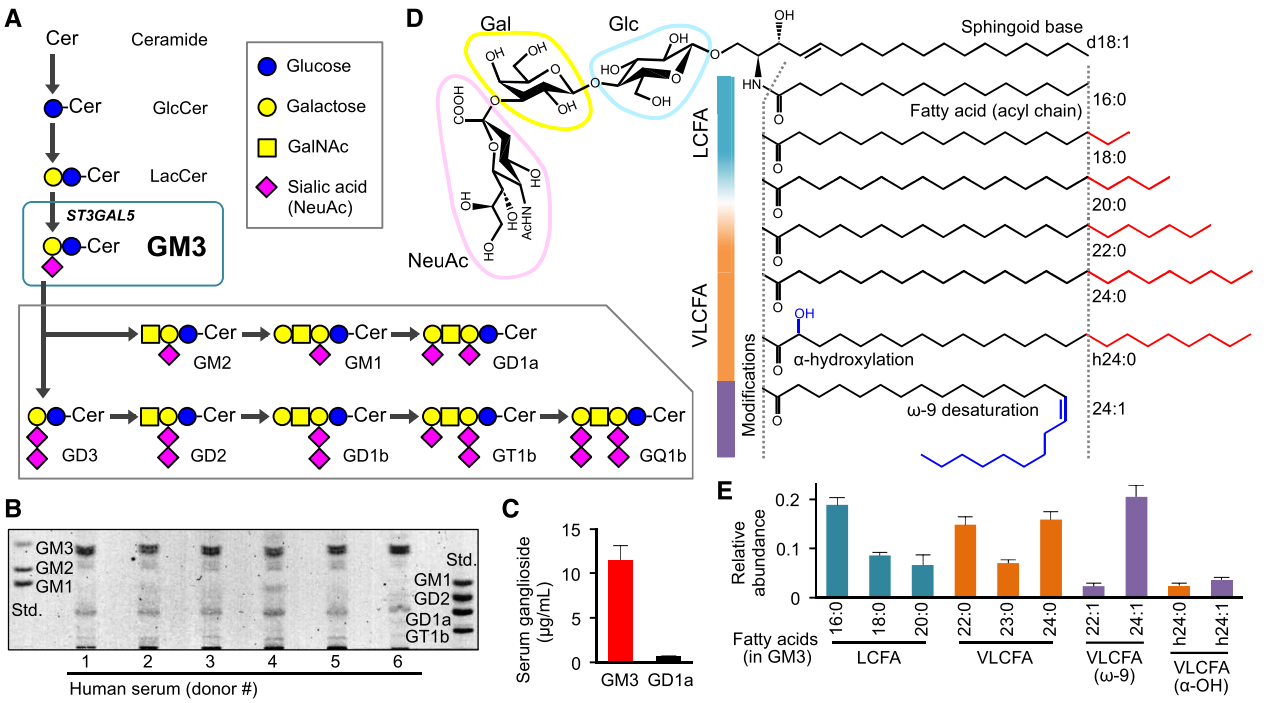

Figure 1. Molecular species of ganglioside GM3 in human serum and the acyl-chain structures.

A Biosynthetic pathway (schematic) of GM3, from ceramide, and to complex gangliosides.

B TLC analysis of ganglioside species in human serum.

C Quantification by densitometry of major ganglioside species GM3 and GD1a in human serum. Data expressed as mean ± SD, n = 6.

D Detailed structures of GM3 species: sialyllactose head group, sphingoid base (d18:1), typical fatty-acid lengths (LCFA, VLCFA), and acyl-chain modifications (α-hydroxylation, ω-9 desaturation).

E Quantification by LC-MS/MS analysis of serum GM3 species with differing acyl-chain structures. Total abundance of 10 species was defined as 1. Data expressed as mean ± SD, n = 6.

et al, 2007); conversely, insulin signaling is restored when GM3 biosynthesis is blocked by glycosyltransferase inhibitors, *e.g.*, D-*threo*-1-phenyl-2-decanoylamino-3-morpholino-1-propanol (D-PDMP) and Genz-123346 (Tagami *et al*, 2002; Zhao *et al*, 2007). Knockout of *GM3S* diminishes not only systemic insulin resistance but also chronic inflammation in adipose tissue (Yamashita *et al*, 2003; Nagafuku *et al*, 2015), suggesting that GM3 might be involved in innate immune signaling upstream of insulin resistance; however, the molecular basis for such relationship remains unclear.

In this study, we investigated how serum GM3 species, carrying different acyl chains, regulate inflammatory signaling and contribute to onset of metabolic disorders. Here, we demonstrate that GM3 acts as an endogenous TLR4 modulator. VLCFA-GM3 synergistically and selectively augmented TLR4 activation by LPS and HMGB1, and in contrast, LCFA and unsaturated VLCFA-GM3 suppressed TLR4 activation. Serum VLCFA-GM3 increased significantly and LCFA-GM3 decreased sharply in metabolic disorders. Computational approaches using artificial intelligence revealed that specific GM3 species are related to clinical symptoms. VLCFA-GM3 also increased in the adipose tissue of obese mice and the increase was attenuated in TLR4-mutant mice, implying that TLR4 signaling itself is involved in production of VLCFA-GM3. Our findings suggest that serum GM3 plays a role of rheostat for TLR4 signaling, and the increase in VLCFA-GM3 is a risk factor for TLR4-mediated disease progression.

Results

VLCFA-GM3 species are involved in progression of chronic inflammation in metabolic disorders

To elucidate the role of GM3 species in pathophysiology of metabolic disorders, we analyzed expression patterns of serum GM3 species in human subjects (Veillon *et al*, 2015; Appendix Fig S1A–I). Sera were collected from human subjects, representing five pathological phases: healthy subjects (control, $n = 24$), visceral fat accumulation (VFA, $n = 38$) in presymptomatic phase, VFA with dyslipidemia (lipidemia, $n = 28$), VFA with hyperglycemia (glycemia, $n = 15$), and VFA with dyslipidemia and hyperglycemia (lipidemia + glycemia, $n = 17$). Scores of homeostatic model assessment for insulin resistance (HOMA-IR) and serum C-reactive protein (CRP) were evaluated as indicators of insulin resistance and chronic inflammation, respectively. HOMA-IR and CRP displayed significant correlation with each other (Appendix Fig S1J), and a gradual increase in the order: control < VFA < lipidemia < glycemia < lipidemia + glycemia (Appendix Fig S1K and L). These findings indicate that the order of the five phases corresponds to increasing severity of insulin resistance and chronic inflammation.

Circulating levels of serum GM3 species were evaluated by LC-MS/MS analysis (Appendix Fig S2A–K). Heat map analysis, which summarizes properties of the ten major species, indicated progressive increase in VLCFA species and decrease in LCFA species in association with increases in HOMA-IR and serum CRP (Fig 2A). LCFA species (16:0, 18:0, 20:0) decreased sharply in VFA, lipidemia, and glycemia (Fig 2B), whereas VLCFA species (22:0, 23:0, 24:0, h24:0) largely increased (Fig 2C). Unsaturated VLCFA species were mostly constant as total (Fig 2D); 22:1 and h24:1 decreased, but 24:1 slightly increased (Fig 2A). The ratio of total VLCFA species to total LCFA/ unsaturated VLCFA species increased notably in presymptomatic and early phases of metabolic disorders (Appendix Fig S2L).

Early-phase increases in body mass index (BMI) (> 25) or abdominal circumference (> 85 cm) were associated with sharp reduction in LCFA species (Figs 2E and EV1A) and increase in VLCFA species (Figs 2F and EV1B). These findings suggest that increases in VLCFA-GM3 species occur in obesity, and play a role in early pathogenesis of metabolic disorders. In cases of severe obesity (BMI > 30 and/or abdominal circumference > 100 cm) and severe metabolic disorders (lipidemia + glycemia), there was moderate reduction in VLCFA-GM3 species (Figs 2F and EV1B) and significant increase in unsaturated species (Figs 2G and EV1C). These findings indicate that desaturation of VLCFA species occurs after onset of metabolic disorders.

Abundance of α-hydroxy VLCFA-GM3 (h24:0) showed a linear increase along with increases in BMI and abdominal circumference (Figs 2H and EV1D), with strong correlation (Fig EV1E and F). α-hydroxy VLCFA-GM3 was also strongly correlated with indicators of insulin resistance and chronic inflammation (ALT, HOMA-IR, CRP) (Figs 2I and J, and EV1G–J). In particular, the ratio of h24:0 to 24:0 was much higher in subjects with abnormal CRP value (> 0.3 mg/dl) (Figs 2K and EV1I), indicating considerable involvement of h24:0 in chronic inflammation. Relationships between these GM3 species and pathophysiology of metabolic disorders are summarized schematically in Fig 2L. In steady state, homeostasis is maintained by balance of GM3 species; in presymptomatic and early phases, VLCFA species increase in correlation with chronic inflammation and insulin resistance; in late phases, modifications such as desaturation and α-hydroxylation could occur in VLCFA species.

Artificial intelligence-based approaches revealed GM3 species specific to disease symptoms

To analyze more detailed relationships between GM3 species and metabolic disorders, we utilized an unbiased approach using self-organization map (SOM), a neural-network-type artificial intelligence model. Subjects were analyzed based on expression patterns of the ten major GM3 species, then mapped onto a two-dimensional (2D) surface such that subjects with similar GM3 patterns are located near each other and form clusters (Fig 3A). SOM analysis gave nearly distinct clusters of control and lipidemia subjects (Fig 3B), indicating increases in VLCFA species and decreases in LCFA/ unsaturated VLCFA species in lipidemia subjects (Fig 3C). These subjects were further mapped into six sub-clusters based on expression patterns of GM3 species: in control, sub-clusters 1 (16:0), 2 (16:0, 18:0, 20:0), and 3 (22:1, 24:1, h24:1); in lipidemia, sub-clusters 4 (22:0), 5 (22:0, 24:0, h24:0, 23:0), and 6 (22:0, 24:0, h24:0, 24:1) (Fig 3D). This classification indicates that elongation, α-hydroxylation, and desaturation of GM3 acyl chains occur corresponding to disease progression (Fig 3E). Sub-clusters 4 and 5 (higher in α-hydroxy VLCFA) showed higher non-HDL cholesterol; sub-cluster 6 (higher in unsaturated VLCFA) showed higher CRP and HOMA-IR (Fig 3F), indicating fatty-acid modifications specific to different disease severities. Optimized SOM analysis, based on four species (16:0, 18:0, 22:0, and 22:1), was able to completely distinguish control

vs. lipidemia subjects (Fig 3G). The receiver operating characteristic (ROC) curve gave excellent scores in sensitivity, specificity, and area under the curve (AUC; Fig 3H). These findings suggest that alterations of serum GM3 species are potential risks of disease progression, and the measurement is a valuable tool for clinical assessment.

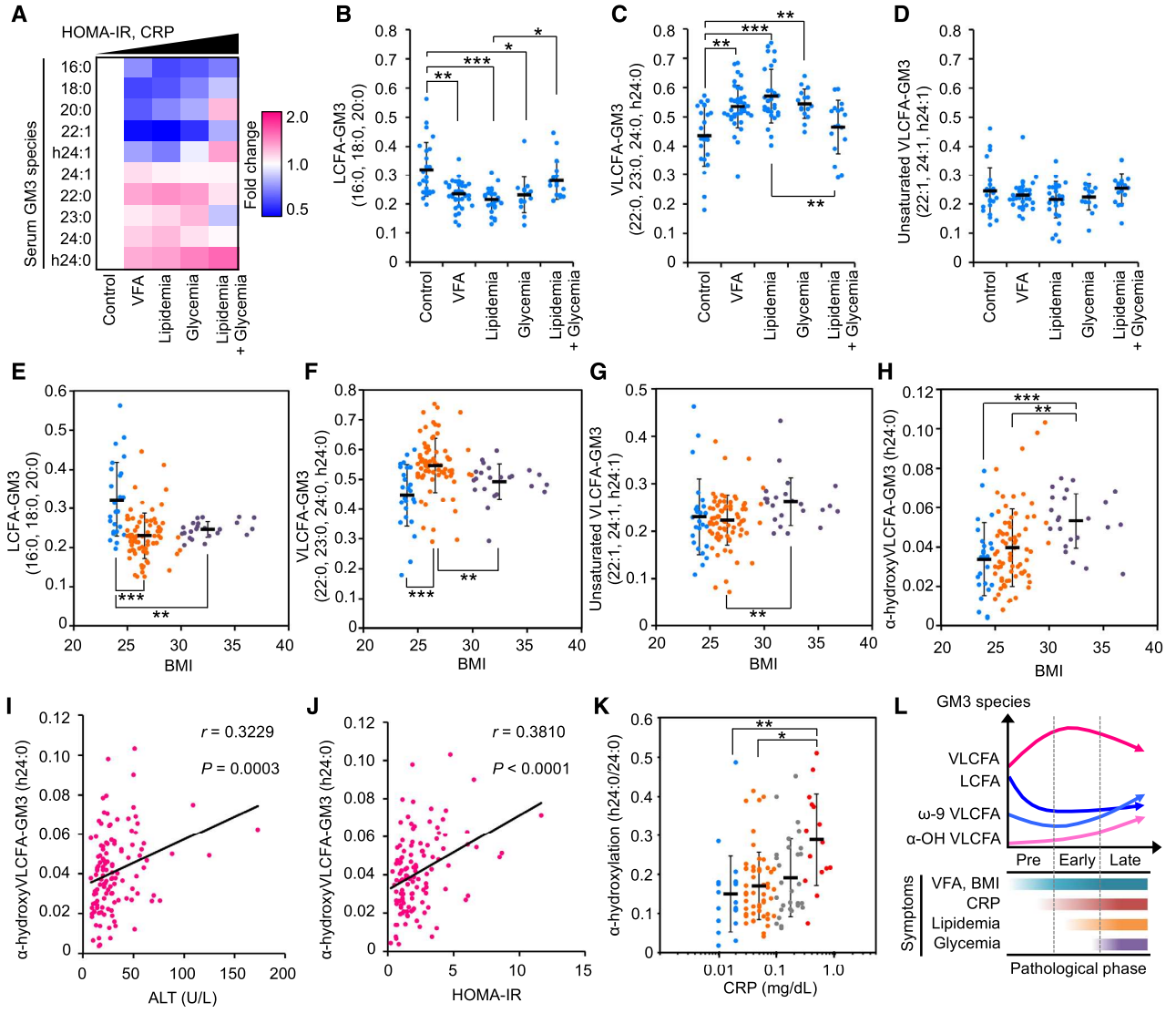

Figure 2. Alterations of relative abundance of GM3 species are involved in disease progression and chronic inflammation.

A Heat map analysis of serum GM3 species in various pathological phases: control (n = 24), VFA (n = 38), lipidemia (n = 28), glycemia (n = 15), and lipidemia + glycemia (n = 17). Colors indicate fold change average of each species relative to control (defined as 1), as shown in key at right. Order of pathological phases corresponds to increments of HOMA-IR and serum CRP.

B–D Properties of various GM3 species as a function of pathological phases: control (n = 24), VFA (n = 38), lipidemia (n = 28), glycemia (n = 15), and lipidemia + glycemia (n = 17). Data shown are relative abundances of total LCFA species (16:0, 18:0, 20:0) (B), total VLCFA species (22:0, 23:0, 24:0, h24:0) (C), and total unsaturated VLCFA species (22:1, 24:1, h24:1) (D) relative to total of ten major GM3 species (defined as 1) in each subject.

E–H Properties of various GM3 species as a function of BMI: LCFA-GM3 (E), VLCFA-GM3 (F), unsaturated VLCFA-GM3 (G), and α-hydroxy VLCFA-GM3 (h24:0) (H). Colors indicate disease severity: light blue, no abnormal scores (n = 25); orange, early-phase obesity (n = 74); purple, severe obesity (n = 23).

I, J Spearman's correlations for GM3 h24:0 vs. ALT (I) and vs. HOMA-IR (J).

K Plots of α-hydroxylation rate (h24:0/24:0) vs. serum CRP. Colors indicate range of CRP value (mg/dl): light blue, 0.01–0.02 (n = 21); orange, 0.03–0.09 (n = 56); gray, 0.10–0.29 (n = 29); red, 0.3–1.0 (diagnostically abnormal; n = 15).

L Association between serum GM3 species and progression of metabolic disorders (schematic).

Data information: Data shown are individual values and mean ± SD, analyzed by two-tailed unpaired t-test with Bonferroni's correction. *P < 0.05, **P < 0.01, and ***P < 0.001 for comparisons between indicated groups.

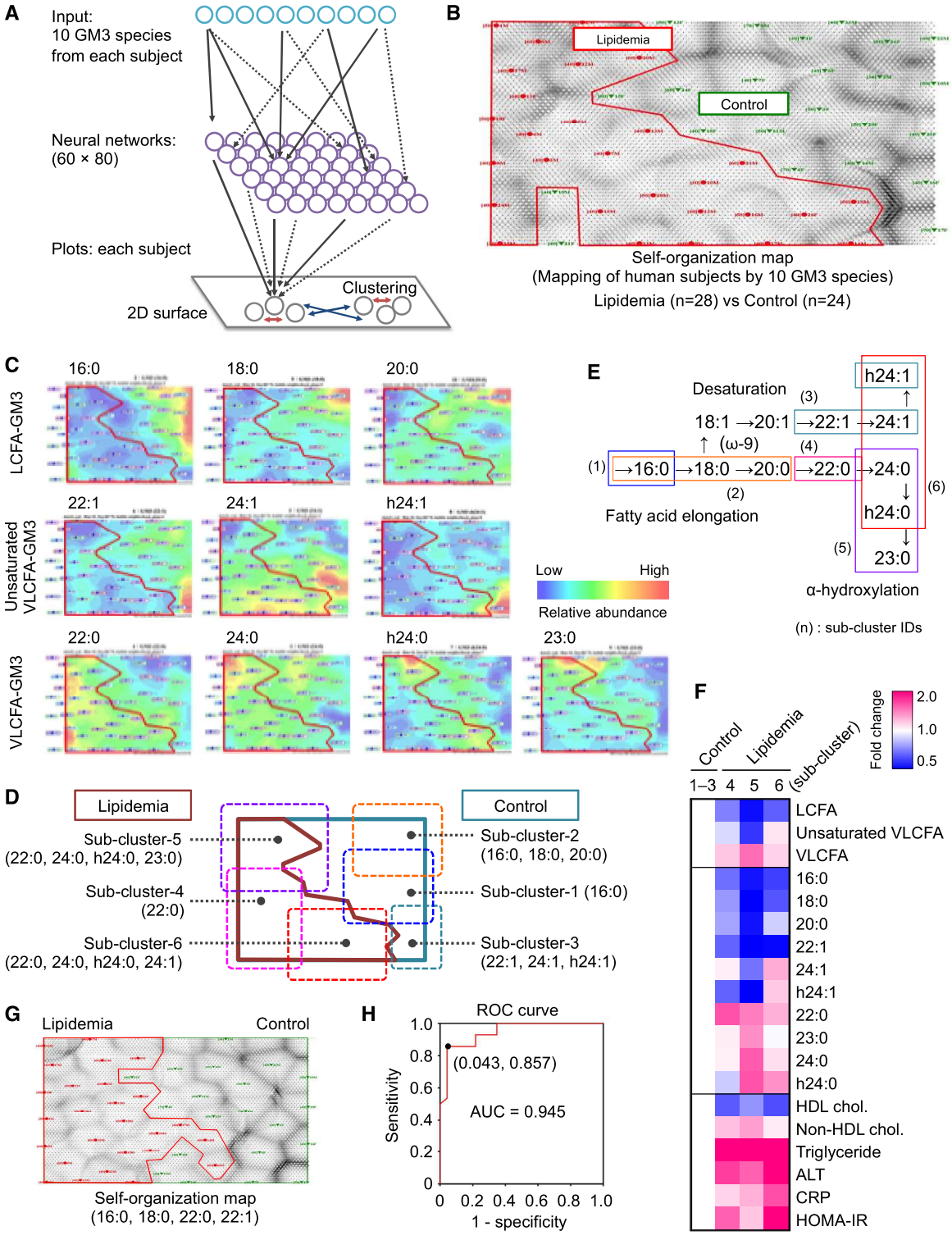
A
Input:
10 GM3 species
from each subject
Neural networks:
(60 × 80)
Plots: each subject
Clustering
2D surface
B
Lipidemia
Control
Self-organization map
(Mapping of human subjects by 10 GM3 species)
Lipidemia (n=28) vs Control (n=24)
C
LCFA-GM3
16:0
18:0
20:0
Unsaturated VLCFA-GM3
22:1
24:1
h24:1
VLCFA-GM3
22:0
24:0
h24:0
23:0
Low
High
Relative abundance
E
Desaturation
(3)
18:1 →20:1 →22:1 →24:1
↑ (ω-9)
(4)
(1) →16:0 →18:0 →20:0 →22:0 →24:0 (6)
(2)
Fatty acid elongation
h24:1
h24:0
(5)
23:0
α-hydroxylation
(n) : sub-cluster IDs
F
Control
Lipidemia
(sub-cluster)
1–3 4 5 6
Fold change
2.0
1.0
0.5
LCFA
Unsaturated VLCFA
VLCFA
16:0
18:0
20:0
22:1
24:1
h24:1
22:0
23:0
24:0
h24:0
HDL chol.
Non-HDL chol.
Triglyceride
ALT
CRP
HOMA-IR
D
Lipidemia
Control
Sub-cluster-5
(22:0, 24:0, h24:0, 23:0)
Sub-cluster-4
(22:0)
Sub-cluster-6
(22:0, 24:0, h24:0, 24:1)
Sub-cluster-2
(16:0, 18:0, 20:0)
Sub-cluster-1 (16:0)
Sub-cluster-3
(22:1, 24:1, h24:1)
G
Lipidemia
Control
Self-organization map
(16:0, 18:0, 22:0, 22:1)
H
ROC curve
Sensitivity
1.0
0.8
0.6
0.4
0.2
0
(0.043, 0.857)
AUC = 0.945
0 0.2 0.4 0.6 0.8 1.0
1 - specificity

Figure 3.

Figure 3. Self-organization map (SOM) analysis based on relative abundances of serum GM3 species.

A Procedure (schematic) for self-organization map (SOM) analysis, a pattern recognition method using neural-network-type artificial intelligence. Complex patterns of multi-dimensional information (in this case, expression patterns of the ten major GM3 species in human subjects) are mapped onto a 2D surface. Subjects having similar GM3 patterns are located proximal to each other and form several clusters (red arrows), whereas subjects having different GM3 patterns are located distal to each other (blue arrows).

B SOM analysis of control and lipidemia subjects based on expression patterns of ten GM3 species.

C Mapping of expression levels of ten GM3 species onto SOM in (B).

D Identification of sub-clusters having different GM3 patterns based on SOM in (B).

E Metabolic pathways for fatty acids: elongation, desaturation, and α-hydroxylation (α-oxidation) (schematic). Sub-clusters identified by SOM analysis are mapped on metabolic pathways.

F Heat map analysis for GM3 species and clinical markers of six clusters. Sample sizes: sub-clusters 1–3 (total), $n = 22$; cluster 4, $n = 7$; cluster 5, $n = 9$; cluster 6, $n = 12$.

G Self-organization map (SOM) based on four GM3 species as indicated at bottom.

H ROC curve derived from Bayesian regularized neural networks (BRNNs) based on four GM3 species in (G).

Serum GM3 species positively and negatively regulate innate immune responses in an acyl-chain-dependent manner

We investigated the effects of GM3 species (16:0, 18:0, 20:0, 22:0, 24:0, h24:0, and 24:1, in Fig 1D) on LPS-mediated activation of human peripheral blood monocytes (Fig 4A). Every GM3 species by themselves did not exhibit notable effects, but VLCFA species (22:0, 24:0) and α-hydroxy VLCFA species (h24:0) synergistically enhanced LPS-mediated production of proinflammatory cytokines, *e.g.*, IL-6, TNF-α, and IL-12/23 p40 (Figs 4B and C, and EV2A). In contrast, LCFA species (16:0, 18:0) strongly inhibited LPS-mediated cytokine production. Unsaturated VLCFA-GM3 24:1 had an inhibitory effect. These enhancing and inhibitory effects were dose-dependent and were observed at physiological concentration (< 10 μM) (Fig EV2B). These findings suggest that serum GM3 species positively and negatively regulate LPS-mediated monocyte activation in an acyl-chain-dependent manner.

Among various types of gangliosides, only VLCFA-GM3 species displayed dose-dependent synergistic activation (Fig 4D and E), and other complex gangliosides exhibited inhibitory effects as reported (Shen *et al*, 2008). Monocyte activation was moderately enhanced in the presence of precursor GSL species and reached to the maximum in the presence of GM3 24:0 (Figs 4F and EV2C–E). GM3 species showed both positive and negative regulations in an acyl-chain structure-dependent manner, but Cer, GlcCer, and LacCer did not show such effects (Figs 4F and EV2C–E). Increasing doses of GM3 16:0, 18:0, and 24:1 reversed the effect of GM3 22:0 and 24:0 (Figs 4G and EV2F and G), suggesting that activation of human monocytes is regulated by the balance of LCFA-GM3, VLCFA-GM3, and unsaturated VLCFA-GM3 species in serum.

VLCFA-GM3 species selectively enhance human TLR4/MD-2 activation

To elucidate the molecular mechanisms underlying GM3-mediated monocyte activation, we screened signaling pathways targeted by GM3 species. Monocytes were co-stimulated by GM3 species in combination with various PAMPs, including ligands for TLR1/2, TLR4, TLR5, TLR2/6, and TLR7/8. We found that VLCFA species selectively synergized with LPS, a TLR4 ligand, but not for other TLR ligands (Figs 5A and EV3A). LCFA species strongly inhibited cytokine production by LPS, and partially by Pam3CSK4, a TLR1/2 ligand, but not by MALP-2, a TLR2/6 ligand. Thus, GM3 species act as endogenous modulators selective for TLR4 signaling. GM3-mediated modulations were also observed in di-/monophosphoryl lipid A species LA506, LA505, and LA504, core structural components of LPS (Fig 5B). VLCFA-GM3 22:0 significantly enhanced cytokine production in the presence of low-dose LA506 (Fig EV3B–D). Moreover, VLCFA species strongly enhanced cytokine production by high-mobility group box-1 (HMGB1) protein (Fig 5C and D), an endogenous TLR2/4 ligand released from dead cells or visceral adipocytes in obese patients (Harris *et al*, 2012; Guzmán-Ruiz *et al*, 2014). HMGB1-mediated IL-6 production was also inhibited by LCFA species (Fig 5C). These findings, taken together, indicate that GM3 species selectively modulate TLR4-mediated cytokine production.

To confirm human TLR4 (hTLR4) as a target molecule of GM3 species, we reconstituted TLR4 signaling pathway in HEK293T cells. NF-κB activity was not increased by LPS or GM3 22:0 in hTLR4 single-expressing cells; however, synergistic enhancement was clearly observed in hTLR4/hMD-2 co-expressing cells (Fig 5E). Neither GM3-mediated enhancement nor LPS-mediated activation was observed in cells co-expressing dominant-negative hTLR4 variant (P714H, in intracellular domain)/hMD-2 (Fig 5E). These findings suggest that hTLR4/hMD-2 complex and its downstream pathway are required for NF-κB activation by GM3 species. Activation of hTLR4/hMD-2 by LPS was strongly enhanced by GM3 22:0, 24:0, and h24:0, but inhibited by GM3 16:0 (Fig 5F). hTLR4/hMD-2 activation enhanced by addition of recombinant soluble hCD14 was strongly suppressed by 16:0 and 18:0 (Fig 5G), consistent with observed inhibition of CD14-positive human cells by long-chain species. Among the downstream targets of TLR4, in addition to NF-κB, the activator protein 1 (AP-1) activity was moderately enhanced by GM3 22:0, but the interferon-stimulated response element (ISRE) activity was enhanced only weakly (Fig EV3E). None of the GM3 species affected NF-κB activation by overexpression of MyD88-adaptor-like (Mal), a proximal adaptor protein of hTLR4 (Fig 5H), indicating that GM3 species target hTLR4/hMD-2 complex upstream of Mal. The result of co-stimulation by LPS plus GM3 species in 1:1 mixture suggests that the balance of extracellular GM3 species controls activation patterns of hTLR4/hMD-2 (Fig 5I and J). 16:0 consistently inhibited TLR4 activation even in the presence of 22:0 or 24:0; 18:0 and 20:0 substantially counteracted enhancement by 22:0 or 24:0; and 24:1 reduced TLR4 activation to basal level by LPS single stimulation (Fig 5I). These findings, taken together, indicate that TLR4 signaling is selectively modulated by balance of GM3 species (Fig 5J).

VLCFA-GM3 species selectively enhance mouse TLR4/MD-2 signaling

We also investigated the effects of GM3 species on mouse TLR4/MD-2 (mTLR4/mMD-2). In RAW macrophages, VLCFA species strongly enhanced TNF-α production by TLR4 ligands LPS and HMGB-1 but not by other TLR ligands, similarly to results in human cells (Fig 6A and B). The enhancement was clearly observed in chronic/weak TLR4 activation by low-dose LPS and was saturated in rapid/strong activation by high-dose LPS (Fig 6B). LCFA-GM3

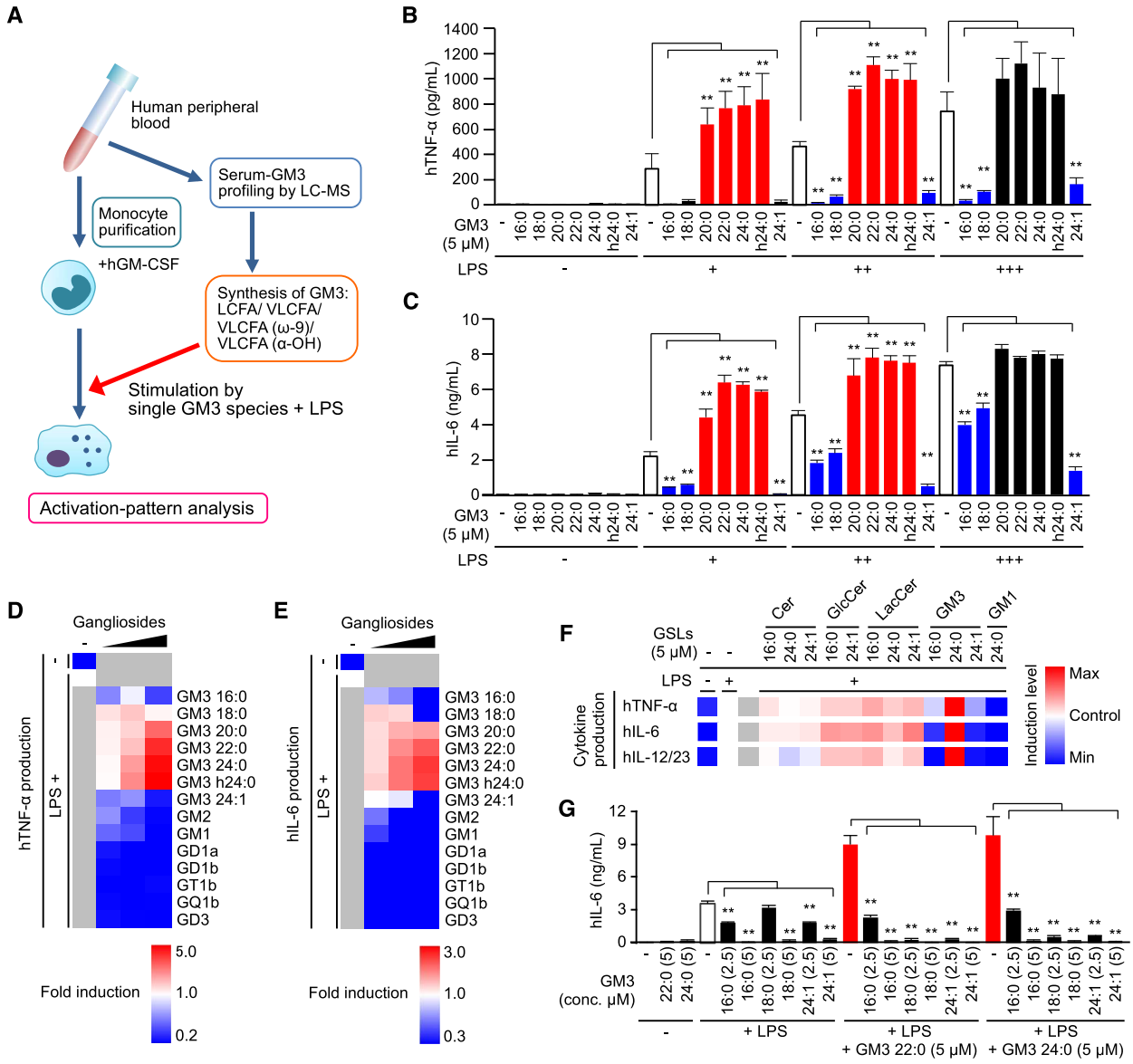

Figure 4. Positive and negative regulation of innate immune responses by serum GM3 species in an acyl-chain-dependent manner.

A Profiling of bioactivities of serum GM3 species in LPS-mediated monocyte activation (schematic).

B, C GM3-mediated enhancement and inhibition of proinflammatory cytokine production from LPS-stimulated monocytes (LPS: 0.06, 0.13, 0.25 ng/ml). TNF-α (B) production and IL-6 (C) production in culture supernatant were measured by ELISA.

D, E Co-stimulation of monocytes by LPS plus GM3 species or complex ganglioside species (1.5, 3.0, 4.5 μM). TNF-α (D) production and IL-6 (E) production were shown in heat maps.

F Co-stimulation of monocytes by LPS plus GM3 species or precursor GSL species. TNF-α production, IL-6 production, and IL-12/23 production were shown in heat maps.

G Inhibitory effect of LCFA and unsaturated VLCFA-GM3 on VLCFA-GM3 species. IL-6 production in culture supernatant was measured by ELISA.

Data information: Data shown are mean ± SD (n = 3), analyzed by Tukey's multiple comparison test. **P < 0.01 for comparisons between indicated groups.

and unsaturated VLCFA-GM3 species moderately enhanced TLR4 activation (Fig 6A), in contrast to results in human cells. These effects were also observed in BMDMs from C3H/HeN (WT TLR4) mice, but not in C3H/HeJ (dominant-negative TLR4, P712H) mice (Fig 6B), indicating that mTLR4 and its downstream signaling pathway are required. Activation patterns of macrophages were

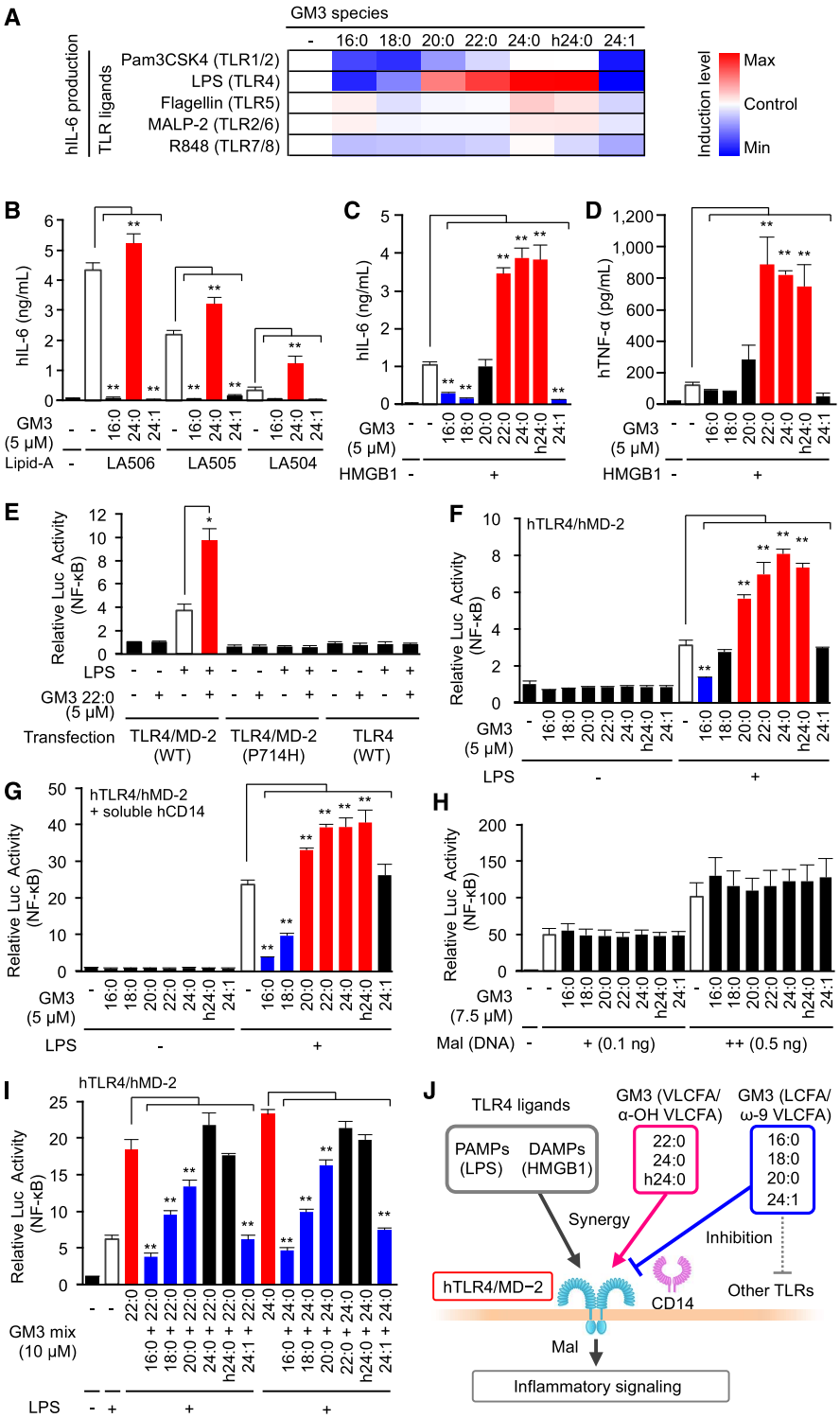

Figure 5.

Figure 5. VLCFA-GM3 species synergistically and selectively control human TLR4/MD-2 activation.

A Co-stimulation of human monocytes by GM3 species plus various TLR ligands: LPS (0.13 ng/ml), TLR4/MD-2, Pam3CSK4 (0.5 μg/ml), TLR1/2, Flagellin (50 ng/ml), TLR5, R848 (0.5 μg/ml), TLR7/8, MALP-2 (1.0 ng/ml), and TLR2/6. IL-6 production in culture supernatant was quantified by ELISA (shown in a heat map).

B Co-stimulation of monocytes by GM3 species (16:0, 24:0, 24:1) plus synthetic TLR4 ligands LA506 (15 ng/ml), LA505 (150 ng/ml), or LA504 (150 ng/ml).

C, D Production of IL-6 (C) and TNF-α (D) in culture supernatant following co-stimulation of monocytes by GM3 species plus human HMGB1.

E Overexpression of hTLR4, hTLR4/hMD-2, and hTLR4 (P714H) /MD-2 in HEK293T cells, and co-stimulation by GM3 22:0 with LPS (5 ng/ml). TLR4 activation was monitored by NF-κB luciferase reporter assay (termed "Relative Luc Activity" on y-axis).

F, G Co-stimulation of hTLR4/hMD-2 by GM3 species plus LPS (5 ng/ml) (F) and further addition of soluble human CD14 (1 μg/ml) (G).

H Stimulation of Mal-overexpressing HEK293T cells by GM3 species.

I Co-stimulation of hTLR4/hMD-2 by LPS (5 ng/ml) plus various mixtures of GM3 species.

J Regulation of hTLR4/hMD-2 by GM3 species balance (schematic).

Data information: Data shown are mean ± SD (A–D and F-I, $n = 3$; E, $n = 4$) analyzed by Tukey's multiple comparison test. *$P < 0.05$ and **$P < 0.01$ for comparisons between indicated groups.

reproduced by overexpression of mTLR4/mMD-2 complex in HEK293T cells (Fig 6C), and NF-κB activity increased progressively associating with acyl-chain length of GM3 species. Addition of soluble mouse CD14 enhanced the synergistic activation by GM3 species, indicating that CD14 facilitate GM3 representation to mTLR4/mMD-2. Among complex gangliosides and precursor GSLs, synergistic activation in the mouse model was highest for VLCFA-GM3 species (Fig 6D and E), similarly to findings in human cells. LCFA-GM3 (16:0, 18:0) induced synergistic activation at physiological concentration to a similar degree as other GM3 species, but they displayed antagonistic effects at higher concentrations (Fig 6D). Molecular characteristics of GM3 species and effects on TLR4/MD-2 are summarized in Fig 6F and Appendix Fig S3. VLCFA-GM3 and LCFA-GM3 displayed enhancement and inhibition for TLR4/MD-2, respectively, correlating with volume of the hydrophobic moiety. Interestingly, lipid A/IVa is known to show agonistic and antagonistic activities correlating with total number of fatty acids, also corresponding to volume of the hydrophobic moiety (Akashi *et al*, 2001; Saitoh *et al*, 2004). Lipid IVa synergizes with LPS or lipid A in low-dose range, but show antagonistic effects in high-dose range (Mueller *et al*, 2004), similarly to LCFA-GM3. These current and reported findings suggest that GM3 species utilize molecular mechanisms closely similar to lipid A/ IVa in regulating TLR4 activation.

VLCFA-GM3 species increase in mouse adipose tissue in metabolic disorders

In view of significant increase in VLCFA-GM3 in early-phase metabolic disorders in humans, we performed comparative studies using mouse models of obesity. Six-week-old *ob/ob* mice, showing early onset of metabolic disorders (Fig EV4A), had an increased abundance of GM3 in visceral adipose tissue (Fig EV4B). We analyzed these GM3 species by LC-MS/MS. Control C57/BL6 mice had 16:0, 18:0, 20:0, 22:0, 23:0, 24:0, and 24:1 as major GM3 species, and a small amount of α-hydroxy species (Fig 7A), showing similar composition to human serum GM3. On the other hand, *ob/ob* mice had notably increased levels of α-hydroxy GM3: a strong increase in VLCFA species (h22:0, h23:0, h24:0), and moderate increase in LCFA and unsaturated VLCFA species (h16:0, h18:0, h20:0, h24:1). These findings suggest that increases in VLCFA-GM3 and α-hydroxylation occur in visceral adipose tissue in obesity and metabolic disorders.

Next, we analyzed diet-induced obese mice as a more chronic and moderate model than *ob/ob* mice. High-fat diet (HFD) in 8-week-old mice for 10 weeks resulted in obesity and increased GM3 levels (Fig EV4C and D). LC-MS/MS analysis showed increase in α-hydroxy GM3 species in HFD (Fig 7B); however, the predominant GM3 species in HFD mice were those with shorter acyl chains (h18:0, h20:0, h22:0) relative to *ob/ob* mice (h22:0, h23:0, h24:0). These findings indicate a correlation between the fatty-acid length of α-hydroxy GM3 and the severity of metabolic disorders.

We previously reported that proinflammatory cytokines released from adipose tissue-resident macrophages induce GM3 production in adipocytes (Nagafuku *et al*, 2015). TLR4 is a key receptor for cytokine productions in adipose tissue (Shi *et al*, 2006; Suganami *et al*, 2017), implying that TLR4 activation itself induces increase in VLCFA-GM3. So, we analyzed GM3 species in HFD C3H/HeN and C3H/HeJ mice by LC-MS/MS. HFD in 8-week-old C3H/HeN mice for 8 weeks resulted in increased body weight, blood glucose level, and visceral adipose tissue weight (Fig EV4E). TLC analysis showed moderate increase in total GM3 (Figs 7C and EV4F), and LC-MS/MS analysis revealed notable increases in α-hydroxy VLCFA-GM3 species in visceral adipose tissues of HFD C3H/HeN mice (Fig 7D). Diabetic phenotypes and increased levels of α-hydroxy VLCFA-GM3 species were ameliorated in HFD C3H/HeJ mice (Figs 7D and EV4E), suggesting that TLR4 signaling is partially involved in production of α-hydroxy VLCFA species in obesity. These findings, taken together, suggest that α-hydroxy VLCFA-GM3 increases in both human serum and mouse adipose tissue (Fig 7E), and an interplay between TLR4 and GM3 species results in a feedback loop from TLR4 to GM3 (shown schematically in Fig 7F).

GM3 species recognition by TLR4/MD-2 induces receptor dimerization/ oligomerization

To elucidate the molecular basis of GM3 recognition and signal transduction, we performed structure-based mutation mapping on TLR4/MD-2 complex. Previously reported crystal structures of TLR4/MD-2 complex (Park *et al*, 2009; Ohto *et al*, 2012a) indicate that two ligand-binding sites are formed on the dimerization interface between two TLR4/MD-2 units (Fig 8A). MD-2 forms hydrophobic pockets that bind to the acyl-chain moiety of LPS, while TLR4 leucine-rich repeats (LRRs) provide charged amino acids that recognize the hydrophilic head group of LPS (Fig 8B). Lys (K) and Arg (R) residues around the LPS-binding pocket were replaced by Ala (A), because these cationic residues may recognize the sialic acid on GM3 saccharide chain. Mutations of R264, K341, and K362 greatly reduced synergistic hTLR4 activation by GM3 22:0 and

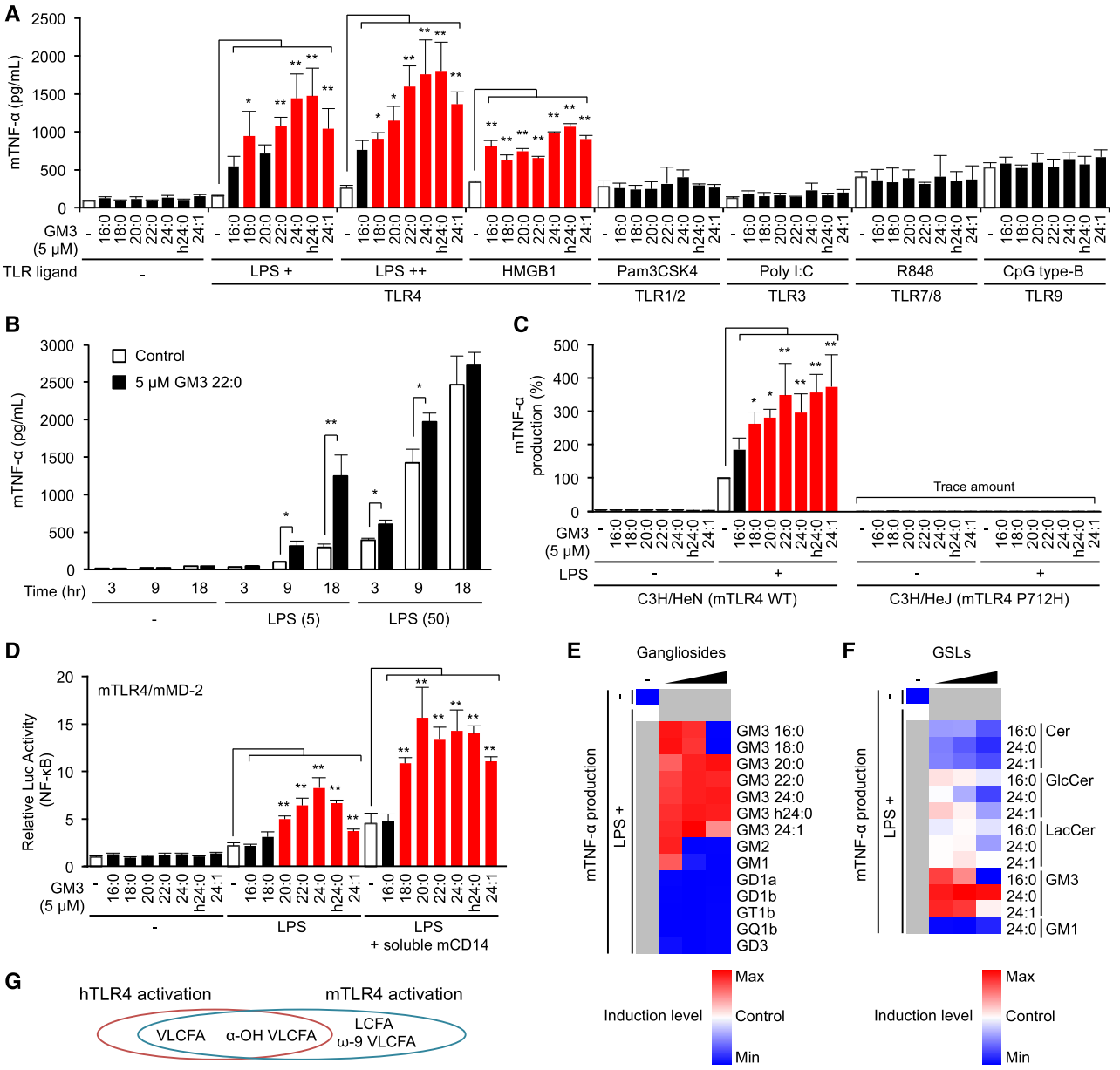

Figure 6. GM3 species selectively modulate mouse TLR4/MD-2 signaling.

A Co-stimulation of RAW macrophages by GM3 species plus various TLR ligands: LPS (0.5, 1.0 ng/ml), bovine thymus HMGB1 (0.25 μg/ml), Pam3CSK4 (50 ng/ml), Poly I:C (10 μg/ml), R848 (4 ng/ml), and CpG type B (20 nM). TNF-α production in culture supernatant was quantified by ELISA.

B Co-stimulation of RAW macrophages by low- and high-dose LPS (0, 5, 50 ng/ml) plus GM3 22:0 (5 μM). Time course of TNF-α production in culture supernatant was quantified by ELISA.

C Co-stimulation of BMDMs from C3H/HeN or C3H/HeJ mice by GM3 species plus LPS (0.5 ng/ml), and TNF-α production in culture supernatant.

D Co-stimulation of mTLR4/mMD-2-expressing HEK293T cells by GM3 species plus LPS (2.5 ng/ml), and further addition of soluble mouse CD14-Fc fusion protein (1 μg/ml).

E, F Co-stimulation of BMDMs from C3H/HeN mice by LPS plus GM3 species and complex ganglioside species (E; 2.5, 5.0, 10 μM), or by LPS plus GM3 species and precursor GSL species (F; 2.5, 5.0, 10 μM) (shown in heat maps).

G Structure–bioactivity relationships of GM3 species with human or mouse TLR4.

Data information: Data shown are mean ± SD (A and B, $n = 3$; C, E, and F, $n = 4$; D, $n = 6$) analyzed by Tukey's multiple comparison test (A, C, and D) or two-tailed unpaired t-test (B). *$P < 0.05$ and **$P < 0.01$ for comparison with stimulation by TLR ligand without GM3 species.

partially reduced hTLR4 activation by LPS single stimulation (Fig 8C). R322, which recognizes a heptulose-phosphate group on LPS oligosaccharide region (Park *et al*, 2009), contributed weakly to GM3-mediated TLR4 activation (Fig 8C). Mutations of R264A, K341A, and K362A in combination effectively suppressed GM3-mediated TLR4 activation (Fig 8D). On the other hand, nickel ion, an allosteric TLR4 ligand (Schmidt *et al*, 2010), did not display synergistic activation with GM3 22:0 (Appendix Fig S4). We also confirmed that R264A, K341A, and K362A had no effect on nickel-mediated hTLR4 activation. These findings indicate that R264, K341, and K362 are required for hTLR4 activation by both LPS and GM3 species and facilitate their synergistic activation, whereas nickel ion does not synergize with GM3 species because its activity is independent of these amino acids.

To clarify MD-2-dependent recognition of GM3 acyl-chain structure, we compared inhibitory effects of GM3 16:0 on mTLR4/mMD-2, hTLR4/hMD-2, and mTLR4/hMD-2, a domain-swapped complex comprised of mouse TLR4 and human MD-2. mTLR4/mMD-2 activation was not affected by 16:0 at physiological concentration (Fig 8E), whereas mTLR4/hMD-2 activation and hTLR4/hMD-2

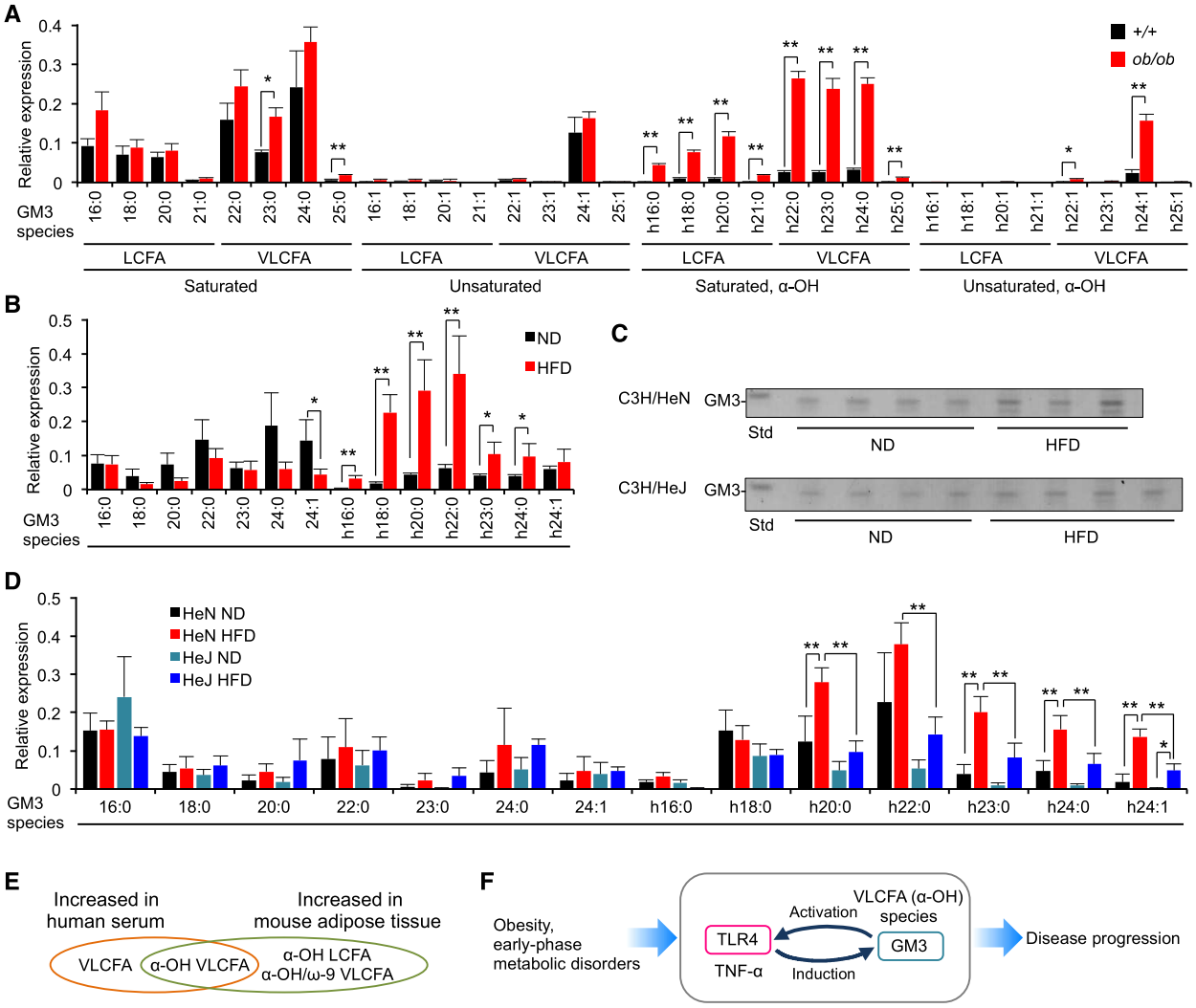

Figure 7. α-hydroxy VLCFA-GM3 species in adipose tissue showed increased abundance in obesity.

A GM3 molecular species of 6-week-old control C57/BL6 mice and *ob/ob* mice were analyzed, respectively, by LC-MS/MS (n = 3).

B GM3 molecular species of normal diet (ND) and high-fat diet (HFD) C57/BL6 mice were analyzed by LC-MS/MS (n = 4).

C TLC analysis of acidic GSL fraction (equivalent to 0.1 mg protein) from epididymal fat pads of C3H/HeN (A) and C3H/HeJ mice (B) on ND or HFD for 8 weeks.

D GM3 molecular species of C3H/HeN mice (ND, HFD) and C3H/HeJ mice (ND, HFD) were analyzed by LC-MS/MS (n = 4).

E Comparison of increased GM3 species in human serum and mouse adipose tissue.

F Feedback loop mediated by TLR4 and GM3 species, promoting disease progression (schematic).

Data information: Data shown are mean ± SD analyzed by two-tailed unpaired t-test (A, B) or by Tukey's multiple comparison test (D). $^*P < 0.05$ and $^{**}P < 0.01$ for comparisons between indicated groups.

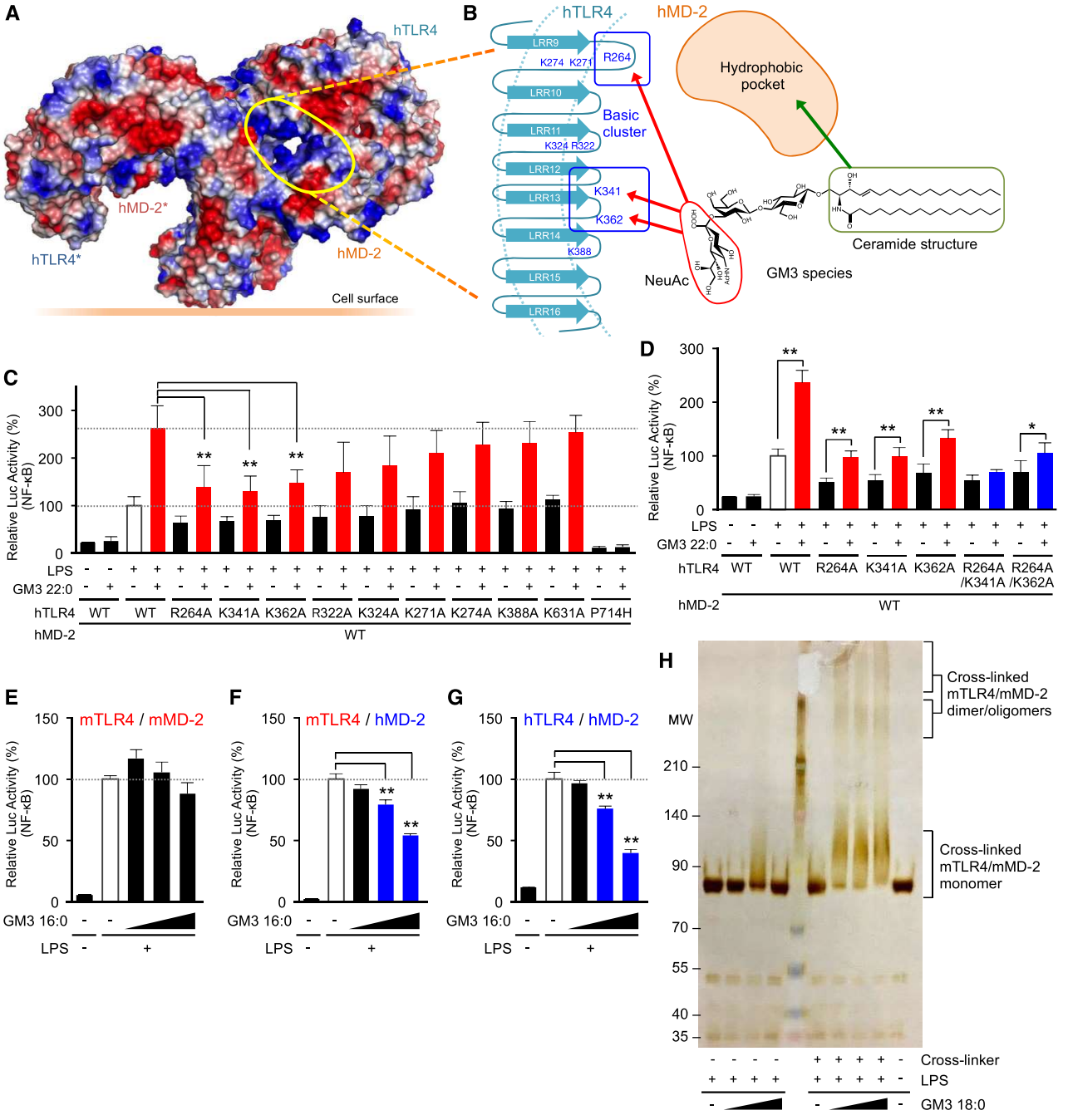

Figure 8. GM3 recognition by TLR4/MD-2 induces receptor oligomerization.

A, B Surface electrostatic potentials of reported crystal structure of human TLR4/MD-2/LPS complex (3FXI), and mapping of putative GM3-binding pocket (A). Candidate basic residues and a hydrophobic pocket recognizing sialic acid and ceramide structure of GM3 are indicated (schematic) (B).

C, D Alanine scanning for basic residues involved in signal transduction via VLCFA-GM3 (n = 5) (C), and combinations of effective mutations (n = 6) (D). Signal transduction was monitored by NF-κB reporter assay.

E–G Comparative inhibitory effects of GM3 16:0 on mTLR4/mMD-2 (E), mTLR4/hMD-2 (domain-swapped complex) (F), and hTLR4/hMD-2 (G) (n = 3).

H Cross-linked SDS–PAGE analysis of recombinant mTLR4 (extracellular domain)/mMD-2 complexed with GM3 18:0, GM3 species enhancing mTLR4 activation.

Data information: Data shown are mean ± SD analyzed by Tukey's multiple comparison test. *P < 0.05, **P < 0.01 for comparisons between indicated groups.

activation were strongly inhibited by 16:0 (Fig 8F and G). Thus, MD-2 evidently provides a basis for selectivity for GM3 species.

To investigate activation state of TLR4/MD-2 complex induced by GM3, we performed chemical cross-linking and SDS–PAGE analysis of recombinant mTLR4 extracellular domain/mMD-2 complex. Addition of LPS, GM3 18:0, and chemical cross-linker induced large mobility shift of mTLR4/mMD-2 complex and observed molecular weights indicate the presence of dimers and higher-order oligomers (Fig 8H). Previous reports indicate that LPS-mediated signal transduction is initiated by dimerization of TLR4/MD-2 unit (Akashi *et al*, 2001; Saitoh *et al*, 2004; Kobayashi *et al*, 2006). Clustering of TLR4 was observed by fluorescent and electron microscopy after LPS stimulation (Visintin *et al*, 2003; Triantafilou *et al*, 2004; Latty *et al*, 2018), and the signaling was mediated by a left-handed helical oligomer of downstream adaptors consisting death domains (Lin *et al*, 2010); *i.e.*, receptor oligomerization may provoke further downstream signaling. These previous and current findings, taken together, suggest that GM3 species act as TLR4-selective endogenous modulators to induce receptor dimerization/ oligomerization, and consequently enhance signal transduction leading to chronic inflammation in metabolic disorders.

Molecular docking approach implicates different binding modes of GM3 species modulating TLR4 activation

To figure out how GM3 species enhance and suppress TLR4 activation depending on the acyl-chain structure, we performed a ligand-macromolecular docking study on hTLR4/hMD-2 complex. Binding modes of VLCFA-GM3 (24:0) and LCFA-GM3 (16:0) were sought on the molecular surface around the hydrophobic pocket of hMD-2 and the basic residues of hTLR4. Docking models of hTLR4/hMD-2/GM3 (24:0 or 16:0) complex are shown in Fig 9A and B. Similarly to LPS and lipid IVa, both GM3 24:0 and 16:0 bound the hydrophobic pocket of hMD-2 via the fatty acid and the sphingoid base (Fig 9C–E). The binding model of GM3 24:0 overlapped closely to Ra-LPS in the crystal structure of reference, and the saccharide chain of GM3 24:0 was surrounded by basic residues of TLR4 (Figs 9C and EV5A–C). The basic residues of TLR4 (K341, K362, and R322), that interact with the saccharide chain of LPS and show conformational changes upon TLR4 activation (Park *et al*, 2009; Ohto *et al*, 2012b), were closely associated with the saccharide chain of GM3 24:0. However, R264, a key residue recognizing 4′-phosphate of LPS and triggering TLR4 activation (Park *et al*, 2009), was far from the saccharide chain of GM3 24:0. These results imply the underlying mechanism of VLCFA-GM3 capability to enhance TLR4 signaling without triggering activation by itself. Since synergistic activation by VLCFA-GM3 was mainly observed in the presence of low-dose LPS or weak TLR4 ligands, VLCFA-GM3 may act as an endogenous LPS mimic without intrinsic activity, which could sensitize TLR4 signaling by decreasing the ligand concentration required for TLR4 activation and increasing dimer/ oligomer formation (Fig 9F).

Next, binding model of GM3 16:0 was compared to lipid IVa in complex with hMD-2 (Figs 9E and EV5D–F). Lipid IVa shows different binding mode in comparison with LPS, with reverse orientation of 4′-phosphate and acyl chains, which may inhibit dimer formation of hTLR4/hMD-2 by presenting hydrophilic groups (phosphate and glucosamine) to the lipophilic dimer interface (Park *et al*, 2009; Ohto *et al*, 2012a; Fig 9C and E). Similarly, GM3 16:0 showed opposite binding mode to GM3 24:0, with reverse orientation of the saccharide chain and the acyl chain (Fig 9D), which may interfere and reduce TLR4 activation through presentation of the saccharide chain to the dimer interface (Figs 9E and EV5D–F). On the other hand, lipid IVa and lipid A (LPS-core structure) are known to show same binding orientations on mTLR4/mMD-2 (Ohto *et al*, 2012a). Binding model of GM3 16:0 on mTLR4/mMD-2 showed almost the same orientation compared with GM3 24:0 (Appendix Fig S5A–C). These comparative analyses implicate the mechanism by which GM3 species can enhance and reduce TLR4 activation in an acyl-chain-dependent manner.

Discussion

TLR4 signaling plays crucial roles in pathogenesis of obesity and metabolic disorders. This study demonstrated that human TLR4/MD-2 received positive regulation by VLCFA-/α-hydroxy VLCFA-GM3 and negative regulation by LCFA-/unsaturated VLCFA-GM3 in the presence of LPS and HMGB1. LCFA-GM3 species such as 16:0 consistently inhibited TLR4 activation even in the presence of VLCFA-GM3 species 22:0 or 24:0; 18:0; and 20:0 (Fig 5I). These findings indicate that GM3 species function as a rheostat for TLR4 signaling (Fig 5J). Increases in VLCFA-/α-hydroxy VLCFA-GM3 species, and decreases in LCFA-GM3 species, were involved in pathogenesis of metabolic disorders via chronic inflammatory processes. Computational approaches revealed that elongation, α-hydroxylation, and desaturation of fatty-acid structures of GM3 were related to signatures of disease progression. α-hydroxy VLCFA-GM3 species were also increased in adipose tissue of obese mice. The increase in α-hydroxy VLCFA-GM3 was attenuated by TLR4 mutation, implying a feedback loop from TLR4 activation to GM3 production, analogous to that for free fatty acids (Suganami *et al*, 2007). GM3 induced dimerization/ oligomerization of TLR4/MD-2, and MD-2 was involved in recognition of the fatty-acid structure of GM3. These findings suggest that GM3 plays an important role in TLR4 signaling, and the increase in VLCFA-GM3 species, showing the strongest synergistic TLR4 activation, is a risk factor for TLR4-mediated disease progression.

Measurement of serum GM3 species will potentially allow evaluation of hidden risks of TLR4-signaling-related inflammatory diseases (*e.g.*, inflammatory bowel disease, chronic kidney disease, rheumatoid arthritis, cancer metastasis) via LPS and endogenous ligands such as HMGB1, S100A8/9 (Mrp8/14), and SAA3 (Vogl *et al*, 2007; Hiratsuka *et al*, 2008; Harris *et al*, 2012). Over 20 GM3 species, in addition to the ten major species examined in this study, are present in human serum (Veillon *et al*, 2015). Moreover, there is increasing evidence for important roles of GSLs in innate immune responses and chronic inflammation (Kondo *et al*, 2013; Nakayama *et al*, 2016; Nagata *et al*, 2017; Nitta *et al*, 2019). Expression pattern analysis utilizing artificial intelligence will allow us to deal effectively with the complexity and variety of GM3 and other GSL species, and to further elucidate the relationships between particular species and inflammatory diseases.

The detailed mechanism whereby GM3 species are secreted and presented to TLR4/MD-2 complex is currently under study. It is supposed that GM3 is secreted as part of a lipoprotein complex

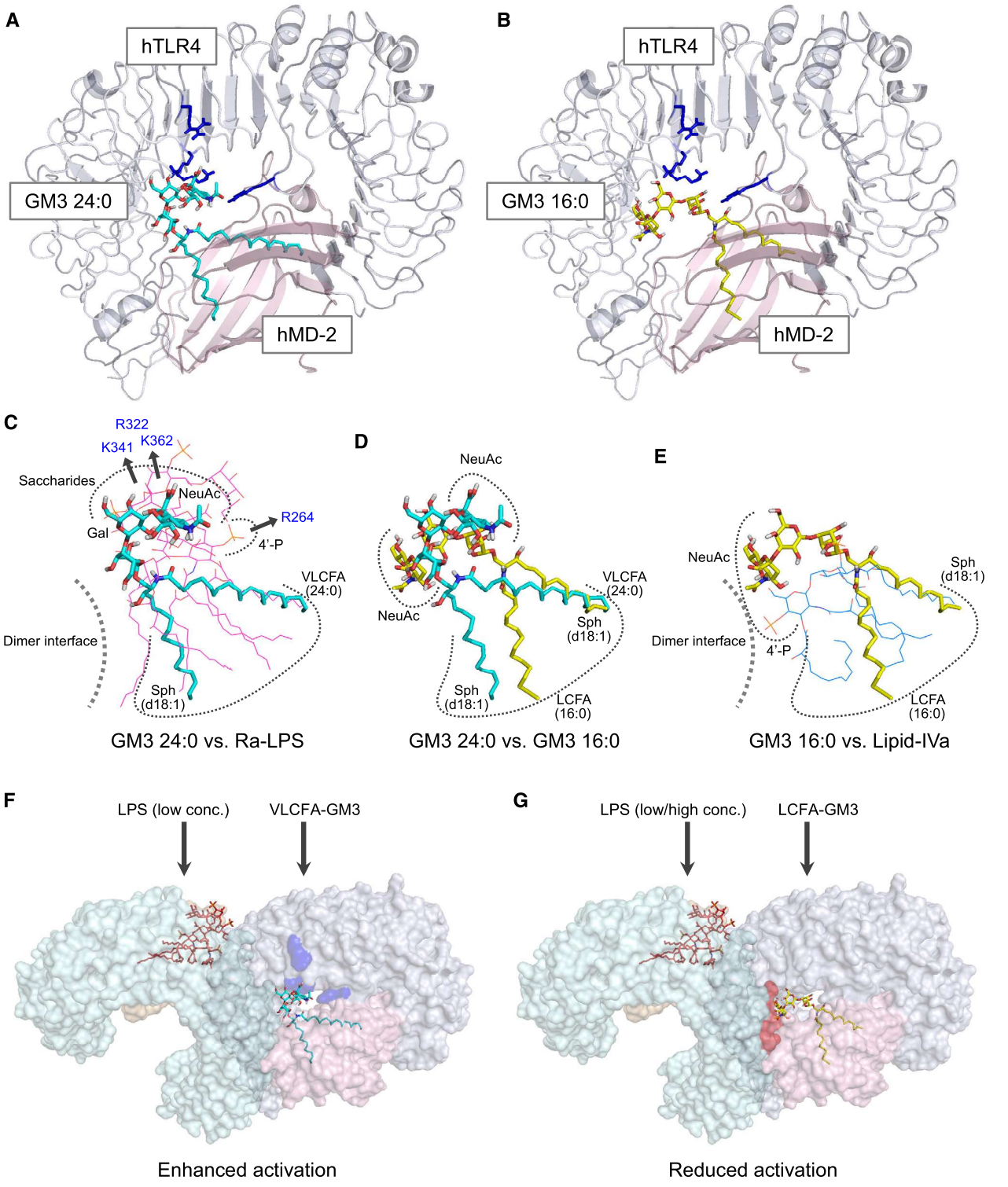

Figure 9. Ligand-macromolecular docking analysis implicates species-specific GM3 recognition by TLR4/MD-2.

A, B Docking model of GM3 24:0 (A) and 16:0 (B) binding to human TLR4/MD-2 complex (3FXI). Basic residues of TLR4 are colored in blue.

C–E Superposition of GM3 24:0 (in docking model) vs. Ra-LPS (in 3FXI) (C), GM3 24:0 vs. GM3 16:0 (in docking model) (D), and GM3 16:0 vs. lipid IVa (in 2E59) (E). Basic residues and the dimer interface are indicated schematically.

F, G Working model for hTLR4 activation enhanced by VLCFA-GM3 species (F) and reduced by LCFA-GM3 (G). Basic residues contributing to GM3 recognition are colored in blue. Residues of dimer interface are colored in red.

(Senn *et al*, 1989; Veillon *et al*, 2015) allowing circulation from the liver to most body tissues, including adipose tissue. TLR4 has been shown to mediate innate immune responses by LDL cholesterol (Stewart *et al*, 2010). Ceramide 24:0 is preferentially incorporated into LDL cholesterol (Boon *et al*, 2013). The present study shows that levels of VLCFA-GM3 and non-HDL cholesterol increase together, whereas levels of LCFA-GM3 and HDL cholesterol decrease together, indicating species-selective incorporation into lipoproteins. However, other secretion pathways, such as exosomes and microvesicles (Skotland *et al*, 2017), may also be involved. Furthermore, α-hydroxylation, mediated by enzymes such as fatty acid-2 hydroxylase (FA2H), may contribute to secretion of GM3 species via reducing hydrophobicity and affecting lipid diffusion (Hama, 2010).

In regard to activation mechanisms, our results displayed that CD14 and MD-2 facilitate GM3 to modulate TLR4 signaling. It is possible that CD14, MD-2, and LPS-binding protein take up serum GM3 species and transport them to TLR4, as reported for LPS (Ryu *et al*, 2017). As shown in docking study, VLCFA-GM3 and LCFA-GM3 may interact with TLR4/MD-2 by utilizing different interaction modes to promote or disrupt dimerization, similarly to lipid A/IVa species and eritoran (a strong antagonist in lipid IVa analogs) (Mullarkey *et al*, 2003; Kim *et al*, 2007; Ohto *et al*, 2007, 2012a; Appendix Fig S3). In particular, molecular features of LCFA-GM3 and unsaturated VLCFA-GM3 resemble those of eritoran: (i) short aliphatic-chain length (C10) in comparison with agonistic lipid A species (C14) and (ii) desaturation (C18:1, ω-7) making a 180-degree turn of the acyl chain in the hydrophobic pocket of MD-2 (Kim *et al*, 2007). Mimetic compounds based on lipid A/IVa precursors (diacyl monosaccharide species), carrying less number of fatty acids, show antagonistic effect (Facchini *et al*, 2018). Thus, less fatty-acid number, shorter acyl-chain length, and desaturation may cooperatively contribute to antagonistic activity by affecting interaction mode. Our findings suggest that GM3 species modulate TLR4 activation by utilizing molecular mechanisms closely related to lipid A/ IVa. Formation of two ligand-binding pockets on the dimerization interface between two TLR4/MD-2 units has been suggested by crystallographic analyses (Park *et al*, 2009; Ohto *et al*, 2012a). Reported binding study of TLR4/MD-2 with lipid A suggests that the maximal binding of the agonistic *E. coli* lipid A was approximately half-fold lower than that of the antagonistic lipid IVa (Akashi *et al*, 2001; Saitoh *et al*, 2004); i.e., under physiological conditions, one ligand pocket is occupied by agonist (e.g., LPS) while the other is vacant or occupied by unknown intrinsic ligands. It may allow GM3 species to modulate dimerization efficiency via the second pocket (Fig 9F and G). Future studies are expected to reveal structures of oligomeric TLR4/MD-2 signalosomes complexed with GM3 species. Additionally, it is known that the dimerization and internalization of mTLR4/MD-2 upon acute stimulation by LPS can be analyzed by flow cytometry (Akashi *et al*, 2003; Zanoni *et al*, 2011; Tan *et al*, 2015), which might enable to detect GM3-mediated receptor dynamics directly on the plasma membrane of living cells.

Biosynthesis of the various GM3 species may depend on several enzymes: fatty-acid elongases (Elovls), acyl-CoA desaturases, ceramide synthases (CerSs), and GM3S. Blocking of 16:0-to-18:0 fatty-acid elongation in mice by *Elovl6* knockout was found to inhibit progression of metabolic disorders through alterations of fatty-acid structures, *i.e.*, increased 16:0 and decreased 18:0-to-24:0 levels (Matsuzaka *et al*, 2007). *Elovl6* deficiency therefore may attenuate increase in VLCFA-GM3 species, and achieve homeostatic balance of acyl-chain structures. On the other hand, increase in LCFA-Cer (16:0) and decreases in VLCFA-Cer (22:0, 24:0) in obese subjects, resulting from imbalance of CerS2/6 expression and inhibition of β-oxidation, were reported to correlate to progression of metabolic disorders (Raichur *et al*, 2014; Turpin *et al*, 2014). Our results imply that such imbalances in Cer species might be involved in decreased production of LCFA-GM3 and increased production of VLCFA-GM3 in metabolic disorders. Fatty-acid desaturation was shown to occur in the resolution phase of innate immune response, and to reduce inflammation (Oishi *et al*, 2017); however, the direct mechanism whereby ω-9 mono-unsaturated VLCFA attenuates chronic inflammation is not completely understood. Increased levels of unsaturated GM3 species in severe metabolic disorders may result from desaturation mechanisms after the activation phase. Both elongase and desaturase genes are regulated by SREBP-1, a key transcription factor in lipid signaling whose activation occurs in parallel with that of NF-κB (Matsuzaka *et al*, 2007; Oishi *et al*, 2017). We previously reported that proinflammatory cytokines TNF-α and IL-1β induce *GM3S* expression and GM3 production in adipocytes (Tagami *et al*, 2002; Nagafuku *et al*, 2015). In the present study, *TLR4* deficiency reduced production of α-hydroxy VLCFA-GM3 (Fig 7D), suggesting the involvement of TLR4 signaling in GM3 production. These previous and current findings indicate that fatty-acid structures and total expression level of GM3 species are controlled by complex, coordinated mechanisms regulated by innate immune signaling, lipid signaling, and other cellular responses.

Moreover, it should be clarified directly in adipose tissue that GM3 species could mediate the adipocyte–macrophage communication in the future study. It would be important to specify the GM3 and other ganglioside species expressed in a specific type of cells, such as macrophages, pre-adipocytes, and differentiated adipocytes, that are mixed in adipose tissue. While pre-adipocytes/adipocytes predominantly express GM3, it is considered that human monocytes and mouse macrophages express GM3 and GM1/GD1a, respectively (Yohe *et al*, 2001; Tanabe *et al*, 2009). However, it remains unclear how ganglioside species and their acyl-chain structures are different in a cell-type-specific manner in the intact adipose tissue. To characterize miscellaneous cells in adipose tissue, in vitro enzymatic digestion/fractionation and antibody-based cell sorting are performed generally. On the other hand, our previous report suggested that GM3 expression in adipocytes was regulated by the co-presence of the resident macrophages in adipose tissue (Nagafuku *et al*, 2015). It has been also known that the activation of GM3 synthase in monocyte/macrophages was easily occurred during culturing in vitro (Gracheva *et al*, 2007). Therefore, the specific method such as the imaging mass spectrometry for GM3 species should be established in order to analyze GM3 species directly in the intact adipose tissues without in vitro cell manipulation (Sugimoto *et al*, 2016).

In regard to potential therapeutic approaches, treatment with supplemental LCFA-GM3 16:0 may inhibit systemic and local production of TNF-α, IL-6, and IL-12/23 via TLR4, and in part via TLR2, driven by LPS and HMGB1. On the other hand, VLCFA-GM3 24:0 could act as a booster for immunological adjuvants such as monophosphoryl lipid A species (LA505, LA504) and other synthetic

TLR4 ligands (Wang *et al*, 2016; Chan *et al*, 2017; Okamoto *et al*, 2017). Utilization of naturally occurring GM3 species may prevent production of autoantibodies (Bowes *et al*, 2002).

In conclusion, our findings would help clarify the pathophysiological roles of serum/ adipose GM3 species in TLR4 signaling, and the complex interplay between glycosphingolipid metabolism and innate immune signaling in metabolic disorders.

Materials and Methods

Ceramide, GSLs, and complex gangliosides

Ceramide species (16:0, 24:0, 24:1) and GlcCer species (16:0, 24:1) were from Avanti Polar Lipids (Alabaster, AL, USA). GlcCer (24:0), LacCer (16:0, 24:0, 24:1), and GM3 (16:0, 18:0, 20:0, 22:0, 24:0, h24:0, 24:1) and GM1 (18:0) were synthesized as described previously (Murase *et al*, 1989; Mauri *et al*, 1999). GM2 (from brain of Tay-Sachs disease patient) was from Matreya (State College, PA, USA). Brain GD1a, GD1b, and GT1b were from Sigma-Aldrich (St. Louis, MO, USA). Brain GQ1b was from AdipoGen Life Sciences (San Diego, CA, USA). Milk GD3 was from Nagara Science Co. (Gifu, Japan). Ceramides, GlcCer, and LacCer species were dissolved at 1 mM in warmed DMSO. Gangliosides were dissolved at 0.5 mM concentration in warmed low-glucose DMEM (Nacalai Tesque; Kyoto, Japan). Stock solutions were stored at −30°C and diluted with low-glucose DMEM to 100 μM concentration prior to experiments.

TLR ligands and recombinant proteins

Toll-like receptors ligands and recombinant proteins were purchased from the following vendors: LPS from *E. coli* O111:B4 (Sigma-Aldrich); human recombinant HMGB1, soluble form human CD14 (BioLegend; San Diego); bovine thymus HMGB1 (Chondrex; Redmond, WA, USA); soluble form mouse CD14-Fc fusion (Sino Biological, Inc.; Beijing, China); Pam3CSK4 and MALP-2 (Novus Biologicals; Littleton, CO, USA); and Poly I:C, R848, Flagellin from *Salmonella typhimurium*, and CpG (ODN 1826) (Enzo Life Sciences; Farmingdale, NY, USA). TLR ligands other than R848 were reconstituted in endotoxin-free water (Nacalai Tesque). R848 was reconstituted in ethanol (Fujifilm Wako; Osaka, Japan). Lipid A and derivatives were previously synthesized (Imoto *et al*, 1985, 1987; Liu *et al*, 1999).

Vector construction

Vector carrying mouse MD-2 and TLR4 cDNA (pDUO-mMD2/ TLR4) was from InvivoGen (San Diego). cDNA fragments, fused with a KpnI site and one Kozak sequence (ACC) at 5′-end and SalI site at 3′-end, were amplified by PCR (KOD-Plus-Neo; Toyobo) and inserted separately into pCDNA3 at KpnI and XhoI sites (Invitrogen). A set of vectors for dual luciferase assay, NF-κB reporter gene (pGL3-ELAM; a firefly luciferase gene controlled by NF-κB-dependent promoter of ELAM-1), control reporter gene (pRL-TK; a Renilla luciferase gene controlled by constitutive active promoter of thymidine kinase), and pCDNA3 vectors carrying human MD-2 and TLR4 cDNA were previously described (Muta & Takeshige, 2001; Fujimoto *et al*, 2004). Reporter vectors for AP-1 and ISRE were purchased (Promega; Australia). Site-directed mutagenesis was performed according to the manufacturer's protocol of QuikChange (Agilent; Santa Clara, CA, USA) with minor modifications.

Purification and stimulation of human monocytes

Heparinized fresh human peripheral blood was diluted to 2× volume with cold (4°C) endotoxin-free PBS (Nacalai Tesque) containing 1 μg/ml polymyxin B (Sigma-Aldrich). Diluted blood was overlaid on cold (4°C) lymphocyte separation solution (Nacalai Tesque) containing 1 μg/ml polymyxin B and centrifuged at 800 *g* for 25 min at 4°C. Peripheral blood mononuclear cell (PBMC) fraction was collected and diluted to 2× volume of wash solution (PBS, 1% heat-inactivated FCS (Biosera), 5 mM EDTA, pH 7.5 (Nacalai Tesque), 1 μg/ml polymyxin B). PBMCs were separated by centrifugation at 600 *g* for 10 min at 4°C, washed twice, resuspended in 750 μl wash solution and incubated with 120 μl anti-human CD14 magnetic particles (BD Biosciences) for 30 min at room temperature. CD14-positive cells (monocytes) were separated by magnetic field and washed 3× with wash solution. Purified cells were resuspended in cold low-glucose DMEM with 0.75% FCS, left on ice for 45 min, counted, diluted to 2.0×10^5 cells/ml with culture medium (low-glucose DMEM, 0.75% FCS, 40 ng/ml recombinant human granulocyte-macrophage colony-stimulating factor (GM-CSF) (BioLegend), and cultured in 96-well plates (100 μl/well) overnight at 37°C under 5% CO_2 atmosphere.

Differentiation of mouse bone marrow-derived macrophages (BMDMs)

Femoral and tibial bone marrows of 12- to 16-week-old nondiabetic C3H/HeN mice (Japan SLC Inc.) were collected in 1% FCS-supplemented low-glucose DMEM, and erythrocytes were lysed in RBC lysis buffer. Bone marrow cells were washed in 1% FCS DMEM and cultured 5–7 days in 10% FCS DMEM supplemented with 40 ng/ml recombinant human macrophage colony-stimulating factor (M-CSF) (BioLegend). Non-adhesive cells were washed out with PBS. Differentiated macrophages were collected by scraping in ice-cold PBS with 1% FCS/ 5 mM EDTA, washed, counted, diluted to 2.0×10^5 cells/ml in 1% FCS DMEM, and cultured in 96-well plates overnight at 37°C under 5% CO_2 atmosphere.

Cell culture and transfection

HEK293T cells (RIKEN BioResource Center; Wako, Japan) were maintained in 10% FCS low-glucose DMEM at 37°C under 5% CO_2 atmosphere. Prior to transfection, cells were diluted to 2.0×10^5/ml in 1% FCS DMEM and cultured in 96-well plates overnight. Cells in each well were transfected with reporter vectors (40 ng pGL3-ELAM, 20 ng pRL-TK) and expression vectors (hTLR4/hMD-2, 20 ng pCDNA3-hMD-2 and 40 ng pCDNA3-hTLR4; mTLR4/mMD-2, 20 ng pCDNA3-mMD-2 and 1 ng pCDNA3-mTLR4; mTLR4/hMD-2, 20 ng pCDNA3-hMD-2 and 1 ng pCDNA3-mTLR4; and hMal, 0.1 or 0.5 ng pCDNA3-hMal), complexed with 0.5 μl Lipofectamine LTX and 0.25 μl Plus reagent in 20 μl Opti-MEM (Invitrogen), and subjected to stimuli 24 h after transfection.

Cell stimulation, ELISA, and luciferase assay

Cells were primed for 30 min with various sphingolipids and then stimulated with TLR ligands. After 18-h culture, media were collected and subjected to ELISA. ELISA kits for human IL-6, human TNF-α, human IL12/23 p40, and mouse TNF-α were from BioLegend. Firefly and Renilla luciferase activities were measured using Dual-Glo Luciferase Assay System (Promega; Australia) on a microplate reader (model Infinite M1000 PRO, Tecan Group; Männedorf, Switzerland).

TLC and LC-MS/MS analysis of GM3 species

Total lipids in lyophilized human serum were extracted with chloroform/ methanol (2:1 and 1:1, v/v) and separated into acidic and neutral fractions on DEAE-Sephadex A-25 anion-exchange columns (GE Healthcare Life Sciences; Nitta *et al*, 2019). Acidic fraction was de-esterified by mild alkaline hydrolysis for phospholipids, followed by desalting using a Sep-Pak C18 cartridge (Waters; Milford, MA, USA). Acidic GSLs in mouse adipose tissues were separated by Ladisch's partitioning method as previously described (Tagami *et al*, 2002). Acidic GSLs (respective protein equivalent 100 μg [mouse adipose tissue] or respective volume equivalent 1 ml [human serum]) were spotted on HPTLC plates, developed, respectively, with chloroform/ methanol/ 0.2% $CaCl_2$ (55:25:10, v/v/v) and chloroform/ methanol/ water (60:25:4, v/v/v), and visualized by orcinol/ sulfuric acid staining. Acidic GSLs were also subjected to LC-MS/MS analysis by running method as described previously (Veillon *et al*, 2015; Go *et al*, 2017). 100 ng of the deuterated GM3 (d18:1-[^{13}C]16:0) was added for internal standard. Relative abundance of a particular GM3 species was expressed as peak area of that species divided by total peak area. For comparison of GM3 species among different mouse groups, total abundance of GM3 species in control group was defined as 1, and the abundances of each GM3 species in both control and fatty (e.g., HFD, *ob/ob*) group were normalized and displayed as relative amounts.

Analysis of LC-MS/MS data of GM3 species in sera of presymptomatic subjects and patients with metabolic disorders

LC-MS/MS data and clinical markers of human subjects were obtained in previous study (Veillon *et al*, 2015), and relative abundances of ten major GM3 species (fatty acid: 16:0, 18:0, 20:0, 22:0, 23:0, 24:0, h24:0, 22:1, 24:1, h24:1) with reference to their total (defined as 1) were newly evaluated for each subject. Trends of each species in terms of pathological phases and Spearman's correlation coefficient in relation to clinical markers of metabolic disorders and chronic inflammation were analyzed. Self-organization map (SOM) and Bayesian regularized neural-network (BRNN) analysis were performed as described previously (Aoki *et al*, 2011).

Animal studies

Six-week-old male *ob/ob* and control background (C57/BL6) mice were from CLEA Japan (Tokyo). Eight-week-old male C57/BL6, C3H/HeN, and C3H/HeJ (TLR4 mutant; Poltorak *et al*, 1998) mice (Japan SLC) were divided randomly into two groups. The control group was fed normal diet (ND) (CE-2; CLEA Japan), while the HFD group was fed high-fat diet (HFD) (D12492; Research Diet; New Brunswick, NJ, USA) ad lib for 8 weeks (C3H/HeN, C3H/HeJ) or 10 weeks (C57/BL6). Epididymal fat pads and blood (from right ventricle) were harvested from sacrificed animals, and non-fasting blood glucose level was measured using Accu-Chek Aviva strips (Roche DC; Japan).

Cross-linking and SDS–PAGE analysis

The recombinant mouse TLR4 (extracellular domain)/mMD-2 proteins were prepared as described previously (Ohto *et al*, 2012a). Mouse TLR4/mMD-2 complex proteins (1.5 μg) were mixed with GM3 18:0 (final 0.0071, 0.71, 71 μM) and incubated at room temperature for 1 h. LPS (0.05 μg) was added to the complex and incubated at 37°C for 1 h. Cross-linking was performed by incubation with 0.6 μmol DMP (dimethyl pimelimidate; Thermo Fisher Scientific) at room temperature for 1 h. Cross-linked protein complex was analyzed by SDS–PAGE (5–10% gradient gel) and silver-stained.

Ligand-macromolecular docking

Molecular editing and lowest-energy calculation of GM3 24:0 and 16:0 were performed on Avogadro molecular editing software (Hanwell *et al*, 2012), and their three-dimensional structures were exported as PDB files. Ligand-macromolecular docking between GM3 species and TLR4/MD-2 complex was performed on AutoDock 4.2 molecular docking software (Morris *et al*, 2009). Grid settings for generating the binding surface on hTLR4/hMD-2 were below: spacing, 0.431 Å; grid points, 60, 80, and 80; center of grids, 25, −13, and 15 (on x-, y-, and z-axis). Grid settings for mTLR4/mMD-2 were below: spacing, 0.431 Å; grid points, 80, 60, and 80; and center of grids, −30, −16, and 17 (on x-, y-, and z-axis). Lamarckian genetic algorithm was used for searching candidate binding modes, and the binding mode with lowest energy was exploited from 100 calculation results. As a benchmark, rigid-rigid dockings of Ra-LPS (conformer in 3FXI) vs. hTLR4/hMD-2 (3FXI, chains A and C) and lipid A (conformer in 3VQ2) vs. mTLR4/mMD-2 (3VQ2, chains A and C) were performed (Appendix Fig S5D and E). Same settings and procedures for calculation were applied for searching rigid-rigid binding modes of GM3 species on human and mouse TLR4/MD-2 complex. All molecular/ protein structures were visualized by PyMOL software (DeLano Scientific).

Ethics and informed consents for human-subjected study

All participants gave their written informed consent prior to their inclusion in the study. The experimental protocol was in agreement with international norms and approved by the ethics committee of the University of Tokyo and Tohoku Medical and Pharmaceutical University.

Statistical analysis

Data were expressed as mean ± SD and analyzed by two-tailed unpaired *t*-test or Tukey's multiple comparison (honesty significant difference) test using Microsoft Excel (Microsoft) and StatPlus:Mac Pro (AnalystSoft; Walnut, CA, USA). Differences between means were considered significant for $P < 0.05$ (*), < 0.01 (**), or < 0.001 (***).

Data availability

The mass spec data of the GM3 species in human serum are available at the database GlycoPOST (https://glycopost.glycosmos.org). The accession number is GPST000057.

Expanded View for this article is available online.

Acknowledgements
The authors are grateful to the Center for Laboratory Animal Science, Tohoku Medical and Pharmaceutical University, for their services, and to Dr. S. Anderson for English editing of the manuscript. This study was supported by grants-in-aids from Ministry of Education, Culture, Sports, Science and Technology of Japan [JSPS KAKENHI: Grants-in-Aid for Scientific Research (B) (JP16H04767 to J.I.), for Exploratory Research (JP17K19569 to J.I.), for Young Scientist (B) (JP17K15450 to H.K.), and for Young Scientist (JP19K16356 to H.K.)], Takeda Science Foundation (J.I.), Fugaku Trust for Medicinal Research (J.I.), and Mizutani Foundation for Glycoscience (J.I.). We would like to thank Drs Yoshiki Yamaguchi (Tohoku Medical and Pharmaceutical University) and Takayuki Kuraishi (Kanazawa University, Japan) for technical supports and discussions.

Author contributions
HK, TN, SG, KI, LV, WN, MF, KK, ASh, UO, TS, TW, HS, SA, KS, MN, YYa, NK, HA, HI, YN, YYo, AZ, AC, ML, MC, LM, ASu, and JI performed the research and analyzed the data. HK, KF, KS, MK, AP, SS, and JI. designed and supervised the research. HK and JI wrote the manuscript.

Conflict of interest
The authors declare that they have no conflict of interest.

References

Akashi S, Nagai Y, Ogata H, Oikawa M, Fukase K, Kusumoto S, Kawasaki K, Nishijima M, Hayashi S, Kimoto M *et al* (2001) Human MD-2 confers on mouse Toll-like receptor 4 species-specific lipopolysaccharide recognition. *Int Immunol* 13: 1595 – 1599

Akashi S, Saitoh S, Wakabayashi Y, Kikuchi T, Takamura N, Nagai Y, Kusumoto Y, Fukase K, Kusumoto S, Adachi Y *et al* (2003) Lipopolysaccharide interaction with cell surface Toll-like receptor 4-MD-2: higher affinity than that with MD-2 or CD14. *J Exp Med* 198: 1035 – 1042

Aoki S, Hoshi K, Kawakami J, Sato K, Satoh K, Mori K, Sugawara A, Saito Y, Yoshida K (2011) Assisting the diagnosis of Graves' hyperthyroidism with pattern recognition methods and a set of three routine tests parameters, and their correlations with free T4 levels: Extension to male patients. *Biomed Pharmacother* 65: 95 – 104

Bikman BT, Summers SA (2011) Ceramides as modulators of cellular and whole- body metabolism. *J Clin Invest* 121: 4222 – 4230

Boon J, Hoy AJ, Stark R, Brown RD, Meex RC, Henstridge DC, Schenk S, Meikle PJ, Horowitz JF, Kingwell BA *et al* (2013) Ceramides contained in LDL are elevated in type 2 diabetes and promote inflammation and skel*et al* muscle insulin resistance. *Diabetes* 62: 401 – 410

Bowes T, Wagner ER, Boffey J, Nicholl D, Cochrane L, Benboubetra M, Conner J, Furukawa K, Furukawa K, Willison HJ (2002) Tolerance to self gangliosides is the major factor restricting the antibody response to lipopolysaccharide core oligosaccharides in Campylobacter jejuni strains associated with Guillain-Barré syndrome. *Infect Immun* 70: 5008 – 5018

Cani PD, Amar J, Iglesias MA, Poggi M, Knauf C, Bastelica D, Neyrinck AM, Fava F, Tuohy KM, Chabo C *et al* (2007) Metabolic endotoxemia initiates obesity and insulin resistance. *Diabetes* 56: 1761 – 1772

Chan M, Kakitsubata Y, Hayashi T, Ahmadi A, Yao S, Shukla NM, Oyama SY, Baba A, Nguyen B, Corr M *et al* (2017) Structure-activity relationship studies of Pyrimido[5,4-b]indoles as selective toll-like receptor 4 ligands. *J Med Chem* 60: 9142 – 9161

Facchini FA, Zaffaroni L, Minotti A, Rapisarda S, Calabrese V, Forcella M, Fusi P, Airoldi C, Ciaramelli C, Billod JM *et al* (2018) Structure-activity relationship in monosaccharide-based toll-like receptor 4 (TLR4) antagonists. *J Med Chem* 61: 2895 – 2909

Fujimoto T, Yamazaki S, Eto-Kimura A, Takeshige K, Muta T (2004) The amino-terminal region of toll-like receptor 4 is essential for binding to MD-2 and receptor translocation to the cell surface. *J Biol Chem* 279: 47431 – 47437

Go S, Go S, Veillon L, Ciampa MG, Mauri L, Sato C, Kitajima K, Prinetti A, Sonnino S, Inokuchi JI (2017) Altered expression of ganglioside GM3 molecular species and a potential regulatory role during myoblast differentiation. *J Biol Chem* 292: 7040 – 7051

Gracheva EV, Samovilova NN, Golovanova NK, Andreeva ER, Andrianova IV, Tararak EM, Prokazova NV (2007) Activation of ganglioside GM3 biosynthesis in human monocyte/macrophages during culturing in vitro. *Biochemistry (Mosc)* 72: 772 – 777

Guzmán-Ruiz R, Ortega F, Rodríguez A, Vázquez-Martínez R, Díaz-Ruiz A, Garcia-Navarro S, Giralt M, Garcia-Rios A, Cobo-Padilla D, Tinahones FJ *et al* (2014) Alarmin high-mobility group B1 (HMGB1) is regulated in human adipocytes in insulin resistance and influences insulin secretion in β-cells. *Int J Obes* 38: 1545 – 1554

Hama H (2010) Fatty acid 2-Hydroxylation in mammalian sphingolipid biology. *Biochim Biophys Acta* 1801: 405 – 414

Hanwell MD, Curtis DE, Lonie DC, Vandermeersch T, Zurek E, Hutchison GR (2012) Avogadro: an advanced semantic chemical editor, visualization, and analysis platform. *J Cheminform* 4: 17

Harris HE, Andersson U, Pisetsky DS (2012) HMGB1: A multifunctional alarmin driving autoimmune and inflammatory disease. *Nat Rev Rheumatol* 8: 195 – 202

Hiratsuka S, Watanabe A, Sakurai Y, Akashi-Takamura S, Ishibashi S, Miyake K, Shibuya M, Akira S, Aburatani H (2008) Maru Y The S100A8-serum amyloid A3-TLR4 paracrine cascade establishes a pre-metastatic phase. *Nat Cell Biol* 10: 1349 – 1355

Hotamisligil GS (2017) Inflammation, metaflammation and immunometabolic disorders. *Nature* 542: 177 – 185

Imoto M, Yoshimura H, Sakaguchi N, Kusumoto S (1985) ShibaT. Total synthesis of *Escherichia coli* lipid A. *Tetrahedron Lett* 26: 1545 – 1548

Imoto M, Yoshimura H, Shimamoto T, Sakaguchi N, Kusumoto S, Shiba T (1987) Total synthesis of *Escherichia coli* lipid A, the endotoxically active principle of cell-surface lipopolysaccharide. *Bull Chem Soc Jpn* 60: 2205 – 2214

Inokuchi JI, Inamori KI, Kabayama K, Nagafuku M, Uemura S, Go S, Suzuki A, Ohno I, Kanoh H, Shishido F (2018) Biology of GM3 ganglioside. *Prog Mol Biol Transl Sci* 156: 151 – 195

Kabayama K, Sato T, Kitamura F, Uemura S, Kang BW, Igarashi Y, Inokuchi J (2007) Dissociation of the insulin receptor and caveolin-1 complex by ganglioside GM3 in the state of insulin resistance. *Proc Natl Acad Sci USA* 104: 13678 – 13683

Kawai T, Akira S (2011) Toll-like receptors and their crosstalk with other innate receptors in infection and immunity. *Immunity* 34: 637 – 650

Kim HM, Park BS, Kim JI, Kim SE, Lee J, Oh SC, Enkhbayar P, Matsushima N, Lee H, Yoo OJ *et al* (2007) Crystal structure of the TLR4-MD-2 complex with bound endotoxin antagonist Eritoran. *Cell* 130: 906 – 917

Kobayashi M, Saitoh S, Tanimura N, Takahashi K, Kawasaki K, Nishijima M, Fujimoto Y, Fukase K, Akashi-Takamura S, Miyake K (2006) Regulatory roles for MD-2 and TLR4 in ligand-induced receptor clustering. *J Immunol* 176: 6211 – 6218

Kondo Y, Ikeda K, Tokuda N, Nishitani C, Ohto U, Akashi-Takamura S, Ito Y, Uchikawa M, Kuroki Y, Taguchi R *et al* (2013) TLR4–MD-2 complex is negatively regulated by an endogenous ligand, globotetraosylceramide. *Proc Natl Acad Sci USA* 110: 4714 – 4719

Latty SL, Sakai J, Hopkins L, Verstak B, Paramo T, Berglund NA, Cammarota E, Cicuta P, Gay NJ, Bond PJ *et al* (2018) Activation of Toll-like receptors nucleates assembly of the MyDDosome signaling hub. *eLife* 7: e31377

Lin SC, Lo YC, Wu H (2010) Helical assembly in the MyD88-IRAK4-IRAK2 complex in TLR/IL-1R signalling. *Nature* 465: 885 – 890

Lingwood D, Simons K (2010) Lipid rafts as a membrane-organizing principle. *Science* 327: 46 – 50

Liu WC, Oikawa M, Fukase K, Suda Y, Kusumoto S (1999) A divergent synthesis of lipid a and its chemically stable unnatural analogues. *Bull Chem Soc Jpn* 72: 1377 – 1385

Lumeng CN (2011) Saltiel AR Inflammatory links between obesity and metabolic disease. *J Clin Invest* 121: 2111 – 2117

Matsuzaka T, Shimano H, Yahagi N, Kato T, Atsumi A, Yamamoto T, Inoue N, Ishikawa M, Okada S, Ishigaki N *et al* (2007) Crucial role of a long-chain fatty acid elongase, Elovl6, in obesity-induced insulin resistance. *Nat Med* 13: 1193 – 1202

Mauri L, Casellato R, Kirschner G, Sonnino S (1999) A procedure for the preparation of GM3 ganglioside from GM1-lactone. *Glycoconjugate J* 16: 197 – 203

Moresco EM, LaVine D, Beutler B (2011) Toll-like receptors. *Curr Biol* 21: R488 – R493

Morris GM, Huey R, Lindstrom W, Sanner MF, Belew RK, Goodsell DS, Olson AJ (2009) Autodock4 and AutoDockTools4: automated docking with selective receptor flexibility. *J Comput Chem*, 16: 2785 – 2791

Mueller M, Lindner B, Kusumoto S, Fukase K, Schromm AB, Seydel U (2004) Aggregates are the biologically active units of endotoxin. *J Biol Chem* 279: 26307 – 26313

Mullarkey M, Rose JR, Bristol J, Kawata T, Kimura A, Kobayashi S, Przetak M, Chow J, Gusovsky F, Christ WJ *et al* (2003) Inhibition of endotoxin response by e5564, a novel Toll-like receptor 4-directed endotoxin antagonist. *J Pharmacol Exp Ther* 304: 1093 – 1102

Murase T, Ishida H, Kiso M, Hasegawa A (1989) A facile, regio- and stereo-selective synthesis of ganglioside GM3. *Carbohydr Res* 188: 71 – 80

Muta T, Takeshige K (2001) Essential roles of CD14 and lipopolysaccharide-binding protein for activation of toll-like receptor (TLR)2 as well as TLR4 Reconstitution of TLR2- and TLR4-activation by distinguishable ligands in LPS preparations. *Eur J Biochem* 268: 4580 – 4589

Nagafuku M, Sato T, Sato S, Shimizu K, Taira T, Inokuchi J (2015) Control of homeostatic and pathogenic balance in adipose tissue by ganglioside GM3. *Glycobiology* 25: 303 – 318

Nagata M, Izumi Y, Ishikawa E, Kiyotake R, Doi R, Iwai S, Omahdi Z, Yamaji T, Miyamoto T, Bamba T *et al* (2017) Intracellular metabolite β-glucosylceramide is an endogenous Mincle ligand possessing immunostimulatory activity. *Proc Natl Acad Sci USA* 114: E3285 – E3294

Nakayama H, Kurihara H, Morita YS, Kinoshita T, Mauri L, Prinetti A, Sonnino S, Yokoyama N, Ogawa H, Takamori K *et al* (2016) Lipoarabinomannan binding to lactosylceramide in lipid rafts is essential for the phagocytosis of mycobacteria by human neutrophils. *Sci Signal* 9: ra101

Nitta T, Kanoh H, Inamori KI, Suzuki A, Takahashi T, Inokuchi JI (2019) Globo-series glycosphingolipids enhance Toll-like receptor 4-mediated inflammation and play a pathophysiological role in diabetic nephropathy. *Glycobiology* 29: 260 – 268

Ohto U, Fukase K, Miyake K, Satow Y (2007) Crystal structures of human MD-2 and its complex with antiendotoxic lipid IVa. *Science* 316: 1632 – 1634

Ohto U, Fukase K, Miyake K, Shimizu T (2012a) Structural basis of species-specific endotoxin sensing by innate immune receptor TLR4/MD-2. *Proc Natl Acad Sci USA* 109: 7421 – 7426

Ohto U, Yamakawa N, Akashi-Takamura S, Miyake K, Shimizu T (2012b) Structural analyses of human Toll-like receptor 4 polymorphisms D299G and T399I. *J Biol Chem* 287: 40611 – 40617

Oishi Y, Spann NJ, Link VM, Muse ED, Strid T, Edillor C, Kolar MJ, Matsuzaka T, Hayakawa S, Tao J *et al* (2017) SREBP1 contributes to resolution of pro-inflammatory TLR4 signaling by reprogramming fatty acid metabolism. *Cell Metab* 25: 412 – 427

Okamoto N, Mizote K, Honda H, Saeki A, Watanabe Y, Yamaguchi-Miyamoto T, Fukui R, Tanimura N, Motoi Y, Akashi-Takamura S *et al* (2017) Funiculosin variants and phosphorylated derivatives promote innate immune responses via the Toll-like receptor 4/myeloid differentiation factor-2 complex. *J Biol Chem* 292: 15378 – 15394

Pal D, Dasgupta S, Kundu R, Maitra S, Das G, Mukhopadhyay S, Ray S, Majumdar SS, Bhattacharya S (2012) Fetuin-A acts as an endogenous ligand of TLR4 to promote lipid-induced insulin resistance. *Nat Med* 18: 1279 – 1285

Park BS, Song DH, Kim HM, Choi BS, Lee H, Lee JO (2009) The structural basis of lipopolysaccharide recognition by the TLR4-MD-2 complex. *Nature* 458: 1191 – 1195

Poltorak A, He X, Smirnova I, Liu MY, Van Huffel C, Du X, Birdwell D, Alejos E, Silva M, Galanos C *et al* (1998) Defective LPS signaling in C3H/HeJ and C57BL/10ScCr mice: mutations in Tlr4 gene. *Science* 282: 2085 – 2088

Raichur S, Wang ST, Chan PW, Li Y, Ching J, Chaurasia B, Dogra S, Öhman MK, Takeda K, Sugii S *et al* (2014) CerS2 haploinsufficiency inhibits β-oxidation and confers susceptibility to diet-induced steatohepatitis and insulin resistance. *Cell Metab* 20: 687 – 695

Ryu JK, Kim SJ, Rah SH, Kang JI, Jung HE, Lee D, Lee HK, Lee JO, Park BS, Yoon TY *et al* (2017) Reconstruction of LPS transfer cascade reveals structural determinants within LBP, CD14, and TLR4-MD2 for efficient LPS recognition and transfer. *Immunity* 46: 38 – 50

Saitoh S, Akashi S, Yamada T, Tanimura N, Kobayashi M, Konno K, Matsumoto F, Fukase K, Kusumoto S, Nagai Y *et al* (2004) Lipid A antagonist, lipid IVa, is distinct from lipid A in interaction with Toll-like receptor 4 (TLR4)-MD-2 and ligand-induced TLR4 oligomerization. *Int Immunol* 16: 961 – 969

Schmidt M, Raghavan B, Müller V, Vogl T, Fejer G, Tchaptchet S, Keck S, Kalis C, Nielsen PJ, Galanos C *et al* (2010) Crucial role for human Toll-like receptor 4 in the development of contact allergy to nickel. *Nat Immunol* 11: 814 – 819

Senn HJ, Orth M, Fitzke E, Wieland H, Gerok W (1989) Gangliosides in normal human serum Concentration, pattern and transport by lipoproteins. *Eur J Biochem* 181: 657 – 662

Shen W, Stone K, Jales A, Leitenberg D, Ladisch S (2008) Inhibition of TLR activation and up-regulation of IL-1R-associated kinase-M expression by exogenous gangliosides. *J Immunol* 180: 4425 – 4432

Shi H, Kokoeva MV, Inouye K, Tzameli I, Yin H, Flier JS (2006) TLR4 links innate immunity and fatty acid-induced insulin resistance. *J Clin Invest* 116: 3015 – 3025

Skotland T, Sandvig K, Llorente A (2017) Lipids in exosomes: Current knowledge and the way forward. *Prog Lipid Res* 66: 30 – 41

Stewart CR, Stuart LM, Wilkinson K, van Gils JM, Deng J, Halle A, Rayner KJ, Boyer L, Zhong R, Frazier WA *et al* (2010) CD36 ligands promote sterile inflammation through assembly of a Toll-like receptor 4 and 6 heterodimer. *Nat Immunol* 11: 155 – 161

Suganami T, Tanimoto-Koyama K, Nishida J, Itoh M, Yuan X, Mizuarai S, Kotani H, Yamaoka S, Miyake K, Aoe S *et al* (2007) Role of the Toll-like receptor 4/NF-κB pathway in saturated fatty acid–induced inflammatory changes in the interaction between adipocytes and macrophages. *Arterioscler Thromb Vasc Biol* 27: 84 – 91

Suganami T, Mieda T, Itoh M, Shimoda Y, Kamei Y, Ogawa Y (2017) Attenuation of obesity-induced adipose tissue inflammation in C3H/HeJ mice carrying a Toll-like receptor 4 mutation. *Biochem Biophys Res Commun* 354: 45 – 49

Sugimoto M, Wakabayashi M, Shimizu Y, Yoshioka T, Higashino K, Numata Y, Okuda T, Zhao S, Sakai S, Igarashi Y *et al* (2016) Imaging mass spectrometry reveals acyl-chain- and region-specific sphingolipid metabolism in the kidneys of sphingomyelin synthase 2-deficient mice. *PLoS ONE* 11: e0152191

Tagami S, Inokuchi J, Kabayama K, Yoshimura H, Kitamura F, Uemura S, Ogawa C, Ishii A, Saito M, Ohtsuka Y *et al* (2002) Ganglioside GM3 participates in the pathological conditions of insulin resistance. *J Biol Chem* 277: 3085 – 3092

Tan Y, Zanoni I, Cullen TW, Goodman AL, Kagan JC (2015) Mechanisms of toll-like receptor 4 endocytosis reveal a common immune-evasion strategy used by pathogenic and commensal bacteria. *Immunity* 43: 909 – 922

Tanabe A, Matsuda M, Fukuhara A, Miyata Y, Komuro R, Shimomura I, Tojo H (2009) Obesity causes a shift in metabolic flow of gangliosides in adipose tissues. *Biochem Biophys Res Commun* 379: 547 – 552

Triantafilou M, Brandenburg K, Kusumoto S, Fukase K, Mackie A, Seydel U, Triantafilou K (2004) Combinational clustering of receptors following stimulation by bacterial products determines lipopolysaccharide responses. *Biochem J* 381: 527 – 536

Turpin SM, Nicholls HT, Willmes DM, Mourier A, Brodesser S, Wunderlich CM, Mauer J, Xu E, Hammerschmidt P, Brönneke HS *et al* (2014) Obesity-induced CerS6-dependent C16:0 ceramide production promotes weight gain and glucose intolerance. *Cell Metab* 20: 678 – 686

Veillon L, Go S, Matsuyama W, Suzuki A, Nagasaki M, Yatomi Y, Inokuchi J (2015) Identification of ganglioside GM3 molecular species in human serum associated with risk factors of metabolic syndrome. *PLoS ONE* 10: e0129645

Visintin A, Latz E, Monks BG, Espevik T, Golenbock DT (2003) Lysines 128 and 132 enable lipopolysaccharide binding to MD-2, leading to Toll-like receptor-4 aggregation and signal transduction. *J Biol Chem* 278: 48313 – 48320

Vogl T, Tenbrock K, Ludwig S, Leukert N, Ehrhardt C, Van Zoelen MA, Nacken W, Foell D, van der Poll T, Sorg C *et al* (2007) Mrp8 and Mrp14 are endogenous activators of toll-like receptor 4, promoting lethal, endotoxin-induced shock. *Nat Med* 13: 1042 – 1049

Wang Y, Su L, Morin MD, Jones BT, Whitby LR, Surakattula MM, Huang H, Shi H, Choi JH, Wang KW *et al* (2016) TLR4/MD-2 activation by a synthetic agonist with no similarity to LPS *Proc. Natl Acad Sci USA* 113: E884 – E893

Wentworth JM, Naselli G, Ngui K, Smyth GK, Liu R, O'Brien PE, Bruce C, Weir J, Cinel M, Meikle PJ *et al* (2016) GM3 ganglioside and phosphatidylethanolamine-containing lipids are adipose tissue markers of insulin resistance in obese women. *Int J Obes (Lond).* 40: 706 – 713

Yamashita T, Hashiramoto A, Haluzik M, Mizukami H, Beck S, Norton A, Kono M, Tsuji S, Daniotti JL, Werth N *et al* (2003) Enhanced insulin sensitivity in mice lacking ganglioside GM3. *Proc Natl Acad Sci USA* 100: 3445 – 3449

Yohe HC, Wallace PK, Berenson CS, Ye S, Reinhold BB, Reinhold VN (2001) The major gangliosides of human peripheral blood monocytes/macrophages: absence of ganglio series structures. *Glycobiology* 11: 831 – 841

Zanoni I, Ostuni R, Marek LR, Barresi S, Barbalat R, Barton GM, Granucci F, Kagan JC (2011) CD14 controls the LPS-induced endocytosis of Toll-like receptor 4. *Cell* 147: 868 – 880

Zhao H, Przybylska M, Wu IH, Zhang J, Siegel C, Komarnitsky S, Yew NS, Cheng SH (2007) Inhibiting glycosphingolipid synthesis improves glycemic control and insulin sensitivity in animal models of type 2 diabetes. *Diabetes* 56: 1210 – 1218

Expanded View Figures

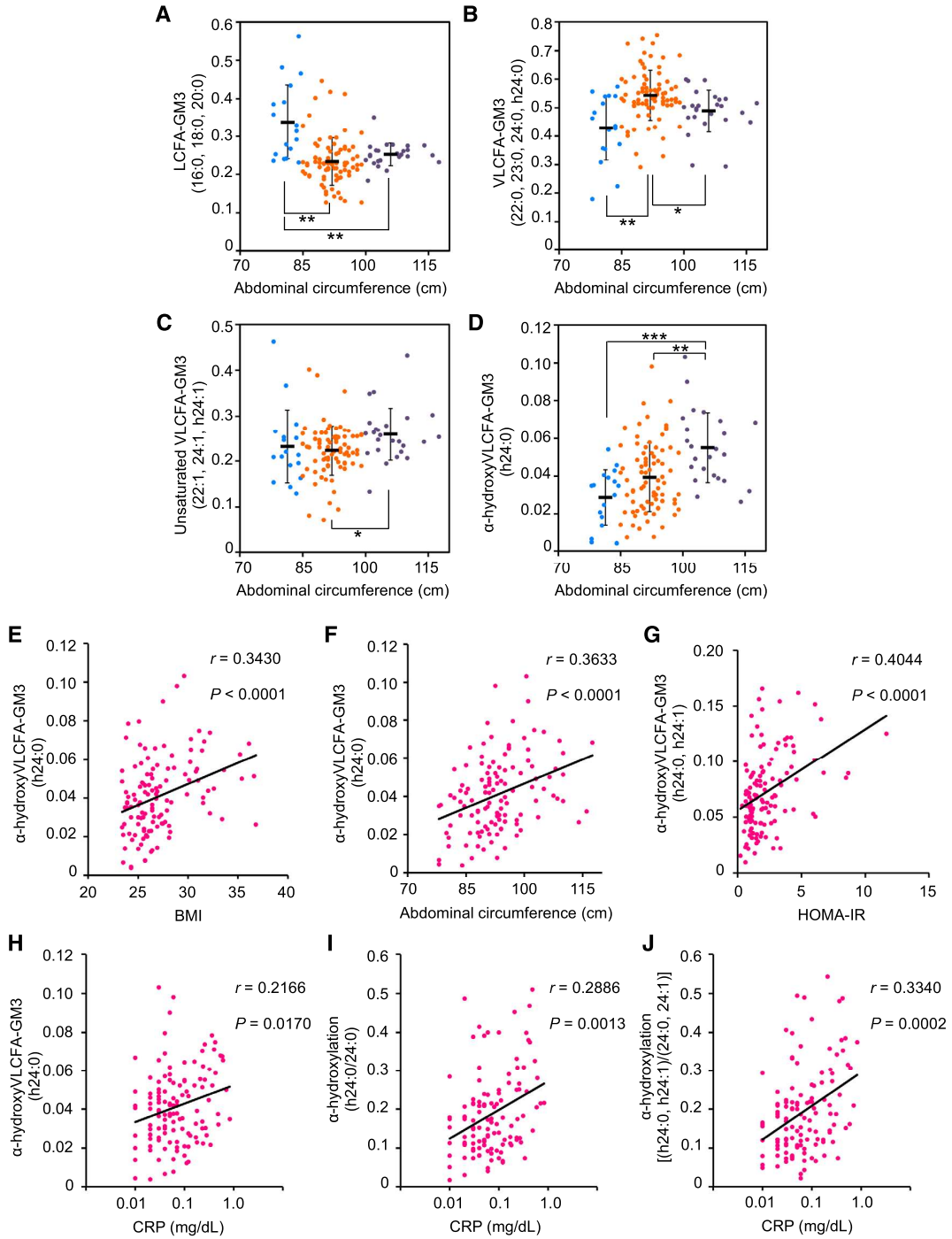

Figure EV1.

◀ **Figure EV1. Properties of various GM3 species as a function of clinical markers of metabolic disorders and chronic inflammation.**

A–D LCFA species (A), VLCFA species (B), unsaturated VLCFA species (C), and α-hydroxy VLCFA-GM3 (h24:0) (D). Colors indicate disease severity: light blue, no abnormal scores (n = 17); orange, early-phase obesity (n = 80); purple, severe obesity (n = 25). Data shown are mean ± SD, analyzed by two-tailed unpaired t-test with Bonferroni's correction. *P < 0.05, **P < 0.01, and ***P < 0.001 for comparisons between indicated groups.

E–J Spearman's correlations for GM3 h24:0 vs. BMI (E), GM3 h24:0 vs. abdominal circumference (F), total of α-hydroxy GM3 (h24:0 and h24:1) vs. HOMA-IR (G), GM3 h24:0 vs. serum CRP (H), α-hydroxylation rate (h24:0 to 24:0) vs. serum CRP (I), and α-hydroxylation rate (h24:0 and h24:1 to 24:0 and 24:1) vs. serum CRP (J).

Data information: Sample sizes: (A–G), n = 122; (H-J), n = 121.

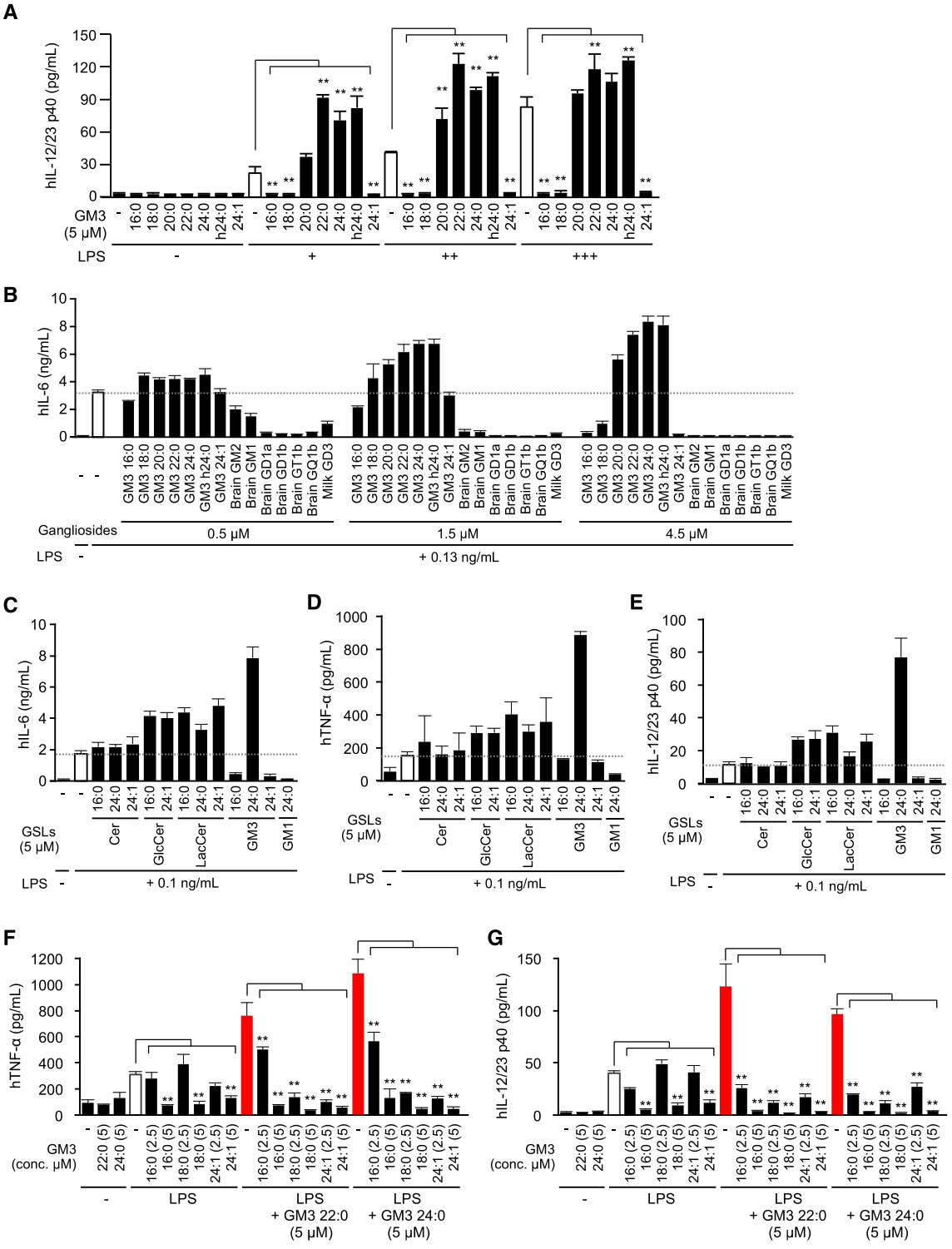
A
hIL-12/23 p40 (pg/mL)
GM3 (5 μM)
LPS
B
hIL-6 (ng/mL)
Gangliosides
0.5 μM
1.5 μM
4.5 μM
LPS
+ 0.13 ng/mL
C
hIL-6 (ng/mL)
D
hTNF-α (pg/mL)
E
hIL-12/23 p40 (pg/mL)
GSLs (5 μM)
Cer
GlcCer
LacCer
GM3
GM1
LPS
+ 0.1 ng/mL
F
hTNF-α (pg/mL)
GM3 (conc. μM)
LPS
LPS + GM3 22:0 (5 μM)
LPS + GM3 24:0 (5 μM)
G
hIL-12/23 p40 (pg/mL)

Figure EV2.

◀ **Figure EV2. Positive and negative regulation of innate immune response by GM3 gangliosides.**

A GM3-mediated enhancement and inhibition of IL-12/23 production from LPS-stimulated monocytes (measured by ELISA).

B Co-stimulation of monocytes by LPS plus GM3 species or complex ganglioside species. IL-6 production in culture supernatant was measured by ELISA.

C–E Co-stimulation of monocytes by LPS plus GM3 species or precursor GSL species. The production of IL-6 (C), TNF-α (D), and IL-12/23 p40 (E) in culture supernatant was measured by ELISA.

F, G Inhibitory effect of LCFA and unsaturated VLCFA-GM3 on VLCFA-GM3 species. The production of TNF-α (F) and IL-12/23 p40 (G) in culture supernatant was measured by ELISA.

Data information: Data shown are mean ± SD ($n = 3$) analyzed by Tukey's multiple comparison test. $^{**}P < 0.01$ for comparison with LPS stimulation without GM3 species (A), or co-stimulation by LPS and proinflammatory GM3 (22:0, 24:0) (F, G).

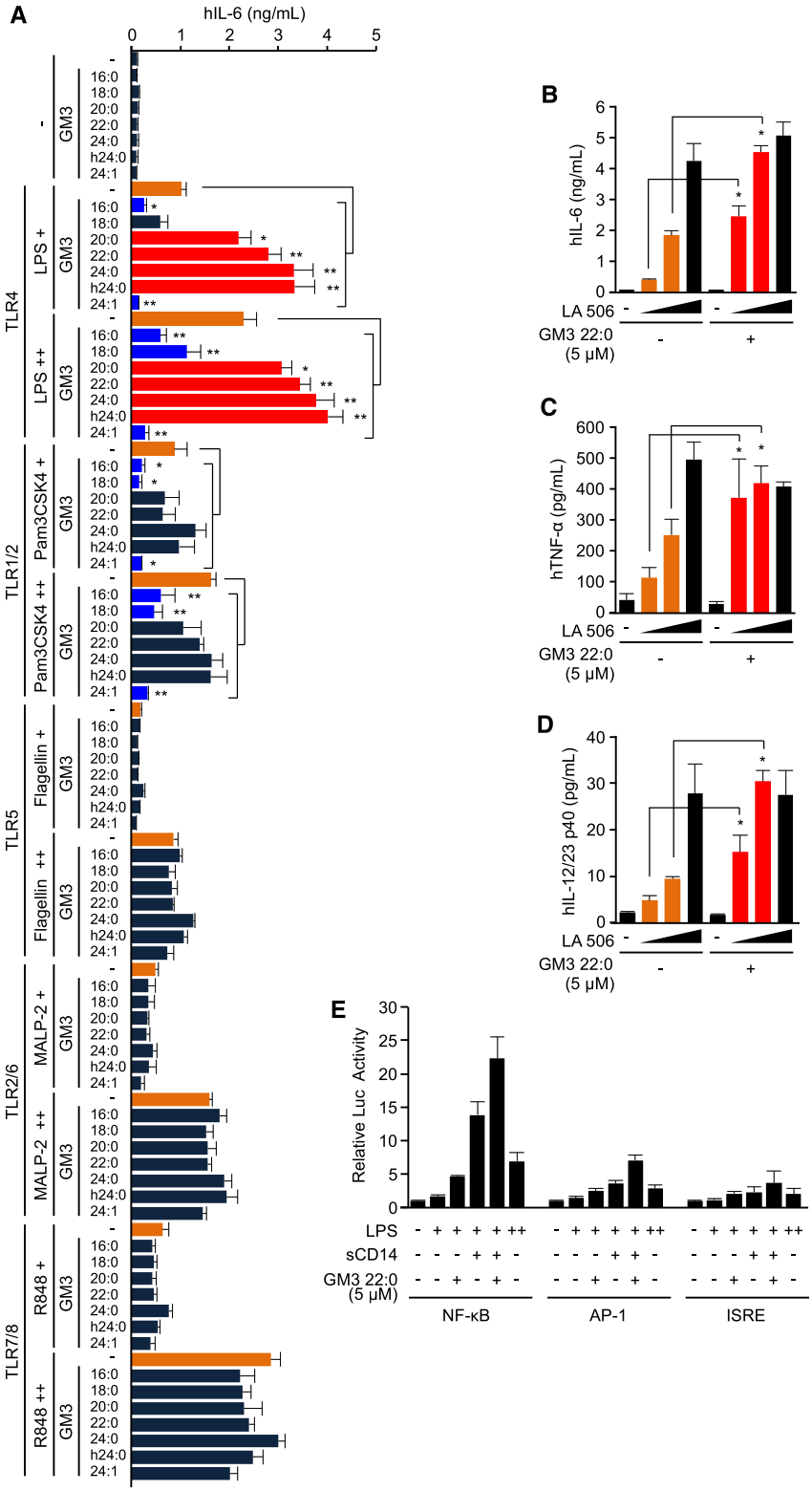

Figure EV3. VLCFA-GM3 species synergistically and selectively control human TLR4/MD-2 activation.

A Co-stimulation of human monocytes by GM3 species plus various TLR ligands: LPS (0.13, 0.25 ng/ml), TLR4/MD-2, Pam3CSK4 (0.25, 0.5 μg/ml), TLR1/2, Flagellin (10, 50 ng/ml), TLR5, R848 (0.25, 0.5 μg/ml), TLR7/8, MALP-2 (0.5, 1.0 ng/ml), and TLR2/6. IL-6 production in culture supernatant was quantified by ELISA.

B–D Production of IL-6 (B), TNF-α (C), and IL-12/23 p40 (D) in culture supernatant following co-stimulation of monocytes by GM3 species plus LA506 (synthetic TLR4 ligand) (3, 10, 30 ng/ml).

E Relative luciferase reporter activities of NF-κB, AP-1, and ISRE in response to LPS (+, 5 ng/ml; ++, 1 μg/ml), sCD14 (1 μg/ml), GM3 22:0 (5 μM), and their combinations. Relative luciferase activity of control condition was defined as 1 for every reporter gene.

Data information: Data shown are mean ± SD (n = 3, A–D; n = 4, E) analyzed by Tukey's multiple comparison test (A) or by two-tailed unpaired t-test (B–D). *P < 0.05 and **P < 0.01 for comparisons between indicated groups.

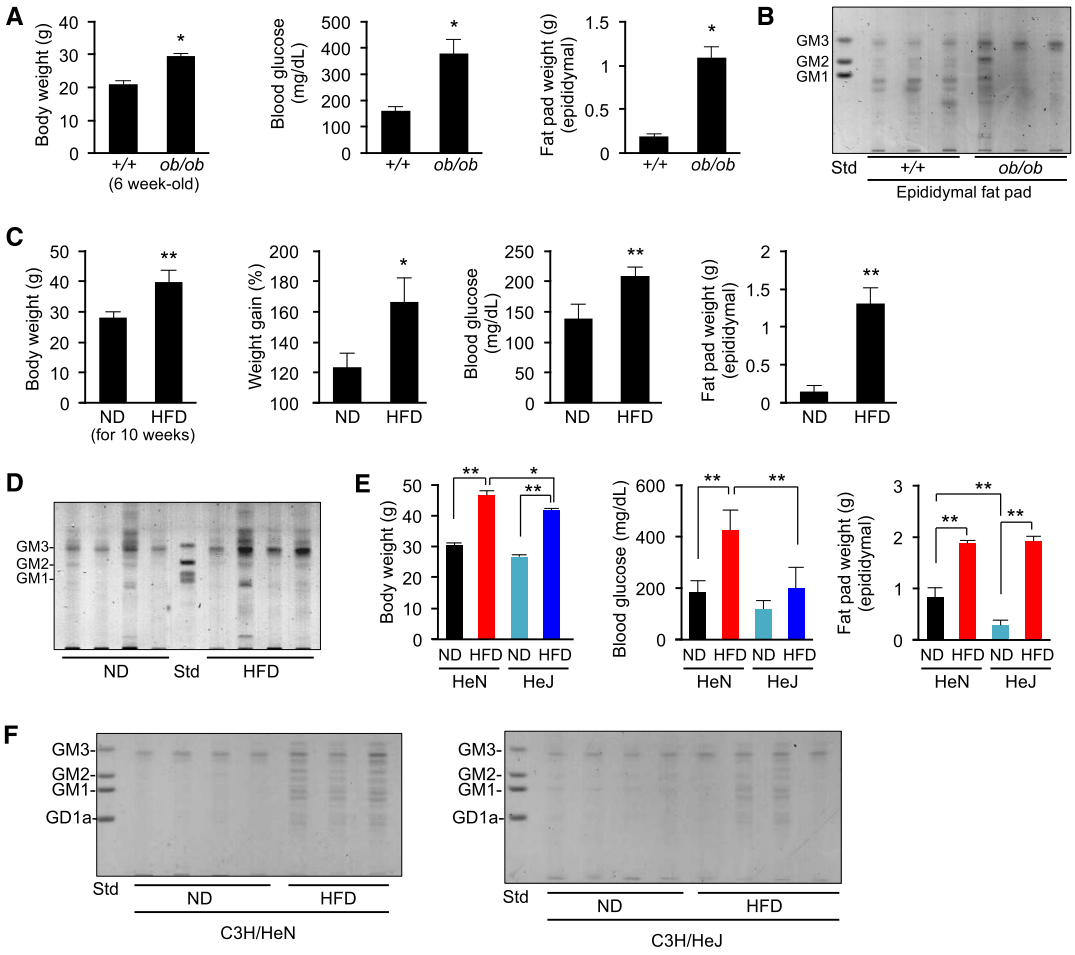

Figure EV4. GM3 ganglioside in adipose tissue showed increased abundance in early-phase obesity and short-term HFD.

A Body weight, blood glucose, and epididymal fat pad weight of 6-week-old control C57/BL6 mice and *ob/ob* mice (n = 3).

B Ganglioside species in epididymal fat pad were analyzed by TLC.

C Body weight, weight gain, blood glucose, and epididymal fat pad weight of normal diet (ND) and high-fat diet (HFD) C57/BL6 mice (n = 4).

D Ganglioside species in epididymal fat pad were analyzed by TLC.

E Body weight, blood glucose, and epididymal fat pad weight of C3H/HeN mice (ND, HFD) and C3H/HeJ mice (ND, HFD) (n = 4).

F Full-size images of Fig 7C. TLC analysis of acidic GSL fraction (equivalent to 0.1 mg protein) from epididymal fat pads of C3H/HeN and C3H/HeJ mice on ND or HFD for 8 weeks.

Data information: Data shown are mean ± SD analyzed by two-tailed unpaired t-test (A, C) or by Tukey's multiple comparison test (E). *P < 0.05 and **P < 0.01 for comparisons between indicated groups.

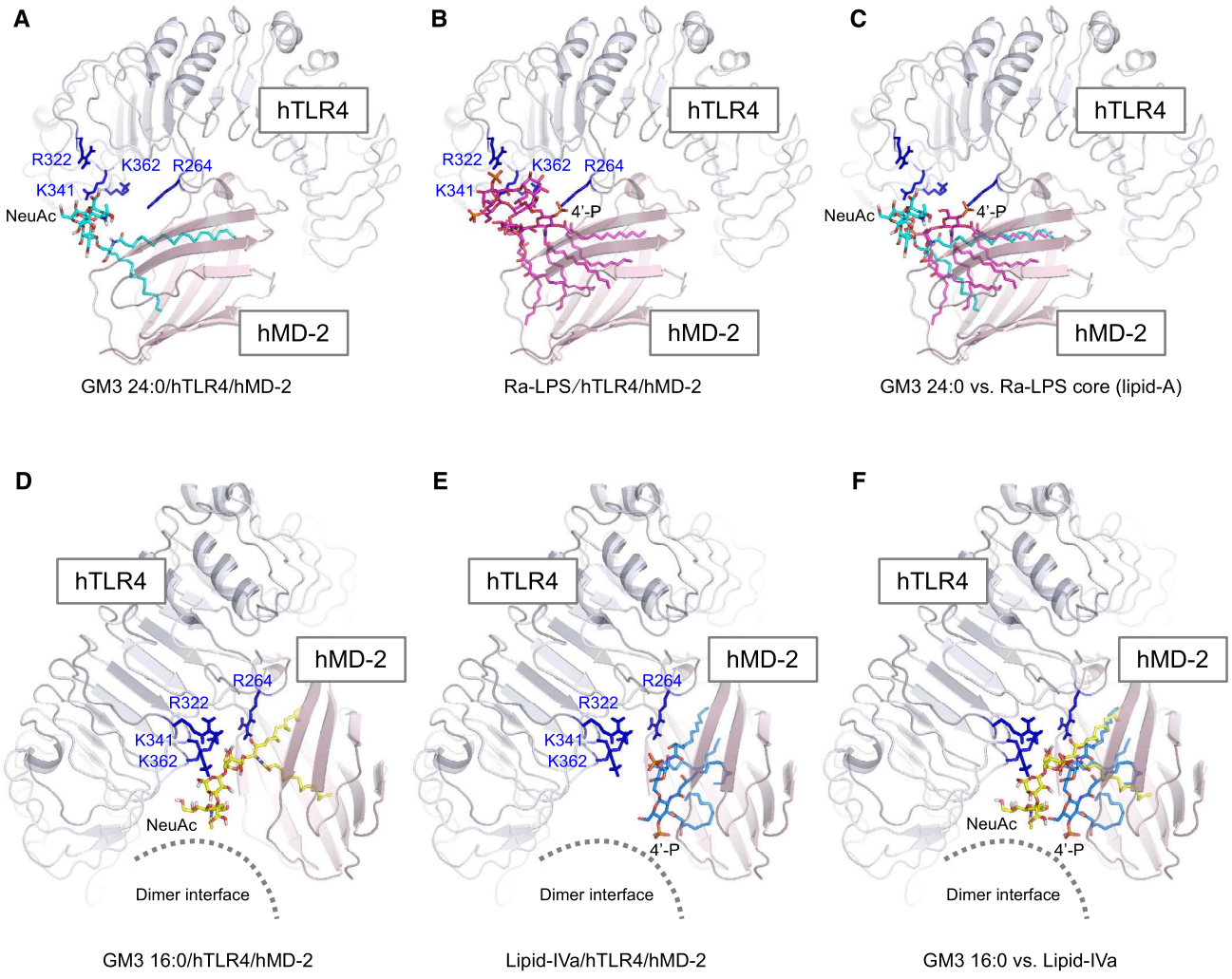

Figure EV5. Binding model of VLCFA/LCFA-GM3 species on hTLR4/hMD-2 and the comparison to LPS and lipid IVa.

A–C Docking model of GM3 24:0 (A), Ra-LPS (in 3FXI) (B), and superposition of GM3 24:0 vs. core structure of Ra-LPS (lipid A) (C).

D–F Docking model of GM3 16:0 (D), lipid IVa (in complex with hMD-2 in 2E59) (E), and superposition of GM3 16:0 vs. lipid IVa (F). Basic residues of hTLR4 are colored in blue.

TABLE OF CONTENT

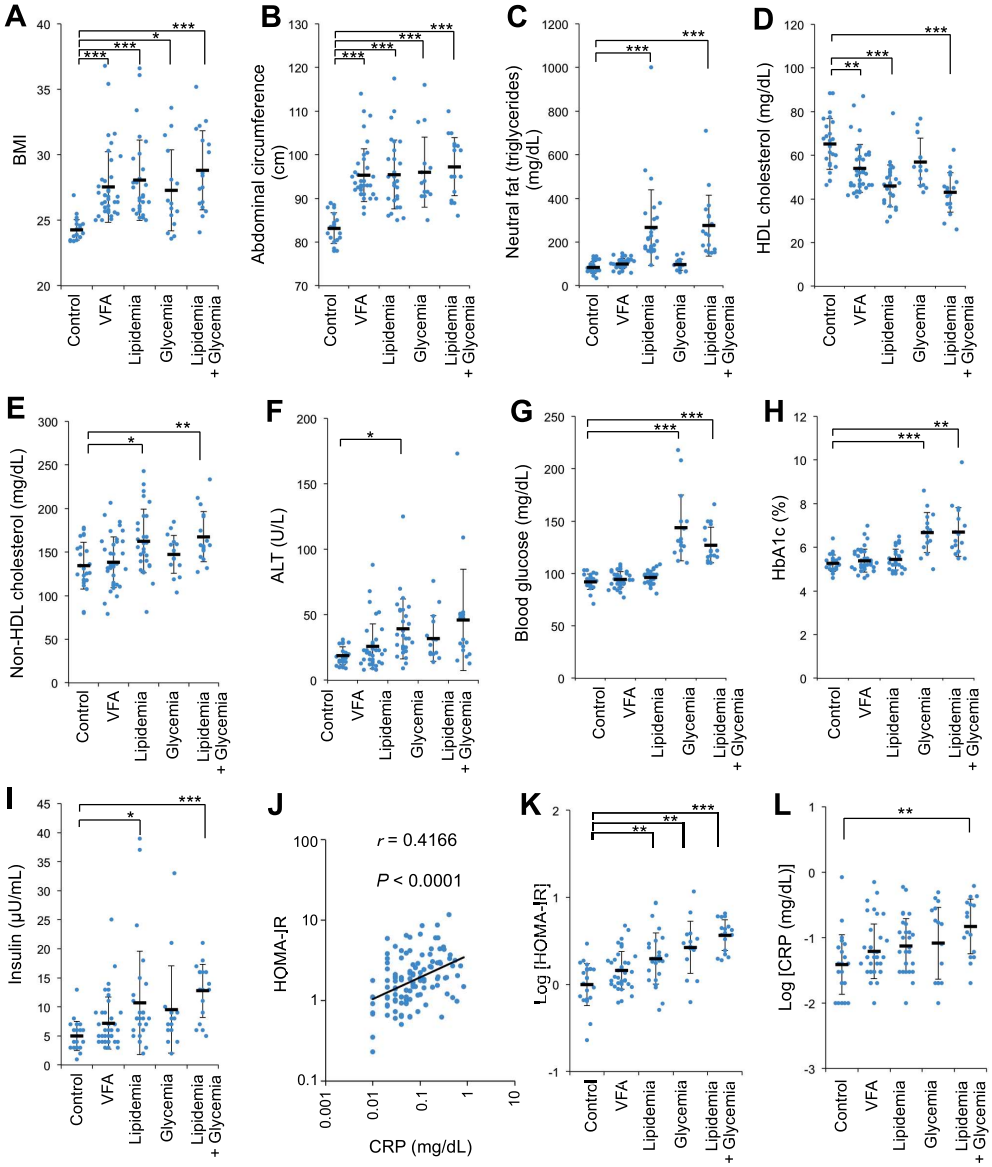

Appendix Figure 1 Values of clinical markers in presymptomatic subjects and patients with metabolic disorders. Values of clinical markers for metabolic disorders and for chronic inflammation in various pathological phases are shown. **(A)** BMI. **(B)** Abdominal circumference. **(C)** Serum natural fat (triglyceride). **(D)** Serum HDL cholesterol. **(E)** Serum non-HDL cholesterol. **(F)** Serum alanine transaminase (ALT). **(G)** Blood glucose. **(H)** HbA1c. **(I)** Serum insulin. **(J)** Spearman's correlation between HOMA-IR and serum CRP. **(K)** HOMA-IR (log scale). **(L)** Serum CRP (log scale). Data shown are individual values and mean ± SD (control, n=24; VFA, n=38; lipidemia, n=28; glycemia, n=15; lipidemia + glycemia, n=17), analyzed by two-tailed unpaired *t*-test with Bonferroni's correction. *p< 0.05, **p< 0.01, ***p< 0.001 for comparisons between indicated groups.

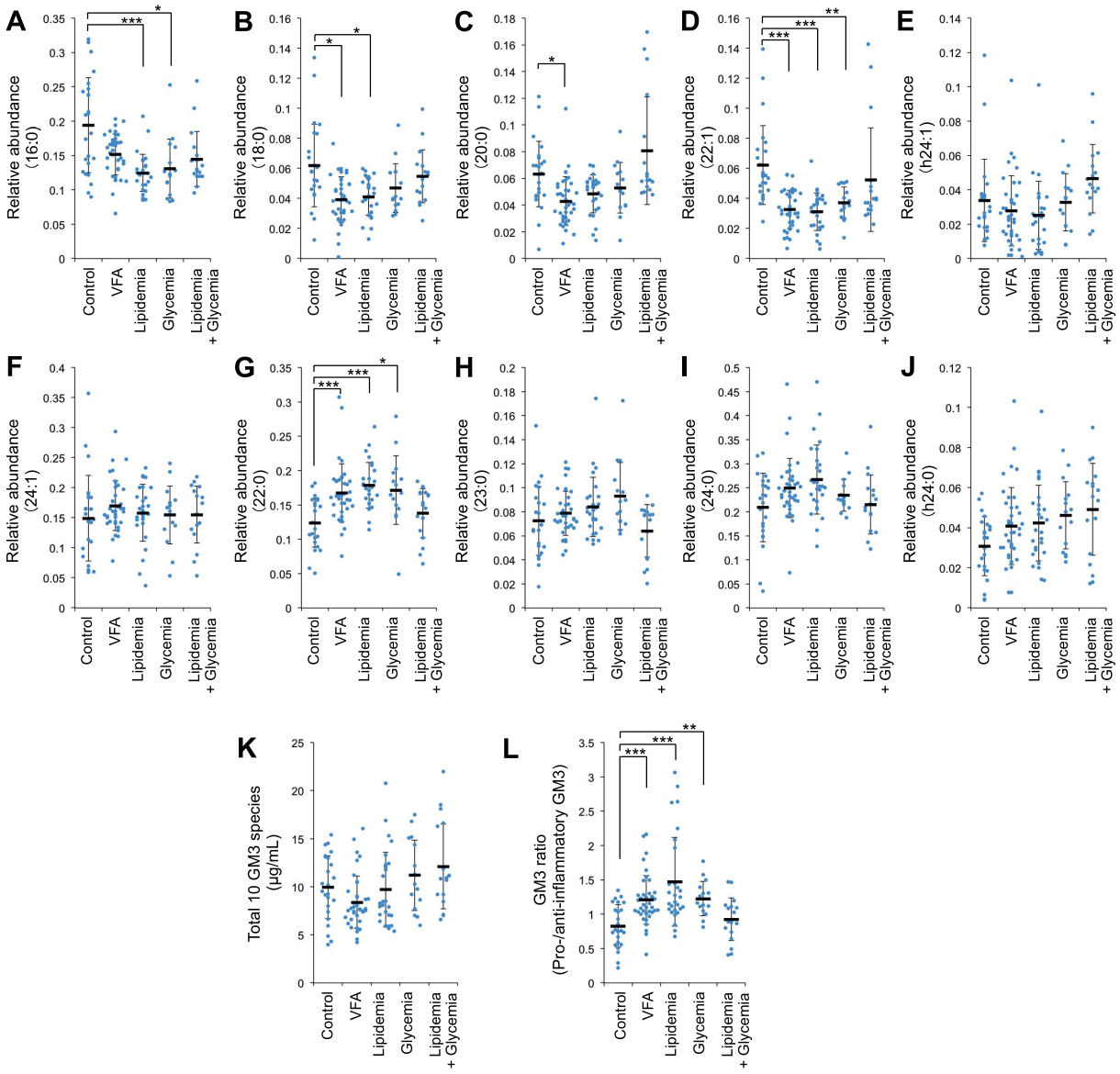

Appendix Figure 2 Relative abundances of major serum GM3 species in various pathological phases.
(A-J) Properties of various GM3 species, classified on the basis of acyl chain structures, as a function of pathological phase. Data shown are relative abundances of GM3 16:0 (A), 18:0 (B), 20:0 (C), 22:1 (D), h24:1 (E), 24:1 (F), 22:0 (G), 22:0 (H), 24:0 (I), and h24:0 (J) relative to total for ten major GM3 species (defined as 1.0) for each subject. **(K)** Total abundances of ten GM3 species (quantified as ratio to internal standard: ^{13}C-labeled GM3 [d18:1-]16:0) for each subject, at various pathological phases. **(L)** Ratios of proinflammatory GM3 (22:0, 24:0, 23:0, h24:0) to anti-inflammatory GM3 (16:0, 18:0, 20:0, 22:1, 24:1, h24:1) for each subject, at various pathological phases. Data shown are individual values and mean ± SD (control, n=24; VFA, n=38; lipidemia, n=28; glycemia, n=15; and lipidemia + glycemia, n=17), analyzed by two-tailed unpaired *t*-test with Bonferroni's correction. *p< 0.05, **p< 0.01, ***p< 0.001 for comparisons between indicated groups.

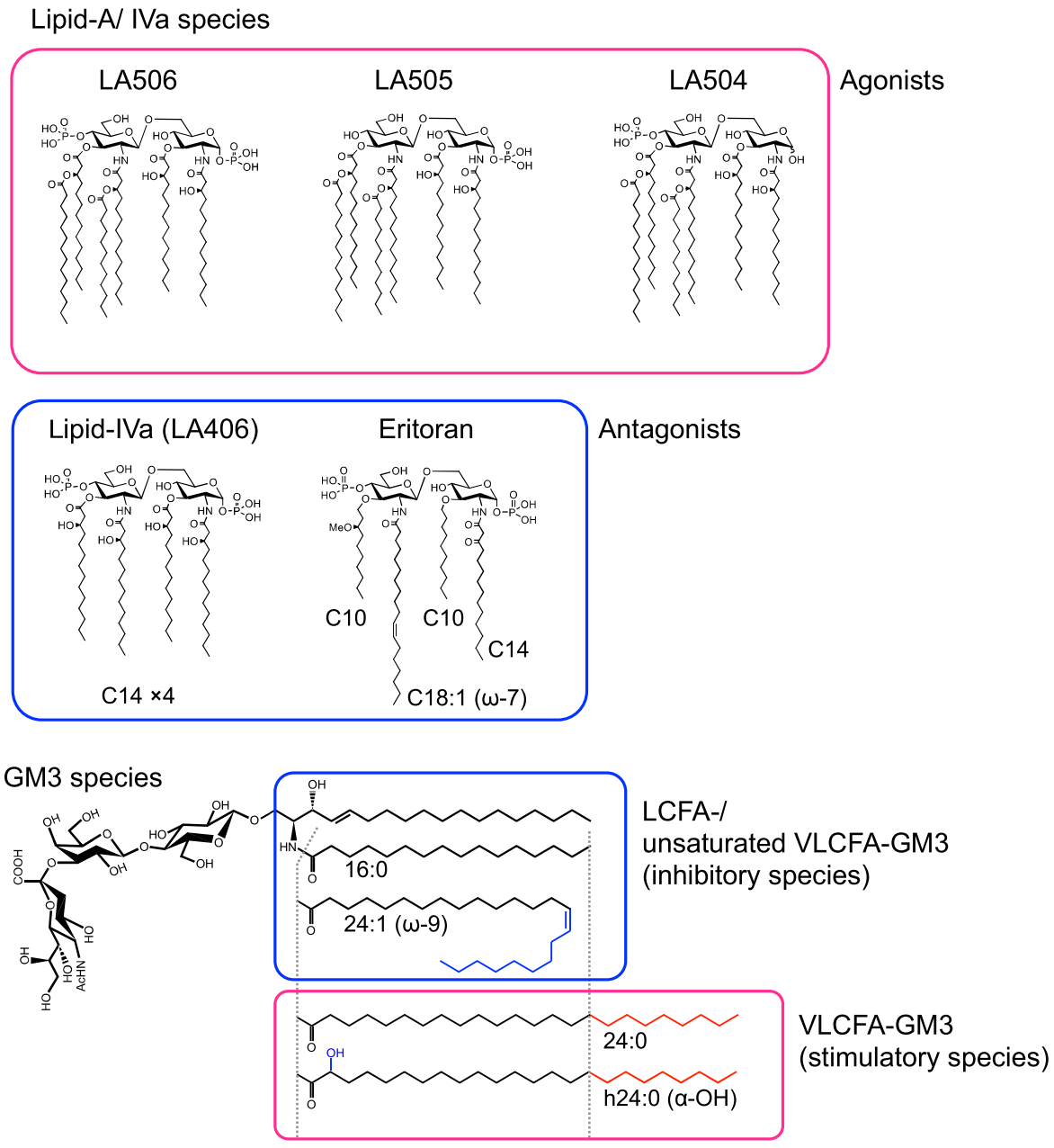

Appendix Figure 3 Molecular characteristics of lipid-A/IVa species, eritoran, and GM3 species. Molecular structures are shown for lipid-A 506 (LA506), lipid-A 505 (LA505), lipid-A 504 (LA504), lipid-IVa (LA406), and eritoran in comparison to GM3 species.

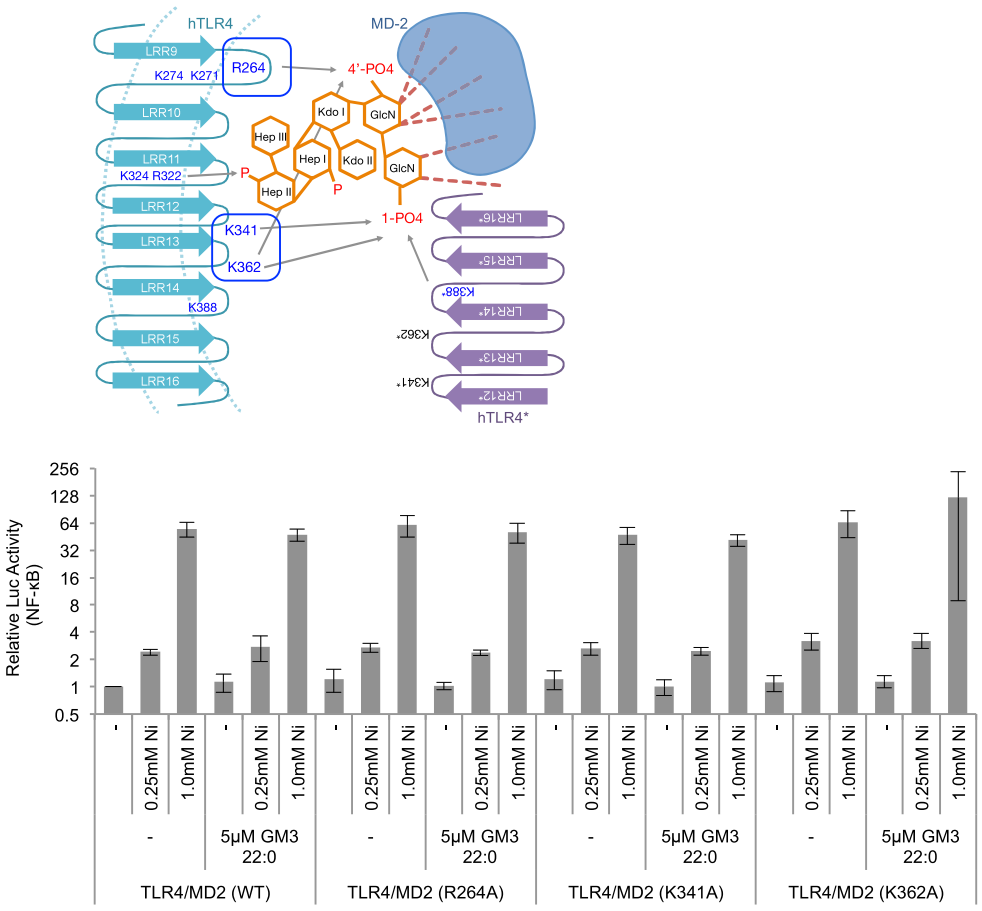

Appendix Figure 4 Co-stimulation of human TLR4/MD-2 variants by nickel ion plus proinflammatory GM3 22:0. Canonical LPS-binding residues on hTLR4/MD-2 complex and co-stimulation of HEK293T cells co-expressing hTLR4/hMD-2 by GM3 22:0 (5 μM) plus $NiSO_4$ (0.25, 1.0 mM). Data shown are mean ± SD (n=3).

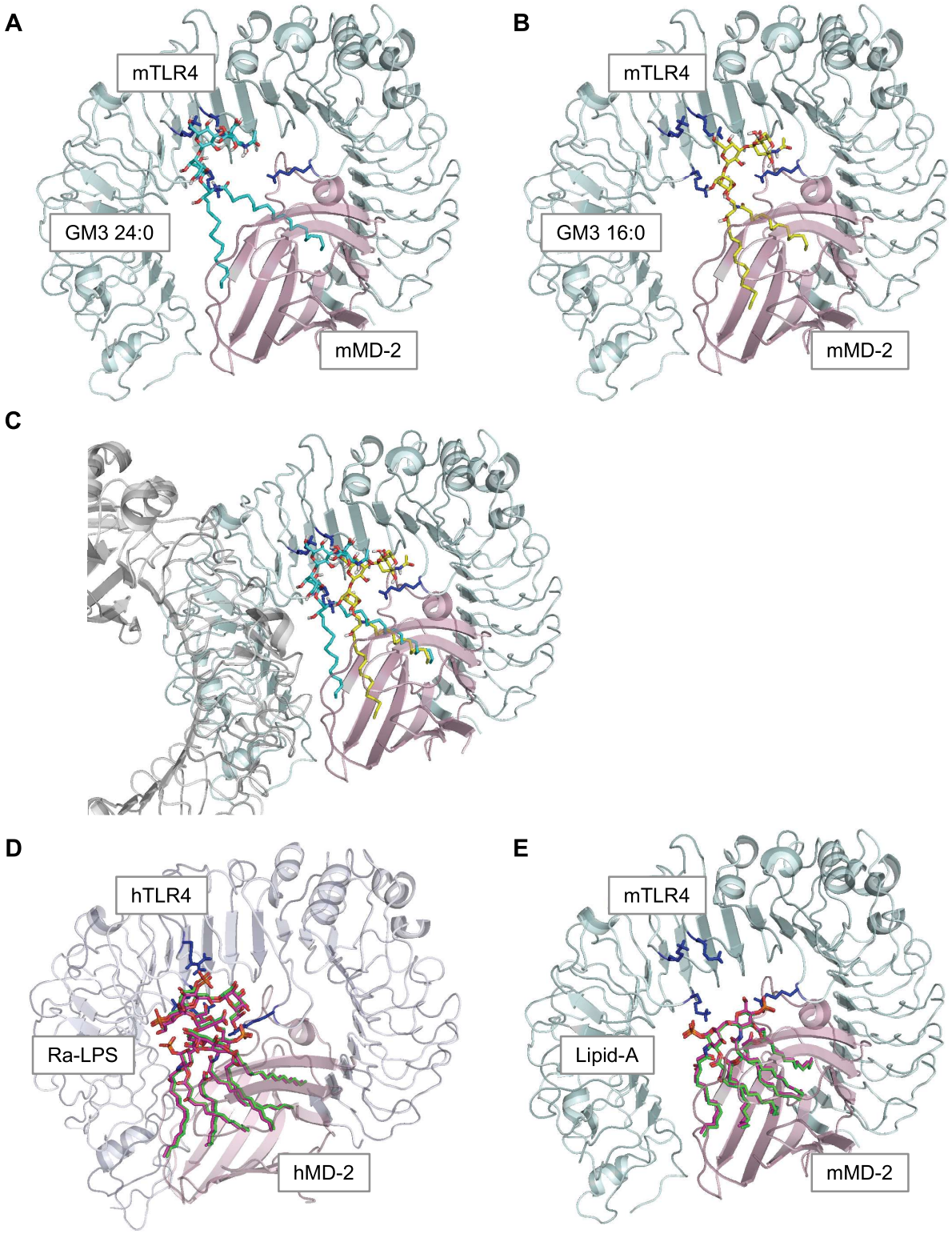

Appendix Figure 5 Binding model of VLCFA/LCFA-GM3 species on mTLR4/mMD-2 and results of benchmark calculation. (A, B) Docking model of GM3 24:0 **(A)** and 16:0 **(B)** binding to mouse TLR4/MD-2 complex (3VQ2). Basic residues of TLR4 are colored in blue. **(C)** Superposition of GM3 24:0 vs. GM3 16:0 on mouse TLR4/MD-2 complex. **(D, E)** Rigid-rigid docking calculation of Ra-LPS on hTLR4/hMD-2 complex **(D)** and lipid-A on mTLR4/mMD-2 **(E)** as a benchmark of this study. Superposition of docking results (green) vs. coordinates in reference structures (magenta) are shown.

グライコリピドミクス

井ノ口　仁一[1]，稲森　啓一郎[1]，上村　聡志[2]，狩野　裕考[1]，新田　昂大[1]，
二瓶　渉[3]，宍戸　史[4]，大野　勲[4]，鈴木　明身[1]

ガングリオシドを含むスフィンゴ糖脂質分子群の細胞特異的・選択的発現が，生体の恒常性維持に欠くべからざる役割を担っている作動原理が解明されつつある．たとえば，慢性炎症時における炎症性サイトカインの刺激によるGM3の細胞膜における増加は，カベオラマイクロドメインからインスリン受容体を解離させ，インスリン抵抗性を惹起する．我々は，これを“マイクロドメイン病”と提唱している．また最近では，GM3および関連ガングリオシドは，小腸上皮細胞におけるNPC1L1のコレステロール取り込みや視床下部におけるレプチン受容体の機能を制御している可能性を見いだしつつある．この細胞膜上におけるスフィンゴ糖脂質の“シス”の作動原理に加えて，GM3分子種のセラミド構造の違いによる多様性が，TLR4（Toll-like receptor 4）の新たな内因性リガンドとして自然免疫応答を正負両方向に制御していることを見いだした．すなわち，GM3分子種のバランスは，生体恒常性の維持に深く関わっていることが示唆される．

1.　はじめに

シアル酸を含有するスフィンゴ糖脂質をガングリオシドと総称する．ガングリオシドファミリーの生合成は，GM3合成酵素（GM3S）によってラクトシルセラミド（LacCer）にシアル酸が転移されGM3が生成することから始まる（**図1**）．そもそもGM3は，糖脂質研究の草分けである山川民夫博士がウマ赤血球からヘマトシドとして同定されたものである[1)]．GM3は，ヒトおよびマウスの脂肪組織や筋肉，ヒト肝臓および血清中など，末梢組織で主要に発現するガングリオシドである．1998年，井ノ口はこのGM3S遺伝子クローニングに参画して以来今日に至るまで，GM3および関連糖脂質の病態生理学的意義についての研究を続けている[2, 3)]．2015年の本誌には，「ガングリオシドファミリーの分子種選択的発現と生理活性脂質としての意義」として我々の30年間の研究の軌跡についてまとめている[4)]．そこでは，1）インスリン抵抗性発症におけるガングリオシドの関与とマイクロドメイン病の提唱，2）T細胞レパトア選択におけるガングリオシドの選択的発現と分子種特異的機構，および3）GM3合成酵素欠損と聴覚機能障害について述べた．

本稿では，1）GM3およびGM2合成酵素の細胞内輸送シグナル，2）摂食制御におけるガングリオシドの役割，3）コレステロール吸収におけるガングリオシドの役割，4）

[1] 東北医科薬科大学分子生体膜研究所機能病態分子学教室（〒981–8558　宮城県仙台市青葉区小松島4丁目4–1）
[2] 東北医科薬科大学医学部医化学教室（〒983–8536　宮城県仙台市宮城野区福室1–15–1）
[3] 大阪大学大学院理学研究科化学専攻天然物有機化学研究室（〒560–0043　大阪府豊中市待兼山町1–1）
[4] 東北医科薬科大学医学部医学教育推進センター（〒983–8536　宮城県仙台市宮城野区福室1丁目15–1）

Glycolipidomics

Jin-ichi Inokuchi[1], Kei-ichiro Inamori[1], Satoshi Uemura[2], Hirotaka Kanoh[1], Takahiro Nitta[1], Wataru Nihei[3], Fumi Shishido[4], Isao Ohno[4] and Akemi Suzuki[1] ([1]Tohoku Medical and Pharmaceutical University, Division of Glycopathology Institute of Molecular Biomembrane and Glycobiology, 4–4–1 Komatsushima, Aoba-ku, Sendai Miyagi, 981–8558, Japan, [2]Tohoku Medical and Pharmaceutical University, Faculty of Medicine, Division of Medicinal Biochemistry, 1–15–1 Fukumuro, Miyagino-ku, Sendai, Miyagi 983–8536, Japan, [3]Osaka University, Graduate School of Science, Department of Chemistry, Division of Natural Product Chemistry, Toyonaka, Osaka 560–0043, Japan, [4]Tohoku Medical and Pharmaceutical University, Faculty of Medicine, Center for Medical Education, 1–15–1 Fukumuro, Miyagino-ku, Sendai, Miyagi 983–8536, Japan)

本論文の図版はモノクロ（冊子版）およびカラー（電子版）で掲載．

DOI: 10.14952/SEIKAGAKU.2020.920323

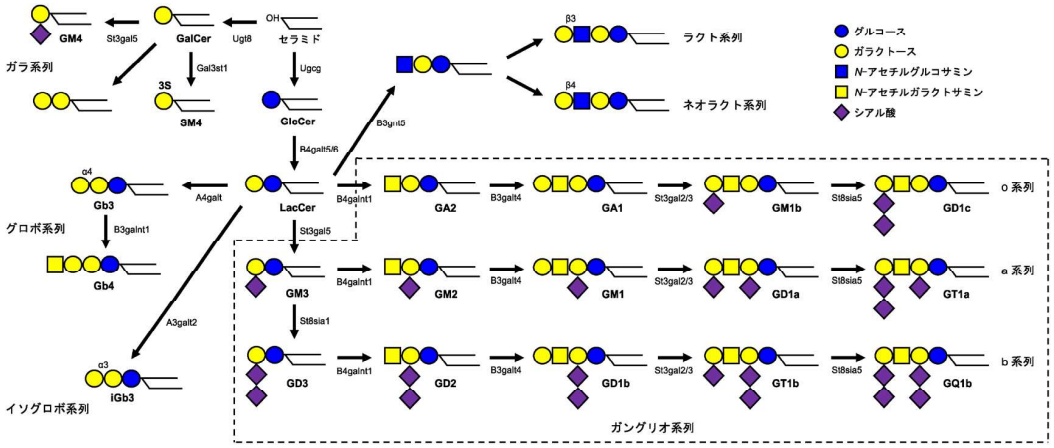

図1　スフィンゴ糖脂質の生合成経路
Box内がガングリオシドファミリー．［Inokuchi, J. & Go, Shinji.（2014）Biosynthetic pathways of glycosphingolipids, in Handbook of Glycosyltransferases and Related Genes, 2nd Ed.（Taniguchi, N. et al., eds.）, pp. 1673–1679, Springer, Tokyo より］

自然免疫におけるGM3およびグロボ系糖脂質分子種の役割，について最近の研究を紹介する．

［山川先生は，2018年10月7日に96歳で永眠されました．ここに謹んで哀悼の意を表するとともに，GM3の生みの親である先生へのプログレスレポートとして本稿を捧げます．］

2.　スフィンゴ糖脂質のLC-MS/MS

スフィンゴ糖脂質は脂質部分としてのスフィンゴイド塩基と脂肪酸が酸アミド結合したセラミドと糖鎖とから構成されるが，その構造解析は糖鎖構造の均一性に注目して行われてきた．精製されたスフィンゴ糖脂質として報告された構造は，糖鎖は単一であるものの，セラミド部分は混合物で，スフィンゴイド塩基と脂肪酸の組成が記載される，というものであった[5, 6]．糖鎖の構造多様性，組織特異的発現，がんや先天性代謝異常症をはじめとする疾患での変化が注目されてきた一方で，脂質部分のセラミド構造には，糖鎖に匹敵する関心が払われてこなかった．脳，神経組織に存在し，シアル酸を含むガングリオシドと総称されるスフィンゴ糖脂質は，他の組織に例をみないほどの含量の多さと構造の特徴から，神経機能に関する多くの研究が現在なお継続されている．一方で，セラミド構造に関する状況はマイクロドメインあるいはラフトの概念が提出されたことで一転し，注目を集めることになった[7]．

スフィンゴ糖脂質の糖鎖構造に関して，これまでに報告された糖鎖が何種類あるか，厳密に数えないと確かな数字をあげることはできないが，数百種になると考えてよいと思われる[5]．一方で単一の糖鎖構造に対して結合しているセラミド構造は何種類存在するのか．この問いはスフィンゴイド塩基の数，脂肪酸の数，その組合わせによるセラミド構造が何種類存在するか，に答えることを意味する．スフィンゴイド塩基は，炭素鎖18，二重結合1個のd18:1 sphingenineを基本に，飽和型のd18:0 sphinganine，水酸基がC4位に1個追加されたt18:0 4-hydroxysphinganineの3種類が主要成分として存在する．炭素鎖16, 20のものも存在し，これらをまとめると9種類となる．脂肪酸は，16:0から24:0の飽和偶数鎖5種，どういう分子機構で生じるか不明であるが23:0の奇数鎖，24:1不飽和偶数鎖，以上のすべての脂肪酸鎖に対してα位（C2位）が水酸化された脂肪酸，総計14種が通常検出される脂質部分の構成要素である．これらからセラミド構造の種類は9×14＝126となる．スフィンゴ糖脂質の可能な分子数は126×数百＝12,600～37,800となる．

セラミド構造に関心が向かわなかったのは，スフィンゴ糖脂質分子そのものを検出する適切な分析法がなかったことによる．この状況は，matrix-assisted laser desorption ionization（MALDI）とelectrospray ionization（ESI）の開発によって，質量分析法（mass spectrometry：MS）に飛躍がもたらされ，一転する．タンパク質やペプチドのイオン化が可能になり，分子イオンを捉え，原子で衝突誘起解離（collision-induced dissociation：CID）を起こし，開裂イオンをMS/MS解析することで，分子の構成要素を解析することが可能になった．アミノ酸配列の解析がプロテオミクス（proteomics）の発展をもたらしたと同様に，この手法でグライコリピドミクス（glycolipidomics）が可能になった．MALDI-MSは感度，操作性に優れているが，イオン化で一部の分子に開裂が起きる．特にシアル酸はイオン化で脱離することが多い．一方でESIはよりソフトなイオン化が可能で，ガングリオシドがシアル酸の開裂を伴わないでイオン化される．液体クロマトグラフィー（LC）と直結できることも利点の一つである．

スフィンゴ糖脂質のLC-MSによる構造解析は，MS^2による糖鎖配列解析とセラミドイオンの検出からなる糖鎖構造の確認とMS^3によるセラミド構造の確認からなる．MS^3によるセラミド構造確認に有効な情報を得るには，前駆体

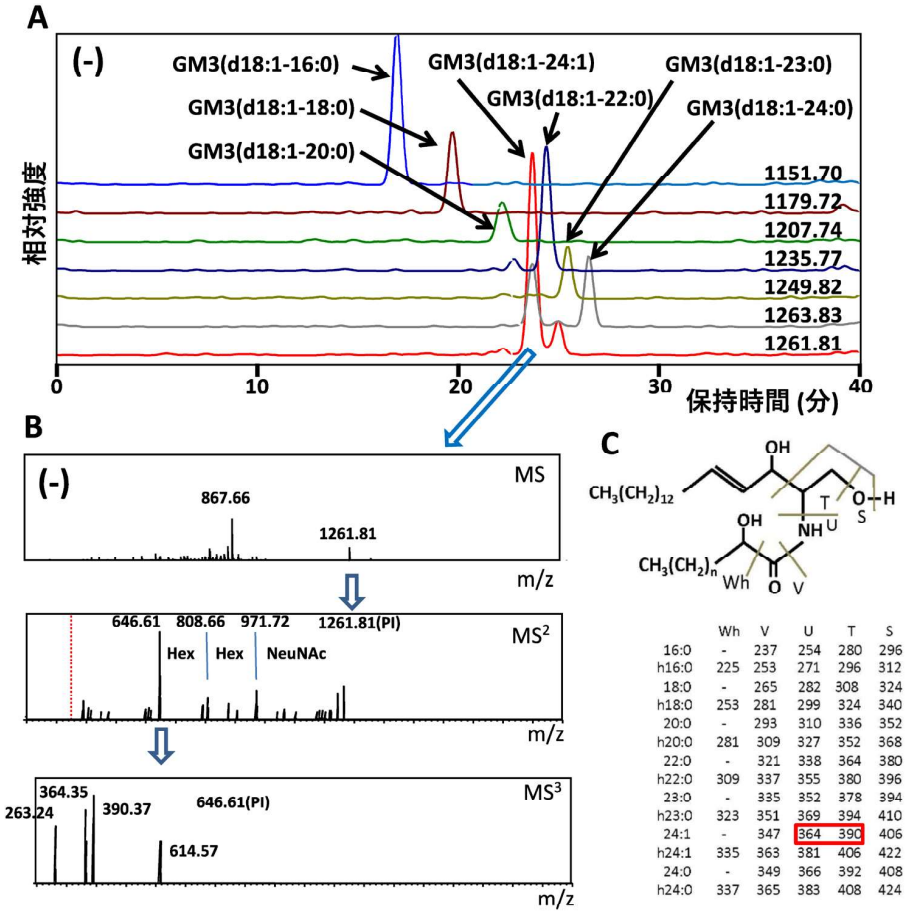

	Wh	V	U	T	S
16:0	-	237	254	280	296
h16:0	225	253	271	296	312
18:0	-	265	282	308	324
h18:0	253	281	299	324	340
20:0	-	293	310	336	352
h20:0	281	309	327	352	368
22:0	-	321	338	364	380
h22:0	309	337	355	380	396
23:0	-	335	352	378	394
h23:0	323	351	369	394	410
24:1	-	347	364	390	406
h24:1	335	363	381	406	422
24:0	-	349	366	392	408
h24:0	337	365	383	408	424

図2　ヒト血清GM3のLC-MSによる構造解析
血清100 µLから調製されたスフィンゴ糖脂質画分の約1/10を，C30カラムを用いた逆相モードによるLCで分離し，負イオンモードで質量分析を行った．(A)は主要GM3分子のマスクロマトグラム．(B)は*m/z* 1261.81イオンのマススペクトルで，MSで分子イオンが検出され（上段），MS^2で1261.81イオンからNeu5Ac（290），Hex（162），Hexが離脱したイオン（971.72, 808.66, 646.61）が検出され（中段），MS^3でセラミドイオン646.61を前駆体イオンとし，由来する263.24（d18:1 sphingenine由来），364.35と390.37［(C)で示す脂肪酸を含むフラグメントイオン］，が検出され（下段），セラミド構造はd18:1–24:1であることが確認できる．(C)はセラミド構造決定に有用なフラグメントイオンのリストと開裂パターン．PI：前駆体イオン．

イオンとするセラミドイオンの十分な強度が必要になる．この解析で構造が確認できれば，実験群と対照群での変化を追跡することが必要になる．量的な変化を微量で検出するためにMS^2の情報に基づく多重反応モニタリング（multiple reaction monitoring：MRM）が利用される．MS^1で特定のイオンを選択し，CIDで開裂イオンを生成し，MS^2で生成イオンを検出する手法である．前駆体イオンと生成イオンを特定して，検出する．構造解析とMRMによる量的変化の解析は異なる質量分析計を使用することになり，後者のMRM解析は前者の構造解析よりも数十倍感度が高い．

実際のルーチン解析の結果をヒト血清のGM3について示す．100 µLの血清から総脂質を得，弱アルカリ処理でエステル結合を持つ主要成分のリン脂質を分解し，中和，脱塩して，LC-MS分析用のサンプルとする．このサンプルにはセラミド，中性スフィンゴ糖脂質，GM3，微量成分としてのその他のガングリオシド，多量のスフィンゴミエリンが存在している．LCはC30カラム（1×50 mm），流量（50 µL/min），溶出溶媒（0.1%の酢酸，アンモニア水を含む，水／メタノール／イソプロパノールの混合溶媒で，疎水性を上昇させる）の条件で行い，溶出液を2種類の質量分析計（島津製作所LC-IT-TOFとLCMS-8060）を用いて負イオンモードで分析した[8]．**図2**にGM3の構造をLC-IT-TOF（LC-ion trap-time of flight）で確認した結果を示す．図2Aのマスクロマトグラムは主要な分子のみを示している．*m/z* 1261.81のピークは図2Bに示すようにMS^2で糖鎖の配列とセラミドの分子量決定，セラミドイオンを前駆体とするMS^3でセラミド構造の確認が行われる．図2Cにセラミド構造決定に有用なフラグメントイオンをリストした．これらのGM3分子の構造確認に基づいて，GM3分子の変動を解析することが求められる．この目的を達成するために，MRMによる解析が行われる．MRM解析の利点は検出のダイナミックレンジが広いこと，特定のイオンのみを検出することから高い検出感度が得られることで

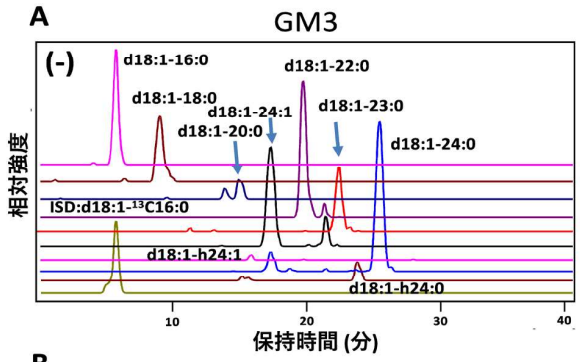

B

検出分子	前駆体イオン		検出イオン	コリジョンエネルギー
GM3(d18:1-16:0)	1151.7	>	290.1	CE: 50.0
GM3(d18:1-18:0)	1179.7	>	290.1	CE: 50.0
GM3(d18:1-20:0)	1207.7	>	290.1	CE: 50.0
GM3(d18:1-22:0)	1235.8	>	290.1	CE: 50.0
GM3(d18:1-23:0)	1249.8	>	290.1	CE: 50.0
GM3(d18:1-24:1)	1261.8	>	290.1	CE: 50.0
GM3(d18:1-h24:1)	1277.8	>	290.1	CE: 50.0
GM3(d18:1-24:0)	1263.8	>	290.1	CE: 50.0
GM3(d18:1-h24:0)	1279.8	>	290.1	CE: 50.0
ISD : GM3(d181-13C16:0)	1167.8	>	290.1	CE: 50.0

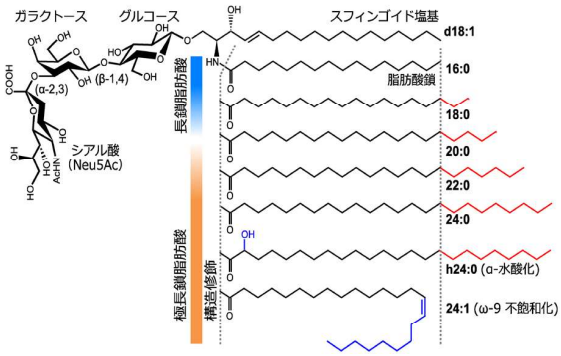

図3　ヒト血清GM3のMRMによる解析
サンプルの調製，LCによる分離の方法は図2と同一．(B)に示す前駆体イオンと脱離したNeu5Ac（*m/z* 290.1）を検出し，(A)のクロマトグラムを得ている．GM3分子の量はISDによって決定できる．ISDは同位体標識GM3（d18:1–^{13}C16:0）で，GM3（d18:1–16:0）は確定できるが，その他のGM3分子については正確な定量はできない．ただし，同一条件でMRM分析することにより，対照，実験群の変化を検出することは可能である．すべてのGM3分子に対応する同位体標識標品が必要になるが，現時点では実現できていない．

ある．**図3**に解析例を示す．この解析ではGM3の分子イオンを前駆体イオンとして特定し，それに由来する*N*-アセチルノイラミン酸（Neu5Ac）フラグメントイオン（*m/z* 290.1）を検出イオンとして検出する．ピーク面積をISD（internal standard）に対して求め，GM3分子のそれぞれの含量を求める．ISDとして^{13}C標識パルミチン酸を持つGM3（d18:1–^{13}C16:0）を使用した．

以上がグライコリピドミクスの一例であるが，上記の調製によるサンプル中には，他のスフィンゴ糖脂質も含まれ，それらの解析も同様に可能である．ガングリオシドは負イオンモードでの解析が適切である．中性糖脂質は陽イオンモードで，スフィンゴシン由来のフラグメントイオンを検出する方が，感度がよい．何を解析対象にするかで，最適な方法をとる必要がある．多くのスフィンゴ糖脂質について，データーベースの整備が望まれる．これまでに著者らが報告した中性スフィンゴ糖脂質[9–11]，ガングリオシド[12–16]の解析文献をあげる．

3.　GM3およびGM2合成酵素の細胞内輸送シグナル

ガングリオシド生合成はゴルジ体の内腔側で行われる．ガングリオシドの生合成量を一定に保つために，基質となる糖供与体（CMP-シアル酸やUDP-ガラクトースなど）と糖受容体（糖脂質）のゴルジ体への輸送は重要だが，その反応を触媒する糖転移酵素の細胞内輸送・維持メカニズムも同様に重要である．多くの糖転移酵素はII型の膜タンパク質であり，小胞体で翻訳され，COPII小胞でゴルジ体へ運ばれる．ゴルジ体では，シス，メディアル，トランスとダイナミックに層成熟を繰り返す層板の中で各糖転移酵素がいるべき場所にとどまる仕組みがあると考えられる[17, 18]．

GM3合成酵素にはN末端側の長さが異なる3種類のアイソフォーム（M1型，M2型，M3型）が発現している（**図4**）[19]．GM3合成酵素の小胞体からゴルジ体への輸送は，膜貫通ドメイン直上のR/K-based motifによって担われており，ここに変異が導入されると小胞体からの搬出効率が低下する[20]．最初に糖転移酵素で同定された小胞体搬出シグナルは［R/K］(X)［R/K］配列であり，COPIIコートタンパク質であるSar1と相互作用することが示された[21]．しかし，少なくとも安定に発現させた全長GM3合成酵素においては，［R/K］(X)［R/K］配列だけでは小胞体搬出に十分ではなく，その近傍のリシン残基も必要であった．この結果から，我々は小胞体搬出シグナルとして，もう少し広範囲に定義したR/K-based motifの使用を提案している[20]．

GM3合成酵素の中でN末端が長いM1型には，ゴルジ体から小胞体への逆行輸送を担うR-based motifがある．R-based motifはCOPIコートタンパク質である*β*-COPと*δ*-COPが作る酸性ポケットに入り込む[22]．おそらくこのCOPIコートタンパク質複合体の構造的制限により，R-based motifは膜から離れた位置でしか機能できず，膜に近接するR/K-based motifとは明確に区別される．M1型はゴルジ体に運ばれた後，R-based motifによって小胞体へ戻されるため，その大部分は小胞体に安定して局在する．その一方で，M2型とM3型はゴルジ体へ運ばれた後，M2型は速やかにリソソームで分解され，M3型は安定してゴルジ体に繋留するといったような異なる運命をたどる．M3型のゴルジ体繋留には小胞体搬出シグナルとしても機能するR/K-based motifが関与しており，このシグナルによってゴルジ体の層板間を循環している．M2型が安定してゴルジ

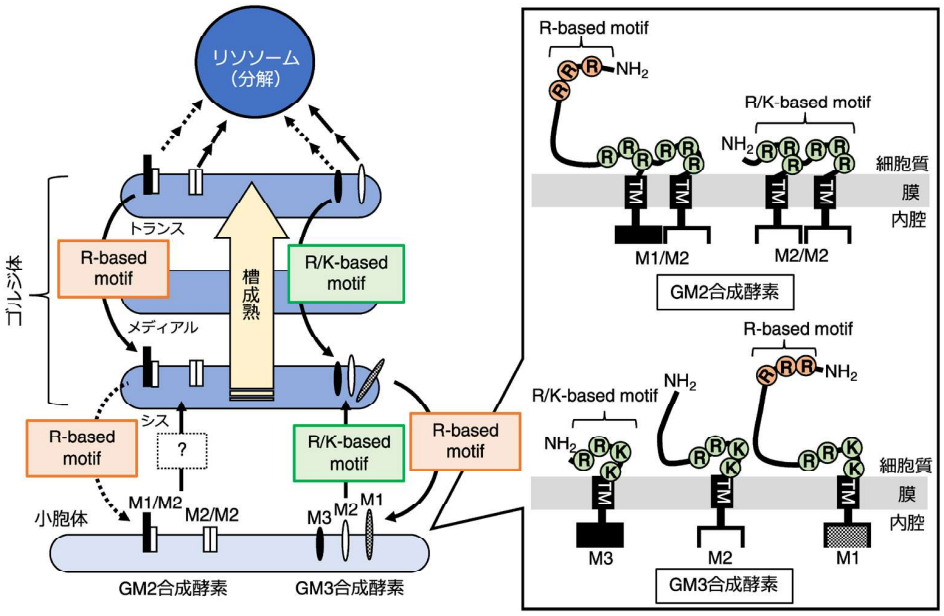

図4　GM3合成酵素およびGM2合成酵素の細胞内動態
GM3合成酵素はN末端の長さの異なるM1型，M2型，M3型のアイソフォームが存在する．GM2合成酵素もまたN末端の長さの異なるM1型とM2型アイソフォームが存在し，二量体を形成する（M1/M2型二量体，M2/M2型二量体）．それぞれが持つ細胞内輸送シグナルに依存して，細胞内動態が異なる．TM：膜貫通領域．

体に局在できないのは，M3型よりも長いN末端側配列が，このゴルジ体繋留に関わるR/K-based motifの機能を抑制するためのようである．この抑制はM1型でもみられ，R-based motif（逆行輸送シグナル）に変異を入れたM1型もまたリソソームで速やかに分解される[19,20]．

GM2合成酵素にはN末端の長さが異なる2種類のアイソフォーム（M1型とM2型）が存在する（図4）．GM2合成酵素がGM3合成酵素と大きく異なるのは，内腔側でシステイン残基を介して二量体を形成することである[23]．M1型をコードするmRNAバリアントの発現が低いため，M1型の発現量はM2型と比べて低く抑えられる．M1型とM2型はそれぞれホモ二量体およびヘテロ二量体を形成することができるが，その発現量比を考慮すると，大部分がM2型／M2型二量体で，一部がM1型／M2型ヘテロ二量体であると考えられる．GM2合成酵素にも膜貫通ドメインの直上にR/K-based motif（小胞体搬出／ゴルジ体繋留シグナル）を有しているが，M2型／M2型二量体やM1型／M2型ヘテロ二量体にとって，この配列は小胞体搬出に必須ではない．GM2合成酵素は二量体形成ができなくなる変異を導入すると小胞体から搬出されないので，GM2合成酵素の立体構造を認識してCOPII小胞に詰め込む積荷受容体がこの輸送に関与していることが示唆される（図4のbox）．

GM2合成酵素のM1型には逆行輸送シグナルであるR-based motifが存在するが，なぜかこのシグナルはGM3合成酵素ほど小胞体へ逆行輸送させる力を持たない．しかし，M1型ホモ二量体はM2型ホモ二量体よりも安定して細胞内にとどまる．M1型／M2型ヘテロ二量体ーがM1型ホモ二量体と同程度の安定性を有しているため，M1型のR-based motifがゴルジ体の層板間の循環に寄与している可能性が考えられる[24]．

このように，GM3合成やGM2合成において，細胞内輸送シグナルによって異なる安定性を付与された複数のアイソフォームが，複雑に絡み合いながらダイナミックなゴルジ体層板内を動き回っている．この複雑性こそが糖脂質生合成の恒常性を生み出す鍵なのかもしれない．

4.　摂食制御におけるガングリオシドの役割

恒常的な摂食調節機構は，生体のエネルギーバランス維持に重要である．視床下部は摂食調節において中心的な役割を持ち，末梢組織から分泌される種々のホルモン等によるエネルギー情報を受け取り，代謝を調節している．白色脂肪細胞が分泌するレプチンは血流を介して中枢に情報を伝え，長期的な摂食抑制作用を示す．視床下部弓状核のPOMC（proopiomelanocortin）ニューロンとAgRP/NPY（Agouti-related peptide/neuropeptide Y）ニューロンはレプチン受容体（LepR）を発現しており，それぞれ摂食抑制および摂食促進に関わるニューロンとして相反する形で調節をしている（**図5**）．POMCニューロンはレプチンによって活性化されると，JAK2（Janus kinase 2）-STAT3（signal transducer and activator of transcription 3）経路の活性化を介してPOMCやSOCS3（suppressor of cytokine signaling 3）等の標的遺伝子の転写を活性化する．前駆体POMCからはα-MSH（α-melanocyte stimulating hormone）が産生され，室傍核にあるメラノコルチン受容体MC4R（melanocortin-4

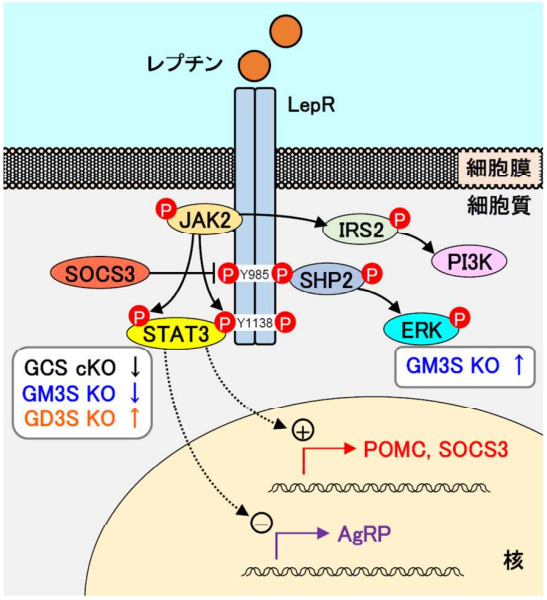

図5　レプチン受容体シグナル経路と各ガングリオシド欠損モデルにおける変化
矢印は，STAT3およびERKの活性化の亢進または減弱を示す．各モデルの脳ガングリオシドの特徴は以下のとおり．GCS cKO：誘導型脳特異的KO. ニューロンでGlcCer以降の糖脂質を欠く．GM3S KO：全身性GM3合成酵素KO. a，b系列ガングリオシドを欠き，o系列が発現．GD3S KO：全身性GD3合成酵素KO. b系列ガングリオシドを欠き，a系列が増加．

receptor）を持つ二次ニューロンを介して摂食を抑制する．一方でSOCS3はレプチン受容体に結合し，そのシグナルを抑制することで負のフィードバックループを形成する．AgRPはMC4Rを抑制し，NPYはNPY受容体を介していずれも摂食を促進するが，レプチンはAgRP/NPYニューロンを抑制することで摂食抑制へと導く[25]．

食餌誘導性肥満はレプチンの作用不全，すなわちレプチン抵抗性を惹起し，さらに末梢組織の慢性炎症を介して全身性のインスリン抵抗性を引き起こす．実際に肥満者においては血中レプチン濃度が高く，さらにレプチンを投与しても十分な減量効果が得られず，レプチン抵抗性の状態にあるとされている[26, 27]．レプチン抵抗性に関してはいくつかの異なる機序が提唱されているが，明確な機序は定かではない．

近年，LepRシグナルにおけるガングリオシドの役割が徐々に明らかにされてきている（図5）．Nordströmらは，誘導型前脳特異的グルコシルセラミド（GlcCer）合成酵素ノックアウト（GCS cKO）マウスが進行性の肥満を呈し，それがガングリオシドの前駆体となるGlcCerの欠失に伴う視床下部ニューロンのLepRシグナルの減弱に起因することを報告した[28]．哺乳動物の脳のガングリオシド組成は，主にa系列とb系列であるGM1, GD1a, GD1b, GT1bなどからなっているが（構造は図1参照），Nordströmらは，視床下部由来神経細胞株N-41において，LepRがGM1およびGD1aと相互作用し，それがLepRシグナルの十分な活性化（STAT3リン酸化）に必要であることを示した．

一方，Jiらは，b系列ガングリオシドを欠くGD3合成酵素ノックアウト（GD3S KO）マウスのレプチン分泌異常と脂肪組織内蓄積を見いだした[29]．このKOマウスの視床下部では，a系列のGM1とGD1aの発現増加とともにLepR発現とSTAT3リン酸化が亢進しており，それが血中レプチンの著しい低値にもかかわらずGD3S KOマウスが肥満を発症しない理由のようである[30]．さらに，N-41細胞にGD3Sを過剰発現させると，a系列の減少とともにレプチン刺激によるSTAT3リン酸化の減弱がみられた．この結果からも，a系列ガングリオシドがLepRシグナルを正に調節していることが示された．

我々のグループは，肥満病態におけるガングリオシドの機能を調べるため，遺伝性肥満モデルにおけるGM3Sノックアウトマウス（GM3S KO）を作製した．KK-A^yマウスは重度の過食とともにレプチン抵抗性を発症するモデルであるが，KK-A^y/GM3S KOマウスでは，レプチンの腹腔内投与に対する視床下部弓状核ニューロンの応答性が維持されていた[31]．N-41細胞を用いてGM3S KO細胞を作製すると，KOマウス脳と同様にa系列ガングリオシドの消失とo系列のGM1bの発現がみられ，レプチン刺激に対するSTAT3リン酸化は減弱する一方でERK（extracellular signal-regulated kinase）のリン酸化が著明に亢進していた．レプチンの抗肥満作用に関してはJAK2-STAT3経路が最もよく研究されているが，SHP2（SH2-containing protein tyrosine phosphatase 2）-ERK経路についてもレプチンの作用に関わることが示されており[32, 33]，KK-A^y/GM3S KOマウスでみられた過食・肥満病態の改善はLepR～ERK経路の亢進によるものと考えられる．

LepRはJAK2-STAT3, SHP2-ERK, PI3K（phosphoinositide 3-kinase）-AKTなどのいくつかの異なるシグナル経路の活性化につながり，エネルギー恒常性の維持以外にも多様な機能を持つことが知られている．どのガングリオシド分子種が，どういった特異性でレプチン受容体機能を調節しているのかについて，詳細な機序の解明が今後の課題である．

5.　コレステロール吸収におけるガングリオシドの役割

近年，腸管からの栄養吸収におけるスフィンゴ糖脂質の重要性が明らかとなってきている．これまでにC57BL6マウスの小腸絨毛における糖脂質組成が，発達の段階において種々の栄養吸収トランスポーターの遺伝子発現の変化と相関するようにダイナミックに変化することが報告されている[34]．また，腸上皮特異的GCS cKOマウスの解析から，スフィンゴ糖脂質が腸管の絨毛構造形成・脂質吸収に必須の因子である可能性が明らかとなっている[35]．我々は，腸管からのコレステロール吸収を担うNiemann-Pick C1 Like 1（NPC1L1）の機能にGM3をはじめとするガングリオシドが重要な役割を果たすことを新たに見いだした[36]．

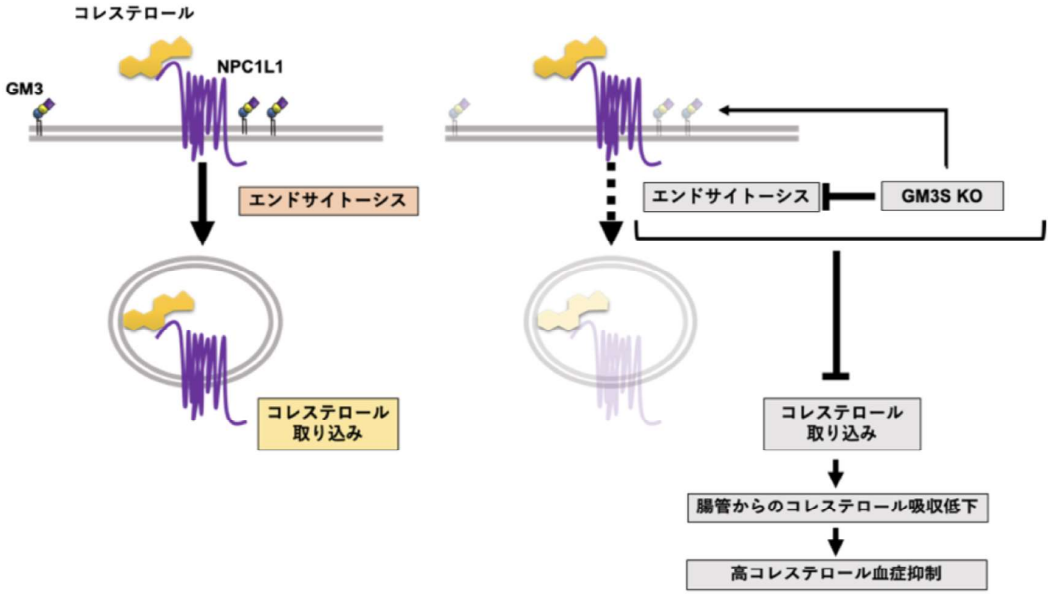

図6　NPC1L1依存的なコレステロール吸収機構とGM3S KOによるNPC1L1の機能抑制
NPC1L1はコレステロールの結合に伴い細胞内へとエンドサイトーシスされることでコレステロールを取り込む．GM3S KOによるガングリオシドの欠損はNPC1L1の局在変化を抑制し，コレステロールの取り込みを低下させる．

腸管からのコレステロール吸収は，長らく特定のトランスポーターが介在しない受動拡散による輸送だと考えられてきたが，2004年にコレステロール特異的な輸送タンパク質として13回膜貫通タンパク質であるNPC1L1が発見された[37, 38]．NPC1L1は，コレステロール，スフィンゴ脂質などの細胞内蓄積を特徴とするNiemann-Pick病C型の原因遺伝子産物，NPC1とアミノ酸配列で約50％の相同性を有する．NPC1L1の発現分布には種差があり，ヒトでは主に小腸刷子縁膜，肝細胞毛細胆管膜において発現する一方で，マウスでは肝臓での発現は低い[38, 39]．NPC1L1を介したコレステロール輸送機構の詳細は未解明な点が多く残されているものの，ここ10年ほどでようやくその一端が明らかとなってきた．NPC1L1は定常状態ではエンドソームに局在し，コレステロール枯渇時には形質膜へとリクルートされ，N末端領域に対するコレステロールの結合をトリガーとして小胞輸送により形質膜のコレステロールを細胞内へと取り込む（**図6**左）[40–42]．我々は，このコレステロール依存的なNPC1L1の局在変化がGM3Sをノックアウトしたヒト293T細胞およびGM3S KOマウスの小腸絨毛において抑制されており，GM3S KOマウスはNPC1L1の機能低下に伴う腸管からのコレステロール吸収抑制により高コレステロール血症に対して抵抗性を示すことを報告している（図6右）[36]．NPC1L1はガングリオシドに富む膜マイクロドメイン（脂質ラフト）に局在し，生理的な機能を発揮するためにはマイクロドメインの足場タンパク質であるフロチリン-1，フロチリン-2との会合を必要とする．NPC1L1を分子標的とした脂質異常症治療薬として用いられているエゼチミブは，NPC1L1とフロチリン-1,2との相互作用を減弱させ，マイクロドメインへの局在化を抑制することでNPC1L1の機能を抑制することが明らかとなっている[40, 43]．フロチリンは，形質膜コレステロール，ガングリオシドを含むスフィンゴ脂質とともにマイクロドメインを形成し，NPC1L1近傍の領域でコレステロールに富む微小環境を作り出すことで，エンドサイトーシスによるコレステロール吸収効率の向上に寄与しているのではないかと考えられているものの，マイクロドメインがNPC1L1の機能においてどのような役割を果たしているのかについてはより詳細な解析が必要である．また，ガングリオシドが実際にNPC1L1の機能にどのような機構で関与しているのか，NPC1L1の機能に寄与しうるガングリオシド分子種に特異性はあるのか等についても今後の研究課題となっている．

6.　自然免疫におけるGM3分子種の役割

近年，スフィンゴ糖脂質を介した自然免疫応答の活性化・調節機構が急速に明らかとなりつつある．セラミドへのグルコース付加によって生じるGlcCerは，抗原提示細胞である樹状細胞において，C型レクチン受容体の一つであるMincleの活性化を引き起こす[44]．Mincleは，肥満時の脂肪組織で発現量が増加しており，さらに*Mincle* KOマウスでは，メタボリックシンドロームの症状が緩和されることもわかってきている[45, 46]．続いて，GlcCerへのガラクトース付加で生成するLacCerは，好中球における自然免疫応答に関与する．LacCerは，抗酸菌細胞壁の糖脂質リポアラビノマンナンの認識に関与し，Srcファミリーチロシンキナーゼ Lynによるシグナル伝達を介して貪食後の食胞成熟と殺菌機構の活性化に大きく寄与する[47]．さらに，LacCerへのガラクトース，*N*-アセチルガラクトサミン付

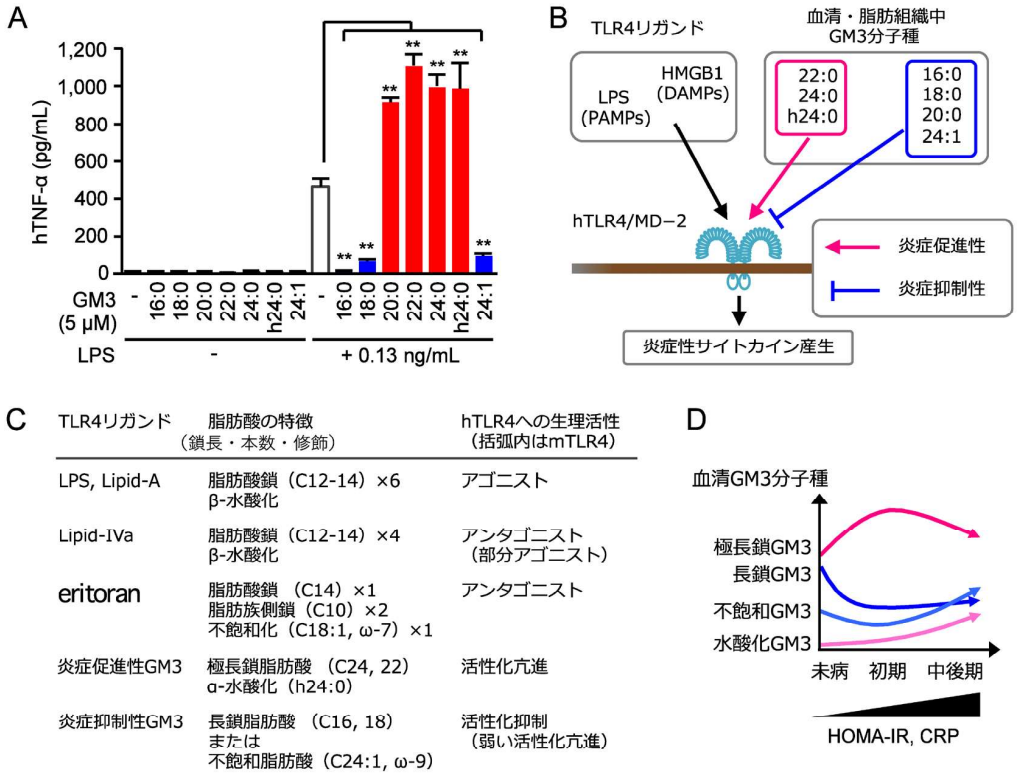

図7　GM3分子種の自然免疫および肥満などの慢性炎症性疾患への関与
（A）GM3分子種によるTLR4活性化制御，（B）GM3分子種によるヒトTLR4/MD-2活性化への作用（模式図），（C）LPSおよびGM3分子種の構造活性相関，（D）メタボリックシンドローム発症過程における血清GM3分子種の挙動（模式図）．hTLR4：ヒトTLR4, mTLR4：マウスTLR4, HOMA-IR：インスリン抵抗性指数，CRP：C反応性タンパク質．

加で生じるグロボ系スフィンゴ糖脂質Gb3およびGb4は，血管内皮細胞やマクロファージにおけるTLR4活性化制御に関与することが報告されている[44, 46]．

脂肪細胞におけるGM3の発現は，組織マクロファージに由来する炎症性サイトカインTNF-αやIL-1βの刺激によって誘導される[48, 49]．肥満時には，脂肪組織へのマクロファージ浸潤が生じ，炎症性サイトカイン産生による慢性炎症を介して，インスリン抵抗性を呈することがよく知られている[44, 45]．食欲抑制ホルモンであるレプチンの欠損によって肥満・メタボリックシンドロームを呈する*ob*/*ob*マウスや，高脂肪食によって誘導された肥満モデルマウスの脂肪組織ではマクロファージ浸潤・慢性炎症が生じるが，内臓脂肪組織におけるGM3の発現量とGM3S遺伝子（*St3gal5*）の発現を調べると，それらが大幅に亢進している[48, 49]．GM3などのスフィンゴ糖脂質は，細胞膜上で互いに集合したクラスター，すなわち，脂質マイクロドメインと呼ばれるシグナル伝達プラットフォームを形成する[3]．我々は，GM3の異常な発現上昇によって，細胞膜上におけるインスリン受容体の拡散速度が影響を受け，シグナル伝達効率が大きく制限されることでインスリン抵抗性を生じることを生細胞分子イメージング法によって示した[50]．一方，GlcCer合成酵素阻害薬であるD-PDMPやGenz-123346を用いてGM3の合成を阻害すると，脂肪細胞におけるインスリン抵抗性が解除される[51]．興味深いのは，GM3S KOマウスにおいては，全身のインスリン感受性が改善するだけでなく，肥満による慢性炎症も大きく緩和されていることである[49, 52]．このことは，インスリン抵抗性よりも上流で，GM3を介した慢性炎症メカニズムが存在することを示唆している．メタボリックシンドロームに関連するTLR4リガンドには，肥満時に脂肪組織中の発現量や血清中への分泌量が増加する特徴があり，GM3もその特徴を満たしている．そこで，実際にGM3がTLR4を介して自然免疫応答を活性化する可能性を検討することにした．

脂肪組織や血清中に存在するGM3には，同じ糖鎖を持ちながら，異なるセラミド構造を持つ多様な分子種が存在している（図3C）．特に，スフィンゴシンと脂肪酸からなるセラミド構造のうち，脂肪酸鎖の鎖長［長鎖脂肪酸（16:0, 18:0, 20:0），極長鎖脂肪酸（22:0, 24:0）］と構造修飾［α-水酸化（h24:0），ω-9不飽和化（24:1）］について，それらの組合わせによる幅広い多様性がみられる（図3C）．興味深いことに，これらのGM3分子種の血清中発現パターンが，メタボリックシンドロームの発症過程で変動することはわかってきたが[12]，一方で各分子種の生理活性とその変動の意義は不明のままであった．

そこで，ヒト末梢血由来単球における自然免疫応答を指標に，代表的なGM3分子種（16:0, 18:0, 20:0, 22:0, 24:0, h24:0, 24:1）の生理活性を検討した（**図7A**）．その

結果，ヒトTLR4/MD-2複合体を介した炎症性サイトカイン産生に対して，長鎖脂肪酸のGM3分子種（16:0, 18:0）は抑制的に作用し，一方，極長鎖脂肪酸のGM3分子種（22:0, 24:0, h24:0）はTLR4活性化を強く促進することがわかった[53]．一方で，極長鎖脂肪酸でも，不飽和化を受けたGM3分子種（24:1）は，TLR4に対して抑制的に作用した．興味深いことに，これらの作用は，LPSやLipid-A, HMGB1などのTLR4リガンドに対して選択的に生じ，その他のTLRリガンドに対しては影響を及ぼさなかった．また，GM3単独では活性化・抑制作用を示さず，TLR4リガンドの存在下で初めて，活性化制御を示す点も特徴的であった．これらを総括すると，GM3分子種は，その脂肪酸構造に依存して炎症抑制性と炎症促進性を併せ持つ，TLR4選択的な内因性モジュレーターであると考えられる（図7B）．

加えて，マウスTLR4/MD-2複合体を介した自然免疫応答に対しても，GM3分子種の生理活性を検討した．極長鎖脂肪酸のGM3分子種については，ヒトの場合と同様にTLR4活性化を強く促進した．ところが，長鎖脂肪酸や不飽和脂肪酸のGM3分子種では，ヒトTLR4に対するような抑制性は認められず，TLR4活性化を弱く促進した．すなわち，マウスTLR4に対しては，GM3分子種全体が炎症促進性を持つこと，その生理活性がアシル鎖長に比例して増大することがわかった．

前述したGM3分子種の生理活性や，ヒトとマウスにおける作用の違いはなぜ生じ，どのようにしてTLR4/MD-2によるGM3認識機構と関係しているのだろうか．LPSがTLR4リガンドとして作用する場合，糖鎖構造はTLR4が，脂肪酸構造はMD-2が，それぞれ認識する[54, 55]．さらにLPSでは，脂肪酸構造の多様性と生理活性の変化について多くの報告がある[55–60]．LPSのコア構造であるLipid-Aは，6本の脂肪酸を持ち，ヒト・マウスのTLR4/MD-2に対してともにアゴニストとして作用する（図7C）．一方，Lipid-Aの前駆体であるLipid-IVaは，4本の脂肪酸を持ち，ヒトTLR4/MD-2ではアンタゴニストとして，マウスTLR4/MD-2では部分アゴニストとして作用する（図7C）．そして，上記の生理活性と脂肪酸数の相関性は，MD-2の生物種に依存しており，マウスTLR4／ヒトMD-2キメラ複合体に対しては，ヒトTLR4/MD-2複合体と同様に，Lipid-IVaによる抑制効果がみられる．さらに，Lipid-IVaアナログであるTLR4阻害剤eritoranは，MD-2への結合を介した阻害効果に関与する不飽和脂肪酸（18:1, ω7）を持つ（図7C）[61]．この二重結合部位で，不飽和脂肪酸鎖は180°反転しつつMD-2の疎水性ポケットに結合しており，見かけの鎖長の短縮と結合力（疎水性）の増大を同時に達成していると考えられる．

GM3は，グルコース，ガラクトース，シアル酸からなる糖鎖と，異なる脂肪酸構造を含むセラミド部分を持つ点で，すなわち糖脂質自体の性質でLPSとよく類似している．したがって，MD-2がGM3の脂肪酸構造の認識に関与する可能性は十分に考えられる．そこで，マウスTLR4/MD-2複合体，ヒトTLR4/MD-2複合体，そしてマウスTLR4／ヒトMD-2からなるキメラ複合体を用いて，GM3 16:0の生理活性を比較検討した．その結果，マウスTLR4／ヒトMD-2キメラ複合体に対しても，ヒトTLR4/MD-2複合体と同様に，GM3 16:0は抑制的に作用した．すなわち，脂肪酸構造にもとづくGM3の生理活性は，MD-2に依存することがわかった．この結果は，もう一つの重要な側面として，GM3が脂質膜上からTLR4を制御する可能性に加え，LPSと同様に糖脂質リガンドとしてMD-2を介してTLR4に作用する可能性を示唆している．Native-PAGE法などを用いたTLR4/MD-2複合体（細胞外ドメイン）とGM3分子種の相互作用解析によっても，GM3とTLR4/MD-2の相互作用や，TLR4/MD-2複合体の二量体化・多量体化と考えられる分子量の増大が確認できた．上記のようなGM3分子種でみられた生理活性と脂肪酸鎖長・修飾の関係性，MD-2への依存性は，Lipid-A/IVaやeritoranの場合とよく類似しており（図7C），脂質構造の大きさによるTLR4の活性化制御機構は，糖脂質性のリガンド間において保存されていると考えられる．

では，どのようにしてGM3分子種の脂肪酸構造の変化がメタボリックシンドロームの発症や進行と関わるのだろうか．そこで，メタボリックシンドロームの発症過程におけるヒト血清GM3分子種の発現量を質量分析法によって測定し，その発現変動パターンを解析した（図7D）．自然免疫応答に対する生理活性をもとにGM3分子種を分類すると，長鎖GM3分子種（16:0, 18:0, 20:0）は炎症抑制性，極長鎖GM3分子種（22:0, 24:0, h24:0）は炎症促進性であり，極長鎖不飽和GM3分子種（24:1, h24:1）は炎症抑制性と考えられる．その結果，炎症抑制性のGM3分子種（16:0, 18:0）は，未病の肥満や初期メタボリックシンドロームにおいて急激に減少していた．一方，炎症促進性のGM3分子種（22:0, 23:0, 24:0, h24:0）は大きく増加していた．特に，水酸化極長鎖GM3 h24:0は，肥満の指標であるBMI，腹囲，そして慢性炎症の指標かつ炎症性サイトカインIL-6の代替マーカーであるCRPおよびインスリン抵抗性の指標であるHOMA-IRと，強い正の相関を示した．また，より重度の肥満・メタボリックシンドロームでは，肥満時に増加した極長鎖GM3が減少に転じ，代わりに不飽和化極長鎖GM3（22:1, 24:1, h24:1）の発現が増加した．これらを総括すると，肥満やメタボリックシンドローム発症初期においては，GM3分子種の炎症促進性シフトに伴って慢性炎症が生じていると考えられる．重症期では，極長鎖脂肪酸の不飽和化によって，GM3の炎症促進性を抑える機構が働いていると考えられる．さらに，肥満モデルマウス（*ob*/*ob*マウス，および高脂肪食負荷マウス）の内臓脂肪組織についてもGM3分子種を解析した．その結果，水酸化極長鎖GM3分子種が大きく増加していた．おそらく，ヒト血清中の水酸化極長鎖GM3の増加は，内臓脂肪組織におけるGM3分子種の変化が反映された可能性がある．こ

れらに加え，内臓脂肪組織における水酸化極長鎖GM3の増加は，TLR4の機能欠損変異体（C3H/HeJ）マウスにおいて緩和されていた．したがって，炎症促進性GM3の発現増加は，その受容体であるTLR4を介した炎症性サイトカイン産生に一部依存していると考えられる．

ガングリオシドの生合成メカニズムは，スフィンゴイド塩基，脂肪酸，そしてシアル酸を含む糖鎖に至るまで，幅広い生体関連因子の生合成・代謝経路に依存している．それゆえ，GM3分子種の発現量を制御する分子メカニズムは，きわめて複雑である．GM3分子種全体の発現量に関わるGM3S遺伝子の発現量は，前述のように，組織マクロファージに由来する炎症性サイトカインTNF-αやIL-1βの刺激によって制御されている[48, 49]．一方で，脂肪酸鎖長の制御に関わる因子としては，これまでに脂肪酸伸長酵素ELOVLが知られている．特に，*Elovl3*-KOマウスや*Elovl6*-KOマウスでは，肥満によるメタボリックシンドロームの進行が緩和されることが知られている[62, 63]．ELOVL6は長鎖脂肪酸16:0を18:0へ，ELOVL3は18:0を20:0に伸長する反応を担っており，極長鎖脂肪酸の前駆体の生合成に関与している．野生型と比べて*Elovl6*-KOマウスの脂肪酸組成は，18:0から24:0において減少しており，マウスTLR4に対する主要な炎症促進性GM3分子種が減少している可能性が予想される．加えて，炎症反応の後期では，脂肪酸の不飽和化が生じ，自然免疫応答の終息に不可欠であることが報告されている[64]．これは，GM3においても，重症期の不飽和GM3の増加として反映されていると考えられる．一方，水酸化修飾は，水酸化による水溶性の増大が血清中へのGM3分泌量に影響する可能性や，α-酸化を介した極長鎖脂肪酸の分解亢進との関連性が考えられる[51]．さらには，肥満時に生じる，セラミド合成酵素CerS2/6の発現変化やβ-酸化の障害も，GM3分子種のバランスの変化に関与する可能性がある[65, 66]．CerS2/6には，長鎖脂肪酸と極長鎖脂肪酸の選択性に違いがあり，それらの発現バランスによってセラミドの脂肪酸組成が制御されうる．これらの分子メカニズムとGM3分子種変化との関連を解明するには，セラミドからGM3に至るまでの網羅的な分子種発現解析と遺伝子発現解析が必要であり，今後の進展が望まれる．このように，GM3分子種は複雑な発現メカニズムを有しているが，一方で，多くの因子に依存するということは，多くの調節点を持つことに他ならない．GM3分子種の発現調節メカニズムは，さまざまなストレスや脂質代謝の変化を受けとり，それをTLR4経由の自然免疫応答へと反映させることが可能なシステムであるのかもしれない．その破綻が，恒常性維持機構としての自然免疫応答を，疾患発症原因である慢性炎症へと導くというのは，想像にかたくない．

7. まとめと今後の展望

ガングリオシドを含むスフィンゴ糖脂質分子群の細胞特異的・選択的発現が，生体の恒常性維持に欠くべからざる役割を担っている作動原理が解明されつつある．さまざまな病態において細胞膜のスフィンゴ糖脂質の質と量が変化することで，細胞膜マイクロドメインに存在している受容体機能の異常が生じる．たとえば，慢性炎症時における炎症性サイトカインの刺激によるGM3の細胞膜における増加は，脂肪細胞におけるカベオラマイクロドメインからインスリン受容体を解離させることで，インスリン抵抗性を惹起する．我々は，これを“マイクロドメイン病”と提唱している．最近では，GM3および関連ガングリオシドは，小腸上皮細胞におけるNPC1L1のコレステロール取り込みや視床下部におけるレプチン受容体の機能を制御している可能性を，GM3Sノックアウトマウスの検討から見いだしつつある[36]．この細胞膜上におけるスフィンゴ糖脂質の作動原理に加えて，本稿の最終節では，ガングリオシドGM3分子種がTLR4の新たな内因性リガンドとして自然免疫応答を制御している可能性について述べた．特筆すべきは，セラミド部分の脂肪酸鎖構造を異にするGM3分子種は，TLR4の活性化を正負両方向に制御することである．極長鎖GM3分子種はTLR4を活性化するが，長鎖GM3分子種は，極長鎖GM3分子種による活性化を中和してしまう．ヒト血清中には約30種のGM3分子種が存在しており，未病ではあるが慢性炎症状態にある（と考えられる）肥満者においては炎症抑制性の長鎖GM3分子種が有意に減少していた（図7D）．すなわち，GM3分子種のバランスは，生体恒常性の維持に関わっており，その変化はマクロファージの活性化を左右する“レオスタット”として機能していると考えられる．また，詳細は別の機会に述べるが，糖尿病性腎症の慢性炎症発症などにおけるグロボシド系糖脂質（Gb3およびGb4）の病態生理学的意義も明らかになりつつある[67, 68]．

スフィンゴ糖脂質分子種構造の多様性を詳細に解析／把握した上でないと，糖脂質研究そのもの自体が成り立たないこと，グライコリピドミクスの生命科学研究における重要性を理解していただければ幸いである．

文　　献

1) Yamakawa, T. & Suzuki, S. (1951) The chemistry of the lipids of posthemolytic residue or stroma of erythrocytes. I. Concerning the ether-insoluble lipids of lyophilized horse blood stroma. *J. Biochem.*, **38**, 199–212.
2) Ishii, A., Ohta, M., Watanabe, Y., Matsuda, K., Ishiyama, K., Sakoe, K., Nakamura, M., Inokuchi, J., Sanai, Y., & Saito, M. (1998) Expression cloning and functional characterization of human cDNA for ganglioside GM3 synthase. *J. Biol. Chem.*, **273**, 31652–31655.
3) Inokuchi, J., Inamori, K., Kabayama, K., Nagafuku, M., Uemura, S., Go, S., Suzuki, A., Ohno, I., Kanoh, H., & Shishido, F. (2018) Biology of GM3 ganglioside. *Prog. Mol. Biol. Transl. Sci.*, **156**, 151–195.
4) 井ノ口仁一（2015）ガングリオシドファミリーの分子種選択的発現と生理活性脂質としての意義．生化学，**87**，558–

570.
5) Yu, R.K., Yanagisawa, M., & Ariga, T. (2007) Glycosphingolipid structures, in Comprehensive Glycoscience, pp. 73–122, Elsevier, Oxford, UK.
6) Merrill, A.H. Jr. (2011) Sphingolipid and glycosphingolipid metabolic pathways in the era of sphingolipidomics. *Chem. Rev.*, **111**, 6387–6422.
7) Simons, K. & Gerl, M.J. (2010) Revitalizing membrane rafts: new tools and insights. *Nat. Rev. Mol. Cell Biol.*, **11**, 688–699.
8) Suzuki, A., Suzuki, M., Ito, E., Nitta, T., & Inokuchi, J.I. (2018) Mass spectrometry of gangliosides. *Methods Mol. Biol.*, **1804**, 207–221.
9) Tanaka, K., Suzuki, A., Aoki, D., & Iwamori, M. (2019) Characterization of a novel glycolipid with a difucosylated H-antigen in human blood group O erythrocytes with monoclonal antibody HMMC-1 and its detection in human uterine cervical carcinoma tissues. *Glycoconj. J.*, **36**, 219–226.
10) Silsirivanit, A., Phoomak, C., Teeravirote, K., Wattanavises, S., Seubwai, W., Saengboonmee, C., Zhan, Z., Inokuchi, J.I., Suzuki, A., & Wongkham, S. (2019) Overexpression of HexCer and LacCer containing 2-hydroxylated fatty acids in cholangiocarcinoma and the association of the increase of LacCer (d18:1–h23:0) with shorter survival of the patients. *Glycoconj. J.*, **36**, 103–111.
11) Ito, E., Waki, H., Miseki, K., Shimada, T., Sato, T.A., Kakehi, K., Suzuki, M., & Suzuki, A. (2013) Structural characterization of neutral glycosphingolipids using high-performance liquid chromatography-electrospray ionization mass spectrometry with a repeated high-speed polarity and MSn switching system. *Glycoconj. J.*, **30**, 881–888.
12) Veillon, L., Go, S., Matsuyama, W., Suzuki, A., Nagasaki, M., Yatomi, Y., & Inokuchi, J. (2015) Identification of ganglioside GM3 molecular species in human serum associated with risk factors of metabolic syndrome. *PLoS One*, **10**, e0129645.
13) Oikawa, N., Matsubara, T., Fukuda, R., Yasumori, H., Hatsuta, H., Murayama, S., Sato, T., Suzuki, A., & Yanagisawa, K. (2015) Imbalance in fatty-acid-chain length of gangliosides triggers Alzheimer amyloid deposition in the precuneus. *PLoS One*, **10**, e0121356.
14) Oikawa, N., Hatsuta, H., Murayama, S., Suzuki, A., & Yanagisawa, K. (2014) Influence of APOE genotype and the presence of Alzheimer's pathology on synaptic membrane lipids of human brains. *J. Neurosci. Res.*, **92**, 641–650.
15) Nagafuku, M., Okuyama, K., Onimaru, Y., Suzuki, A., Odagiri, Y., Yamashita, T., Iwasaki, K., Fujiwara, M., Takayanagi, M., Ohno, I., et al. (2012) CD4 and CD8 T cells require different membrane gangliosides for activation. *Proc. Natl. Acad. Sci. USA*, **109**, E336–E342.
16) Ito, E., Tominaga, A., Waki, H., Miseki, K., Tomioka, A., Nakajima, K., Kakehi, K., Suzuki, M., Taniguchi, N., & Suzuki, A. (2012) Structural characterization of monosialo-, disialo- and trisialo-gangliosides by negative ion AP-MALDI-QIT-TOF mass spectrometry with MS(n) switching. *Neurochem. Res.*, **37**, 1315–1324.
17) Kurokawa, K., Osakada, H., Kojidani, T., Waga, M., Suda, Y., Asakawa, H., Haraguchi, T., & Nakano, A. (2019) Visualization of secretory cargo transport within the Golgi apparatus. *J. Cell Biol.*, **218**, 1602–1618.
18) Yano, H., Yamamoto-Hino, M., Abe, M., Kuwahara, R., Haraguchi, S., Kusaka, I., Awano, W., Kinoshita-Toyoda, A., Toyoda, H., & Goto, S. (2005) Distinct functional units of the Golgi complex in Drosophila cells. *Proc. Natl. Acad. Sci. USA*, **102**, 13467–13472.
19) Uemura, S., Yoshida, S., Shishido, F., & Inokuchi, J. (2009) The cytoplasmic tail of GM3 synthase defines its subcellular localization, stability, and in vivo activity. *Mol. Biol. Cell*, **20**, 3088–3100.
20) Uemura, S., Shishido, F., Kashimura, M., & Inokuchi, J. (2015) The regulation of ER export and Golgi retention of ST3Gal5 (GM3/GM4 synthase) and B4GalNAcT1 (GM2/GD2/GA2 synthase) by arginine/lysine-based motif adjacent to the transmembrane domain. *Glycobiology*, **25**, 1410–1422.
21) Giraudo, C.G. & Maccioni, H.J. (2003) Endoplasmic reticulum export of glycosyltransferases depends on interaction of a cytoplasmic dibasic motif with Sar1. *Mol. Biol. Cell*, **14**, 3753–3766.
22) Michelsen, K., Schmid, V., Metz, J., Heusser, K., Liebel, U., Schwede, T., Spang, A., & Schwappach, B. (2007) Novel cargo-binding site in the beta and delta subunits of coatomer. *J. Cell Biol.*, **179**, 209–217.
23) Li, J., Yen, T.Y., Allende, M.L., Joshi, R.K., Cai, J., Pierce, W.M., Jaskiewicz, E., Darling, D.S., Macher, B.A., & Young, W.W. Jr. (2000) Disulfide bonds of GM2 synthase homodimers. Antiparallel orientation of the catalytic domains. *J. Biol. Chem.*, **275**, 41476–41486.
24) Shishido, F., Uemura, S., Kashimura, M., & Inokuchi, J. (2017) Identification of a new B4GalNAcT1 (GM2/GD2/GA2 synthase) isoform, and regulation of enzyme stability and intracellular transport by arginine-based motif. *Biochim. Biophys. Acta Biomembr.*, **1859**, 2001–2011.
25) Yeo, G.S. & Heisler, L.K. (2012) Unraveling the brain regulation of appetite: Lessons from genetics. *Nat. Neurosci.*, **15**, 1343–1349.
26) Heymsfield, S.B., Greenberg, A.S., Fujioka, K., Dixon, R.M., Kushner, R., Hunt, T., Lubina, J.A., Patane, J., Self, B., Hunt, P., et al. (1999) Recombinant leptin for weight loss in obese and lean adults: A randomized, controlled, dose-escalation trial. *JAMA*, **282**, 1568–1575.
27) Considine, R.V., Sinha, M.K., Heiman, M.L., Kriauciunas, A., Stephens, T.W., Nyce, M.R., Ohannesian, J.P., Marco, C.C., McKee, L.J., Bauer, T.L., et al. (1996) Serum immunoreactive-leptin concentrations in normal-weight and obese humans. *N. Engl. J. Med.*, **334**, 292–295.
28) Nordstrom, V., Willershauser, M., Herzer, S., Rozman, J., von Bohlen Und Halbach, O., Meldner, S., Rothermel, U., Kaden, S., Roth, F.C., Waldeck, C., et al. (2013) Neuronal expression of glucosylceramide synthase in central nervous system regulates body weight and energy homeostasis. *PLoS Biol.*, **11**, e1001506.
29) Ji, S., Ohkawa, Y., Tokizane, K., Ohmi, Y., Banno, R., Furukawa, K., Kiyama, H., & Furukawa, K. (2015) b-Series gangliosides crucially regulate leptin secretion in adipose tissues. *Biochem. Biophys. Res. Commun.*, **459**, 189–195.
30) Ji, S., Tokizane, K., Ohkawa, Y., Ohmi, Y., Banno, R., Okajima, T., Kiyama, H., Furukawa, K., & Furukawa, K. (2016) Increased a-series gangliosides positively regulate leptin/Ob receptor-mediated signals in hypothalamus of GD3 synthase-deficient mice. *Biochem. Biophys. Res. Commun.*, **479**, 453–460.
31) Inamori, K., Ito, H., Tamura, Y., Nitta, T., Yang, X., Nihei, W., Shishido, F., Imazu, S., Tsukita, S., Yamada, T., et al. (2018) Deficient ganglioside synthesis restores responsiveness to leptin and melanocortin signaling in obese KKAy mice. *J. Lipid Res.*, **59**, 1472–1481.
32) Balland, E., Dam, J., Langlet, F., Caron, E., Steculorum, S., Messina, A., Rasika, S., Falluel-Morel, A., Anouar, Y., Dehouck, B., et al. (2014) Hypothalamic tanycytes are an ERK-gated conduit for leptin into the brain. *Cell Metab.*, **19**, 293–301.

33) Rahmouni, K., Sigmund, C.D., Haynes, W.G., & Mark, A.L. (2009) Hypothalamic ERK mediates the anorectic and thermogenic sympathetic effects of leptin. *Diabetes*, **58**, 536–542.
34) Yoneshige, A., Sasaki, A., Miyazaki, M., Kojima, N., Suzuki, A., & Matsuda, J. (2010) Developmental changes in glycolipids and synchronized expression of nutrient transporters in the mouse small intestine. *J. Nutr. Biochem.*, **21**, 214–226.
35) Jennemann, R., Kaden, S., Sandhoff, R., Nordstrom, V., Wang, S., Volz, M., Robine, S., Amen, N., Rothermel, U., Wiegandt, H., et al. (2012) Glycosphingolipids are essential for intestinal endocytic function. *J. Biol. Chem.*, **287**, 32598–32616.
36) Nihei, W., Nagafuku, M., Hayamizu, H., Odagiri, Y., Tamura, Y., Kikuchi, Y., Veillon, L., Kanoh, H., Inamori, K., Arai, K., et al. (2018) NPC1L1-dependent intestinal cholesterol absorption requires ganglioside GM3 in membrane microdomains. *J. Lipid Res.*, **59**, 2181–2187.
37) Betters, J.L. & Yu, L. (2010) NPC1L1 and cholesterol transport. *FEBS Lett.*, **584**, 2740–2747.
38) Altmann, S.W., Davis, H.R. Jr., Zhu, L.J., Yao, X., Hoos, L.M., Tetzloff, G., Iyer, S.P., Maguire, M., Golovko, A., Zeng, M., et al. (2004) Niemann–Pick C1 Like 1 protein is critical for intestinal cholesterol absorption. *Science*, **303**, 1201–1204.
39) Davies, J.P., Scott, C., Oishi, K., Liapis, A., & Ioannou, Y.A. (2005) Inactivation of NPC1L1 causes multiple lipid transport defects and protects against diet-induced hypercholesterolemia. *J. Biol. Chem.*, **280**, 12710–12720.
40) Zhang, J.H., Ge, L., Qi, W., Zhang, L., Miao, H.H., Li, B.L., Yang, M., & Song, B.L. (2011) The N-terminal domain of NPC1L1 protein binds cholesterol and plays essential roles in cholesterol uptake. *J. Biol. Chem.*, **286**, 25088–25097.
41) Ge, L., Wang, J., Qi, W., Miao, H.H., Cao, J., Qu, Y.X., Li, B.L., & Song, B.L. (2008) The cholesterol absorption inhibitor ezetimibe acts by blocking the sterol-induced internalization of NPC1L1. *Cell Metab.*, **7**, 508–519.
42) Yu, L., Bharadwaj, S., Brown, J.M., Ma, Y., Du, W., Davis, M.A., Michaely, P., Liu, P., Willingham, M.C., & Rudel, L.L. (2006) Cholesterol-regulated translocation of NPC1L1 to the cell surface facilitates free cholesterol uptake. *J. Biol. Chem.*, **281**, 6616–6624.
43) Ge, L., Qi, W., Wang, L.J., Miao, H.H., Qu, Y.X., Li, B.L., & Song, B.L. (2011) Flotillins play an essential role in Niemann–Pick C1-like 1-mediated cholesterol uptake. *Proc. Natl. Acad. Sci. USA*, **108**, 551–556.
44) Nagata, M., Izumi, Y., Ishikawa, E., Kiyotake, R., Doi, R., Iwai, S., Omahdi, Z., Yamaji, T., Miyamoto, T., Bamba, T., et al. (2017) Intracellular metabolite beta-glucosylceramide is an endogenous Mincle ligand possessing immunostimulatory activity. *Proc. Natl. Acad. Sci. USA*, **114**, E3285–E3294.
45) Tanaka, M., Ikeda, K., Suganami, T., Komiya, C., Ochi, K., Shirakawa, I., Hamaguchi, M., Nishimura, S., Manabe, I., Matsuda, T., et al. (2014) Macrophage-inducible C-type lectin underlies obesity-induced adipose tissue fibrosis. *Nat. Commun.*, **5**, 4982.
46) Ichioka, M., Suganami, T., Tsuda, N., Shirakawa, I., Hirata, Y., Satoh-Asahara, N., Shimoda, Y., Tanaka, M., Kim-Saijo, M., Miyamoto, Y., et al. (2011) Increased expression of macrophage-inducible C-type lectin in adipose tissue of obese mice and humans. *Diabetes*, **60**, 819–826.
47) Nakayama, H., Kurihara, H., Morita, Y.S., Kinoshita, T., Mauri, L., Prinetti, A., Sonnino, S., Yokoyama, N., Ogawa, H., Takamori, K., et al. (2016) Lipoarabinomannan binding to lactosylceramide in lipid rafts is essential for the phagocytosis of mycobacteria by human neutrophils. *Sci. Signal.*, **9**, ra101.
48) Nagafuku, M., Sato, T., Sato, S., Shimizu, K., Taira, T., & Inokuchi, J. (2015) Control of homeostatic and pathogenic balance in adipose tissue by ganglioside GM3. *Glycobiology*, **25**, 303–318.
49) Tagami, S.J.I., Kabayama, K., Yoshimura, H., Kitamura, F., Uemura, S., Ogawa, C., Ishii, A., Saito, M., Ohtsuka, Y., Sakaue, S., et al. (2002) Ganglioside GM3 participates in the pathological conditions of insulin resistance. *J. Biol. Chem.*, **277**, 3085–3092.
50) Kabayama, K., Sato, T., Saito, K., Loberto, N., Prinetti, A., Sonnino, S., Kinjo, M., Igarashi, Y., & Inokuchi, J. (2007) Dissociation of the insulin receptor and caveolin-1 complex by ganglioside GM3 in the state of insulin resistance. *Proc. Natl. Acad. Sci. USA*, **104**, 13678–13683.
51) Hama, H. (2010) Fatty acid 2-hydroxylation in mammalian sphingolipid biology. *Biochim. Biophys. Acta*, **1801**, 405–414.
52) Yamashita, T., Hashiramoto, A., Haluzik, M., Mizukami, H., Beck, S., Norton, A., Kono, M., Tsuji, S., Daniotti, J.L., Werth, N., et al. (2003) Enhanced insulin sensitivity in mice lacking ganglioside GM3. *Proc. Natl. Acad. Sci. USA*, **100**, 3445–3449.
53) Kanoh, H., Nitta, T., Go, S., Inamori, K., Veillon, L., Nihei, W., Fujii, M., Kabayama, K., Shimoyama, A., Fukase, K., et al. (2020) Homeostatic and pathogenic roles of GM3 ganglioside molecular species in TLR4 signaling in obesity. *EMBO J.*, in press. https://www.embopress.org/doi/10.15252/embj.2019101732
54) Park, B.S., Song, D.H., Kim, H.M., Choi, B.S., Lee, H., & Lee, J.O. (2009) The structural basis of lipopolysaccharide recognition by the TLR4-MD-2 complex. *Nature*, **458**, 1191–1195.
55) Mueller, M., Lindner, B., Kusumoto, S., Fukase, K., Schromm, A.B., & Seydel, U. (2004) Aggregates are the biologically active units of endotoxin. *J. Biol. Chem.*, **279**, 26307–26313.
56) Saitoh, S., Akashi, S., Yamada, T., Tanimura, N., Kobayashi, M., Konno, K., Matsumoto, F., Fukase, K., Kusumoto, S., Nagai, Y., et al. (2004) Lipid A antagonist, lipid IVa, is distinct from lipid A in interaction with Toll-like receptor 4 (TLR4)-MD-2 and ligand-induced TLR4 oligomerization. *Int. Immunol.*, **16**, 961–969.
57) Akashi, S., Nagai, Y., Ogata, H., Oikawa, M., Fukase, K., Kusumoto, S., Kawasaki, K., Nishijima, M., Hayashi, S., Kimoto, M., et al. (2001) Human MD-2 confers on mouse Toll-like receptor 4 species-specific lipopolysaccharide recognition. *Int. Immunol.*, **13**, 1595–1599.
58) Wang, M.H., Feist, W., Herzbeck, H., Brade, H., Kusumoto, S., Rietschel, E.T., Flad, H.D., & Ulmer, A.J. (1990) Suppressive effect of lipid A partial structures on lipopolysaccharide or lipid A-induced release of interleukin 1 by human monocytes. *FEMS Microbiol. Immunol.*, **2**, 179–185.
59) Galanos, C., Luderitz, O., Rietschel, E.T., Westphal, O., Brade, H., Brade, L., Freudenberg, M., Schade, U., Imoto, M., Yoshimura, H., et al. (1985) Synthetic and natural Escherichia coli free lipid A express identical endotoxic activities. *Eur. J. Biochem.*, **148**, 1–5.
60) Galanos, C., Lehmann, V., Luderitz, O., Rietschel, E.T., Westphal, O., Brade, H., Brade, L., Freudenberg, M.A., Hansen-Hagge, T., Luderitz, T., et al. (1984) Endotoxic properties of chemically synthesized lipid A part structures. Comparison of synthetic lipid A precursor and synthetic analogues with biosynthetic lipid A precursor and free lipid A. *Eur. J. Biochem.*, **140**, 221–227.
61) Kim, H.M., Park, B.S., Kim, J.I., Kim, S.E., Lee, J., Oh, S.C., Enkhbayar, P., Matsushima, N., Lee, H., Yoo, O.J., et al. (2007) Crystal structure of the TLR4-MD-2 complex with bound endotoxin antagonist Eritoran. *Cell*, **130**, 906–917.
62) Zadravec, D., Brolinson, A., Fisher, R.M., Carneheim, C., Csikasz, R.I., Bertrand-Michel, J., Boren, J., Guillou, H., Rudling,

M., & Jacobsson, A. (2010) Ablation of the very-long-chain fatty acid elongase ELOVL3 in mice leads to constrained lipid storage and resistance to diet-induced obesity. *FASEB J.*, **24**, 4366–4377.
63) Matsuzaka, T., Shimano, H., Yahagi, N., Kato, T., Atsumi, A., Yamamoto, T., Inoue, N., Ishikawa, M., Okada, S., Ishigaki, N., et al. (2007) Crucial role of a long-chain fatty acid elongase, Elovl6, in obesity-induced insulin resistance. *Nat. Med.*, **13**, 1193–1202.
64) Oishi, Y., Spann, N.J., Link, V.M., Muse, E.D., Strid, T., Edillor, C., Kolar, M.J., Matsuzaka, T., Hayakawa, S., Tao, J., et al. (2017) SREBP1 contributes to resolution of pro-inflammatory TLR4 signaling by reprogramming fatty acid metabolism. *Cell Metab.*, **25**, 412–427.
65) Turpin, S.M., Nicholls, H.T., Willmes, D.M., Mourier, A., Brodesser, S., Wunderlich, C.M., Mauer, J., Xu, E., Hammerschmidt, P., Bronneke, H.S., et al. (2014) Obesity-induced CerS6-dependent C16:0 ceramide production promotes weight gain and glucose intolerance. *Cell Metab.*, **20**, 678–686.
66) Raichur, S., Wang, S.T., Chan, P.W., Li, Y., Ching, J., Chaurasia, B., Dogra, S., Ohman, M.K., Takeda, K., Sugii, S., et al. (2014) CerS2 haploinsufficiency inhibits beta-oxidation and confers susceptibility to diet-induced steatohepatitis and insulin resistance. *Cell Metab.*, **20**, 687–695.
67) Kondo, Y., Ikeda, K., Tokuda, N., Nishitani, C., Ohto, U., Akashi-Takamura, S., Ito, Y., Uchikawa, M., Kuroki, Y., Taguchi, R., et al. (2013) TLR4-MD-2 complex is negatively regulated by an endogenous ligand, globotetraosylceramide. *Proc. Natl. Acad. Sci. USA*, **110**, 4714–4719.
68) Nitta, T., Kanoh, H., Inamori, K., Suzuki, A., Takahashi, T., & Inokuchi, J. (2019) Globo-series glycosphingolipids enhance Toll-like receptor 4-mediated inflammation and play a pathophysiological role in diabetic nephropathy. *Glycobiology*, **29**, 260–268.

著者寸描

●井ノ口　仁一（いのくち　じんいち）

東北医科薬科大学分子生体膜研究所・薬学部機能病態分子学教室特任教授．薬学博士．

■略歴　福岡県に生まれる．福岡大学薬学部を卒業．同大学院，生化学教室助手を経て，1985年ミシガン大学医学部神経化学研究所博士研究員．91年生化学工業東京研究所主任研究員を経て，98年北海道大学大学院薬学研究科助教授．2006年より現職．

■研究テーマと抱負　生体恒常性維持機構におけるスフィンゴ糖脂質の分子種特異的な作動原理を解明し，慢性炎症を基礎疾患とする様々な病態への関与を明らかにすることが使命であると考えている．

■ウェブサイト　http://www.tohoku-mpu.ac.jp/laboratory/kinoubyoutai/TOP.html

■趣味　音楽鑑賞，ガーデニング．

BBA - General Subjects 1865 (2021) 129870

Contents lists available at ScienceDirect

BBA - General Subjects

journal homepage: www.elsevier.com/locate/bbagen

α1,6-Fucosyltransferase contributes to cell migration and proliferation as well as to cancer stemness features in pancreatic carcinoma

Caixia Liang [a], Tomohiko Fukuda [a], Tomoya Isaji [a], Chengwei Duan [a], Wanli Song [a], Yuqin Wang [b], Jianguo Gu [a,*]

[a] Division of Regulatory Glycobiology, Institute of Molecular Biomembrane and Glycobiology, Tohoku Medical and Pharmaceutical University, 4-4-1 Komatsushima, Aoba-ku, Sendai, Miyagi 981-8558, Japan
[b] Department of Pharmacology, Pharmacy College, Nantong University, Nantong, Jiangsu Province 226001, China

ARTICLE INFO

Keywords:
Cancer stemness
Core fucosylation
FUT8
N-glycans
Pancreatic cancer

ABSTRACT

Background: Pancreatic carcinoma is one of the deadliest malignant diseases, in which the increased expression of α1,6-fucosyltransferase (FUT8), a sole enzyme responsible for catalyzing core fucosylation, has been reported. However, its pathological roles and regulatory mechanisms remain largely unknown. Here, we use two pancreatic adenocarcinoma cell lines, MIA PaCa-2 and PANC-1 cells, as cell models, to explore the relationship of FUT8 with the malignant transformation of PDAC.
Methods: FUT8 knockout (FUT8-KO) cells were established by the CRISPR/Cas9 system. Cell migration was analyzed by transwell and wound-healing assays. Cell proliferation was examined by MTT and colony-formation assays. Cancer stemness markers and spheroid formations were used to analyzed cancer stemness features.
Results: Deficiency of FUT8 inhibited cell migration and proliferation in both MIA PaCa-2 and PANC-1 cells compared with wild-type cells. Moreover, the expression levels of cancer stemness markers such as EpCAM, CXCR4, c-Met, and CD133 were decreased in the FUT8-KO cells compared with wild-type cells. Also, the spheroid formations in the KO cells were loose and unstable, which could be reversed by restoration with FUT8 gene in the KO cells. Additionally, FUT8-KO increased the chemosensitivity to gemcitabine, which is the first-line therapy for advanced pancreatic cancer.
Conclusions: FUT8-KO reduced the cell proliferation and migration. Our results are the first to suggest that the expression of FUT8 is involved in regulating the stemness features of pancreatic cancer cells.
General significance: FUT8 could provide novel insights for the treatment of pancreatic carcinoma.

1. Introduction

Pancreatic ductal adenocarcinoma (PDAC) accounts for 90% of all pancreatic cancers, which makes it one of the most aggressive forms of malignancy that always has a poor prognosis [1]. PDAC is the fourth-leading cause of cancer-related death in the world, and the 5-year survival rate remains at approximately 5% [2,3]. Pancreatic cancer is highly metastatic and resistant to chemotherapy and radiotherapy [4,5]. Therefore, there is an urgent clinical need to develop novel therapeutic strategies for PDAC.

Abnormal glycosylation changes including sialylation, fucosylation, and high-branched glycans on the surface of cancer cells have been confirmed as positively related to tumor progression and metastasis, which has provided new strategies for tumor treatment [6,7]. Recent research has shown that aberrant glycosylation is common in pancreatic cancer [8,9]. For example, the sialyltransferase enzymes ST6Gal1 and ST3Gal3 are overexpressed in pancreatic cancer tissue, thereby promoting distant metastasis [10,11]. Sialyl Lewis A antigen is well known as CA19-9, which has been used to detect pancreatic cancer according to Lewis and Secretor genotypes [12]. Fucosylation is a common glycosylation type in PDAC, and its increase can be detected in the serum of patients with pancreatic cancer [13]. The level of fucosylated

Abbreviations: AAL, aleuria aurantia lectin; CSC, cancer stem cell; EGFR, epidermal growth factor receptor; FBS, fetal bovine serum; 2FF, 2-fluoro-L-fucose; FUT8, α1,6-fucosyltransferase; GAPDH, glyceraldehyde-3-phosphate dehydrogenase; KO, knockout; PDAC, pancreatic ductal adenocarcinoma; PhoSL, pholiota squarrosa lectin; WT, wild type.

* Corresponding author.
E-mail address: jgu@tohoku-mpu.ac.jp (J. Gu).

https://doi.org/10.1016/j.bbagen.2021.129870
Received 4 December 2020; Received in revised form 3 February 2021; Accepted 5 February 2021
Available online 9 February 2021

haptoglobin was increased in serum of patients with pancreatic cancer as compared to in healthy controls, and it has been used for diagnostic screening and as a tumor marker [14–16]. Core fucosylation of N-glycans catalyzed by α1,6-fucosyltransferase (FUT8), are obviously higher in cancer tissues than in normal pancreatic ductal tissues [17,18]. In fact, aberrant FUT8 expression and activation has also been observed in other malignant tumors such as liver [19,20] lung [21] ovarian [22] breast [23] and colorectal [24]. FUT8 is critical for signaling receptors involved in many physiological and pathological processes such as cell growth, adhesion, and tumor metastasis. The core fucosylation of TGF-β receptors facilitates TGF-β ligand binding and EMT in breast tumors [25–27]. In embryonic fibroblasts, deficient core fucosylation leads to a blockage of α3β1 integrin-mediated cell migration and cell signaling [28]. Lack of core fucosylation in a pro-B cell line could induce autodimerization of Fms-like tyrosine kinase 3, and activate several downstream signaling pathways [29]. In addition, suppression of core fucosylation enhanced the activity of pro-inflammatory cytokines such as IFN-γ and IL-6, resulting in increased sensitivity of microglia and astrocytes in neuroinflammation [30]. These results highlight the multifaceted roles of FUT8 in cancer development and progression. However, the underlying molecular mechanisms of FUT8 in the malignant transformation of PDAC and whether FUT8 could be a potential therapeutic target remains largely unknown.

The present study addressed these questions via in vitro examination of two typical pancreatic cancer cell lines: MIA PaCa-2 and PANC-1 [9,31]. We used CRISPR/Cas9-mediated gene editing to obtain FUT8 knockout (FUT8-KO) cells from both cell lines. We found that FUT8-KO reduced the cell proliferation and migration, and suppressed the characteristics of cancer stem cells (CSC) such as CSC biomarker and spheroid formation as well as chemoresistance. These results suggest that FUT8 may be a potential therapeutic target for PDAC.

2. Materials and methods

2.1. Antibodies and reagents

The experiments were performed using the following antibodies and reagents: rabbit antibodies against epidermal growth factor receptor (EGFR) (4267S) and peroxidase-conjugated secondary antibody against rabbit (7074S) were purchased from Cell Signaling Technology; mouse antibodies against EGFR (sc-120) were obtained from Santa Cruz Biotechnology; mouse antibodies against α-Tubulin (T6199), peroxidase-conjugated secondary against mouse (AP124P) and fibronectin (F0895) were acquired from MilliporeSigma; mouse antibodies against integrin β1 (P5D2) were obtained from Development Studies Hybridoma Bank; Biotinylated aleuria aurantia lectin (AAL) was purchased from the Seikagaku Corp (Japan); Biotinylated pholiota squarrosa lectin (PhoSL), which specifically recognizes core fucosylated N-glycans, was a gift from Dr. Yuka Kobayashi (J-oil Mills, Tokyo, Japan); goat anti-mouse IgG Alexa Fluor 647 and streptavidin-conjugate Alexa Fluor 647 were obtained from Invitrogen; An ABC kit was acquired from Vector Laboratories; 2-fluoro-L-fucose (2FF), a specific fluorinated analog of fucose, was obtained from Synchem, Inc., IL, USA; Difco ™ Agar Noble (214220) was purchased from BD Biosciences; Gemcitabine (G6423) and cycloheximide were purchased from Sigma-Aldrich and Wako, Japan; PrimeScript RT reagent Kit with gDNA Eraser (Perfect Real Time) (RR047A) was purchased from Takara, Japan; Quick Taq HS DyeMix (DTM-101) was purchased from TOYOBO, Japan; and, Dulbecco's modified Eagle's medium (DMEM) and fetal bovine serum (FBS) were obtained from Gibco and Invitrogen, respectively.

2.2. Cell lines and cell culture

Human pancreatic adenocarcinoma cell lines MIA PaCa-2 and PANC-1 were obtained from the RIKEN cell bank (Japan). These two cell lines were cultured in DMEM supplied with 10% FBS and incubated at 37 °C in a humidified atmosphere containing 5% CO_2. Cells were passaged when the confluence reached approximately 80%.

2.3. RT-PCR for mRNA expression analysis

For each sample, total RNA was extracted from cells using TRIzol Reagent (Invitrogen) according to the manufacturer's instructions. Total RNA (1 μg) was reverse-transcribed using a PrimeScript RT reagent kit (Takara Bio Inc.). The PCR primer sequences are listed in Table 1.

2.4. Generation of CRISPR/Cas9-based FUT8-KO cells and establishment of FUT8 rescued cells

CRISPR/Cas9-based knockout was performed as described previously with minor modifications [30,32]. Briefly, the sgRNA-specifying oligo sequences (sequences one: 5′- CACCGATTGATCAGGGGCCAGCTAT-3′ and 5′-AAACATAGCTGGCCCCTGATCAATC-3′; sequences two: 5′- CACCGTACTACCTCAGTCAGACAGA-3′ and 5′-AAACTCTGTCTGACTGAGGTAGTAC-3′) spanning *Homo sapiens* FUT8 (NM_178155.3) were chosen from the CRISPR/Cas9 KO library and cloned into pSpCas9 (BB)-2A-GFP (PX458) (Addgene, #48138), which was a kind gift from Dr. Feng Zhang [33]. The plasmids were then electroporated into the MIA PaCa-2 and PANC-1 cells according to the manufacturer's instructions (Amaxa® cell line Nucleofector R kit V). After 2 days of transfection, GFP-positive cells were sorted using FACS Aria II (BD Bioscience). Then negative selections with PhoSL lectin were sorted three times and grown as single clones during 2 to 3 weeks. The FUT8-KO cells were identified via flow cytometric and lectin blot analysis.

To establish a stable rescue cell line, the virus production and infection were performed as described previously [34]. Briefly, the lentivirus vectors (CSIV-TRE-RfA-CMV-KT-FUT8) were transfected into 293 T cells with packaging plasmids by calcium phosphate. The target cells were cultured for 48 h, and the lentivirus supernatants were collected for infection. After infection for 72 h, the Kusabira Orange-positive cells (CSIV-TRE-RfA-CMV-KT) were sorted using FACSAria II (BD bioscience). Then positive selections with PhoSL lectin were sorted and the stable cell lines were used in subsequent studies.

2.5. Flow cytometry analysis

Cells were detached by brief exposure to 0.25% trypsin containing 1 mM EDTA and resuspended at a density of 5×10^6 cells/mL. After washing with ice-cold PBS, the cells were treated with anti-EGFR antibody (1:500), anti-integrin β1 antibody (1:1000), and biotinylated PhoSL (1:1000) for 1 h at 4 °C, respectively. Subsequently, cells were incubated with goat anti-mouse IgG Alexa Fluor 647 (1:1000) or streptavidin-conjugate Alexa Fluor 647 (1:1000) for 1 h at 4 °C in dark. Then, the cells were washed and resuspended in 1 mL MACS buffer (PBS containing 0.1% BSA, 1 mM EDTA, and 0.005% NaN_3). Fluorescence data were collected using a FACS Calibur flow cytometer (BD Biosciences).

Table 1
Primer sequences for RT-PCR.

Target gene	Primer sequences (5′-3′)	
	Forward sequences	Reverse sequences
EGFR	GACAGCTATGAGATGGAGGAAGA	ATCCGAAGGAGGAGTATGTGTGA
EpCAM	GCTTTATGATCCTGACTGCG	CAGCCTTCTCATACTTTGCC
CXCR4	GAAGCTGTTGGCTGAAAAGG	TGGAGTGTGACAGCTTGGAG
c-Met	CAATGTGAGATGTCTCCAGC	CCTTGTAGATTGCAGGCAGA
CD133	*CAGAGTACAACGCCAAACCA*	*AAATCACGATGAGGGTCAGC*
ALDH1A1	GCACGCC AGACTTACCTGTC	CCTCCTCAGTTGCA GGATTAAAG
CD44	TGAGCATCGGATTTGAGAC	CATACTGGGAGGTGTTGGA
CD24	GGCACTGCTCCTACCCACGCAG	GCCACATTGGAATTCCAGACGCC
GAPDH	CGGAGTCAACGGATTTGGTCGTA	AGCCTTCTCCATGGTGGTGAAGAC

2.6. Western blotting

Western blot analysis was performed according to a procedure established in our previous study [29]. Briefly, the cells were washed twice with cold PBS and then lysed with Tris-buffered saline (TBS) containing 1% Triton X-100, protease inhibitors, and phosphatase inhibitors (Nacalai Tesque, Japan). The resultant mixture was gently blended in a rotor shaker for 1 h at 4 °C and the supernatant was obtained by centrifugation at 15,000 rpm for 15 min at 4 °C. The cell lysates were separated on 7.5% SDS–PAGE gel under reducing conditions, and the proteins were transferred to polyvinylidene difluoride (PVDF) membranes (Millipore). Immunoreactive bands were performed to analyze the samples by the Immobilon Western Chemiluminescent HRP Substrate (MilliporeSigma).

2.7. Transwell cell migration assay

The effect of FUT8 on cancer cell migration was determined using a 24-well format (8-μm pores; Corning). The bottom of the devices was coated with 10 μg/mL fibronectin overnight at 4 °C and then blocked with 1% BSA in PBS at 37 °C for 1 h. Cells (1×10^5) in 400 μL of serum-free medium were seeded into the upper chamber. The lower chamber of a 24-well plate contained 500 μL of 10% FBS culture medium. Following incubation times as indicated, cells across pores were fixed with 4% paraformaldehyde and stained with crystal violet solution for 30 min. For each chamber, three fields were randomly chosen and cells were counted.

2.8. Wound-healing assay

Briefly, 1×10^6 human pancreatic cancer cells were seeded into 6-well plates that had been pre-coated with 10 μg/mL fibronectin overnight at 4 °C. A wound was scratched in the confluent cell layer using a 200 μL pipette tip after 24 h of incubation, and floating cells were gently removed using PBS. A phase-contrast microscope (Olympus, Japan) was used to record the wound areas at 0 and 24 h. The migration capability was evaluated by measuring the migration distance.

2.9. Cell growth and colony formation analysis

The cell growth rates were measured using an MTT (#341–01823, Dojindo) assay. MIA PaCa-2 (3×10^3 cells/well) and PANC-1 (5×10^3 cells/well) cells were grown in a 96-well plate at 37 °C in DMEM containing 10% FBS. Every other day until day 3, the absorbance values of each well were measured at 490 nm using a microplate reader (Infinite M1000, TECAN, Japan).

For a colony-formation assay, the different cell lines (1×10^3 cells) were seeded onto 6-well plates in triplicate per cell line, and were then incubated in DMEM containing 10% FBS at 37 °C. The medium was changed twice weekly. After 2 weeks, the cells were fixed with 4% formaldehyde for 20 min and then stained with 0.25% crystal violet for 30 min. Representative photographs were taken and the colony (containing more than 50 cells) numbers were counted.

2.10. Xenograft assay

The animal experiments in this study were carried out according to guidelines recommended by the Institutional Animal Care and Use Committee and approved by the Tohoku Medical and Pharmaceutical University Research Ethics Board. Briefly, four-week-old female BALB/c-nu mice were purchased from Charles River Laboratories, Japan. After 1 week of adaptive rearing, wild type and FUT8-KO MIA PaCa-2 cells (3×10^6) in 100 μL PBS were subcutaneously injected into the left and right flanks, respectively ($n = 6$). Tumor sizes were measured by caliper every 5 days and tumor volumes were calculated using the formula $V = 1/2(\text{length} \times \text{width}^2)$. The mice were euthanized at 30 days after injection, and the tumors were photographed and measured.

2.11. Spheroid formation assay

A spheroid culture was conducted by growing cancer cell suspensions in agarose-coated 96-well plates. Briefly, 50 μL of 1.5% (*w/v* in PBS) agarose was added to each well of the 96-well microplates. Pancreatic cancer cells (1×10^4) in 200 μL DMEM medium were then seeded on the pre-coated plates with incubation at 37 °C under 5% CO_2 for 6 days. Half of the supernatant was replaced with fresh medium every 2 days. Spheroid formations were observed and photographed using a phase-contrast microscope (Olympus, Japan). Following culture at indicating times, the spheres were transferred to new plates and the robustness was checked via gentle pipetting.

2.12. Cytotoxicity assay

MTT assays were performed to evaluate cell viability. The same numbers of cells (5×10^3 cells per well) were seeded onto 96-well plates and exposed to gemcitabine at various concentrations (0, 1, 3, 10, 30 and 100 nM) in the normal culture media. After the MIA PaCa-2 and PANC-1 cells were cultured for 3 and 4 days, respectively, 10 μL of MTT solution (5 mg/mL) was added to each well followed by incubation at 37 °C for 4 h. And then 100 μL of DMSO was added into each well, and cell viability was evaluated by reading the plates at an absorbance of 490 nm using a microplate reader.

2.13. Statistical analysis

Prism 5.0 software (GraphPad Software, CA, USA) was used to conduct statistical analysis. All data are presented as the mean ± S.E.M. Statistical significance was calculated via a two-tailed unpaired Student's *t*-test, and the significance was defined as $P < 0.05$ (*P < 0.05; **$P < 0.01$; ***$P < 0.001$; ns: no significance).

3. Results

3.1. Establishment of FUT8 knockout (FUT8-KO) cells

To understand molecular mechanisms of FUT8 on pancreatic cancer cells, we established FUT8-KO of MIA PaCa-2 and PANC-1 cells using the CRISPR/Cas9 system. To verify the FUT8-KO cells, the expression levels of core fucosylation were examined via flow cytometric analysis using PhoSL (Fig. 1A), and lectin blotting with AAL (Fig. 1B). Both lectins preferentially recognized the core fucosylated N-glycans. Compared with wild-type (WT) cells, the reactive abilities with AAL or PhoSL were almost abolished in the FUT8-KO cells, which indicated a silencing of the FUT8 gene. Furthermore, the genomic sequence analysis for target regions showed that a 265-base or 19-base deletion was found in MIA PaCa-2 and PANC-1 KO cells, respectively (supplementary data). What is more, the reactive abilities to AAL were rescued when re-expressing FUT8 in both MIA PaCa-2 and PANC-1 KO cells (Fig. 1B). In addition, we noticed that the FUT8-KO cells, especially for MIA PaCa-2, appeared to be readily aggregated, compared with the WT cells (Fig. 1C). These results suggested that FUT8 has a potential role in regulating the morphological changes of pancreatic cancer cells.

3.2. FUT8-KO suppressed tumor cell migration in vitro

Compared with the WT of MIA PaCa-2 cells, the FUT8-KO significantly suppressed the cell migration, which were demonstrated in the transwell assay (Fig. 2A) and wound-healing assay (Fig. 2C). Consistently, FUT8-KO also significantly decreased cell migration in the transwell assay in PANC-1 cells (Fig. 2B), although this effect was not observed in the wound-healing assay (Fig. 2D). To further confirm that the effects were indeed caused by the absence of FUT8, we restored

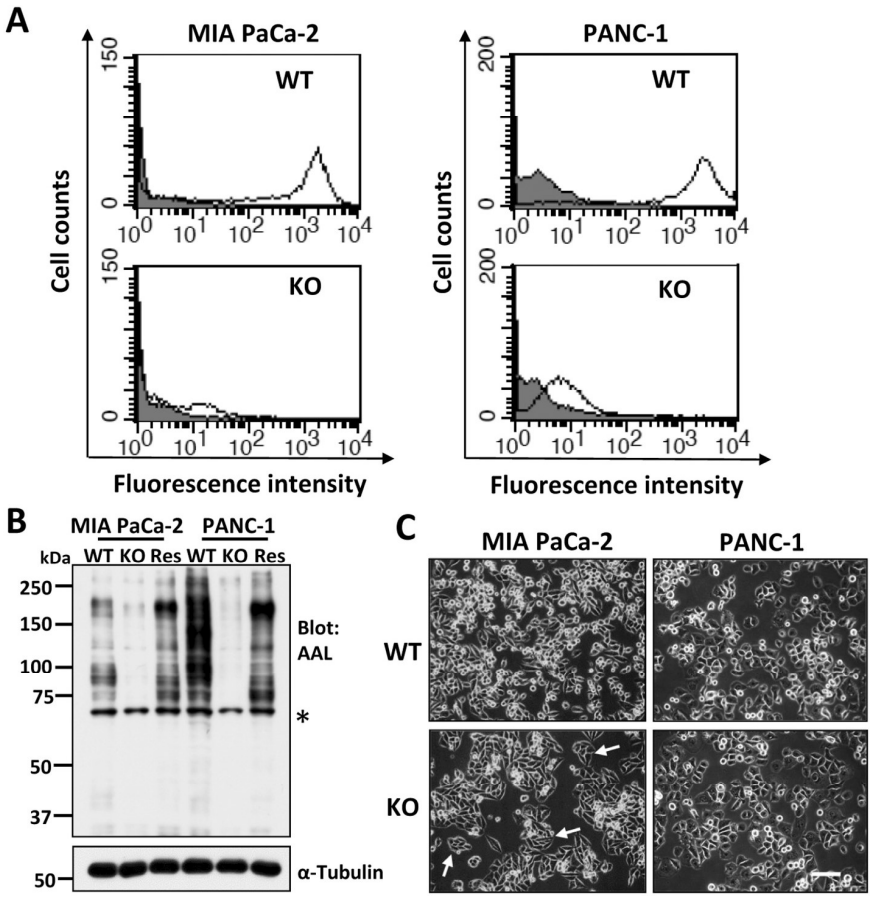

Fig. 1. Established FUT8 deficient cells. Establishment of FUT8-KO MIA PaCa-2 and PANC-1 cells. (A) The expression levels of core fucosylation on the cell surface were analyzed by flow cytometry using PhoSL lectin. (B) Equal amounts of cell lysates were detected by AAL lectin blot, and α-Tubulin was used as a loading control. Asterisks indicate the nonspecific bands. (C) Representative cell morphology images were taken using a phase-contrast microscope. Scale bar: 50 μm. WT, wild-type; KO, FUT8 knockout; Res, restoration with FUT8 gene in FUT8-KO cells.

FUT8 expression in both KO cells (Res). As expected, the cell migration was greatly improved in the Res cells, by comparison with the KO cells (Fig. 2A, B). Apparently, in both assays, PANC-1 cells moved much faster than MIA PaCa-2 cells, which may suggest that PANC-1 cells have a higher metastatic potential than MIA PaCa-2 cells. These results indicated that the silencing of FUT8 resulted in decreased cell migration in PDAC.

3.3. Deficiency of FUT8 inhibited cell proliferation and colony formation

Although an aberrant expression of FUT8 has been identified in different kinds of cancers, its functional contribution to cancers has been inconclusive. The expression of FUT8 was decreased in gastric cancer, and upregulation of FUT8 suppressed the proliferation of gastric cancer cells [35]. By contrast, the FUT8 expression was enhanced in hepatitis B virus-related hepatocellular carcinoma, and the knockdown of FUT8 inhibited the proliferation of tumors [36]. The efficiency of DEN-induced hepatoma was dramatically suppressed in FUT8-KO mice [37]. To investigate the functional roles of FUT8 in PDAC, we conducted MTT and colony formation. The FUT8-KO significantly inhibited cell proliferation in both cells. The restoration with FUT8 gene in the KO cells enhanced cell proliferation (Fig. 3A, B). The colony sizes and numbers were significantly decreased in FUT8-KO cells compared with each of WT cells (Fig. 3C, D). These results supported the notion that FUT8 expression regulates cell proliferation and survival.

3.4. Lack of FUT8 suppressed EGFR expression

EGFR is known to play an important role in tumor cell growth and malignancy [38]. EGFR-mediated cellular signaling is crucial for several cancer cell lines such as lung [39] and gastric cancers [40]. In fact, a deficiency of core fucosylation has down-regulated EGFR-mediated cell signaling and decreased the cell proliferation of non-small cell lung cancer [41] and fibroblasts [42]. One proposal for an underlying mechanism is that a lack of core fucosylation on EGFR could result in a conformation change that decreases EGF ligand binding, but not EGFR expression. This phenomenon has been observed in HepG2 cells [37,43]. In the present study, we found that FUT8-KO significantly suppressed the expression of EGFR in MIA PaCa-2 cells. These tendencies were also observed in PANC-1 cells (Fig. 4A, B). The RT-PCR results were shown that there was no significant difference in the mRNA expression levels between WT and KO cells, indicating that deletion of FUT8 does not affect FUT8 expression at transcriptional level (Fig. 4C). To further confirm effects of FUT8-KO on EGFR expression, we checked protein stability using cycloheximide (CHX), an inhibitor of protein synthesis. The expression level of EGFR was significantly decreased in FUT8-KO MIA PaCa-2 cells treated with CHX compared to the untreated cells, but this decrease was not observed in the WT cells (Fig. 4D), suggesting that FUT8 may regulate protein stability. As a control, we also examined the expression of integrin β1, which is involved in mediating many functional effects such as cell adhesion, migration and intracellular signaling [44]. FUT8-KO did not affect its expression on the cell surface (Fig. 4E). Curiously, the expression levels of β1 in PANC-1 cells were significantly higher than in MIA PaCa-2 cells, which could explain why the migratory abilities of PANC-1 cells were much higher than that in MIA PaCa-2 cells, as shown in Fig. 2. Taken together, these results suggest core fucosylation of EGFR regulates both its ligand binding as well as its expression in protein levels.

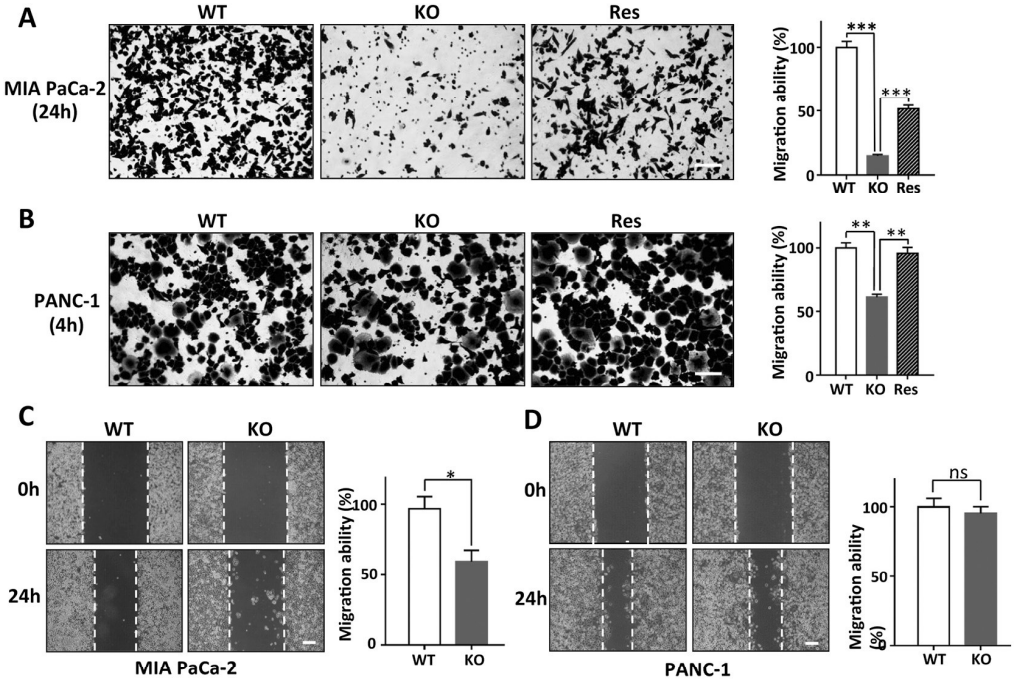

Fig. 2. Effects of FUT8-KO on cell migration. Impacts of FUT8-KO on cell migration were measured by transwell and wound-healing assays. The migratory abilities were examined by transwell assay in MIA PaCa-2 for 24 h (A) and PANC-1 for 4 h (B). The numbers of migrated cells were counted from three randomly selected areas in each group. The migratory abilities of each WT cells were set as 100. Scale bar: 50 μm. The wound-healing assays were performed in MIA PaCa-2 (C) and PANC-1 (D) cells, and incubated for 24 h after scratching. The data were obtained from three independent experiments. All values are reported as the mean ± S.E.M ($n = 3$). The migratory abilities of each of the WT cells were set as 100. Scale bar: 100 μm. *$P < 0.05$; **$P < 0.01$; ***$P < 0.001$; ns: no significance.

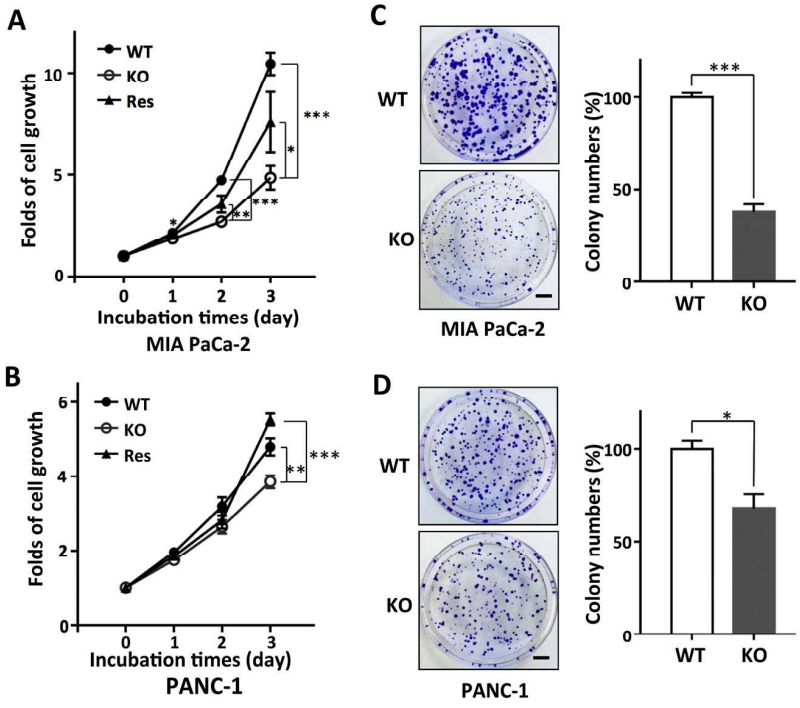

Fig. 3. Effects of FUT8-KO on cell proliferation and colony formation. Cell proliferation was measured using MTT as described MATERIALS AND METHODS. The cell numbers were examined at the indicated points in MIA PaCa-2 (A) and PANC-1 (B) cells, and each of the cell numbers seeded into culture wells at 0 day were set as 1. The colony-forming abilities were assayed in MIA PaCa-2 (C) and PANC-1 (D) cells. The data were obtained from three independent experiments. All values are reported as the mean ± S.E.M (n = 3). The abilities of each of the WT cells were set as 100. Scale bar: 30 mm. *P < 0.05; **P < 0.01; ***$P < 0.001$.

3.5. Inhibition of 2FF on tumorigenesis in vitro

A fluorinated analog of fucose, 2FF, functions as a metabolic fucosylation inhibitor, which is taken up by cells and converted to GDP-2FF through endogenous salvage pathways [45,46]. First, we conducted lectin blotting with AAL to ensure the efficiency of 2FF. In MIA PaCa-2 cells, reactivity with AAL was effectively inhibited by a 2FF concentration at 30 μM, whiles the inhibitory effect was observed at 500 μM in

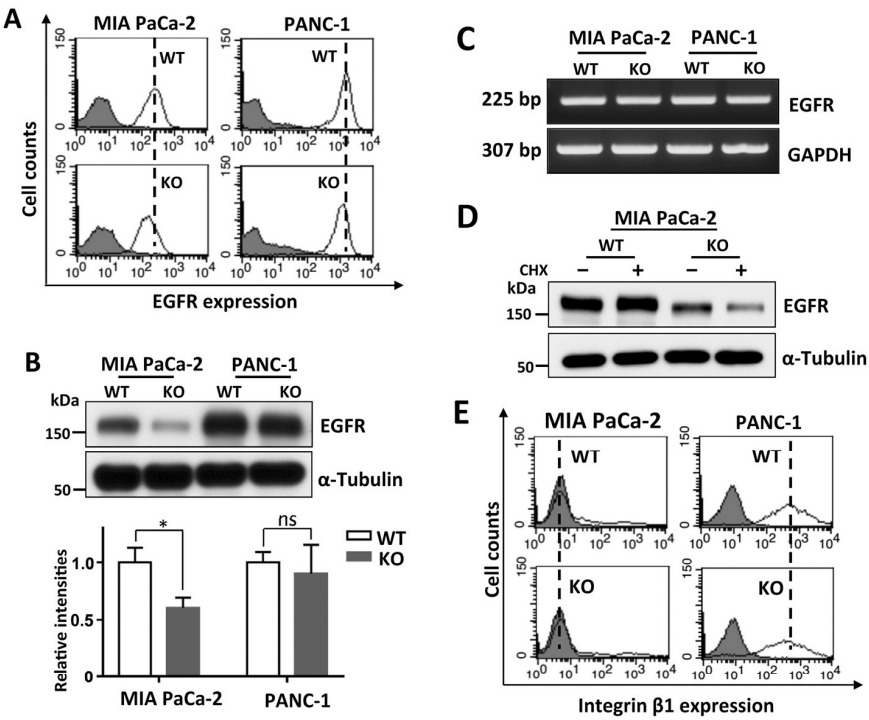

Fig. 4. Effects of FUT8 deficiency on EGFR and integrin β1 expression. (A) The expression levels of EGFR on the cell surface were analyzed by flow cytometry assay using an anti-EGFR antibody. (B) The same amounts of cell lysates were probed with EGFR by immunoblotting, and α-Tubulin was used as a loading control. The data were obtained from three independent experiments. All values are reported as the mean ± S.E.M ($n = 3$). *$P < 0.05$; ns: no significance. (C) The mRNA expression levels of EGFR were detected by RT-PCR. GAPDH was used as a control. (D) MIA PaCa-2 cells were treated with cycloheximide (CHX) at 50 μg/mL for 24 h, and then EGFR levels in cell lysates were monitored by immunoblotting. (E) The expression levels of integrin β1 were analyzed by flow cytometry analysis.

PANC-1 cells (Fig. 5A), suggesting that 2FF selectively blocks cellular fucosylation in different cells. Thus, we treated MIA PaCa-2 and PANC-1 cells with 2FF at 100 μM and 500 μM for 3 days, respectively. The migration capabilities of MIA PaCa-2 cells, but not that of PANC-1 cells, were significantly suppressed by the treatment with 2FF, compared with the WT cells (Fig. 5B). The MTT assay showed that 2FF treatment significantly inhibited cell proliferation in both cells (Fig. 5C).

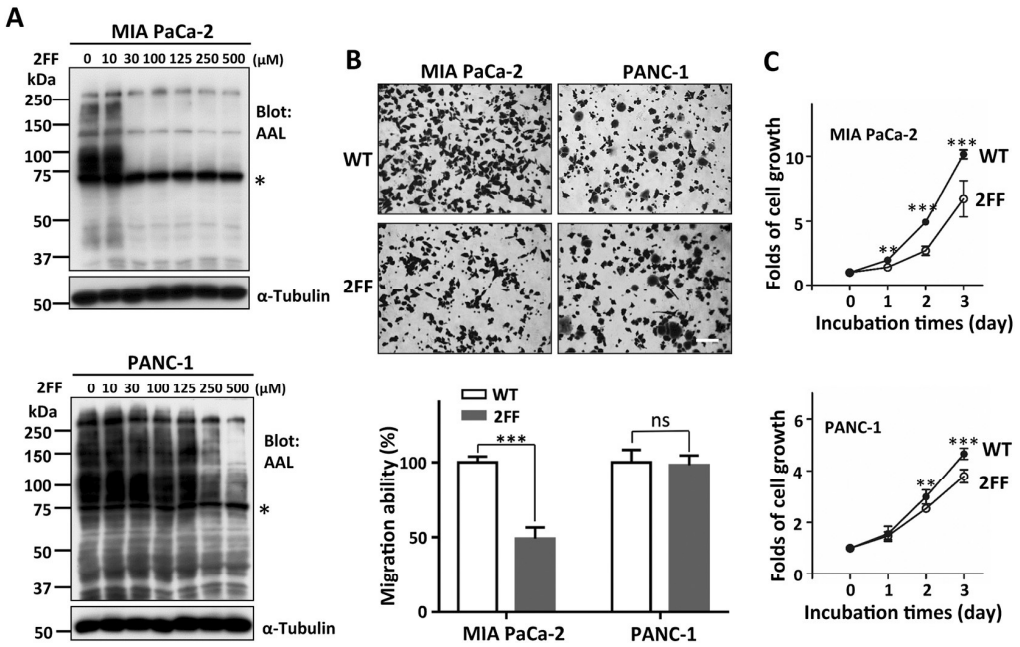

Fig. 5. Effects of 2FF on core fucosylation and cell migration as well as proliferation. (A) The cells were cultured with 2FF, an inhibitor of fucosylation, for 3 days at the indicated concentrations. Equal amounts of cell lysates were detected by AAL lectin blot, and α-Tubulin was used as a loading control. Asterisks indicate the nonspecific bands. (B) Cells were pre-treated with or without 2FF for 3 days and seeded (1×10^5) into the upper chamber of a transwell. After incubation for 12 and 4 h for MIA PaCa-2 and PANC-1 cells, respectively, cells across pores were stained with crystal violet and quantitated. The data were obtained from three independent experiments. All values are reported as the mean ± S.E.M (n = 3). Scale bar: 50 μm. (C) The cells were cultured with 2FF, and cell proliferation was assessed by MTT assay. The data were obtained from three independent experiments. All values are reported as the mean ± S.E.M (n = 3). **P < 0.01; ***P < 0.001; ns: no significance. (For interpretation of the references to colour in this figure legend, the reader is referred to the web version of this article.)

3.6. Inhibitory effect of FUT8-KO on tumor growth in vivo

To further evaluate the effect of FUT8 on tumor growth, we built xenograft models in nude mice using MIA PaCa-2 cells, and found that FUT8-KO suppressed subcutaneous xenograft growth compared with that in the WT group (Fig. 6A). The tumor volume and weight of the FUT8-KO group were lower than that in the WT group (Fig. 6B, C). The curves for tumor growth in the FUT8-KO group showed a significantly lower rate than those in the WT group (Fig. 6D). These findings suggest that FUT8 deficiency inhibits tumor growth in PDAC in vivo.

3.7. Deficiency of FUT8 downregulated the stemness of pancreatic cancer cells

To understand whether FUT8 expression affects CSC-like characteristics, the expression levels of CSC-related biomarkers were examined using RT-PCR. Interestingly, FUT8-KO suppressed the expression levels of biomarkers such as EpCAM, CXCR4, c-Met, and CD133 (Fig. 7A). We further compared the abilities to form spheroid bodies. The FUT8-KO cells showed a large spheroid body with a loose sphere structure at each of the different incubated times, by comparison with the WT cells in both MIA PaCa-2 and PANC-1 cells (Fig. 7B, C). These phenomena were clearly observed after agitation. The spheroid bodies were more easily disrupted in FUT8-KO cells compared with those of the WT cells or those KO cells restored with FUT8 gene.

3.8. Deletion of FUT8 increased drug sensitivity

Chemoresistance is also one of the characteristics of CSCs. Gemcitabine is regarded as a standard treatment for advanced pancreatic cancer [47,48]. As shown in Fig. 8A, treatment with low concentrations of gemcitabine significantly suppressed cell viability in FUT8-KO MIA PaCa-2 cells, compared with that in WT cells. A similar trend was also observed in PANC-1 cells (Fig. 8B). Again, these results suggest that the expression of FUT8 may greatly contribute to cancer stemness.

4. Discussion

In the present study, we found that either a deficiency of FUT8 or a blockage of fucosylation using 2FF in pancreatic cancer cells could suppress cell migration and proliferation, and the subsequent tumor growth, in a subcutaneous xenograft model. Furthermore, FUT8-KO downregulated cancer stemness features, which were evaluated using the expression levels of CSC biomarkers, the capabilities of spheroid formation, and chemoresistance. These results clearly suggest that regulating core fucosylation may provide a potential therapeutic direction for developing a novel treatment for pancreatic carcinoma.

CSCs are a very small subpopulation of cells in the tumor population. These cells have the capacity to self-renew and to generate differentiated cancer progenies [49,50]. CSCs not only drive tumor initiation and growth but also mediate tumor metastasis, relapse and chemo/radioresistance [51–53]. Pancreatic carcinoma tumors have shown relatively higher rates of malignancy and metastasis [54]. Fucosylated glycan has pivotal roles in tumor development to malignancy and metastasis. Terao et al. reported that cancer stem cell-like pancreatic cancer phenotypes exhibit much higher levels of fucosylated glycans compared with non-CSC types of cells [55]. An up-regulation of both fucosyltransferases FUT3 and FUT6 increased sLe^x expression, which enhanced the sphere formation and cell invasion in oral CSCs [56]. Here, we found that FUT8-KO significantly decreased the expression levels of CSC biomarkers such as EpCAM, CXCR4, c-Met and CD133. A similar trend has been observed in other CSC biomarkers such as ALDH1A1, CD44 and CD24 (Fig. 7A). In addition, spheroid formation showed that the wild-type cells form structures that are more compact and rigid compared with the corresponding FUT8-KO cells (Fig. 7B, C). Therefore, it would be plausible to speculate that the decreased tumorigenesis of PDAC by FUT8-KO is attributable to its functions in CSCs. In a consistent manner, FUT8-KO greatly increased the chemosensitivity for gemcitabine. Taken together, these data clearly suggest the expression of FUT8 contributes to the stemness features of pancreatic cancer cells. This phenomenon may not be restricted to PDAC, but could also apply to

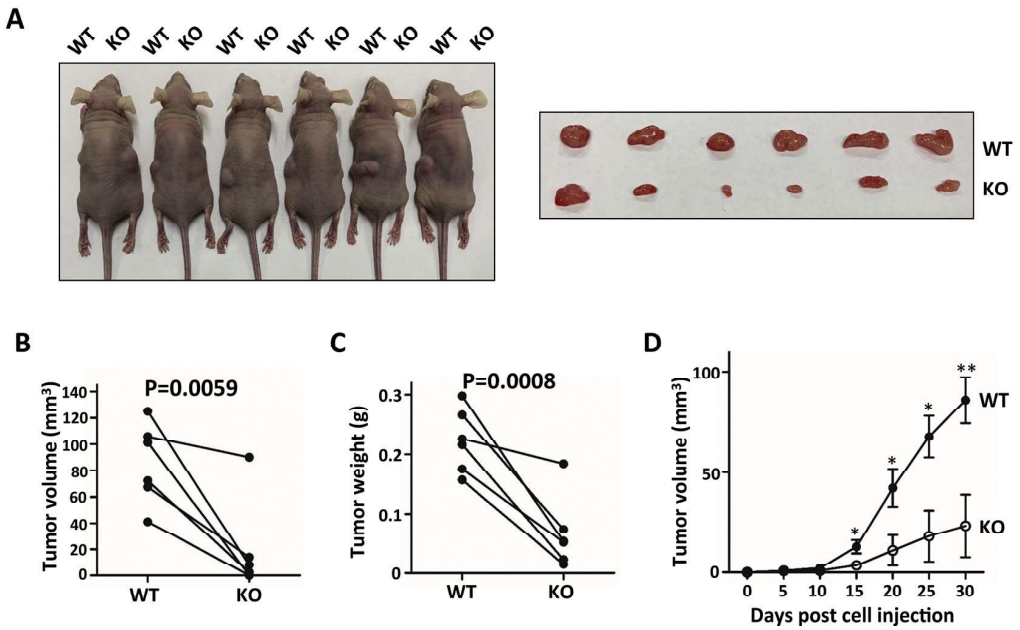

Fig. 6. FUT8-KO suppressed tumor growth in vivo. Female BALB/c-nu mice were inoculated with MIA PaCa-2 WT and FUT8-KO cells (3×10^6) on the left and right flanks, respectively. (A) Images of tumor-bearing nude mice on day 30 after injection were taken after the animals were euthanized (left panel) and each corresponding pair of dissected tumor tissues (right panel). (B) Tumor volume (V) was monitored by measuring the length and width with a vernier caliper and calculated using the formula $V = 1/2(\text{length} \times \text{width}^2)$. (C) Tumor weight in the two groups was measured using electronic scales. *D*, Tumor growth curves for tumor volume were measured every 5 days. *P < 0.05; **P < 0.01.

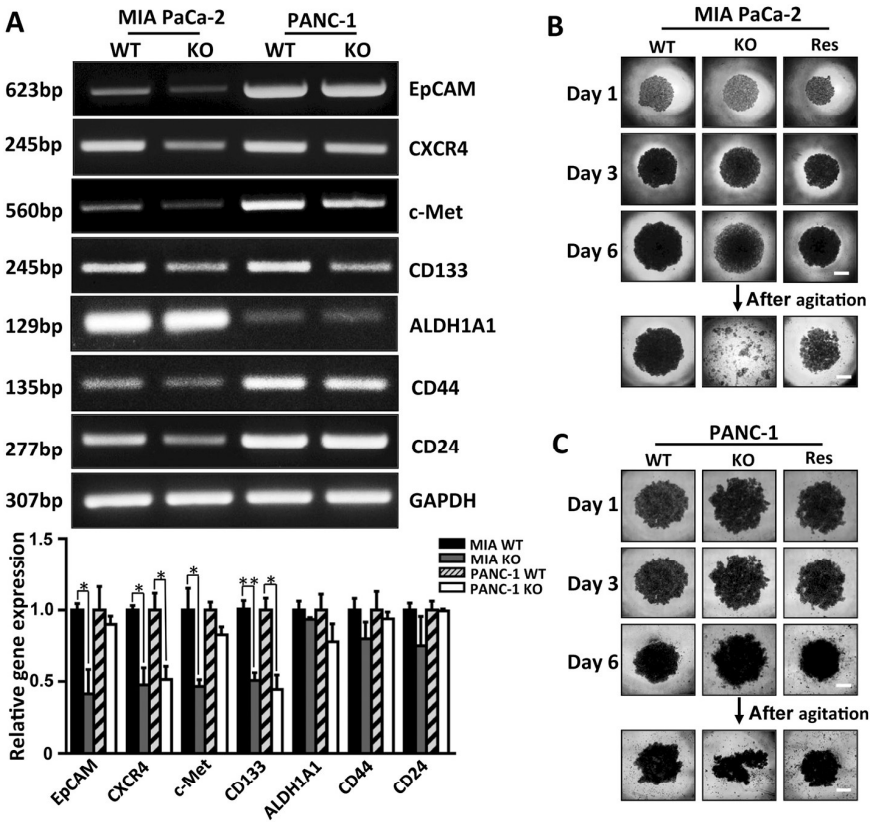

Fig. 7. Effects of FUT8-KO on stemness features in MIA PaCa-2 and PANC-1 cells. (A) The mRNA levels of some representative CSC biomarkers were examined by RT-PCR. GAPDH was used as a loading control. The data were obtained from three independent experiments. All values are reported as the mean ± S.E.M (n = 3). *P < 0.05; **P < 0.01. The images of spheroids for MIA PaCa-2 cells (B) and PANC-1 cells (C) were photographed by phase-contrast microscopy at day 1, 3 and 6 of culture. The stability or rigidity of the sphere was checked after agitating using yellow tips and then photographed. Scale bar: 250 μm. (For interpretation of the references to colour in this figure legend, the reader is referred to the web version of this article.)

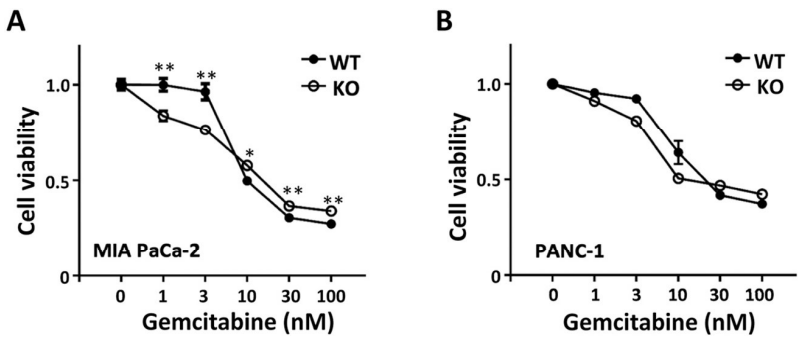

Fig. 8. Loss of FUT8 chemosensitized the cells to gemcitabine, an antipancreatic cancer drug. The WT and the FUT8-KO of MIA PaCa-2 cells (A) or PANC-1 cells (B) were cultured in the presence of gemcitabine at indicated concentrations for 3 and 4 days, respectively, and then cell viabilities were examined using MTT assay. The inhibitory ratio for cell viability was normalized to that of each group without gemcitabine as 1. Data are reported as the mean ± S.E.M (n = 3). *P < 0.05; **P < 0.01.

other cancers. In fact, increased core fucosylation has been associated with distal metastasis, tumor recurrence and poorer survival of patients with lung and breast cancers [26,57], and upregulated FUT8 expression by activation of Wnt/β-catenin signaling pathway could promote EMT and stemness in breast cancer cells [58]. Thus, alterations in core fucosylation could generally have a big impact on the development and progression of other types of cancers.

Notably, the effects of core fucosylation on biological functions may vary among different cell types. FUT8-KO suppressed Smad-2 activation through the TGF-β activation pathway in lung tissue and in fibroblasts [27], but promoted Smad-2 activation via the activin activation pathway in PC12 cells [25]. In the present study, the inhibitory effects on spheroid formation and cell migration by FUT8-KO in PANC-1 cells were smaller than those in MIA PaCa-2 cells (Figs. 2, 7B and C), although a similar tendency was observed. In fact, tumors in different locations may display different clinical parameters and malignant potential. PANC-1 and MIA PaCa-2 cell lines are known to originate from pancreatic head and body/tail cancers, respectively [31]. In the present study, PANC-1 cells exhibited much higher expression levels of metastasis-associated molecules such as EphA2 and c-Met [59,60], as well as EpCAM and CD44 compared with the levels in MIA PaCa-2 cells. In addition, PANC-1 cells expressed higher levels of adhesive molecule integrin β1 (Fig. 4E). Therefore, we would speculate that the regulatory functions of FUT8 are dependent on cell types, wherein the expression levels of target glycoproteins for FUT8 are different. Of course, the underlying mechanism for the contribution that FUT8 makes to cancer stemness features will require further study.

Core fucosylation is known to regulate biological functions via the influence of protein expression. We previously reported that FUT8-KO suppressed VEGFR-2 expression, which contributed to the cause of emphysema-like changes in FUT8-KO mice [61]. In similar manner, blocking core fucosylation by 2FF reduced cell-surface PD-1 expression and the binding of PD-1 to its ligand PDL-1 [62] due to an increase in degradation of PD-1 by proteasomes [63]. Here, FUT8-KO suppressed

EGFR protein expression levels (Fig. 4), which is contradictory to our previous observation that FUT8-KO did not affect EGFR expression levels in mouse embryonic fibroblasts [42]. Considering the association of EGFR with other receptors such as integrins that may affect endocytosis [64], we speculated that those discrepancies could have been due to cell types, in which expression levels of EGFR-associated proteins are different.

In conclusion, this study demonstrated some important functions of FUT8 in PDAC progression, is the first to show that FUT8 is involved in the regulation of cancer stemness features, which means that FUT8 is a potential novel target for PDAC treatment.

Author contributions

C. Liang, T. Fukuda, T. Isaji, Y. Wang and J. Gu designed the research; C. Liang performed all experiments; C. Liang, C. Duan and W. Song performed flow cytometric analysis; T. Isaji, C. Duan and W. Song and T. Fukuda assisted with experiments; T. Fukuda, T. Isaji, Y. Wang and J. Gu analyzed and interpreted the data; C. Liang, T. Fukuda and J. Gu wrote and revised the manuscript; and all authors approved the final version of the manuscript.

Funding sources

This work was supported in part by a Grant-in-Aid for Scientific Research (19H03184 and 18K06914 to J.G.) from the Japan Society for the Promotion of Science, by a grant from National Natural Science Foundation of China (No. 31670807), and by a Grant-in-Aid for Scientific Research on Innovative Areas (20H04909 to J.G.) from the Ministry of Education, Culture, Sports, Science, and Technology of Japan.

CRediT authorship contribution statement

Caixia Liang: Conceptualization, Methodology, Investigation, Data curation, Software, Validation, Writing-original draft preparation. **Tomohiko Fukuda:** Conceptualization, Methodology, Visualization, Data curation, Supervision, Writing-reviewing and editing. **Tomoya Isaji:** Methodology, Visualization, Data curation, Software, Validation. **Chengwei Duan:** Methodology, Investigation. **Wanli Song:** Methodology, Investigation. **Yuqin Wang:** Conceptualization, Methodology, Validation, Funding acquisition, Writing-reviewing and editing. **Jianguo Gu:** Conceptualization, Validation, Supervision, Funding acquisition, Writing-reviewing and editing, Project administration.

Declaration of Competing Interest

The authors have no conflict of interest to declare.

Appendix A. Supplementary data

Supplementary data to this article can be found online at https://doi.org/10.1016/j.bbagen.2021.129870.

References

[1] F. Bray, J. Ferlay, I. Soerjomataram, R.L. Siegel, L.A. Torre, A. Jemal, Global cancer statistics 2018: GLOBOCAN estimates of incidence and mortality worldwide for 36 cancers in 185 countries, CA Cancer J. Clin. 68 (2018) 394–424.
[2] M. Hidalgo, Pancreatic cancer, N. Engl. J. Med. 362 (2010) 1605–1617.
[3] R.L. Siegel, K.D. Miller, A. Jemal, Cancer statistics, 2020, CA Cancer J. Clin. 70 (2020) 7–30.
[4] S. Zeng, M. Pöttler, B. Lan, R. Grützmann, C. Pilarsky, H. Yang, Chemoresistance in pancreatic cancer, Int. J. Mol. Sci. (2019) 20.
[5] L. Wei, J.Y. Wen, J. Chen, X.K. Ma, D.H. Wu, Z.H. Chen, J.L. Huang, Oncogenic ADAM28 induces gemcitabine resistance and predicts a poor prognosis in pancreatic cancer, World J. Gastroenterol. 25 (2019) 5590–5603.
[6] J.N. Contessa, M.S. Bhojani, H.H. Freeze, A. Rehemtulla, T.S. Lawrence, Inhibition of N-linked glycosylation disrupts receptor tyrosine kinase signaling in tumor cells, Cancer Res. 68 (2008) 3803–3809.
[7] S.S. Pinho, C.A. Reis, Glycosylation in cancer: mechanisms and clinical implications, Nat. Rev. Cancer 15 (2015) 540–555.
[8] J. Munkley, The glycosylation landscape of pancreatic cancer, Oncol. Lett. 17 (2019) 2569–2575.
[9] H.M. Park, M.P. Hwang, Y.W. Kim, K.J. Kim, J.M. Jin, Y.H. Kim, Y.H. Yang, K. H. Lee, Y.G. Kim, Mass spectrometry-based N-linked glycomic profiling as a means for tracking pancreatic cancer metastasis, Carbohydr. Res. 413 (2015) 5–11.
[10] M. Perez-Garay, B. Arteta, E. Llop, L. Cobler, L. Pages, R. Ortiz, M.J. Ferri, C. de Bolos, J. Figueras, R. de Llorens, F. Vidal-Vanaclocha, R. Peracaula, alpha2,3-Sialyltransferase ST3Gal IV promotes migration and metastasis in pancreatic adenocarcinoma cells and tends to be highly expressed in pancreatic adenocarcinoma tissues, Int. J. Biochem. Cell Biol. 45 (2013) 1748–1757.
[11] C.C. Hsieh, Y.M. Shyr, W.Y. Liao, T.H. Chen, S.E. Wang, P.C. Lu, P.Y. Lin, Y. B. Chen, W.Y. Mao, H.Y. Han, M. Hsiao, W.B. Yang, W.S. Li, Y.P. Sher, C.N. Shen, Elevation of beta-galactoside alpha2,6-sialyltransferase 1 in a fructoseresponsive manner promotes pancreatic cancer metastasis, Oncotarget. 8 (2017) 7691–7709.
[12] G. Luo, M. Guo, K. Jin, Z. Liu, C. Liu, H. Cheng, Y. Lu, J. Long, L. Liu, J. Xu, Q. Ni, X. Yu, Optimize CA19-9 in detecting pancreatic cancer by Lewis and Secretor genotyping, Pancreatology. 16 (2016) 1057–1062.
[13] E. Miyoshi, Y. Kamada, Application of glycoscience to the early detection of pancreatic cancer, Cancer Sci. 107 (2016) 1357–1362.
[14] E. Miyoshi, S. Shinzaki, K. Moriwaki, H. Matsumoto, Identification of fucosylated haptoglobin as a novel tumor marker for pancreatic cancer and its possible application for a clinical diagnostic test, Methods Enzymol. 478 (2010) 153–164.
[15] K. Morishita, N. Ito, S. Koda, M. Maeda, K. Nakayama, K. Yoshida, S. Takamatsu, M. Yamada, H. Eguchi, Y. Kamada, E. Miyoshi, Haptoglobin phenotype is a critical factor in the use of fucosylated haptoglobin for pancreatic cancer diagnosis, Clin. Chim. Acta 487 (2018) 84–89.
[16] N. Okuyama, Y. Ide, M. Nakano, T. Nakagawa, K. Yamanaka, K. Moriwaki, K. Murata, H. Ohigashi, S. Yokoyama, H. Eguchi, O. Ishikawa, T. Ito, M. Kato, A. Kasahara, S. Kawano, J. Gu, N. Taniguchi, E. Miyoshi, Fucosylated haptoglobin is a novel marker for pancreatic cancer: a detailed analysis of the oligosaccharide structure and a possible mechanism for fucosylation, Int. J. Cancer 118 (2006) 2803–2808.
[17] K. Tada, M. Ohta, S. Hidano, K. Watanabe, T. Hirashita, Y. Oshima, A. Fujnaga, H. Nakanuma, T. Masuda, Y. Endo, Y. Takeuchi, Y. Iwashita, T. Kobayashi, M. Inomata, Fucosyltransferase 8 plays a crucial role in the invasion and metastasis of pancreatic ductal adenocarcinoma, Surg. Today 50 (2020) 767–777.
[18] K. Watanabe, M. Ohta, K. Yada, Y. Komori, Y. Iwashita, K. Kashima, M. Inomata, Fucosylation is associated with the malignant transformation of intraductal papillary mucinous neoplasms: a lectin microarray-based study, Surg. Today 46 (2016) 1217–1223.
[19] Y. Zhang, J. Zhu, H. Yin, J. Marrero, X.-X. Zhang, D.M. Lubman, ESI-LC-MS method for Haptoglobin Fucosylation analysis in hepatocellular carcinoma and liver cirrhosis, J. Proteome Res. 14 (2015) 5388–5395.
[20] H. Nie, X. Liu, Y. Zhang, T. Li, C. Zhan, W. Huo, A. He, Y. Yao, Y. Jin, Y. Qu, X.-L. Sun, Y. Li, Specific N-glycans of hepatocellular carcinoma cell surface and the abnormal increase of Core-α-1, 6-fucosylated Triantennary glycan via N-acetylglucosaminyltransferases-IVa regulation, Sci. Rep. 5 (2015) (16007–16007).
[21] Y.C. Liu, H.Y. Yen, C.Y. Chen, C.H. Chen, P.F. Cheng, Y.H. Juan, C.H. Chen, K. H. Khoo, C.J. Yu, P.C. Yang, T.L. Hsu, C.H. Wong, Sialylation and fucosylation of epidermal growth factor receptor suppress its dimerization and activation in lung cancer cells, Proc. Natl. Acad. Sci. U. S. A. 108 (2011) 11332–11337.
[22] T. Takahashi, Y. Ikeda, E. Miyoshi, Y. Yaginuma, M. Ishikawa, N. Taniguchi, alpha1,6fucosyltransferase is highly and specifically expressed in human ovarian serous adenocarcinomas, Int. J. Cancer 88 (2000) 914–919.
[23] G.R. Wi, B.I. Moon, H.J. Kim, W. Lim, A. Lee, J.W. Lee, H.J. Kim, A lectin-based approach to detecting carcinogenesis in breast tissue, Oncol. Lett. 11 (2016) 3889–3895.
[24] T. Osuga, R. Takimoto, M. Ono, M. Hirakawa, M. Yoshida, Y. Okagawa, N. Uemura, Y. Arihara, Y. Sato, F. Tamura, T. Sato, S. Iyama, K. Miyanishi, K. Takada, T. Hayashi, M. Kobune, J. Kato, Relationship between increased Fucosylation and metastatic potential in colorectal cancer, J. Natl. Cancer Inst. 108 (2016).
[25] W. Gu, T. Fukuda, T. Isaji, H. Hashimoto, Y. Wang, J. Gu, α1,6-Fucosylation regulates neurite formation via the activin/phospho-Smad2 pathway in PC12 cells: the implicated dual effects of Fut8 for TGF-β/activin-mediated signaling, FASEB J. 27 (2013) 3947–3958.
[26] C.F. Tu, M.Y. Wu, Y.C. Lin, R. Kannagi, R.B. Yang, FUT8 promotes breast cancer cell invasiveness by remodeling TGF-β receptor core fucosylation, Breast Cancer Res. 19 (2017) 111.
[27] X. Wang, S. Inoue, J. Gu, E. Miyoshi, K. Noda, W. Li, Y. Mizuno-Horikawa, M. Nakano, M. Asahi, M. Takahashi, N. Uozumi, S. Ihara, S.H. Lee, Y. Ikeda, Y. Yamaguchi, Y. Aze, Y. Tomiyama, J. Fujii, K. Suzuki, A. Kondo, S.D. Shapiro, C. Lopez-Otin, T. Kuwaki, M. Okabe, K. Honke, N. Taniguchi, Dysregulation of TGF-beta1 receptor activation leads to abnormal lung development and emphysema-like phenotype in core fucose-deficient mice, Proc. Natl. Acad. Sci. U. S. A. 102 (2005) 15791–15796.
[28] Y. Zhao, S. Itoh, X. Wang, T. Isaji, E. Miyoshi, Y. Kariya, K. Miyazaki, N. Kawasaki, N. Taniguchi, J. Gu, Deletion of core fucosylation on alpha3beta1 integrin down-regulates its functions, J. Biol. Chem. 281 (2006) 38343–38350.
[29] C. Duan, T. Fukuda, T. Isaji, F. Qi, J. Yang, Y. Wang, S. Takahashi, J. Gu, Deficiency of core fucosylation activates cellular signaling dependent on FLT3 expression in a Ba/F3 cell system, FASEB J. 34 (2020) 3239–3252.
[30] X. Lu, D. Zhang, H. Shoji, C. Duan, G. Zhang, T. Isaji, Y. Wang, T. Fukuda, J. Gu, Deficiency of α1,6-fucosyltransferase promotes neuroinflammation by increasing

the sensitivity of glial cells to inflammatory mediators, Biochimica et biophysica acta, General Subj. 1863 (2019) 598–608.
[31] Q. Ling, X. Xu, S.S. Zheng, H. Kalthoff, The diversity between pancreatic head and body/tail cancers: clinical parameters and in vitro models, Hepatobiliary Pancreat, Dis. Int. 12 (2013) 480–487.
[32] G. Zhang, T. Isaji, Z. Xu, X. Lu, T. Fukuda, J. Gu, N-acetylglucosaminyltransferase-I as a novel regulator of epithelial-mesenchymal transition, FASEB J. 33 (2019) 2823–2835.
[33] F.A. Ran, P.D. Hsu, J. Wright, V. Agarwala, D.A. Scott, F. Zhang, Genome engineering using the CRISPR-Cas9 system, Nat. Protoc. 8 (2013) 2281–2308.
[34] T. Isaji, S. Im, W. Gu, Y. Wang, Q. Hang, J. Lu, T. Fukuda, N. Hashii, D. Takakura, N. Kawasaki, H. Miyoshi, J. Gu, An oncogenic protein Golgi phosphoprotein 3 up-regulates cell migration via sialylation, J. Biol. Chem. 289 (2014) 20694–20705.
[35] Y.P. Zhao, X.Y. Xu, M. Fang, H. Wang, Q. You, C.H. Yi, J. Ji, X. Gu, P.T. Zhou, C. Cheng, C.F. Gao, Decreased core-fucosylation contributes to malignancy in gastric cancer, PLoS One 9 (2014) e94536.
[36] J. Ji, X. Gu, M. Fang, Y. Zhao, C. Yi, A. Wang, C. Gao, Expression of alpha 1,6-fucosyltransferase 8 in hepatitis B virus-related hepatocellular carcinoma influences tumour progression, Dig. Liver Dis. 45 (2013) 414–421.
[37] Y. Wang, T. Fukuda, T. Isaji, J. Lu, S. Im, Q. Hang, W. Gu, S. Hou, K. Ohtsubo, J. Gu, Loss of alpha1,6-fucosyltransferase inhibits chemical-induced hepatocellular carcinoma and tumorigenesis by down-regulating several cell signaling pathways, FASEB J. 29 (2015) 3217–3227.
[38] A. De Luca, A. Carotenuto, A. Rachiglio, M. Gallo, M.R. Maiello, D. Aldinucci, A. Pinto, N. Normanno, The role of the EGFR signaling in tumor microenvironment, J. Cell. Physiol. 214 (2008) 559–567.
[39] A. Leonetti, S. Sharma, R. Minari, P. Perego, E. Giovannetti, M. Tiseo, Resistance mechanisms to osimertinib in EGFR-mutated non-small cell lung cancer, Br. J. Cancer 121 (2019) 725–737.
[40] L. Wang, H. Zhang, J. Zheng, X. Wei, J. Du, H. Lu, Q. Sun, W. Zhou, R. Zhang, Y. Han, Dual silencing of EGFR and HER2 enhances the sensitivity of gastric cancer cells to gefitinib, Mol. Carcinog. 57 (2018) 1008–1016.
[41] F. Li, S. Zhao, Y. Cui, T. Guo, J. Qiang, Q. Xie, W. Yu, W. Guo, W. Deng, C. Gu, T. Wu, α1,6-Fucosyltransferase (FUT8) regulates the cancer-promoting capacity of cancer-associated fibroblasts (CAFs) by modifying EGFR core fucosylation (CF) in non-small cell lung cancer (NSCLC), Am. J. Cancer Res. 10 (2020) 816–837.
[42] X. Wang, J. Gu, H. Ihara, E. Miyoshi, K. Honke, N. Taniguchi, Core fucosylation regulates epidermal growth factor receptor-mediated intracellular signaling, J. Biol. Chem. 281 (2006) 2572–2577.
[43] Y. Zhou, T. Fukuda, Q. Hang, S. Hou, T. Isaji, A. Kameyama, J. Gu, Inhibition of fucosylation by 2-fluorofucose suppresses human liver cancer HepG2 cell proliferation and migration as well as tumor formation, Sci. Rep. 7 (2017) 11563.
[44] D. Barkan, A.F. Chambers, β1-integrin: a potential therapeutic target in the battle against cancer recurrence, Clin. Cancer Res. 17 (2011) 7219–7223.
[45] C.D. Rillahan, A. Antonopoulos, C.T. Lefort, R. Sonon, P. Azadi, K. Ley, A. Dell, S. M. Haslam, J.C. Paulson, Global metabolic inhibitors of sialyl- and fucosyltransferases remodel the glycome, Nat. Chem. Biol. 8 (2012) 661–668.
[46] N.M. Okeley, S.C. Alley, M.E. Anderson, T.E. Boursalian, P.J. Burke, K. M. Emmerton, S.C. Jeffrey, K. Klussman, C.L. Law, D. Sussman, B.E. Toki, L. Westendorf, W. Zeng, X. Zhang, D.R. Benjamin, P.D. Senter, Development of orally active inhibitors of protein and cellular fucosylation, Proc. Natl. Acad. Sci. U. S. A. 110 (2013) 5404–5409.
[47] H.A. Burris 3rd, M.J. Moore, J. Andersen, M.R. Green, M.L. Rothenberg, M. R. Modiano, M.C. Cripps, R.K. Portenoy, A.M. Storniolo, P. Tarassoff, R. Nelson, F. A. Dorr, C.D. Stephens, D.D. Von Hoff, Improvements in survival and clinical benefit with gemcitabine as first-line therapy for patients with advanced pancreas cancer: a randomized trial, J. Clin. Oncol. 15 (1997) 2403–2413.
[48] Y.J. Min, K.R. Joo, N.H. Park, T.K. Yun, Y.W. Nah, C.W. Nam, J.H. Park, Gemcitabine therapy in patients with advanced pancreatic cancer, Korean J. Intern. Med. 17 (2002) 259–262.
[49] A. Kreso, J.E. Dick, Evolution of the cancer stem cell model, Cell Stem Cell 14 (2014) 275–291.
[50] M. Luo, S.G. Clouthier, Y. Deol, S. Liu, S. Nagrath, E. Azizi, M.S. Wicha, Breast cancer stem cells: current advances and clinical implications, Methods Mol. Biol. 1293 (2015) 1–49.
[51] M.Z. Dewan, S. Ahmed, Y. Iwasaki, K. Ohba, M. Toi, N. Yamamoto, Stromal cell-derived factor-1 and CXCR4 receptor interaction in tumor growth and metastasis of breast cancer, Biomed. Pharmacother. 60 (2006) 273–276.
[52] C.P. Tanase, A.I. Neagu, L.G. Necula, C. Mambet, A.M. Enciu, B. Calenic, M. L. Cruceru, R. Albulescu, Cancer stem cells: involvement in pancreatic cancer pathogenesis and perspectives on cancer therapeutics, World J. Gastroenterol. 20 (2014) 10790–10801.
[53] J.E. Visvader, G.J. Lindeman, Cancer stem cells in solid tumours: accumulating evidence and unresolved questions, Nat. Rev. Cancer 8 (2008) 755–768.
[54] M. Amrutkar, I.P. Gladhaug, Pancreatic cancer chemoresistance to gemcitabine, Cancers (Basel). 9 (2017).
[55] N. Terao, S. Takamatsu, T. Minehira, T. Sobajima, K. Nakayama, Y. Kamada, E. Miyoshi, Fucosylation is a common glycosylation type in pancreatic cancer stem cell-like phenotypes, World J. Gastroenterol. 21 (2015) 3876–3887.
[56] V. Desiderio, P. Papagerakis, V. Tirino, L. Zheng, M. Matossian, M.E. Prince, F. Paino, L. Mele, F. Papaccio, R. Montella, G. Papaccio, S. Papagerakis, Increased fucosylation has a pivotal role in invasive and metastatic properties of head and neck cancer stem cells, Oncotarget. 6 (2015) 71–84.
[57] R. Honma, I. Kinoshita, E. Miyoshi, U. Tomaru, Y. Matsuno, Y. Shimizu, S. Takeuchi, Y. Kobayashi, K. Kaga, N. Taniguchi, H. Dosaka-Akita, Expression of fucosyltransferase 8 is associated with an unfavorable clinical outcome in non-small cell lung cancers, Oncology. 88 (2015) 298–308.
[58] H.F. Yang, M. Yu, H.D. Jin, J.Q. Yao, Z.L. Lu, I.B. Yabasin, Q. Yan, Q.P. Wen, Fentanyl promotes breast cancer cell stemness and epithelial-mesenchymal transition by upregulating α1, 6-fucosylation via Wnt/β-catenin signaling pathway, Front. Physiol. 8 (2017) 510.
[59] M.S. Duxbury, H. Ito, M.J. Zinner, S.W. Ashley, E.E. Whang, EphA2: a determinant of malignant cellular behavior and a potential therapeutic target in pancreatic adenocarcinoma, Oncogene. 23 (2004) 1448–1456.
[60] L.W. Qian, K. Mizumoto, N. Maehara, K. Ohuchida, N. Inadome, M. Saimura, E. Nagai, K. Matsumoto, T. Nakamura, M. Tanaka, Co-cultivation of pancreatic cancer cells with orthotopic tumor-derived fibroblasts: fibroblasts stimulate tumor cell invasion via HGF secretion whereas cancer cells exert a minor regulative effect on fibroblasts HGF production, Cancer Lett. 190 (2003) 105–112.
[61] X. Wang, T. Fukuda, W. Li, C.X. Gao, A. Kondo, A. Matsumoto, E. Miyoshi, N. Taniguchi, J. Gu, Requirement of Fut8 for the expression of vascular endothelial growth factor receptor-2: a new mechanism for the emphysema-like changes observed in Fut8-deficient mice, J. Biochem. 145 (2009) 643–651.
[62] M. Okada, S. Chikuma, T. Kondo, S. Hibino, H. Machiyama, T. Yokosuka, M. Nakano, A. Yoshimura, Blockage of core fucosylation reduces cell-surface expression of PD-1 and promotes anti-tumor immune responses of T cells, Cell Rep. 20 (2017) 1017–1028.
[63] N. Zhang, M. Li, X. Xu, Y. Zhang, Y. Liu, M. Zhao, P. Li, J. Chen, T. Fukuda, J. Gu, X. Jin, W. Li, Loss of core fucosylation enhances the anticancer activity of cytotoxic T lymphocytes by increasing PD-1 degradation, Eur. J. Immunol. 50 (2020) 1820–1833.
[64] Q. Hang, T. Isaji, S. Hou, S. Im, T. Fukuda, J. Gu, Integrin α5 suppresses the phosphorylation of epidermal growth factor receptor and its cellular signaling of cell proliferation via N-glycosylation, J. Biol. Chem. 290 (2015) 29345–29360.

 DOI: 10.1002/eji.202048543 Eur. J. Immunol. 2020. 50: 1820–1833

Clinical

European Journal of Immunology

Tumor immunology

Research Article

Loss of core fucosylation enhances the anticancer activity of cytotoxic T lymphocytes by increasing PD-1 degradation

Nianzhu Zhang[*1], *Ming Li*[*1], *Xing Xu*[2], *Yingshu Zhang*[1], *Yancheng Liu*[2], *Meng Zhao*[2], *Peng Li*[2], *Jun Chen*[3], *Tomohiko Fukuda*[4], *Jianguo Gu*[4], *Xun Jin*[2] *and Wenzhe Li*[1]

[1] College of Basic Medical Sciences, Dalian Medical University, Dalian, Liaoning, China
[2] Tianjin Medical University Cancer Institute and Hospital. National Clinical Research Center for Cancer, Key Laboratory of Cancer Prevention and Therapy, Tianjin. Tianjin's Clinical Research Center for Cancer, Tianjin, China
[3] Second Affiliated Hospital of Dalian Medical University, Dalian, Liaoning, China
[4] Institute of Molecular Biomembrane and Glycobiology, Tohoku Medical and Pharmaceutical University, Sendai, Miyagi, Japan

As an immune checkpoint, programmed cell death 1 (PD-1) and its ligand (PD-L1) pathway plays a crucial role in $CD8^+$ cytotoxic T lymphocytes (CTL) activation and provides antitumor responses. The N-glycans of PD-1 and PD-L1 are highly core fucosylated, which are solely catalyzed by the core fucosyltransferase (Fut8). However, the precise biological mechanisms underlying effects of core fucosylation of PD-1 and PD-L1 on CTL activation have not been fully understood. In this study, we found that core fucosylation was significantly upregulated in lung adenocarcinoma. Compared to those of $Fut8^{+/+}$OT-I mice, the lung adenocarcinoma formation induced by urethane was markedly reduced in $Fut8^{-/-}$OT-I mice. De-core fucosylation of PD-1 compromised its expression on $Fut8^{-/-}$ CTL, resulted in enhanced $Fut8^{-/-}$ CTL activation and cytotoxicity, leading to more efficient tumor eradication. Indeed, loss of core fucosylation significantly enhanced the PD-1 ubiquitination and in turn led to the degradation of PD-1 in the proteasome. Our current work indicates that inhibition of core fucosylation is a unique strategy to reduce PD-1 expression for the antilung adenocarcinoma immune therapy in the future.

Keywords: Core fucosylation · CTL activation · Lung adenocarcinoma · Programmed cell death 1 (PD-1) · Ubiquitination

Additional supporting information may be found online in the Supporting Information section at the end of the article.

Correspondence: Dr. Wenzhe Li
e-mail: liwenzhe@dmu.edu.cn; jinx2354@163.com

*These two authors contributed equally to this work.

Introduction

Lung cancer is the most frequently occurring type of cancer. Over 80% of lung cancer cases are nonsmall cell lung cancer (NSCLC) with poor clinical outcomes and an average 5-year survival rate of no more than 10% [1]. Among the major subtypes of NSCLC, lung adenocarcinoma is one of the most common pathologic types but is often diagnosed late, when local invasion and metastases have already occurred.

In cancer, alterations in protein glycosylation are closely correlated with malignant transformation and tumor progression [2]. One of the most common tumor-associated glycan modifications is core fucosylation catalyzed by core fucosyltransferase (Fut8). Fut8 is the sole glycosyltransferase to catalyze the transfer of a fucose residue from GDP-fucose to the innermost *N*-acetylglucosamine (GlcNAc) residue of *N*-glycans via the α1,6-linkage in the Golgi apparatus of mammalian cells (Fig. 1A) [3]. The high expression of Fut8 was found to be associated with an unfavorable clinical outcome in hepatocellular carcinoma, prostate cancer, melanoma, ovarian cancer, NSCLC, and breast cancer [4–8].

Cytotoxic T lymphocytes (CTLs) are key players during the immune response to eliminate tumorigenic cells [9]. The major mechanism by which activated CTLs destroy tumor cells is by the release of lytic granules (LGs), such as perforin and granzymes, at the tight junction between CTLs and tumor cells [9]. Programmed cell death protein-1 (PD-1, CD279) is a negative regulator of CTL-mediated killing efficiency, likely by regulating the release of LGs and CTL activation [10]. PD-1 is a type 1 transmembrane protein containing an immunoreceptor tyrosine-based inhibitory motif and an immunoreceptor tyrosine-based switch motif (ITSM), which is induced upon the activation of $CD8^+$ T cells. Upon PD-1 ligand (PD-L1, CD274) ligation, PD-1 recruits the Src homology region 2 domain-containing phosphatase (SHP)-1 and SHP-2 phosphatases to its ITSM and transmits inhibitory signals resulting in T-cell dysfunction against tumor cells [11]. Conversely, inhibition of the interaction between PD-1 and PD-L1 enhances the T-cell response and mediates antitumor activity [12]. Indeed, PD-1 (NM-005018) is a glycoprotein, containing four core fucosylated *N*-glycans: N^{49}, N^{58}, N^{74}, and N^{116} [13], while the four core fucosylated *N*-glycans of PD-L1 (NM-001267706) are N^{35}, N^{192}, N^{200}, and N^{219} [14]. In the interaction between PD-1/PD-L1, the β-folding (CC 'FG) of the PD-1 IgV domain and the β-folding (GFCC') of the PD-L1 IgV domain form the contact surface, and the N^{74} residue aligns with the interface between PD-1 and PD-L1 [15]. Most studies on the regulation of the PD-1/PD-L1 pathway focus on the transcriptional and translational levels. For example, PD-1 expression on CTLs is regulated by interferon α (IFN-α) [16], nuclear factor of activated T-cells c1 (NFATc1) [17], and adapter proteins SKAP55 and ADAP [18]. The expression of PD-L1 is regulated by the chemokine-like molecules, CMTM6 and CMTM4 [19]. *N*-Glycosylation of PD-L1 has been shown to play an important role in the expression and stability of PD-L1 [20]. The glycosylation of PD-1 is also essential for the binding of nivolumab to PD-1, as nivolumab binds to only glycosylated PD-1 expressed in mammalian cell lines but not nonglycosylated PD-1 expressed in *E.* coli (https://www.accessdata.fda.gov/drugsatfda_docs/nda/2014/125554Orig1s000PharmR.pdf). This indicates the importance of PD-1 glycosylation on immune checkpoints. Fut8-mediated core fucosylation has been shown to be an important posttranslational process [21] that regulates protein conformation, stability, and functional expression; however, few studies have focused on the posttranslation modification of PD-1, such as core fucosylation.

Here we reports that core fucosylation was significantly increased in the sera and cancerous tissue of lung adenocarcinoma patients. Ablation of Fut8 suppresses PD-1 expression on CTLs and resulted in enhanced $Fut8^{-/-}$ CTL activation and cytotoxicity and more efficient tumor eradication. Functionally, loss of core fucosylation significantly enhanced PD-1 ubiquitination and the degradation of PD-1 by the proteasome. Collectively, our study expands our current understanding of the role of core fucosylation in tumor immunology.

Results

The Fut8 gene is significantly upregulated in lung adenocarcinoma

To understand the relationship between glycosyltransferases and tumorigenesis of lung adenocarcinoma, we selected 104 glycosyltransferases from CAZY database and generated Volcano plot for differentially expressed genes in lung adenocarcinoma. From the Volcano plot analysis (Fig. 1B), the Fut8 showed high expression in lung adenocarcinoma ($p = 1.57 \times 10^{-30}$). Next, we evaluated core fucosylation and the expression of PD-L1 in tumor samples from 92 lung adenocarcinoma patients by immunohistochemistry staining of tissue microarrays. As illustrated in Fig. 1C, core fucosylation was significantly increased in lung adenocarcinoma samples compared with adjacent tissue. This was confirmed by lectin blot with biotin-labeled Aspergillus Oryzae Lectin (AOL), which preferentially recognizes core fucosylated *N*-glycans [22]. Among the 92 lung adenocarcinoma tissues from patients with different clinical stages, the proportion of high Fut8-expressing tissues was 56.5%, in contrast, among the adjacent tissues of these patients, 40.9% had high Fut8 expression levels (Fig. 1D, $p = 0.036$ and Supporting Information Table S1A). Furthermore, the high expression of PD-L1 was observed in adenocarcinoma tissue (56.5%) and lower expression of PD-L1 was found in adjacent tissue (97.93%) (Fig. 1E, $p = 0.001$ and Supporting Information Table S1B). The chi-squared test and Spearman's rank correlation analysis of the clinicopathological significance showed that the level of core fucosylation was highly associated with lung tumor T stage ($p = 0.001$) and Tumor, Node and Metastasis (TNM) stage ($p = 0.011$) (Supporting Information Table S2). Compared with I/II stages, the expression of Fut8 was significantly upregulated in the III/IV stages (Fig. 1F). Core fucosylation was closely associated with the overall survival (OS) rate of patients ($p = 0.012$), but not with PD-L1 expression ($p = 0.212$) (Fig. 1G). Moreover, high expression of both Fut8 and PD-L1 showed significantly lower OS

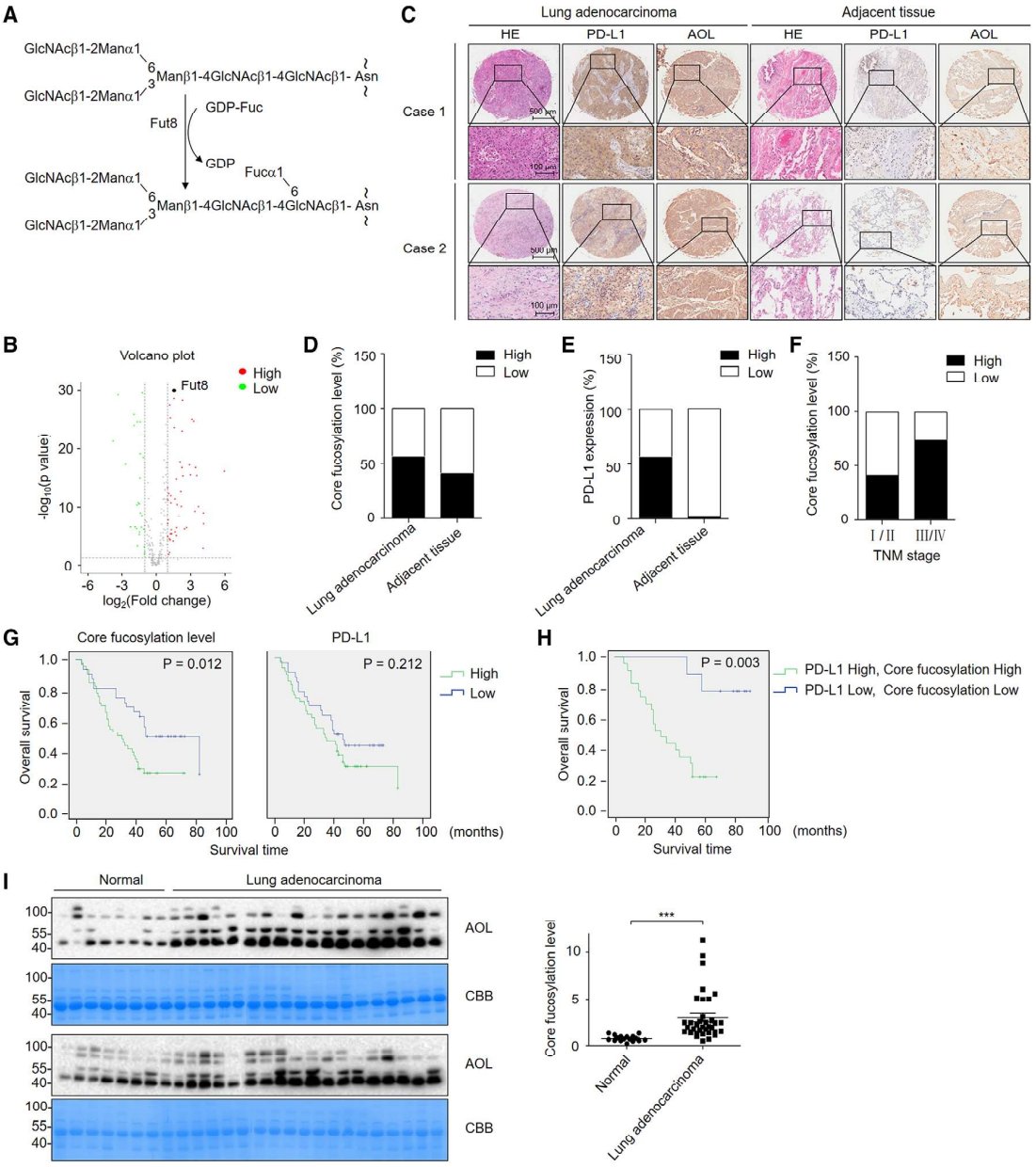

Figure 1. Fut8 and PD-L1 were upregulated in lung adenocarcinoma. (A) The biological reaction of Fut8. Fut8 transfers fucose to the innermost GlcNAc residue of complex *N*-glycans via α1,6-linkage (core fucosylation). Asn, asparagine; Fuc, fucose; GDP-Fuc, GDP-fucopyranoside; Man, mannose. GlcNAc, *N*-acetylglucosamine. (B) Volcano plot for the 104 glycosyltransferases expressions in lung adenocarcinoma data. The red circle signs represent significantly upregulated genes, and the green circle signs represent significantly downregulated genes. The *x*-axis is the fold-change (FC) value, and the *y* axis is $-\log_{10}$ (*p* value). (C) Representative images of immunohistochemical analysis of core fucosylation level and PD-L1 level of lung adenocarcinoma and adjacent tissue from human lung adenocarcinoma tissue microarray. Microarray plates were incubated with LCA (1:300) or anti-PD-L1 Ab (1:150). After washing, secondary antibody was incubated and visualized with DAB. No yellow or lightest yellow determines low expression and medium or deep yellow determines high expression. (D) Differential core fucosylation level in lung adenocarcinoma and adjacent tissue. Significance of correlation between core fucosylation level in lung adenocarcinoma and adjacent tissue was determined by using the chi-square test. (E) Differential expression rates of PD-L1 in lung adenocarcinoma and adjacent tissue. (F) Correlation of core fucosylation level in relation to clinicopathologic variables of 92 lung adenocarcinoma patients with the methods of the chi-square test and Spearman rank correlation analysis. Percentages of core fucosylation level in different TNM stages (stage I/II and stage III/IV) were depicted. (G) Kaplan–Meier OS curves for lung adenocarcinoma patients with low (blue) or high (green) core fucosylation level and PD-L1 expression, respectively. (H) Kaplan–Meier OS curves for lung adenocarcinoma patients with both low (blue) or both high (green) core fucosylation level and PD-L1 expression [stage I and stage II (n = 41), stage III, and stage IV (n = 26) in panel C-H]. (I) Comparative analysis of the core fucosylation levels in sera of 36 lung adenocarcinoma patients and 16 healthy donors. The core fucosylation levels in serum samples (2 μg) were detected by AOL (1:20 000) blot. The gel was stained with coomassie brilliant blue (CBB). ***$p < 0.001$ [Student's *t*-test (unpaired)]. Data (I) were shown as mean ± SD triplicates and were representative of three independent experiments.

rate in lung adenocarcinoma patients (Fig. 1H, $p = 0.003$). Furthermore, univariate analyses showed that the core fucosylation ($p = 0.015$), T stage ($p = 0.003$), and TNM stage ($p = 0.001$) were significantly associated with poor OS (Supporting Information Table S3). Multivariate analysis also indicated that high TNM stage was an independent prognostic factor for OS ($p = 0.001$) and a significant hazard ratio (HR) predictor for lung adenocarcinoma ($p = 0.012$) (Supporting Information Table S3). Furthermore, core fucosylation was dramatically increased in the sera of patients with lung adenocarcinoma compared with the healthy controls (Fig. 1I, $p < 0.001$). Collectively, these data suggested that increased Fut8 expression contributes to the tumorigenesis of lung adenocarcinoma.

Ablation of Fut8 in CD8$^+$ T cells suppresses the tumorigenesis of lung adenocarcinoma

To further investigate the role of Fut8 in lung adenocarcinoma generation, we established urethane-induced lung adenocarcinoma using Fut8$^{+/+}$ and Fut8$^{-/-}$ mice. Core fucosylation was not detected in Fut8$^{-/-}$ lung tissues (Fig. 2A) and in the lysates of Fut8$^{-/-}$ lung cells (Fig. 2B). Fut8 enzymatic activity was also deleted in Fut8$^{-/-}$ lungs (Fig. 2C). Notably, compared with the Fut8$^{+/+}$ mice, urethane-induced tumor formation was significantly reduced in Fut8$^{-/-}$ mice (Fig. 2D and E, $p < 0.001$). To elucidate the effect of tumor-infiltrating CD8$^+$ T cells (TILs) on antitumor immunity in Fut8$^{-/-}$ mice, Fut8$^{-/-}$ mice were treated with anti-CD8 Ab and the depletion efficiency was confirmed (Supporting Information Figure S1). Interestingly, urethane-induced tumor formation was mainly recovered in Fut8$^{-/-}$ mice with antibody-mediated depletion of CD8$^+$ T cells (CD8-depletion) (Fig. 2D and E, $p < 0.001$). However, no significant difference in cell viability was found between the Fut8$^{+/+}$, Fut8$^{-/-}$, and CD8-depletion Fut8$^{-/-}$ cancer cells (Fig. 2F).

Given the importance of Fut8 in affecting the proliferation of NSCLC [23], we generated Fut8 stable knockdown cells using the human lung adenocarcinoma cell lines A549 and H1299. The knockdown efficiency of the Fut8 gene in A549 (Fig. 2G) and H1299 (Fig. 2I) cells was confirmed. The Fut8 knockdown did not influence the cell viability in A549 cells (Fig. 2H) and H1299 cells (Fig. 2J). Furthermore, loss of Fut8 in A549 cells or H1299 cells did not affect tumor formation in nude mice (Supporting Information Figure S2). These results indicated that the Fut8 ablation in CTLs play an important role in tumor eradication, rather than those in tumor cells.

Loss of core fucosylation enhances CTL activation and cytotoxicity

CTLs are a major effector cell population required for protection against tumor growth [24]. To identify the role of Fut8 in CTL activation, OT-I mice were crossed with Fut8$^{+/-}$ mice to generate Fut8$^{+/+}$OT-I and Fut8$^{-/-}$OT-I mice. CTLs were isolated from Fut8$^{+/+}$OT-I and Fut8$^{-/-}$OT-I mice and stimulated with $OVA_{257\text{-}264}$ (Fig. 3A). Compared with Fut8$^{+/+}$OT-I CTLs, Fut8$^{-/-}$OT-I CTLs showed larger cluster formation, indicating enhanced activation of CTLs from Fut8$^{-/-}$OT-I mice (Fig. 3B, $p < 0.001$). Moreover, the proportion of activated CTLs (CD69$^+$) was significantly higher among the Fut8$^{-/-}$OT-I CTLs compared with the Fut8$^{+/+}$OT-I CTLs (Fig. 3C).

To clarify whether the ablation of Fut8 promotes CTL activation and subsequent CTL-induced tumor killing activity, we compared the cytotoxic capacity between Fut8$^{+/+}$ CTLs and Fut8$^{-/-}$ CTLs against urethane-induced lung adenocarcinoma. As shown in Fig. 3D, Fut8$^{-/-}$ CTLs showed significantly higher cytotoxic capacity ($p < 0.001$). However, no significant differences in the cytotoxic capacity between Fut8$^{+/+}$ CTLs and Fut8$^{-/-}$ CTLs after anti-PD-1 Ab treatment were found (Fig. 3D).

E. G7-OVA cells are a model system for studying major histocompatibility complex class I restricted responses of OT-I CTLs. To further address the enhancement of Fut8$^{-/-}$ CTL-mediated tumor cell killing, we performed the lactate dehydrogenase (LDH) assay to measure the OT-I CTL-mediated cytotoxicity. As shown in Fig. 3E, Fut8$^{-/-}$OT-I CTLs showed higher cytotoxic capacity of E. G7-OVA cells than Fut8$^{+/+}$OT-I CTLs ($p < 0.001$). Moreover, we observed a lower percentage of CFSE-labeled E. G7-OVA cells following coculture with Fut8$^{-/-}$OT-I CTLs compared with Fut8$^{+/+}$OT-I CTLs (Fig. 3F, $p < 0.001$).

IL-2 and IFN-γ are directly involved in antitumor immune regulation; thus, we compared the cytokine production by Fut8$^{+/+}$OT-I CTL and Fut8$^{-/-}$OT-I CTL. The mRNA expression of IL-2 and IFN-γ was significantly upregulated in Fut8$^{-/-}$OT-I CTLs compared with Fut8$^{+/+}$OT-I CTLs (Fig. 3G, $p < 0.001$). To elucidate the function of Fut8 in CTL activation, clinical carcinoma tissue of lung adenocarcinoma patients, who had received primary surgery, were collected and treated with Fut8 shRNA lentivirus particles. As shown in Fig. 3H, PD-1 expression was significantly decreased by Fut8 knockdown and granzyme B secretion was increased. Taken together, our results suggested that loss of Fut8 could enhance CTL-mediated cytotoxicity via downregulated PD-1 expression.

Loss of core fucosylation promotes PD-1 ubiquitination and its degradation

To assess whether core fucosylation regulates PD-1 expression on CTLs, we isolated the CTLs from Fut8$^{+/+}$ and Fut8$^{-/-}$ splenic cells (Fig. 4A) and analyzed the PD-1 expression. As shown in Fig. 4B, the PD-1 positive cells (PD-1$^+$) from Fut8$^{-/-}$ CTLs were remarkably decreased compared with Fut8$^{+/+}$ CTLs. Moreover, the cell surface of the majority of the CD8$^+$ T cells (about 93%) was modified by core fucosylation (Fig. 4B, $p < 0.001$). Notably, the expression of PD-1 was dramatically reduced in the cell lysates of Fut8$^{-/-}$ CTLs (Fig. 4C), while PD-1 expression was significantly decreased by ablation of Fut8 after $OVA_{257\text{-}264}$ stimulation (Fig. 4D). Actually, PD-1 expression significantly increased in lung adenocarcinoma tissues (n = 515) (Fig. 4E, $p < 0.001$) (Data from Ualcan). We also found that the mRNA expression of Fut8 was

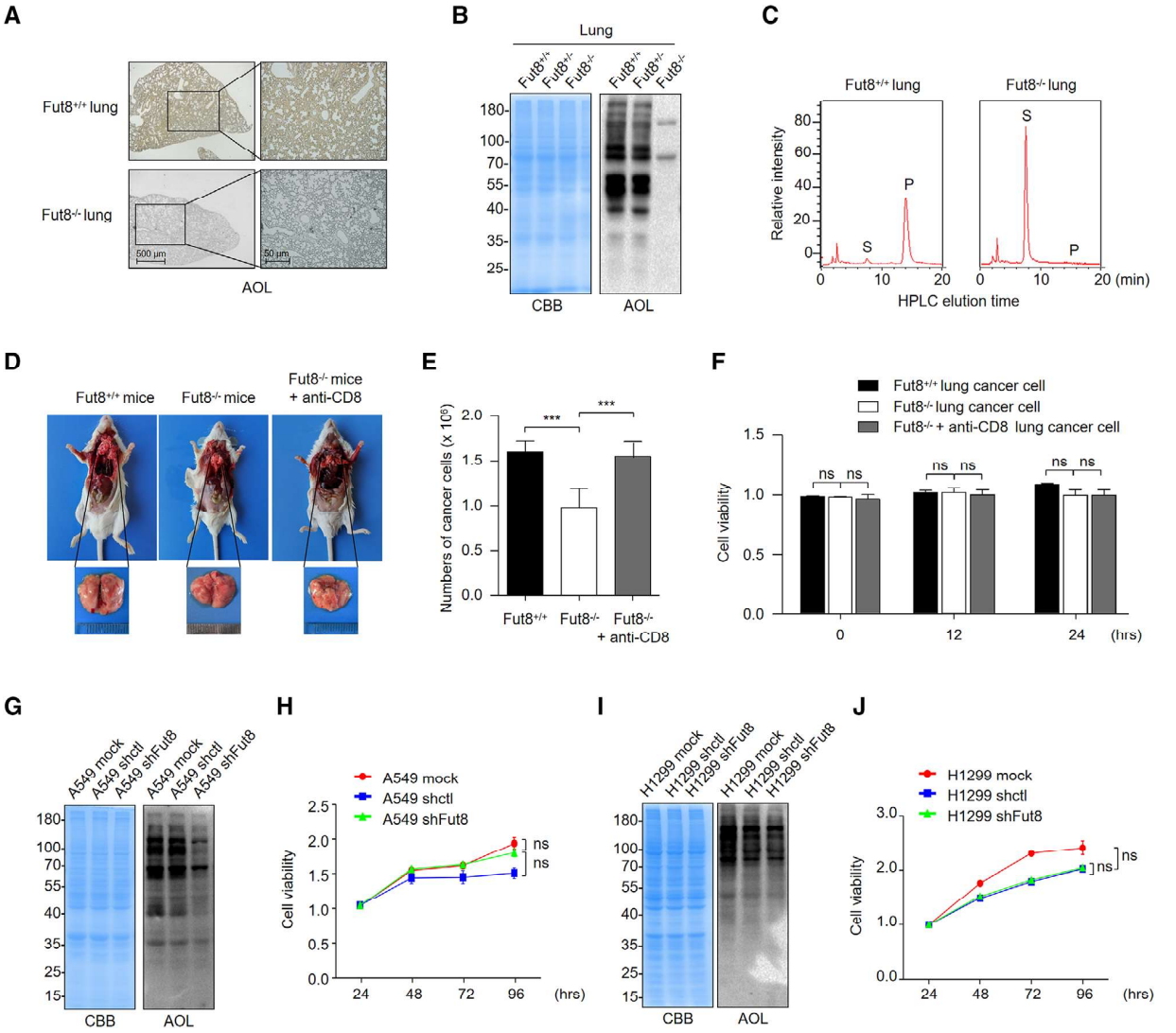

Figure 2. Reduction of urethane-induced tumor incidence in Fut8$^{-/-}$ mice. (A) Immunohistochemical analysis of Fut8$^{+/+}$ and Fut8$^{-/-}$ lung. Sections were incubated with AOL (1:200). (B) Lectin blot of Fut8$^{+/+}$ and Fut8$^{-/-}$ lung. 10 μg lung lysates were run on 10% SDS–PAGE gel and stained with CBB and AOL (1:5000). (C) Fut8 enzymatic activity. Cells from Fut8$^{+/+}$ and Fut8$^{-/-}$ mice were isolated from lungs. S is the peptide substrate, and P is the product of fucosylation [Fut8$^{+/+}$ and Fut8$^{-/-}$ lung (n = 6 per group) in panel A–C]. (D) Photographs of lungs of the Fut8$^{+/+}$, Fut8$^{-/-}$, and CD8-depletion Fut8$^{-/-}$ mice. Urethane-induced lung adenocarcinoma in Fut8$^{+/+}$, Fut8$^{-/-}$, and CD8-depletion Fut8$^{-/-}$ mice. (E) Tumor cell numbers in Fut8$^{+/+}$, Fut8$^{-/-}$, and CD8-depletion Fut8$^{-/-}$ mice were counted by digestion of tumor tissue into single cells. $^{***}p < 0.001$ [Student's *t*-test (unpaired)]. (F) Cell proliferation was detected by MTT assay. Tumor cells were from urethane-injected Fut8$^{+/+}$, Fut8$^{-/-}$, and CD8-depletion Fut8$^{-/-}$ mice [(n = 6 per group) in panel D–F]. ns, no significant difference [Student's *t*-test (unpaired)]. (G) Fut8 knockdown in A549 cells. Cell lysates (10 μg) were run on 10% SDS–PAGE gel and stained with CBB and AOL (1:5000). (H) A549 derivative cell proliferation was detected by MTT assay. ns, no significant difference [Student's *t*-test (unpaired)]. (I) Fut8 knockdown in H1299 cells. Cell lysates (10 μg) were run on 10% SDS–PAGE gel and stained with CBB and AOL (1:5000). (J) H1299 derivative cell proliferation was detected by MTT assay. ns, no significant difference [Student's *t*-test (unpaired)]. Data (A–J) were shown as mean ± SD of triplicates and were representative of three independent experiments.

significantly increased in high PD-1 expressed (PD-1^{hi}) TILs compared to those with low PD-1 expressed (PD-1^{low}) TILs in NSCLC patients (Fig. 4F, $p < 0.01$) (Data from NCBI). These results suggested that loss of core fucosylation suppressed the expression of PD-1 both on cell surface and in the whole cell lysates of CTLs.

To further investigate the regulation of PD-1 expression by Fut8 ablation, we generated PD-1 overexpressing Jurkat T cells (Jurkat-PD-1) (Fig. 5A) and Fut8 knockdown Jurkat-PD-1 cells (Fig. 5B). PD-1 expression was significantly reduced in Jurkat-PD-1-shFut8 cells, and the reintroduction of the Fut8 gene into Jurkat-PD-1-shFut8 cells resulted in recovery of PD-1 expression (Fig. 5C),

indicating that core fucosylation affected the PD-1 expression of CTLs.

Denatured or misfolded proteins are destroyed by the ubiquitin (Ub)-proteosome system. The ubiquitination of PD-1 was dramatically increased in Jurkat-PD-1-shFut8 cells compared with Jurkat-PD-1-shctl cells (Fig. 5D). FBXO38 (E3 ubiquitin ligase) primarily mediates PD-1 polyubiquitination at Lys233 in Jurkat cells [25]. In immunoprecipitation assay with an anti-FBXO38 Ab, Fut8 knockdown resulted in higher expression level of PD-1 (Fig. 5E), accompanied with increased PD-1 ubiquitination in the Jurkat-PD-1-shFut8 cells. To further confirm the function of FBXO38 in PD-1 degradation, Jurkat-PD-1-shFut8 cells were treated with siRNA for FBXO38. The reduced PD-1 expression in the Jurkat-PD-1-shFut8 cells was significantly increased after FBXO38 gene silencing (Fig. 5F). To investigate the involvement of the 26S proteasome machinery in PD-1 degradation, we subsequently treated Jurkat-PD-1-shFut8 cells with the proteasome inhibitor MG132. As anticipated, the degradation of PD-1 was significantly suppressed after MG132 treatment (Fig. 5G). Moreover, the increased PD-1 ubiquitination in the Jurkat-PD-1-shFut8 cells was significantly suppressed by MG132 treatment (Fig. 5H). These data showed that loss of core fucosylation promoted PD-1 ubiquitination by increasing binding to FBXO38 and subsequent degradation of PD-1 by the 26S proteasome.

Loss of core fucosylation inhibits tumor formation by enhancing CTL activation

Since Fut8 ablation could enhance CTL-mediated cytotoxicity, we speculated that loss of core fucosylation could inhibit tumor formation in xenograft mice. We first evaluated the influence of core fucosylation on tumor formation in tumor-bearing mice. $Fut8^{+/+}$OT-I and $Fut8^{-/-}$OT-I mice were randomly divided into three groups and inoculated subcutaneously with E. G7-OVA cells. Once tumors were well established, mice were treated with $OVA_{257\text{-}264}$ (Fig. 6A). By measuring the tumor volume (Fig. 6B), size (Fig. 6C), and weight (Fig. 6D, $p = 0.045$), we found that the tumor growth was significantly suppressed in the xenograft tumors of $Fut8^{-/-}$OT-I mice. The proportion of activated CTLs was significantly increased in $Fut8^{-/-}$OT-I CTLs compared with the $Fut8^{+/+}$OT-I CTLs after treatment with $OVA_{257\text{-}264}$ (Fig. 6E). Moreover, the percentage of PD-1^{+} cells was reduced in $Fut8^{-/-}$OT-I CTLs compared with the $Fut8^{+/+}$OT-I CTLs (Fig. 6F).

Because $OVA_{257\text{-}264}$ could function as an activator for CTL-mediated immune responses, we further examined whether this response could protect mice grafted with tumor cells. $Fut8^{+/+}$OT-I and $Fut8^{-/-}$OT-I mice were immunized with $OVA_{257\text{-}264}$ before xenograft tumor challenge (Fig. 6G). Tumor volume (Fig. 6H), size (Fig. 6I), and weight (Fig. 6J, $p < 0.001$) were significantly decreased in $Fut8^{-/-}$OT-I mice. Our results indicated that loss of core fucosylation inhibits tumor formation by enhancing CTL activation.

Discussion

Increased core fucosylation is involved with the development of several malignant tumors and is linked to the severity of cancers [4–8]. In the process of epithelial-mesenchymal transformation of NSCLC, deletion of E-cadherin can increase the expression of β-catenin protein, which in turn binds to the lymphatic enhancer binding factor-1 (LEF-1)/T cell factor site on the Fut8 promoter and results in upregulation of protein core fucosylation [26]. During the present study, we found that core fucosylation was significantly upregulated in lung adenocarcinoma patients and increased core fucosylation was associated with high TNM stage and poorer survival. These observations pinpoint the contribution of hyper core fucosylation to lung adenocarcinoma severity and pathogenesis.

The tumor microenvironment exploits the PD-1 pathway to evade immune surveillance, in which the expression of PD-1 on the infiltrating CTL is promoted, and in turn induces the ectopic expression of PD-L1 of the tumor cells [27]. Blockade of PD-1 expression clearly improved the antitumor effect, and the efficacy of a fully human anti-PD-1 monoclonal antibody in a clinical trial has been reported [23, 28]. A series of studies revealed transcriptional regulation of PD-1 extensively [16–18]. However, it is largely unknown how PD-1 expression is posttranslationally regulated. Glycosylation and ubiquitination are both posttranscriptional regulation mechanisms that could determine the structure and function of the protein [29]. *N*-Glycosylation is essential for the expression of PD-1 [20]. A sharp reduction in PD-1 expression was observed in the whole cell lysates and on the cell surface of Jurkat-PD-1-shFut8 cells. Consistent with this, ablation of core fucosylation can reduce cell-surface expression of PD-1 in the 68-41 murine T-cell line [13]. Fut8-mediated core fucosylation could modify the function of corresponding glycoproteins, such as protein conformation, stability, and functional expression [30–32]. Thus, we speculated that core fucosylation could affect PD-1 ubiquitination. As expected, Fut8 ablation enhanced the interaction between PD-1 and FBXO38 and promoted PD-1 ubiquitination. The increased PD-1 ubiquitination was then suppressed by MG132 treatment. Indeed, STAT5, which is downstream of IL-2 signaling, was found to bind to the FBXO38 promoter in activated CTLs [33]. Given that the mRNA expression of IL-2 was also upregulated in $Fut8^{-/-}$OT-I CTLs, IL-2-induced FBXO38 expression resulted in enhanced PD-1 ubiquitination, which correlated with lower PD-1 protein abundance on the surface of activated CTLs. The reduced PD-1 expression was restored by MG132 treatment, suggesting that de-core fucosylated PD-1 undergoes fast protein degradation.

Core fucosylation plays a vital role in NSCLC development and progression [7, 26]. Fut8 expression was significantly upregulated in PD-1^{hi} TILs compared to those in PD-1^{low} TILs in NSCLC patients. Adenocarcinoma is the most common NSCLC; it occupies about 40% of NSCLC. Core fucosylation is significantly increased in lung adenocarcinoma; thus, it is reasonable to consider that the high core fucosylation in the tumor microenvironment may

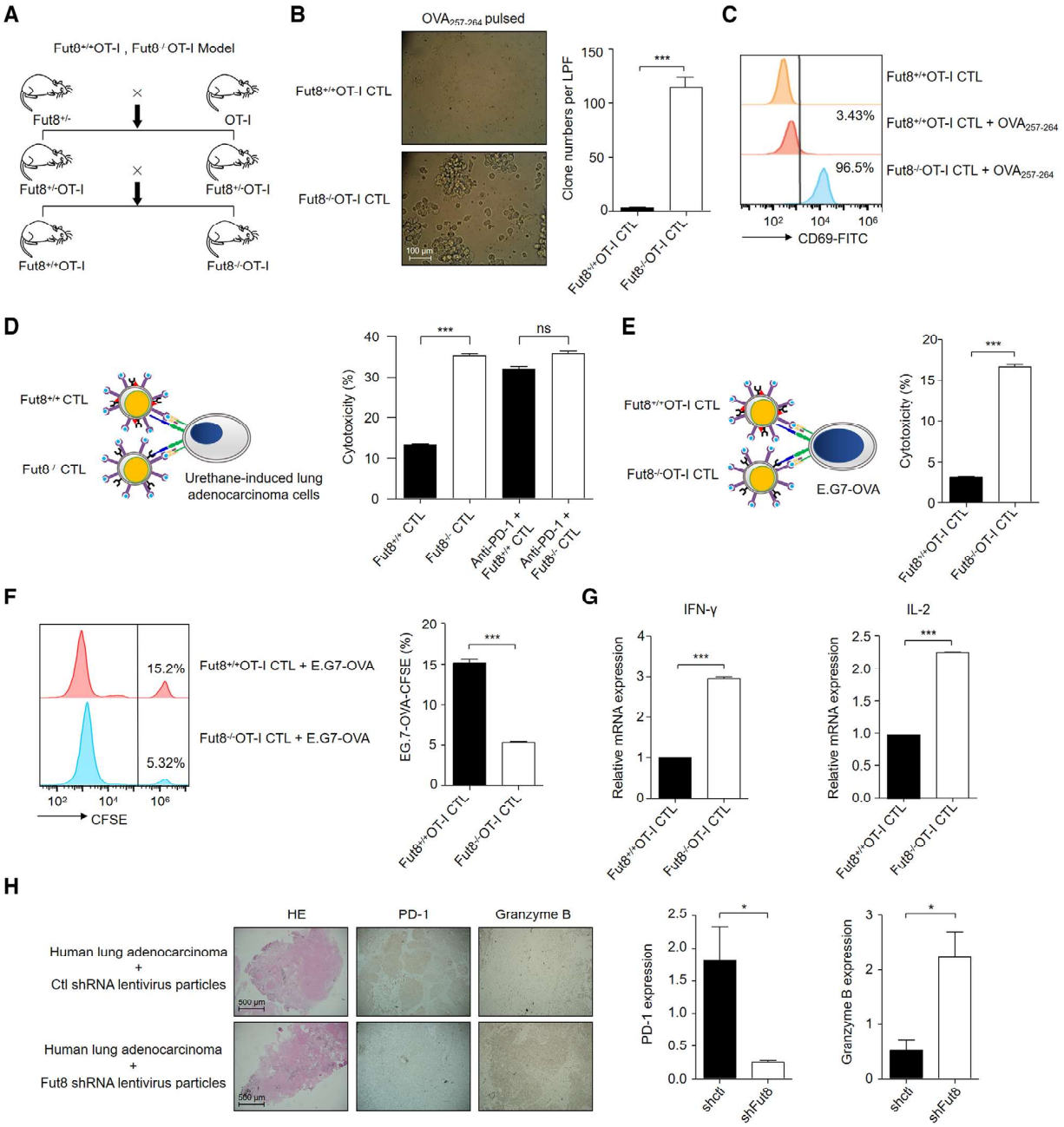

Figure 3. Loss of core fucosylation enforced the activation and cytotoxicity of CTL. (A) Hybridization model of Fut8$^{+/-}$ mice and OT-I mice. Fut8$^{+/-}$ and OT-I mice were hybridized to obtain Fut8$^{+/+}$OT-I and Fut8$^{-/-}$OT-I mice. CTL were extracted from Fut8$^{+/+}$OT-I and Fut8$^{-/-}$OT-I mice splenic cells and activated with $OVA_{257-264}$. (B) Images of highly purified Fut8$^{+/+}$OT-I CTL and Fut8$^{-/-}$OT-I CTL after activation of 48 h with $OVA_{257-264}$ (10 μg/mL) and cultured with IL-2 (50 ng/mL) under bright field. CTL were extracted from mice spleen by MACS. Clone numbers of Fut8$^{+/+}$OT-I and Fut8$^{-/-}$OT-I CTLs were counted under different views of low-power fields. (C) CTL activation. Activated Fut8$^{+/+}$OT-I CTL and Fut8$^{-/-}$OT-I CTL were stained with anti-CD69 Ab (1:100). Numbers indicated the percentage of CD69^{+} cells, and 10 000 events were acquired for each analysis [Fut8$^{+/+}$OT-I and Fut8$^{-/-}$OT-I mice (n = 3 per group) in panel A–C]. ***$p < 0.001$ [Student's *t*-test (unpaired)]. (D) In vitro cytotoxicity models of CTL (effector cell, E) and urethane-induced primary lung adenocarcinoma cells (target cell, T). Fut8$^{+/+}$ and Fut8$^{-/-}$ CTLs were treated with or without anti-PD-1 Ab (10 μg/mL). E: T = 5: 1. Cell killing assay was performed using an LDH assay kit [urethane-induced Fut8$^{+/+}$ and Fut8$^{-/-}$ mice (n = 3 per group) in panel D]. ***$p < 0.001$; ns, no significant difference [Student's *t*-test (unpaired)]. (E) In vitro cytotoxicity models of Fut8$^{+/+}$OT-I and Fut8$^{-/-}$OT-I CTL (E) and E. G7-OVA cells (T). E. G7-OVA cells (10^5 cells/mL) were pulsed with $OVA_{257-264}$ (10 μg/mL) for 90 min. Fut8$^{+/+}$OT-I and Fut8$^{-/-}$OT-I CTL were stimulated with $OVA_{257-264}$ (10 μg/mL) for 48 h before coculturing. The cytotoxicity of Fut8$^{+/+}$OT-I CTL and Fut8$^{-/-}$OT-I CTL against E. G7-OVA cells at an E: T of 5:1 was analyzed using an LDH detection assay kit [Fut8$^{+/+}$OT-I and Fut8$^{-/-}$OT-I mice (n = 3 per group) in panel E]. ***$p < 0.001$ [Student's *t*-test (unpaired)]. (F) Cytotoxicity was measured by flow cytometry. The cytotoxicity of Fut8$^{+/+}$OT-I CTL and Fut8$^{-/-}$OT-I CTL against E. G7-OVA cells at an E: T of 5:1 for 10 h was analyzed. E. G7-OVA target cells were labeled with CFSE for 30 min at 37°C [Fut8$^{+/+}$OT-I and

Fut8$^{-/-}$OT-I mice (n = 3 per group) in panel F]. ***$p < 0.001$ [Student's *t*-test (unpaired)]. (G) Relative IFN-γ and IL-2 mRNA expression of Fut8$^{+/+}$OT-I CTL and Fut8$^{-/-}$OT-I CTL were assessed by RT-qPCR. GAPDH was used as a loading control [Fut8$^{+/+}$OT-I and Fut8$^{-/-}$OT-I mice (n = 3 per group) in panel G]. ***$p < 0.001$ [Student's *t*-test (unpaired)]. Histograms show the quantification data of IFN-γ and IL-2 relative to GAPDH. (H) Expressions of PD-1 and granzyme B in lung adenocarcinoma patient specimens by Fut8 knockdown. The sections were incubated with anti-PD-1 Ab (1:200) and anti-granzyme B Ab (1:100) (n = 3 in panel H). *$p < 0.05$ [Student's *t*-test (unpaired)]. Data (B–H) were shown as mean ± SD of triplicates and were representative of three independent experiments.

promote the expression of PD-1 and PD-L1 at the posttranslational level and, therefore, suppress CTL activation. Blocking core fucosylation of PD-1 enhanced T-cell activation [13]. We clarified that Fut8 ablation significantly promoted the CTL cytotoxic capacity with sharply reduced PD-1 expression. Furthermore, loss of core fucosylation dramatically increased the cytotoxicity ability of CTL upon $OVA_{257\text{-}264}$ stimulation in Fut8$^{-/-}$OT-I CTL, and the tumor formation in Fut8$^{-/-}$OT-I xenograft mice was significantly inhibited. Moreover, the urethane-induced lung adenocarcinoma was significantly decreased in Fut8$^{-/-}$ mice and the tumor formation was mainly recovered in Fut8$^{-/-}$ mice with depletion of CTLs. Indeed, Fut8 could modify multiple proteins and the hyper core fucosylation could promote the expression of molecules correlated with tumorigenesis [2]. Knockdown of Fut8 gene downregulated the expression of genes associated with tumor malignancy and suppressed tumor metastasis, tumor growth, and survival in NSCLC [26]. However, there is no significant difference in cell viability between the Fut8$^{+/+}$ and Fut8$^{-/-}$ cancer cells. These results suggested that the loss of core fucosylation can enhance the cytotoxic activity of CTLs, rather than suppress tumor cell proliferation.

Tumor development is accompanied by changes in the expression of glycosyltransferases and glycosidases, and these changes play a powerful role in regulating CTL response. The most important finding of the present study is the identification of the

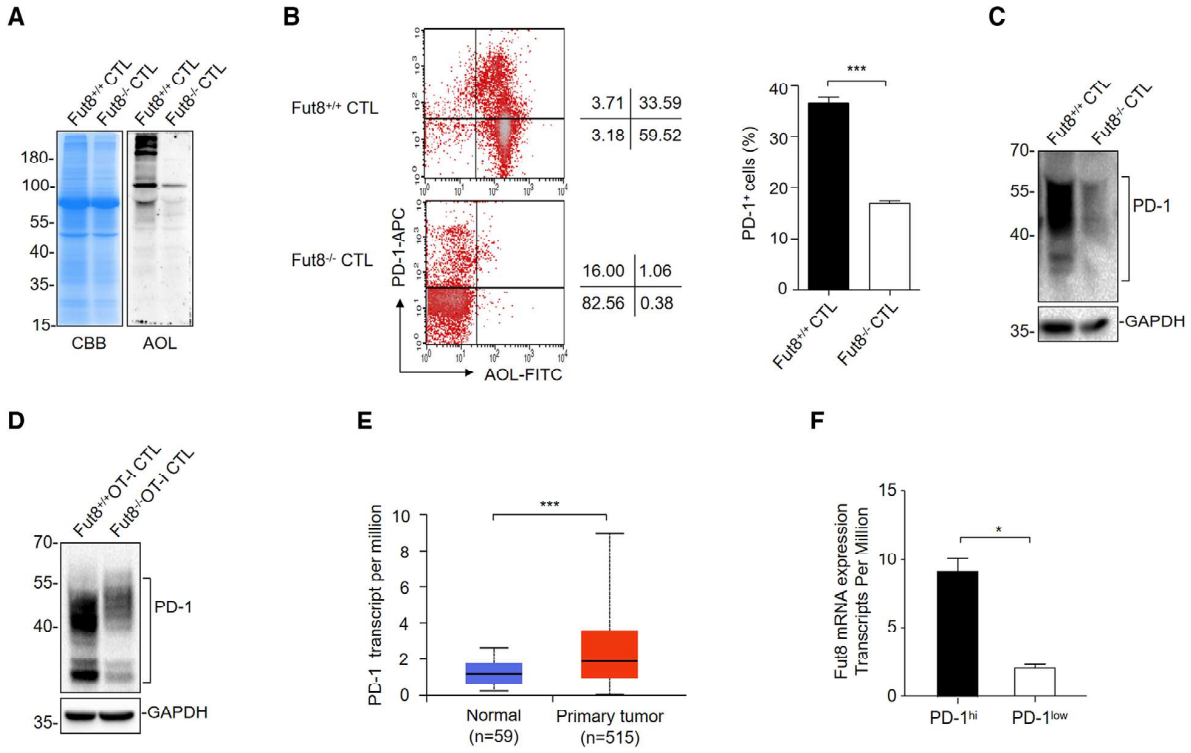

Figure 4. PD-1 expression was significantly reduced in Fut8$^{-/-}$ CTLs. (A) AOL blot of Fut8$^{+/+}$ CTL and Fut8$^{-/-}$ CTL. 10 μg CTL lysates were run on 10% SDS–PAGE gel, and the membrane was stained with CBB and AOL (1:5000) [Fut8$^{+/+}$ and Fut8$^{-/-}$ mice (n = 3 per group)]. (B) PD-1 and AOL expression were measured by a polychromatic flow cytometry assay. CTL were extracted from splenic cells [Fut8$^{+/+}$ and Fut8$^{-/-}$ mice (n = 3 per group)] and incubated with anti-PD-1 Ab (1:1000) and AOL (1:10 000). ***$p < 0.001$ [Student's *t*-test (unpaired)]. (C) PD-1 expression of Fut8$^{+/+}$ CTL and Fut8$^{-/-}$ CTL detected by Western blot. CTL were extracted from Fut8$^{+/+}$ and Fut8$^{-/-}$ mice splenic cells [Fut8$^{+/+}$ and Fut8$^{-/-}$ mice (n = 3 per group)]. 20 μg CTL lysates were stained with anti-PD-1 Ab (1:1000). Anti-GAPDH Ab (1:10 000) was used as a loading control. (D) PD-1 expression of activated Fut8$^{+/+}$OT-I CTL and Fut8$^{-/-}$OT-I CTL. CTL was extracted from Fut8$^{+/+}$OT-I and Fut8$^{-/-}$OT-I mice splenic cells and activated with $OVA_{257\text{-}264}$ (10 μg/mL) in the presence of IL-2 (20 ng/mL) for 48 h [Fut8$^{+/+}$OT-I and Fut8$^{-/-}$OT-I mice (n = 3 per group)]. 20 μg CTL lysates were stained with anti-PD-1 Ab (1:1000). Anti-GAPDH Ab (1:10 000) was used as a loading control. Data (A–D) were shown as mean ± SD of triplicates and were representative of three independent experiments. (E) Boxplot from Ualcan showing the relative expression of PD-1 in 59 normal and 515 lung adenocarcinoma samples. (F) Fut8 mRNA expression in high expressed PD-1 (PD-1^{hi}) TILs and low expressed PD-1 (PD-1^{low}) TILs from NSCLC patients. *$p < 0.05$; [Student's *t*-test (unpaired)].

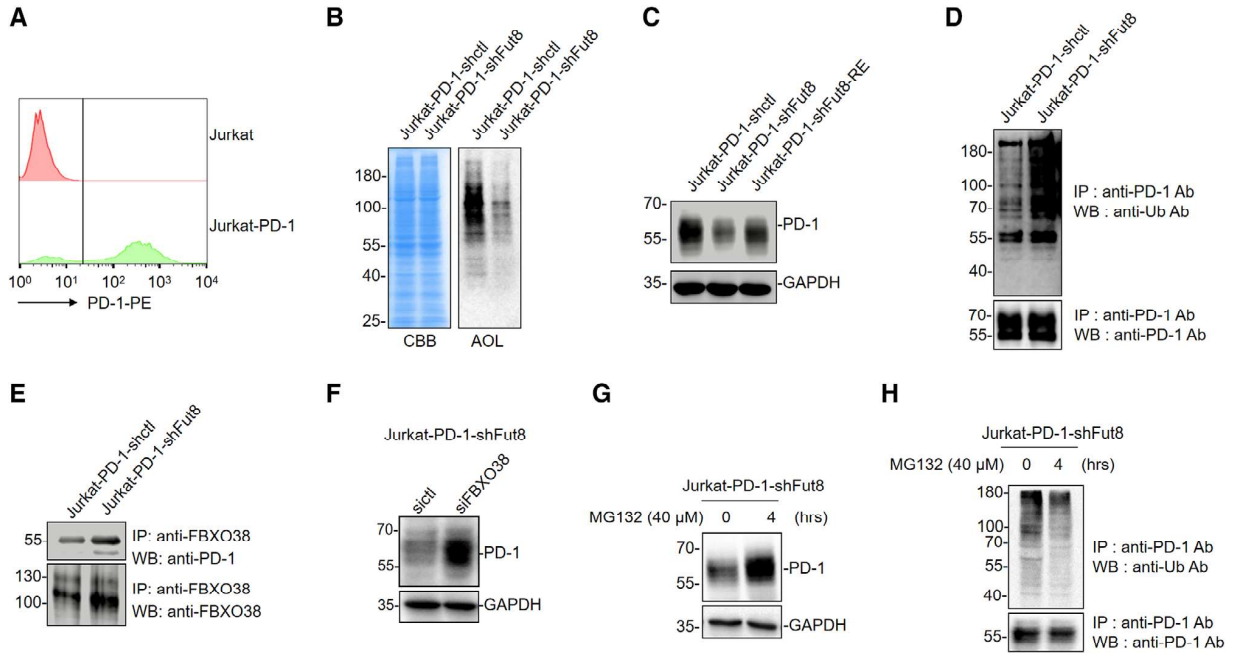

Figure 5. Loss of core fucosylation promotes PD-1 ubiquitination and its degradation in the proteasome. (A) Establishment of PD-1 overexpressing Jurkat T cells (Jurkat-PD-1). Jurkat T cells were transfected with PD-1-CV358-GFP plasmid, and the PD-1 expression on cell surface was verified by flow cytometry [Anti-PD-1 Ab (1:1000)]. (B) Core fucosylation level in Fut8 knockdown Jurkat-PD-1 cell (Jurkat-PD-1-shFut8). 10 μg cell lysates were run on 10% SDS–PAGE gel and stained with AOL (1:5000) and CBB staining. (C) The PD-1 expression in Jurkat-PD-1-shctl, Jurkat-PD-1-shFut8 and Jurkat-PD-1-shFut8-RE cells. 20 μg cell lysates were run on 10% SDS-PAGE gel and stained with anti-PD-1 Ab (1:1000). Anti-GAPDH Ab (1:10 000) was used as a loading control. (D) PD-1 ubiquitination in Jurkat-PD-1-shFut8 cells. Cell lysates (200 μg) were immunoprecipitated with an anti-PD-1 Ab. The immunoprecipitates were probed with the anti-Ub Ab (1:200) and anti-PD-1 Ab (1:1000). (E) Expression of FBXO38 in Jurkat-PD-1-shFut8 cells. Cell lysates (200 μg) were immunoprecipitated with an anti-FBXO38 Ab, and probed with the anti-PD-1 Ab (1:1000) and anti-FBXO38 Ab (1:1000). (F) PD-1 expression in Jurkat-PD-1-shFut8 cells by siFBXO38 treatment. 20 μg cell lysates were run on 10% SDS–PAGE gel and stained with anti-PD-1 Ab (1:1000). Anti-GAPDH Ab (1:10 000) was used as a loading control. (G) PD-1 expression after MG132 treatment in Jurkat-PD-1-shFut8. Jurkat-PD-1-shFut8 cells were treated with MG132 (40 μM) for 4 h. 20 μg cell lysates were run on 10% SDS-PAGE gel and stained with anti-PD-1 Ab (1:1000). Anti-GAPDH Ab (1:1000) was used as a loading control. (H) PD-1 ubiquitination of Jurkat-PD-1-shFut8 cells after treatment with 40 μM MG132 for 4 h. Cell lysates (200 μg) were immunoprecipitated with an anti-PD-1 Ab. The immunoprecipitates were then probed with the anti-Ub Ab (1:200) and anti-PD-1 Ab (1:1000). Data (A–H) were representative of three independent experiments.

regulation role of Fut8 in PD-1 expression on CTLs, which in turn, regulates several parameters of antitumor related events, such as CTL activation, cytotoxicity, and cancer eradication in lung adenocarcinoma. Based on the data showing that blocking core fucosylation in tumor promotes antitumor immunity of CTLs through downregulated PD-1 expression, we propose that Fut8 ablation could be considered as a rational immunotherapy strategy for lung cancer.

Materials and methods

Antibodies

Anti-Ub Ab (P4D1) was from Santa Cruz Biotechnology. Anti-human PD-1 Ab (D4W2J), anti-mouse PD-1 Ab (D7D5W), anti-human PD-L1 Ab (E1L3N), and anti-granzyme B Ab (D6E9W) were from Cell Signaling Technology (Beverly, MA, USA). InVivoMab anti-CD8 Ab (53-5.8) and anti-PD-1 Ab (RMP1-14) were from Bio X Cell. Anti-GAPDH Ab (1E6D9) was from Proteintech Group (Chicago, IL, USA). Anti-mouse PD-L1 Ab (ab213480), anti-FBXO38 Ab (ab87729) and HRP-conjugated streptavidin (ab7403) were from Abcam (Cambridge, UK). Anti-CD16/32 Ab (2.4G2), FITC-labeled anti-mouse CD69 Ab (H1.2F3), APC-labeled hamster anti-mouse CD279 (PD-1) Ab (J43), APC-labeled anti-CD8 Ab (53-6.7), and PE-labeled anti-human CD279 (PD-1) Ab (EH12.2 H7) were from e-Bioscience (Beijing, China). Andy Fluor TM 488 Streptavidin was from GeneCopoeia (Guangzhou, China). Horseradish peroxidase (HRP)-conjugated anti-mouse IgG, HRP-conjugated anti-rabbit IgG, and HRP-conjugated streptavidin were from Beyotime (Shanghai, China). $OVA_{257-264}$ was from SciLight Biotechnology (Beijing, China), and IL-2 was from Multi Science (Hangzhou, China).

Human lung adenocarcinoma tissue microarray analysis

Human lung adenocarcinoma tissue microarrays, including 92 lung adenocarcinoma and their corresponding adjacent lung tis-

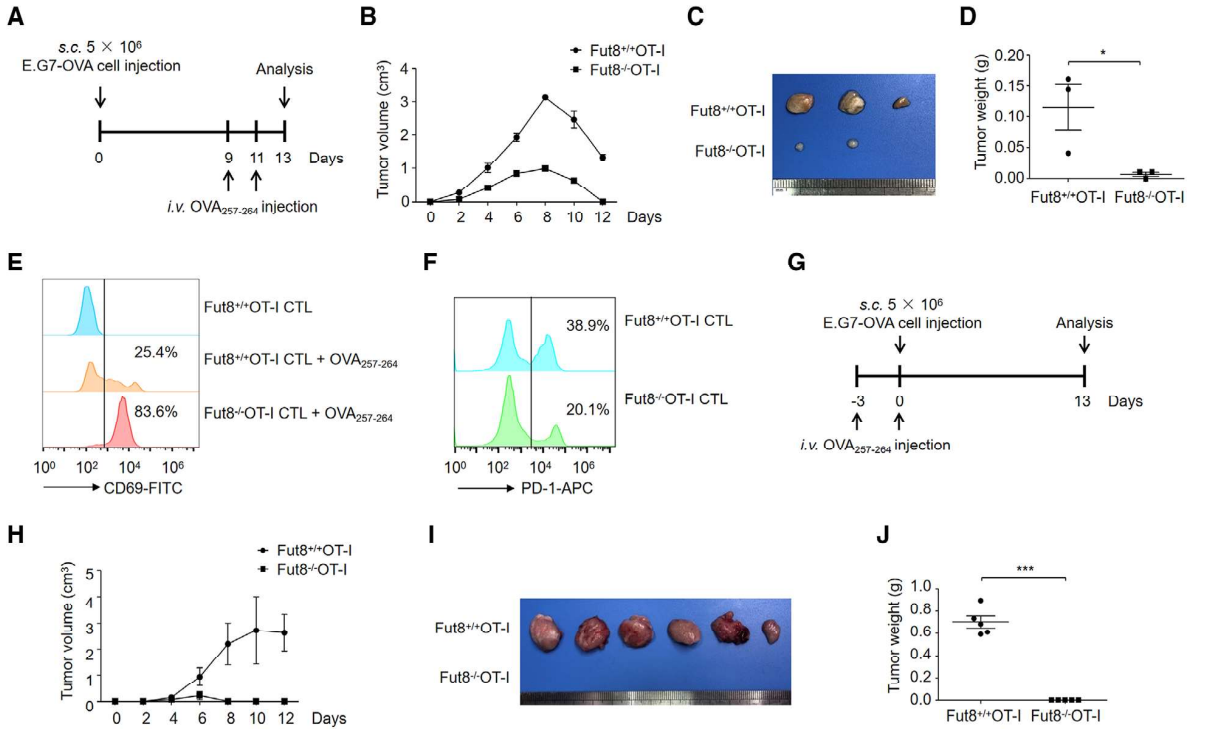

Figure 6. Loss of core fucosylation inhibits tumor formation on xenograft-bearing mice. (A) Experimental outline. Fut8$^{+/+}$OT-I and Fut8$^{-/-}$OT-I mice were injected s.c. with 5 × 10^6 E. G7-OVA cells on bilateral backside, abdomen, and armpit of mice. Once tumors were well established on day 9, xenograft-bearing mice received i.v. with 2.5 mg/g $OVA_{257-264}$ in PBS. Two days later, mice were treated with the same amount of $OVA_{257-264}$ again. Mice were sacrificed on day 13. (B) Tumor volume was measured every 2 days. (C) The sizes of tumor mass were shown on day 13 after tumor cell challenge. (D) Tumor weight of resected xenograft tumor was measured and plotted. (E) Percentage of CD69$^+$ cells. CD8$^+$ T cells were isolated from mice splenic cells by MACS. Fut8$^{+/+}$OT-I and Fut8$^{-/-}$OT-I CTLs were stained with anti-CD69 Ab (1:100). Numbers indicated the percentage of CD69$^+$ cells, and 10 000 events were acquired for each analysis. (F) Percentage of PD-1$^+$ cells. Fut8$^{+/+}$OT-I and Fut8$^{-/-}$OT-I CTLs were stained with anti-PD-1 Ab (1:1000). [Fut8$^{+/+}$OT-I and Fut8$^{-/-}$OT-I mice (n = 3 per group) in panel A–F]. $^*p < 0.05$ [Student's *t*-test (unpaired)]. (G) Experimental outline. Fut8$^{+/+}$OT-I and Fut8$^{-/-}$OT-I mice were injected i.v. with 2.5 mg/g $OVA_{257-264}$ in PBS on day −3 and day 0 (−3 and 0 were days before tumor challenge). On day 0, Fut8$^{+/+}$OT-I and Fut8$^{-/-}$OT-I mice were injected s.c. with 5 × 10^6 E. G7-OVA cells. Mice were sacrificed on day 13. (H) Tumor volume was measured every 2 days. (I) The sizes of tumor mass were shown on day 13 after tumor cell challenge. (J) Tumor weight of resected xenograft tumor was measured and plotted. [Fut8$^{+/+}$OT-I and Fut8$^{-/-}$OT-I mice (n = 3 per group) in panel G–J]. $^{***}p < 0.001$ [Student's *t*-test (unpaired)]. Data (C, E, F, and I) were representative of three independent experiments. Data (B, D, H, and J) were shown as mean ± SD of triplicates and were representative of three independent experiments.

sues, were performed by Outdo Biotech Company (Shanghai, China). All of the patients with complete surgical resection were collected between July 2008 and June 2013 in China. The OS for the corresponding patients was calculated from the day of surgery to the day of death or to the last follow-up. The associations of pathological characteristics with cumulative survival were evaluated using Kaplan–Meier analysis.

Clinical samples

Serum samples were collected from 36 lung adenocarcinoma patients and 16 healthy donors. Lung adenocarcinoma samples were collected from 10 lung adenocarcinoma patients. The diagnosis of lung adenocarcinoma was made based on clinical manifestation, serology, imaging, and histopathology. Lung adenocarcinoma tissue and serum were from patients between April 2017 and April 2019 in Tianjin Medical University Cancer Institute & Hospital, Tianjin, China. The Ethics Committee at the hospital approved the study (No. Bc2019025).

Mice

Fut8$^{-/-}$ mice were generated as previously described [34]. OT-I mice were obtained from Biomedical Research Institute of Nanjing University, Nanjing, China. Fut8$^{+/+}$OT-I mice and Fut8$^{-/-}$OT-I mice were generated by crossing heterozygous Fut8$^{+/-}$OT-I mice. Mice were maintained in a room illuminated for 12 hours (08:00 to 20:00) and kept at 24 ± 1°C with free access to food and water in the specific pathogen-free laboratory animal facility of Dalian Medical University, Dalian, China. All the animal works were approved by the Ethics Committee of Dalian Medical University (No. AEE17013).

Western blot and lectin blot analysis

Equal amounts of protein samples were separated by sodium dodecyl sulfate polyacrylamide gel electrophoresis (SDS–PAGE), and separated proteins were transferred to the nitrocellulose membrane (Merck Millipore, USA). Membranes were blocked with 5% fat-free milk or 5% BSA in TBS-T (10 mM Tris–HCl, 150 mM NaCl, and 0.1% Tween 20) for 1 h at RT. Following incubation with the appropriate primary antibodies or AOL (Vector Laboratories) at 4°C overnight, the membranes were incubated with the HRP-conjugated streptavidin or HRP-labeled secondary Abs at RT for 1 h, and visualized with an ECL system (Amersham, Sweden).

Immunohistochemistry

Tissues were embedded in paraffin after fixed in 4% paraformaldehyde, and 5 μm sections were prepared. Sections were deparaffinized in xylene and hydrated through a 100, 90, 80, and 70% ethanol to PBS. Slides were incubated with 3% H_2O_2 for 30 min and blocked with an avidin/biotin blocking kit (Vector Laboratories, USA). Slides were then incubated with primary antibody for 1 h. After washing, secondary antibody was incubated for 40 min at 37°C and visualized with 3,3′-diaminobenzidine (DAB) (Solarbio, China). The intensity of staining was analyzed by integrated optical density using Image-Pro® Plus software (version 6.0; Media Cybernetics, USA).

Fut8 enzyme activity assay

The Fut8 enzyme activity was measured as described previously [31]. In brief, 30 μg cell lysates as the enzyme source were added to the assay buffer (200 mM MES, 1% Triton X-100) supplemented with donor (500 μM GDP-L-fucose) and substrate [50 μM GnGn-Asn-4-(2-pyridylamine) butylamine]. The mixture was incubated at 37°C for 8 h, and the reaction was stopped by heating at 100°C for 5 min. Reaction products were subjected to high-performance liquid chromatography with a fluorescent detector (Waters, USA).

Establishment of mouse lung adenocarcinoma model and $CD8^+$ T-cell depletion

For lung adenocarcinoma mice model, 8-week-old $Fut8^{+/+}$ and $Fut8^{-/-}$ mice (n = 6 per group) were received intraperitoneal (i.p.) injections of urethane (1 mg/g body weight; U2500; Merck Millipore, Germany) freshly dissolved in 0.9% saline solution every 3 days, they were monitored according to Institutional Animal Care and Use Committee (IACUC) animal facilities rules and regulations.

For CD8-depletion, $Fut8^{-/-}$ mice (n = 6 per group) were administered i.p. injection at a dose of 500 μg anti-CD8 Ab on three consecutive days (day -3, -2, and -1) prior to establishment of mouse lung adenocarcinoma model. The depletion of $CD8^+$ T cells were evaluated by flow cytometry.

Lung adenocarcinoma cells extraction from urethane-induced mice

Mice were sacrificed, and tumor tissue was separated from lung and cut into pieces. The tumor tissue was digested with 0.25% trypsin (Gibco, USA). Single tumor cell suspensions were prepared by passing through 30 μm nylon mesh. Tumor cells were cultured in RPMI 1640 medium.

Cell proliferation assay

Cell proliferation was measured using the 3-(4,5-dimethylthiazol-2-yl)-2,5 diphenyltetrazolium bromide (MTT; Sigma, Germany). Cells were plated in a 96-well plate, and 10 mg/mL MTT was added for the last 4 h at 37°C. After incubation, the media was removed and 200 μL dimethylsulfoxide (DMSO) (Sigma, Germany) was added to each well. Cell viability was assessed at 595 nm with the microplate reader (Thermo, Finland).

Cell lines and culture conditions

A549, H1299, E. G7-OVA, Jurkat, and 293T cells were obtained from the American Type Culture Collection (ATCC, USA). A549, H1299, Jurkat, and E. G7-OVA cells were maintained in RPMI 1640 medium (Gibco, USA), and 293T cells were maintained in Dulbecco's modified Eagle's medium (Gibco, USA). All cells were cultured in medium supplemented 10% FBS (BI, China), penicillin (60 μg/mL), and streptomycin (100 μg/mL) (Sangon, China) and maintained in an incubator with 5% CO_2 at 37°C.

Cell lysis

Cells were centrifuged at 200 × *g* for 3 min and lysed on ice with protein lysis buffer (50 mM Tris–HCl pH = 8.0, 1% Trion X-100, 150 mM NaCl, 10% glycerol, 2 mM EDTA, 100 μM PMSF) for 30 min. Then cells were centrifuged at 20 000 × *g* at 4°C for 10 min. The supernatants were collected, and protein concentration was measured by the bicinchoninic acid protein assay (BCA assay kit; Takara, China).

Establishment of Fut8 knockdown and Fut8 reintroduced cells

The pLKO.1 shRNA lenti-virus system was used to generate shRNA virus against human *Fut8* gene (shFut8). The shFut8 (sense: TCTCAGAATTGGCGCTATG, antisense: CATAGCGCCAATTCTGAGA, vector: psi-LVRU6GP) [5] and negative control (shctl) were purchased from Genecopoeia (Guangzhou, China). Positive cells were obtained by puromycine (3 μg/mL) selection.

To prepare *Fut8* reintroduced cells, pLHCXsi-U6-*Fut8* mutant expression vectors resistant to the siRNAs expressed in

Jurkat-PD-1-shFut8 cells were prepared. The pLHCXsi-U6-*Fut8* mutant vector was transduced to Jurkat-PD-1-shFut8 cells by lipofectamine, and Fut8 restored (Jurkat-PD-1-shFut8-RE) cells were generated after selection with 300 μg/mL hygromycin.

FBXO38 siRNA transfection

Lipofectamine 3000 (#L3000-015, Invitrogen) was used for the siRNA transfection according to the manufacture instructions. The siRNA for FBXO38 (5′-GGUGGUGGCCGAGAGUGGAAAUAAU-3′) and negative control (shctl) were synthesized in Genecopoeia.

Xenograft tumor models

To generate tumor xenografts in nude mice, 5×10^6 of A549 shctl, A549 shFut8 cells, and H1299 shctl, H1299 shFut8 in 150 μL of PBS were injected subcutaneously (s.c.) into bilateral armpit of mice. Tumor size was measured every other day.

To generate tumor xenografts, 5×10^6 of E. G7-OVA cells in 150 μL of PBS were injected by the same way as above into $Fut8^{+/+}$OT-I and $Fut8^{-/-}$OT-I mice. $OVA_{257\text{-}264}$ peptides (2.5 mg/g) were injected into tail vain (i.v.) twice at day -3 and day 0 before tumor cells were injected or at day 9 and day 11 after tumor inoculation. Mice were sacrificed at day 13. Tumor volumes were calculated according to the following formula: tumor volume = (length) × $(\text{width})^2 \times 0.5$, and tumor weights were recorded.

Flow cytometric analysis

Cells were isolated from spleen and incubated with an anti-CD16/CD32 (2.4G2) mAb to block Fcγ receptors. The cells were stained on ice for 1 h with several combinations of mAbs, as indicated in the figure legends. Flow cytometry was performed on a FACS-Calibur (Becton Dickinson, USA) and analyzed with FlowJo software (Tree Star). The flow cytometry experiments were performed according to the guidelines [35].

MACS magnetic cell sorting

Single splenic cell suspensions were prepared by first grinding the tissues and passing through 30 μm nylon mesh. Red blood cells were lysed with 0.83% NH_4Cl and 0.17 M Tris–HCl (pH 7.65) for 5 min at RT. $CD8^+$ T cells were positively isolated with anti-CD8a (Ly-2) Ab magnetic beads (Miltenyi, Germany). The purified cells were routinely more than 95% pure detected by flow cytometry.

Lactate dehydrogenase assay

CTLs were activated with 10 μg/mL $OVA_{257\text{-}264}$ for 48 h supplied with 50 ng/mL recombinant mouse IL-2. CTL and E. G7-OVA were regarded as effector cell (E) and target cell (T), respectively. E. G7-OVA cells were cultured with activated CTLs for indicated time. For antibody treatment assay, CTLs were incubated with 10 μg/mL anti-PD-1 (RMP1-14) Ab before coculture. Released LDH was measured with the kit (Cytotoxicity LDH Assay Kit-WST®, CK12).

Quantitative RT-PCR

Total RNA from cells was extracted using RNAiso Plus reagent (TaKaRa, China). cDNAs were synthesized using PrimeScript RT Master Mix (TaKaRa, China). RT-PCR was performed using SYBR Green Master Mix by an Applied Biosystems Prism 7000 Sequence Detection System (Applied Biosystems, Japan). Relative fold changes of target genes amplification were calculated according to the $2^{-\Delta\Delta Ct}$ method. Primers for IL-2 (sense: 5′-CCT GAG CAG GAT GGA GAA TTA CA-3′, antisense: 5′-TCC AGA ACA TGC CGC AGA G-3′), and INF-γ (sense: 5′-CGG CAC AGT CAT TGA AAG CCT A-3′, antisense: 5′-GCC AGT TCC AGA TAT CCA A-3′) were used for RT-qPCR.

Establishment of PD-1 overexpressed Jurkat cells

Jurkat cells were transfected with control or GV358-PD1-GFP plasmids using the lentiviral packing systems. Virus infection was conducted by incubating virus solution with cells for 48 h, and the positive cells were selected by 3 μg/mL puromycine.

Immunoprecipitation

Cell extracts (500 μg) were mixed with the indicated antibodies overnight with gentle shaking and then added 20 μL protein G-Sepharose (50% slurry) (Sangon, China) for another incubation for 2 h at 4°C. The pull-downed samples were boiled for 5 min in 25 μL 2 × Laemmli sample buffer.

Statistical analysis

Data were presented as mean ± standard deviation (SD) from at least three biologically repeated experiments. Two-tailed Student's *t*-tests were performed to compare the statistical differences between groups using GraphPad Prism software version 7, $p < 0.05$ was considered statistically significant. $^*p < 0.05$, $^{**}p < 0.01$, $^{***}p < 0.001$.

Acknowledgements: This work was supported by the National Natural Science Foundation of China (31870797, 31570797,

81572891), Liaoning Provincial Program for Top Discipline of Basic Medical Sciences, and Tianjin Science and Technology Support Plan Key Projects (18YFZCSY00550).

Conflict of interest: The authors declare no commercial or financial conflict of interest.

References

1 **Ramalingam, S. S.**, **Perol, M.**, **Reck, M.**, **Kowalyszyn, R. D.**, **Gautschi, O.**, **Kimmich, M.**, **Cho, E. K.** et al., Efficacy and safety of ramucirumab with docetaxel versus placebo with docetaxel as second-line treatment of advanced non-small-cell lung cancer: a subgroup analysis according to patient age in the REVEL trial. *Clin. Lung Cancer* 2018. **19**: 270–279.

2 **Tateno, H.**, **Nakamura-Tsuruta, S.** and **Hirabayashi, J.**, Comparative analysis of core-fucose-binding lectins from *Lens culinaris* and *Pisum sativum* using frontal affinity chromatography. *Glycobiology* 2009. **19**: 527–536.

3 **Wilson, J. R.**, **Williams, D.** and **Schachter, H.**, The control of glycoprotein synthesis: *N*-acetylglucosamine linkage to a mannose residue as a signal for the attachment of L-fucose to the asparagine-linked *N*-acetylglucosamine residue of glycopeptide from alpha1-acid glycoprotein. *Biochem. Biophys. Res. Commun.* 1976. **72**: 909–916.

4 **Lv, X.**, **Song, J.**, **Xue, K.**, **Li, Z.**, **Li, M.**, **Zahid, D.**, **Cao, H.** et al., Core fucosylation of copper transporter 1 plays a crucial role in cisplatin-resistance of epithelial ovarian cancer by regulating drug uptake. *Mol. Carcinog.* 2019. **58**: 794–807.

5 **Li, W.**, **Nakagawa, T.**, **Koyama, N.**, **Wang, X.**, **Jin, J.**, **Mizuno-Horikawa, Y.**, **Gu, J.** et al., Down-regulation of trypsinogen expression is associated with growth retardation in alpha1,6-fucosyltransferase-deficient mice: attenuation of proteinase-activated receptor 2 activity. *Glycobiology* 2006. **16**: 1007–1019.

6 **Li, W.**, **Liu, Q.**, **Pang, Y.**, **Jin, J.**, **Wang, H.**, **Cao, H.**, **Li, Z.** et al, Core fucosylation of μ heavy chains regulates assembly and intracellular signaling of precursor B cell receptors. *J. Biol. Chem.* 2012. **287**: 2500–2508.

7 **Honma, R.**, **Kinoshita, I.**, **Miyoshi, E.**, **Tomaru, U.**, **Matsuno, Y.**, **Shimizu, Y.**, **Takeuchi, S.** et al., Expression of fucosyltransferase 8 is associated with an unfavorable clinical outcome in non-small cell lung cancers. *Oncology* 2015. **88**: 298–308.

8 **Tu, C. F.**, **Wu, M. Y.**, **Lin, Y. C.**, **Kannagi, R.** and **Yang, R. B.**, FUT8 promotes breast cancer cell invasiveness by remodeling TGF-beta receptor core fucosylation. *Breast Cancer Res.* 2017. **19**: 111.

9 **Meiraz, A.**, **Garber, O. G.**, **Harari, S.**, **Hassin, D.** and **Berke, G.**, Switch from perforin-expressing to perforin-deficient CD8(+) T cells accounts for two distinct types of effector cytotoxic T lymphocytes in vivo. *Immunology* 2009. **128**: 69–82.

10 **Cho, H.**, **Kang, H.**, **Lee, H. H.** and **Kim, C. W.**, Programmed cell death 1 (PD-1) and cytotoxic T lymphocyte-associated antigen 4 (CTLA-4) in viral hepatitis. *Int. J. Mol. Sci.* 2017. **18**: 1517.

11 **Chemnitz, J. M.**, **Parry, R. V.**, **Nichols, K. E.**, **June, C. H.** and **Riley, J. L.**, SHP-1 and SHP-2 associate with immunoreceptor tyrosine-based switch motif of programmed death 1 upon primary human T cell stimulation, but only receptor ligation prevents T cell activation. *J. Immunol.* 2004. **173**: 945–954.

12 **Hamanishi, J.**, **Mandai, M.**, **Matsumura, N.**, **Abiko, K.**, **Baba, T.** and **Konishi, I.**, PD-1/PD-L1 blockade in cancer treatment: perspectives and issues. *Int. J. Clin. Oncol.* 2016. **21**: 462–473.

13 **Okada, M.**, **Chikuma, S.**, **Kondo, T.**, **Hibino, S.**, **Machiyama, H.**, **Yokosuka, T.**, **Nakano, M.** et al., Blockage of core fucosylation reduces cell-surface expression of PD-1 and promotes anti-tumor immune responses of T cells. *Cell Rep.* 2017. **20**: 1017–1028.

14 **Li, C. W.**, **Lim, S. O.**, **Xia, W.**, **Lee, H. H.**, **Chan, L. C.**, **Kuo, C. W.**, **Khoo, K. H.** et al., Glycosylation and stabilization of programmed death ligand-1 suppresses T-cell activity. *Nat. Commun.* 2016. **7**: 12632.

15 **Lin, D. Y.**, **Tanaka, Y.**, **Iwasaki, M.**, **Gittis, A. G.**, **Su, H. P.**, **Mikami, B.**, **Okazaki, T.** et al., The PD-1/PD-L1 complex resembles the antigen-binding Fv domains of antibodies and T cell receptors. *Proc. Natl. Acad. Sci. U. S. A.* 2008. **105**: 3011–3016.

16 **Terawaki, S.**, **Chikuma, S.**, **Shibayama, S.**, **Hayashi, T.**, **Yoshida, T.**, **Okazaki, T.** and **Honjo, T.**, IFN-alpha directly promotes programmed cell death-1 transcription and limits the duration of T cell-mediated immunity. *J. Immunol.* 2011. **186**: 2772–2779.

17 **Martinez, G. J.**, **Pereira, R. M.**, **Aijo, T.**, **Kim, E. Y.**, **Marangoni, F.**, **Pipkin, M. E.**, **Togher, S.** et al., The transcription factor NFAT promotes exhaustion of activated CD8(+) T cells. *Immunity* 2015. **42**: 265–278.

18 **Liu, Q.**, **Krishnasamy, Y.**, **Rehman, H.**, **Lemasters, J. J.**, **Schnellmann, R. G.** and **Zhong, Z.**, Disrupted renal mitochondrial homeostasis after liver transplantation in rats. *PLoS One* 2015. **10**: e0140906.

19 **Mezzadra, R.**, **Sun, C.**, **Jae, L. T.**, **Gomez-Eerland, R.**, **de Vries, E.**, **Wu, W.**, **Logtenberg, M. E. W.** et al., Identification of CMTM6 and CMTM4 as PD-L1 protein regulators. *Nature* 2017. **549**: 106–110.

20 **Morales-Betanzos, C. A.**, **Lee, H.**, **Gonzalez Ericsson, P. I.**, **Balko, J. M.**, **Johnson, D. B.**, **Zimmerman, L. J.** and **Liebler, D. C.**, Quantitative mass spectrometry analysis of PD-L1 protein expression, *N*-glycosylation and expression stoichiometry with PD-1 and PD-L2 in human melanoma. *Mol. Cell. Proteomics* 2017. **16**: 1705–1717.

21 **Ho, W. L.**, **Hsu, W. M.**, **Huang, M. C.**, **Kadomatsu, K.** and **Nakagawara, A.**, Protein glycosylation in cancers and its potential therapeutic applications in neuroblastoma. *J. Hematol. Oncol.* 2016. **9**: 100.

22 **Matsumura, K.**, **Higashida, K.**, **Ishida, H.**, **Hata, Y.**, **Yamamoto, K.**, **Shigeta, M.**, **Mizuno-Horikawa, Y.** et al., Carbohydrate binding specificity of a fucose-specific lectin from *Aspergillus oryzae*: a novel probe for core fucose. *J. Biol. Chem.* 2007. **282**: 15700–15708.

23 **Brahmer, J. R.**, **Drake, C. G.**, **Wollner, I.**, **Powderly, J. D.**, **Picus, J.**, **Sharfman, W. H.**, **Stankevich, E.** et al., Phase I study of single-agent anti-programmed death-1 (MDX-1106) in refractory solid tumors: safety, clinical activity, pharmacodynamics, and immunologic correlates. *J. Clin. Oncol.* 2010. **28**: 3167–3175.

24 **Do, J. S.**, **Choi, Y. H.**, **Shin, S. H.**, **Yi, H. K.**, **Hwang, P. H.** and **Nam, S. Y.**, Committed memory effector type 2 cytotoxic T (Tc2) cells are ineffective in protective anti-tumor immunity. *Immunol. Lett.* 2004. **95**: 77–84.

25 **Meng, X.**, **Liu, X.**, **Guo, X.**, **Jiang, S.**, **Chen, T.**, **Hu, Z.**, **Liu, H.** et al., FBXO38 mediates PD-1 ubiquitination and regulates anti-tumour immunity of T cells. *Nature* 2018. **564**: 130–135.

26 **Chen, C. Y.**, **Jan, Y. H.**, **Juan, Y. H.**, **Yang, C. J.**, **Huang, M. S.**, **Yu, C. J.**, **Yang, P. C.** et al., Fucosyltransferase 8 as a functional regulator of nonsmall cell lung cancer. *Proc. Natl. Acad. Sci. U. S. A.* 2013. **110**: 630–635.

27 **Kerr, K. M.** and **Nicolson, M. C.**, Non-Small Cell Lung Cancer, PD-L1, and the Pathologist. *Arch. Pathol. Lab. Med.* 2016. **140**: 249–254.

28 **Jiang, Y.**, **Zhao, X.**, **Fu, J.** and **Wang, H.**, Progress and challenges in precise treatment of tumors with PD-1/PD-L1 blockade. *Front. Immunol.* 2020. **11**: 339.

29 **Shrikhande, G. V.**, **Scali, S. T.**, **da Silva, C. G.**, **Damrauer, S. M.**, **Csizmadia, E.**, **Putheti, P.**, **Matthey, M.** et al., O-Glycosylation regulates ubiquitination and degradation of the anti-inflammatory protein A20 to accelerate atherosclerosis in diabetic ApoE-null mice. *PLoS One* 2010. **5**: e14240.

30 **Calderon, A. D.**, **Liu, Y.**, **Li, X.**, **Wang, X.**, **Chen, X.**, **Li, L.** and **Wang, P. G.**, Substrate specificity of FUT8 and chemoenzymatic synthesis of core-fucosylated asymmetric N-glycans. *Org. Biomol. Chem.* 2016. **14**: 4027–4031.

31 **Li, W.**, **Yu, R.**, **Ma, B.**, **Yang, Y.**, **Jiao, X.**, **Liu, Y.**, **Cao, H.** et al., Core fucosylation of IgG B cell receptor is required for antigen recognition and antibody production. *J. Immunol.* 2015. **194**: 2596–2606.

32 **Liang, W.**, **Mao, S.**, **Li, M.**, **Zhang, N.**, **Sun, S.**, **Fang, H.**, **Zhang, J.** et al., Ablation of core fucosylation attenuates the signal transduction via T cell receptor to suppress the T cell development. *Mol. Immunol.* 2019. **112**: 312–321.

33 **Serman, T. M.** and **Gack M. U.**, FBXO38 drives PD-1 to destruction. *Trends Immunol.* 2019. **40**: 81–83.

34 **Wang, X.**, **Inoue, S.**, **Gu, J.**, **Miyoshi, E.**, **Noda, K.**, **Li, W.**, **Mizuno-Horikawa, Y.** et al., Dysregulation of TGF-beta1 receptor activation leads to abnormal lung development and emphysema-like phenotype in core fucose-deficient mice. *Proc. Natl. Acad. Sci. U. S. A.* 2005. **102**: 15791–15796.

35 **Cossarizza, A.**, **Chang, H. D.**, **Radbruch, A.**, **Acs, A.**, **Adam, D.**, **Adam-Klages, S.**, **Agace, W. W.** et al., Guidelines for the use of flow cytometry and cell sorting in immunological studies (second edition). *Eur. J. Immunol.* 2019. **49**: 1457–1973.

Full correspondence: Dr. Wenzhe Li, College of Basic Medical Sciences, Dalian Medical University, 9-Western Section, Lvshun South Road, Dalian, Liaoning 116044, China
e-mail: liwenzhe@dmu.edu.cn
Xun Jin, Tianjin Medical University Cancer Institute and Hospital. National Clinical Research Center for Cancer, Key Laboratory of Cancer Prevention and Therapy, Tianjin. Tianjin's Clinical Research Center for Cancer, Tianjin, China
e-mail: jinx2354@163.com

The peer review history for this article is available at https://publons.com/publon/10.1002/eji.202048543

Received: 27/1/2020
Revised: 24/4/2020
Accepted: 25/5/2020
Accepted article online: 27/5/2020

Glycobiology, 2020, vol. 30, no. 10, 802–816
doi: 10.1093/glycob/cwaa029
Advance Access Publication Date: 5 April 2020
Original Article

Cancer Biology

Catfish egg lectin affects influx and efflux rates of sunitinib in human cervical carcinoma HeLa cells

Shigeki Sugawara[2], Madoka Takayanagi[2,3], Shota Honda[2], Takeo Tatsuta[2], Yuki Fujii[4], Yasuhiro Ozeki[5], Jun Ito[6], Makoto Sato[6], and Masahiro Hosono[2,1]

[2]Division of Cell Recognition Study, Institute of Molecular Biomembrane and Glycobiology, Tohoku Medical and Pharmaceutical University, 4-4-1 Komatsushima, Aoba-ku, Sendai 981-8558, Japan, [3]Chemiluminescent Reagents Department, R&D Section, Kagamida Factory, DENKA SEIKEN Co. Ltd., 1359-1 Kagamida, Kigoshi Gosen-shi, Niigata 959-1695, Japan, [4]Graduate School of Pharmaceutical Sciences, Nagasaki International University, 2825-7 Huis Ten Bosch, Sasebo, Nagasaki 859-3298, Japan, [5]Department of Life and Environmental System Science, Laboratory of Glycobiology and Marine Biochemistry, Graduate School of NanoBio Sciences, Yokohama City University, 22-2 Seto, Kanazawa-ku, Yokohama 236-0027, Japan, and [6]Department of Urology, Faculty of Medicine, Tohoku Medical and Pharmaceutical University, 1-15-1 Fukumuro, Miyagino-ku, Sendai 983-8536, Japan

[1]To whom correspondence should be addressed: Tel: +81-22-727-0114; Fax: +81-22-727-0092; e-mail: mhosono@tohoku-mpu.ac.jp

Received 15 August 2019; Revised 24 March 2020; Editorial Decision 24 March 2020; Accepted 24 March 2020

Abstract

New treatment protocols are aiming to reduce the dose of the multitargeted tyrosine kinase inhibitor sunitinib, as sunitinib elicits many adverse effects depending on its dosage. *Silurus asotus* egg lectin (SAL) has been reported to enhance the incorporation of propidium iodide as well as doxorubicin into Burkitt's lymphoma Raji cells through binding to globotriaosylceramide (Gb3) on the cell surface. The objective of this study was to examine whether SAL enhances the cytotoxic effect of sunitinib in Gb3-expressing HeLa cells. Although the treatment with SAL delayed the cell growth and enhanced the propidium iodide uptake, cell death accompanied by membrane collapse was not observed. The viability of sunitinib-treated HeLa cells was significantly reduced when the treatment occurred in combination with SAL compared to their separate usage. Sunitinib uptake significantly increased for 30 min in SAL-treated cells, and this increment was almost completely abolished by the addition of L-rhamnose, a hapten sugar of SAL, but not by D-glucose. After removal of SU from the medium, the intracellular sunitinib level in SAL-treated cells was higher than in untreated cells for 24 h, which was not observed in Gb3-deficient HeLa cells. Furthermore, we observed that SAL promoted the formation of lysosome-like structures, which are LAMP1 positive but not acidic in HeLa cells, which can trap sunitinib. Interestingly, SAL-induced vacuolation in HeLa cells was not observed in another Gb3 positive Raji cells. Our findings suggest that SAL/Gb3 interaction promoted sunitinib uptake and suppressed sunitinib excretion and that sunitinib efficiently exerted cytotoxicity against HeLa cells.

Key words: globotriaosylceramide, rhamnose-binding lectin, sunitinib, vacuolation

Introduction

Conventional cancer chemotherapy is often associated with the risk of adverse drug reactions such as blood disorders due to bone marrow suppression, nausea/vomiting, diarrhea/constipation and pain, all of which reduce the quality of life of cancer patients (Carelle et al. 2002). The main disadvantage of this treatment is that most anticancer drugs do not always specifically target cancer cells. Hence, development of drugs targeting molecules specifically or predominantly expressed in cancer cells, but not in normal cells, is an active area of research. These approaches, based on molecular, cellular, biochemical and immunological methods, have succeeded in producing a variety of targeted molecule-specific anticancer drugs.

Tyrosine kinases (TKs), known to be involved in cell proliferation and differentiation, are overexpressed in certain types of cancer cells (Sawyers 2004). Therefore, TK is currently an effective therapeutic target for cancer chemotherapy, and many compounds that inhibit TKs have been developed so far. Sunitinib (SU, SUTENT®) is a TK inhibitor that targets vascular endothelial growth factor receptor (VEGFR)-1, VEGFR-2, VEGFR-3, platelet-derived growth factor receptor (PDGFR)α/PDGFRβ, tyrosine protein kinase kit (c-kit) and fms-related TK 3 (Abrams et al. 2003; Mendel et al. 2003; Croci et al. 2014). SU is mainly used for the treatment of metastatic renal cell carcinoma (mRCC); it also exerts a cytotoxic effect in a variety of solid tumors, for example, gastrointestinal stromal tumor and pancreatic neuroendocrine tumors (Demetri et al. 2006; Raymond et al. 2011; Boegemann et al. 2018). However, SU is also known to cause many adverse effects such as anemia, lymphopenia, neutropenia, thrombocytopenia and leucopenia, depending on its dosage (Aparicio-Gallego et al. 2011). Therefore, development of alternative treatment protocols that can reduce the dose of SU is urgently required.

Silurus asotus egg lectin (SAL), belonging to the rhamnose-binding lectin (RBL) family, is found in catfish eggs and is capable of binding to globotriaosylceramide (Gb3) in glycosphingolipid-enriched microdomains (GEM) on the cell membrane (Hosono et al. 1993; Hosono et al. 1999; Kawano et al. 2009; Hosono et al. 2013). We have previously shown that SAL decreased the survival rate of Gb3-expressing Burkitt's lymphoma Raji cells by inducing G0/G1 phase arrest (Sugawara et al. 2017). Furthermore, we showed that SAL promoted propidium iodide (PI) uptake into Raji cells (Sugawara, Hosono, et al. 2005). Although the apparent molecular mechanism of this effect has not been elucidated, we conducted further studies and demonstrated that SAL also increases the uptake of doxorubicin (Dox) into Raji cells and consequently enhances the cytotoxic effect of Dox (Sugawara, Sasaki, et al. 2005). The combined use of SAL halved the dose of Dox required to attain cell viability similar to that observed in its single treatment (Sugawara et al. 2011). In addition, we showed that the cytotoxic effects of vinblastine (VBL) and irinotecan (CPT-11) were significantly increased in SAL-pretreated Raji cells (Sugawara et al. 2011). These results suggest that the combined use of SAL and other chemotherapeutic drugs resulted in an additive or synergistic effect between anticancer agents in Gb3-expressing cancer cells, which may lead to the reduction in their therapeutic dose.

Tekisogullari and Topcul (2013) and Shin et al. (2009) reported that SU reduces the viability of human cervical cancer HeLa cells, which express Gb3 on their surface (Tekisogullari and Topcul 2013; Shin et al. 2009). In this study, we observed that SAL significantly decreased the viability of HeLa cells in combination with SU and revealed two underlying mechanisms involved in this phenomenon: an increase in uptake and a decrease in efflux. SAL enhanced SU incorporation via binding to the carbohydrate moiety of Gb3 and subsequently induced accumulation of SU in the vacuole membrane newly formed after SAL pretreatment of HeLa cells. Our observations provide some important insights into lectin-combinatorial cancer chemotherapy.

Results

Effects of SAL on HeLa cells

We have previously reported that SAL significantly increased PI incorporation in Raji cells and decreased their proliferation without inducing cell death (Sugawara, Hosono, et al. 2005; Sugawara et al. 2017). According to the results from flow cytometric analysis, PI incorporation also increased in SAL-treated HeLa cells (Figure 1A). PI cannot normally permeate membranes of live cells, and PI incorporation usually follows membrane collapse in cells at the late apoptotic or necrotic phase (Tsujimoto 1997). The WST-8 assay showed that the viability of SAL-treated HeLa cells was reduced to 82% (Figure 1B). However, this method does not directly reflect the proliferative ability. Therefore, we investigated whether SAL reduced cell proliferation using the RealTime-Glo^{MT} cell viability assay reagent, which is capable of monitoring the number of living cells in culture in real time. As shown in Figure 1C, SAL reduced cell proliferation in a time-dependent manner. Additionally, lactate dehydrogenase (LDH) leakage was not detected in cells treated with SAL for 24 h (Figure 1D), and the morphology of HeLa cells did not change at a concentration of SAL up to 200 µg/mL (Supplementary Figure S1). Hence, these results suggest that SAL induces PI uptake in HeLa cells without membrane collapse-associated cell death as observed in Raji cells.

Combined effect of SAL and SU in HeLa cells

Based on previous studies, we predicted that SAL may increase the incorporation of certain small molecule drug, such as Dox, in HeLa cells (Supplementary Figure S2).

Hence, we tested the cytotoxic effect of SU on HeLa cells. SU treatment reduced the viability of HeLa cells in a dose-dependent manner (Figure 2A, left panel). As 12.5 and 25 µM SU moderately decreased cell viability to 80 and 50%, respectively, we used these concentrations for the subsequent combination assay. As shown in Figure 2A (right panel), pretreatment with SAL (50 µg/mL) enhanced the toxicity of SU by reducing cell viability to 51 and 26%, respectively. Furthermore, the cytotoxicity-promoting effects of SAL were reversed by the addition of L-rhamnose, the most potent inhibitory sugar, but not by D-glucose (Figure 2B). Therefore, SAL may act in combination with SU against HeLa cells via a carbohydrate-binding manner.

Alteration of SU influx and efflux by SAL

To elucidate the mechanism by which the effect of SU is enhanced in SAL-treated HeLa cells, we analyzed the content of intracellular SU utilizing its autofluorescence (Nowak-Sliwinska et al. 2015). As shown in Figure 3A, SU was incorporated in proportion to its concentration. The intracellular SU content increased after SAL treatment, which was abolished in the presence of L-rhamnose but not D-glucose (Figure 3B). To further determine whether SAL affects SU efflux, we temporally observed the residual amount of intracellular SU after

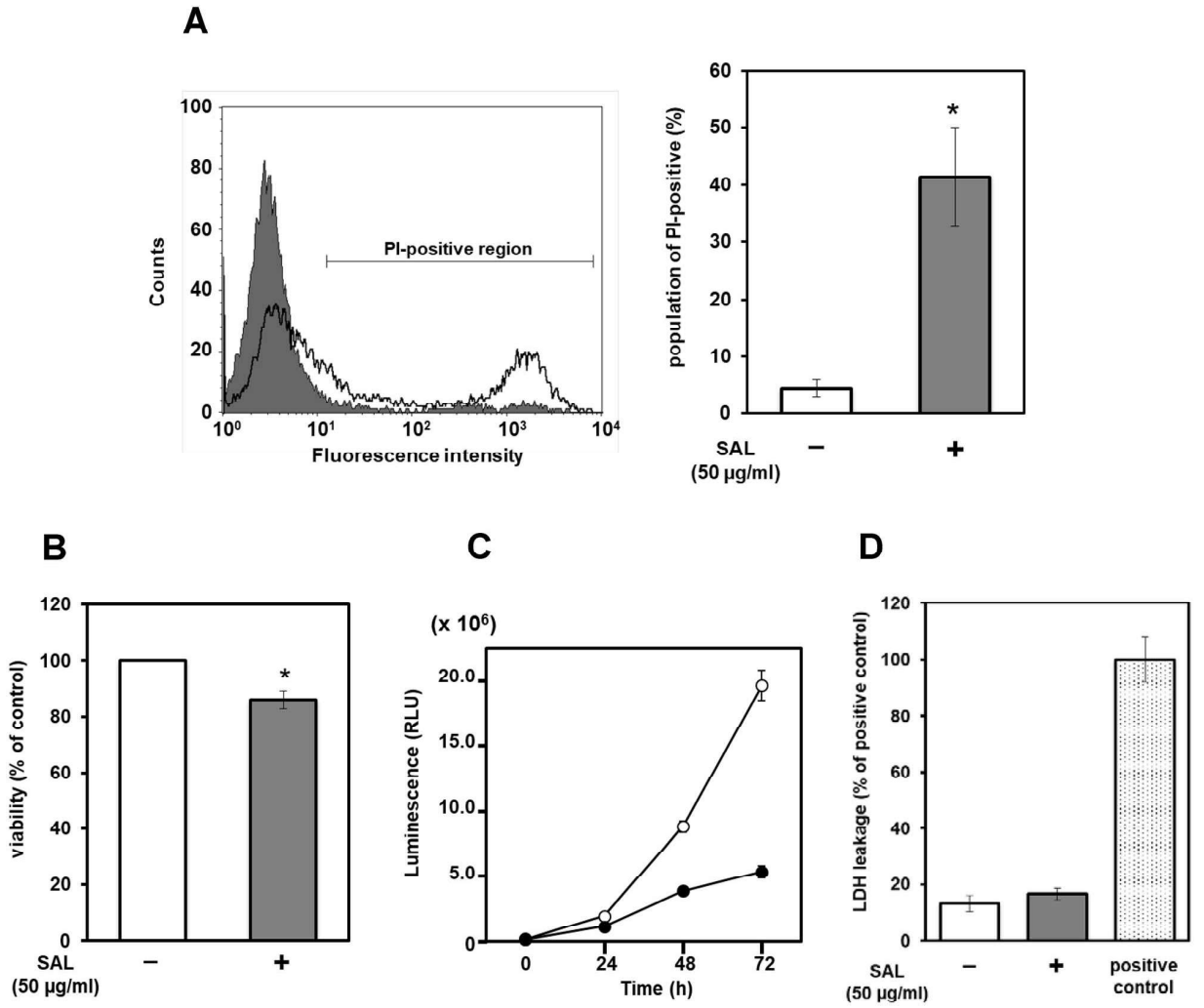

Fig. 1. SAL accelerates PI incorporation and reduces proliferation, but has no cytotoxic effect on HeLa cells. (**A**) Cells (1×10^5) were treated with (solid line) or without (shaded histogram) SAL (50 μg/mL) for 24 h at 37°C. Population of PI-positive cells was determined using FACSCalibur (left panel). The right panel shows the percentage of PI-positive cells. (**B**) Cells (5×10^3) were treated with (+) or without (−) SAL (50 μg/mL) for 48 h at 37°C. Cell viability was assessed using the WST-8 assay. (**C**) Cells (5×10^2) were treated with (closed circles) or without (open circles) SAL (50 μg/mL) at 37°C for 0, 24, 48 and 72 h. Cell growth was measured using the RealTime-Glo^{MT} viability assay. Luminescence was monitored after every 24 h for 3 d. (**D**) Cells (1×10^4) were cultured in a serum-free medium for 24 h. Subsequently, cells were treated with (+) or without (−) SAL (50 μg/mL) for 24 h at 37°C. Total intracellular LDH (positive control) was determined by incubating HeLa cells in lysis solution. LDH leakage was measured using CytoTox-ONE homogeneous membrane integrity assay. Each value represents the mean value ± SE for three independent experiments performed in triplicate. $^*P < 0.05$ vs. untreated control cells. This figure is available in black and white in print and in colour at Glycobiology online.

removing it from the culture medium using confocal laser scanning microscopy. Only weak SU fluorescence was detected in control HeLa cells 3 h after SU removal (Figure 3C). Conversely, intense fluorescence of residual SU was observed in SAL-treated cells even after 24 h. In the time-course analysis using the "Operetta" high-content imaging system (PerkinElmer, Hamburg, Germany), SU uptake reached a plateau level within 10 min in SAL-untreated cells but increased till 30 min to a significantly higher level in SAL-treated cells (Figure 3D). After removal of SU from the medium, the intracellular SU level in SAL-treated cells was higher than in untreated cells till 24 h. These results suggest that SAL promoted the influx but retarded the efflux of SU from HeLa cells. As SU is known to be excreted by the membrane transporter P-glycoprotein (P-gp) or breast cancer resistance protein (BCRP) (Kunimatsu et al. 2013), we assessed whether SAL altered the expression of P-gp and BCRP in HeLa cells. The expression of both transporters increased slightly but never decreased after SAL treatment (Figure 3E). In addition, SAL enhanced an influx of rhodamine (Rho) 123, a substrate of P-gp, but did not affect the efflux from HeLa cells (Supplementary Figure S3). Therefore, it is clear that the accumulation of SU is not because of the decrease in the expression nor in the activity of multidrug resistance transporters.

Incorporation of SU by Gb3/SAL interaction at the cell surface

Next, we knocked out α1,4-galactosyltransferase (A4GALT), also called Gb3 synthase, in HeLa cells to obtain a Gb3-deficient cell line (Gb3-KO). As shown in Figure 4A and B, Gb3 was hardly detected

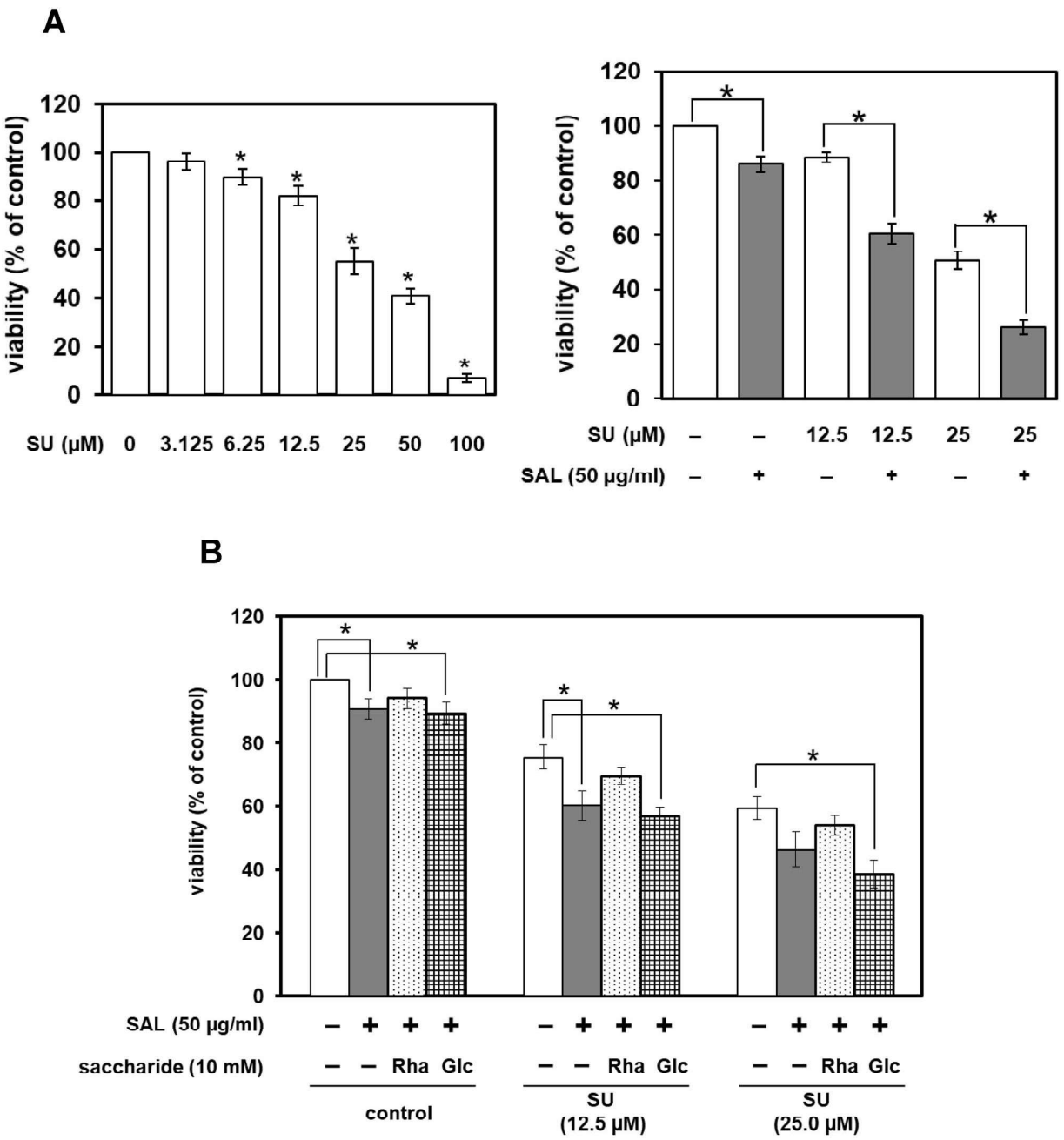

Fig. 2. SAL enhances the antitumor effects of SU on Hela cells. (**A**) Cells (5×10^3) were treated with SU (0, 3.12, 6.25, 12.5, 25, 50 and 100 μM) for 24 h at 37°C (left panel). Cells (5×10^3) were pretreated with SAL (0 and 50 μg/mL) for 24 h at 37°C. Then, SAL-pretreated cells were treated with SU (0, 12.5 and 25 μM) for 24 h at 37°C (right panel). (**B**) Cells (5×10^3) were pretreated with SAL (0 and 50 μg/mL) and SAL/saccharide (10 mM) for 24 h at 37°C. Then, SAL- and SAL/saccharide-pretreated cells were treated with SU (12.5 or 25 μM) for 24 h at 37°C. Cell viability was measured using the WST-8 assay. Each value represents the mean value ± SE for three independent experiments performed in triplicate. $^*P < 0.05$ vs. untreated control cells. This figure is available in black and white in print and in colour at Glycobiology online.

in the Gb3-KO cells compared to wild-type cells, and no change was observed in the proportion of PI-positive cells when both cells were treated with SAL (50 μg/mL, 24 h) (Figure 5A). The viability of Gb3-KO cells treated with SAL was also comparable to that of wild-type cells (Supplementary Figure S4). Although SU treatment decreased the viability of Gb3-KO cells in a dose-dependent manner (Figure 5B, left panel), similar to that in wild-type HeLa cells, the combined effect with SAL was abolished (Figure 5B, right panel). Furthermore, SU influx and efflux conditions after treatment with SAL were not altered in Gb3-KO HeLa cells (Figure 5C and D), indicating that the direct interaction between Gb3 and SAL promoted SU uptake and suppressed its excretion.

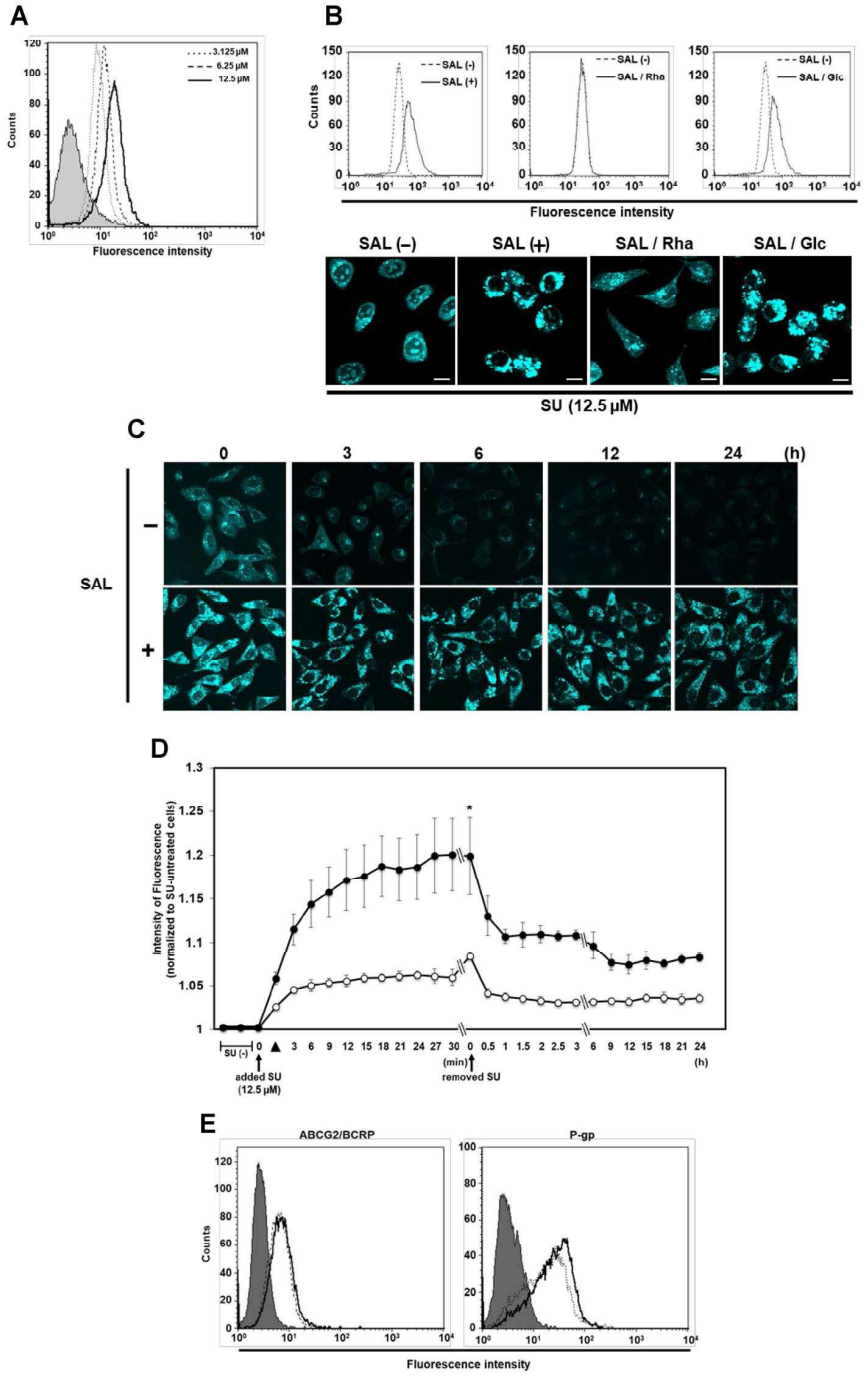

Fig. 3. SAL promotes SU influx and suppresses SU efflux in Hela cells. (**A**) Cells (1×10^5) were treated with SU (dotted line, 3.12 μM; broken line, 6.25 μM; solid line, 12.5 μM) for 30 min at 37°C. The autofluorescence of SU was detected using FACSCalibur. Fluorescence intensity of control cells: shaded histogram. (**B**) Cells (3×10^4) were pretreated with SAL (0 and 50 μg/mL) and SAL/saccharide (10 mM) for 24 h at 37°C. Subsequently, cells were treated with SU (12.5 μM) for 30 min at 37°C. Intracellular SU was detected using FACSCalibur (upper panels) and confocal laser scanning microscopy (lower panels). (**C**) Cells (3×10^4) were pretreated with or without SAL (50 μg/mL) at 37°C for 24 h. Thereafter, cells were treated with SU (12.5 μM) at 37°C for 30 min. After SU was removed from the medium, the residual quantity of SU in the cells was observed using confocal laser scanning microscopy at the indicated time points. SU is represented by a pseudo cyan color. (**D**) Time-course analysis was performed, in which the autofluorescence of SU in the cells was measured using Operetta CLS. HeLa cells were treated with (closed circles) or without (open circles) SAL (50 μg/mL) for 24 h at 37°C. Subsequently, these cells were treated with SU (12.5 μM). SU influx and efflux were analyzed every 3 min after SU was added to the medium at 0 min and after every 0.5 or 3 h after SU was removed from the medium at 0 h, respectively. The closed triangle indicates the time immediately after SU addition. (**E**) Cells (1×10^5) were pretreated with (solid line) or without (broken line) SAL (50 μg/mL) at 37°C for 24 h. BCRP and P-gp expression of SAL-treated HeLa cells were analyzed using anti-ABCG2 mAb and AF488-tagged goat anti-mouse mAb (left panel) and biotin-labeled P-gp-reactive MRK16 mAb and fluorescein isothiocyanate (FITC)-conjugated streptavidin (right panel), respectively. The degree of ABCG2/BCRP and P-gp expression on HeLa cell membranes was determined in the same way as described in (**A**). Fluorescence intensity of control cells: shaded histogram. Each value represents the mean value ± SE for three independent experiments performed in triplicate. $*P < 0.05$ vs. untreated control cells. Photographs were captured using a 60× objective lens. Scale bar, 10 μm. This figure is available in black and white in print and in colour at Glycobiology online.

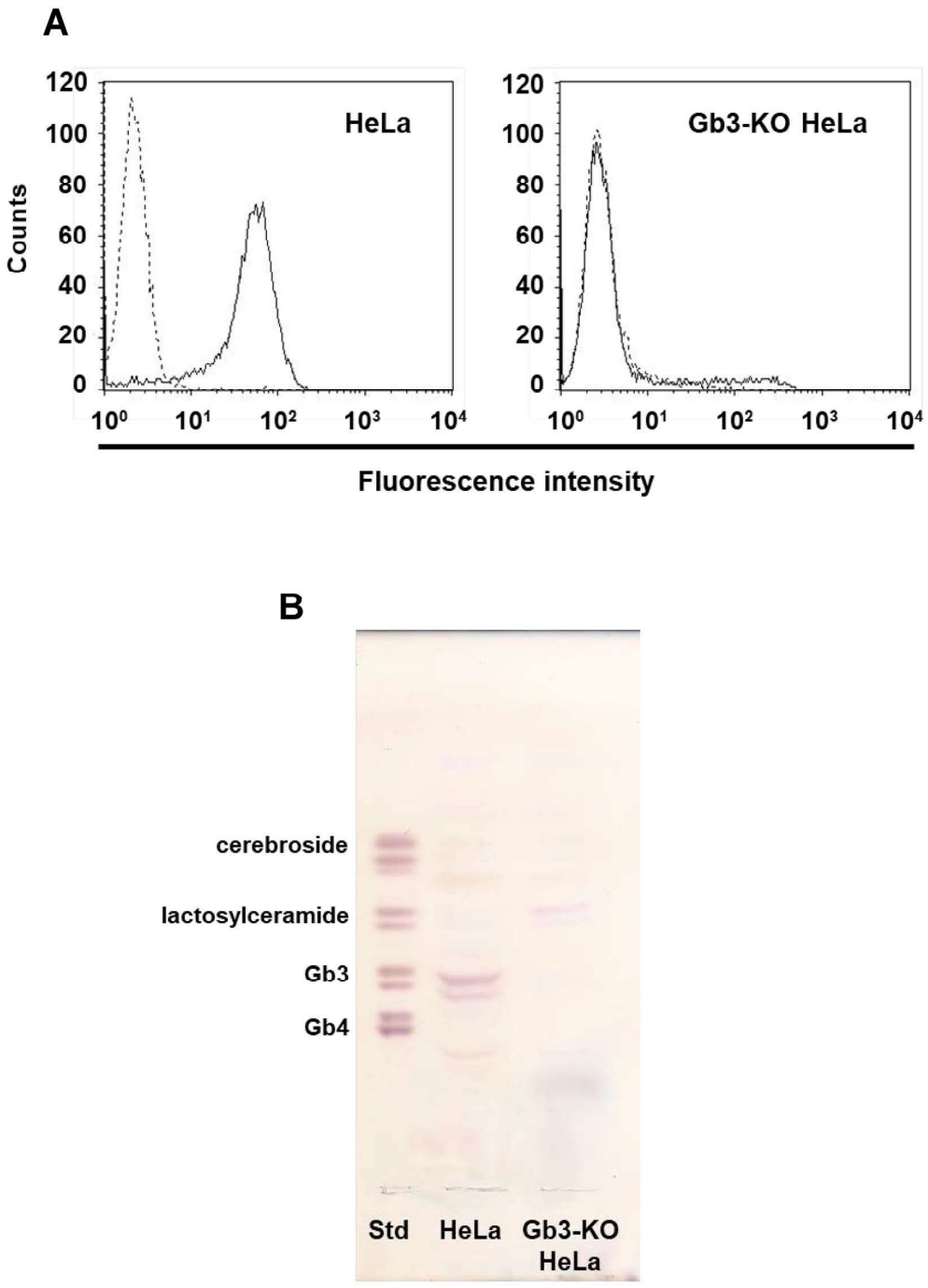

Fig. 4. Confirmation of Gb3 expression in HeLa and Gb3-KO HeLa cells. (**A**) Flow cytometric analysis of Gb3 on HeLa and Gb3-KO HeLa cells. Cells (2×10^5) were treated with anti-Gb3 mAb and AF488-tagged goat anti-mouse mAb (solid line). The degree of Gb3 expression on HeLa and Gb3-KO HeLa cell membranes was determined using FACSCalibur. Fluorescence intensity of control cells: dashed line. (**B**) Total glycosphingolipids isolated from HeLa and Gb3-KO HeLa were separated on TLC using the solvent system described in Materials and methods, and TLC plates were visualized with orcinol-H_2SO_4 reagent. On the standard lane (Std), an aliquot of the standard mixture containing cerebrosides, lactosylceramide, Gb3 and Gb4 was developed. This figure is available in black and white in print and in colour at Glycobiology online.

Alteration of intracellular distribution of SU by SAL in HeLa cells

Figure 3 shows that SAL influenced the uptake and excretion of SU. To gain insight regarding the mechanism of SAL-induced suppression of SU efflux from HeLa cells, we focused on the distribution of SU with and without treatment with SAL. The fluorescence of SU was widely distributed as "dots" in the cytosol of SAL-untreated HeLa cells, whereas a number of characteristic "circular"

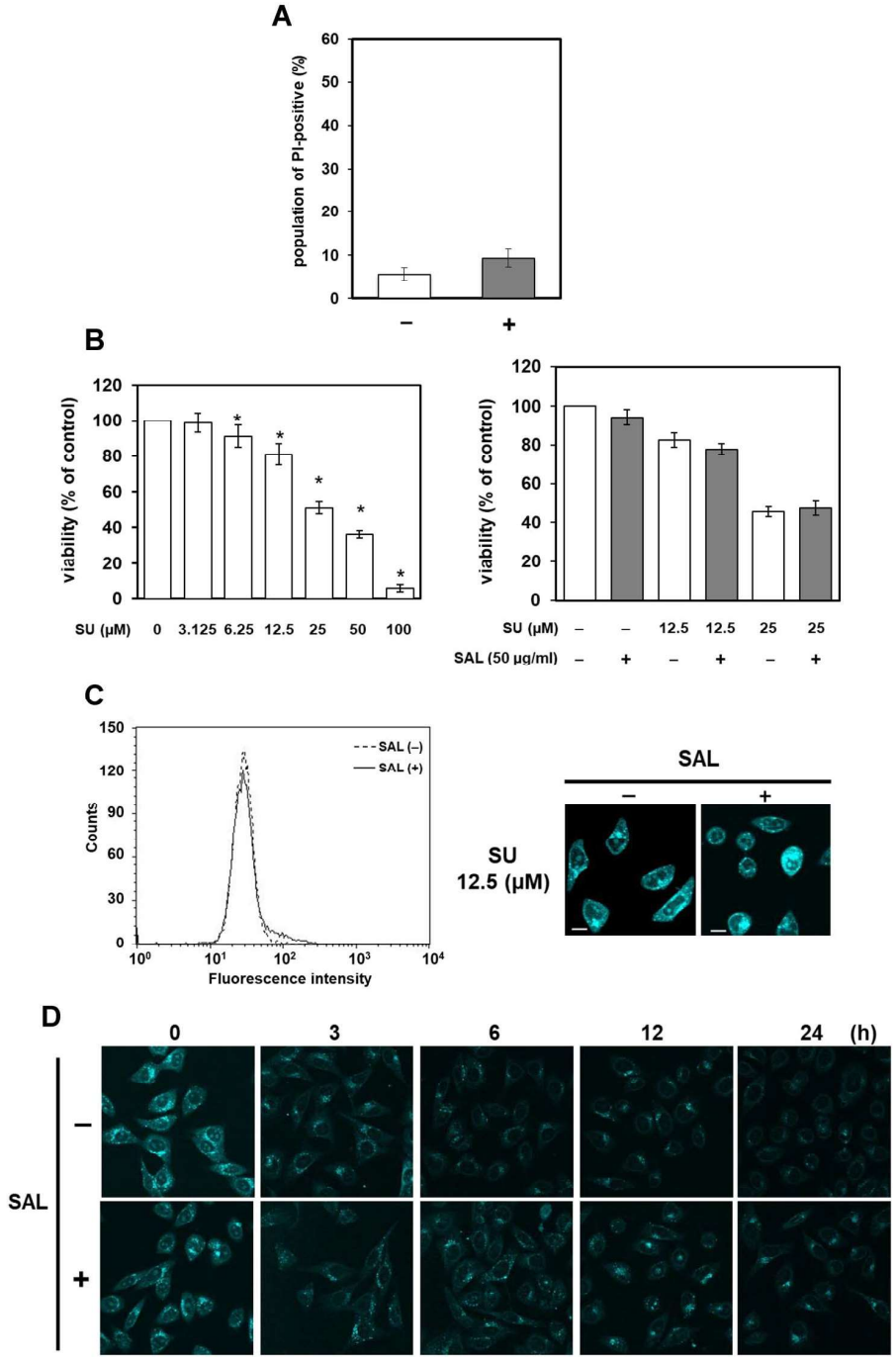

Fig. 5. SAL does not enhance the antitumor effects of SU on G3-KO HeLa cells. (**A**) Gb3-KO HeLa cells (1×10^5) were treated with (+) or without (−) SAL (50 μg/mL) for 24 h at 37°C. Population of PI-positive cells was determined using FACSCalibur. (**B**) Gb3-KO HeLa cells (5×10^3) were treated with SU (0, 3.12, 6.25, 12.5, 25, 50 and 100 μM) for 24 h at 37°C (left panel). Gb3-KO HeLa cells (5×10^3) were pretreated with SAL (0 and 50 μg/mL) for 24 h at 37°C. Then, SAL-pretreated cells were treated with SU (0, 12.5 and 25 μM) for 24 h at 37°C (right panel). Cell viability was determined using the WST-8 assay. (**C**) Gb3-KO HeLa cells (3×10^4) were pretreated with (+) or without (−) SAL (50 μg/mL) for 24 h at 37°C. Subsequently, the cells were treated with SU (12.5 μM) for 30 min at 37°C. Intracellular SU was detected using FACSCalibur (left panel) and confocal laser scanning microscopy (right panels). (**D**) Cells (3×10^4) were pretreated with (+) or without (−) SAL (50 μg/m) at 37°C for 24 h. Thereafter, the cells were treated with SU (12.5 μM) at 37°C for 30 min. After SU was removed from the medium, the residual quantity of SU in the cells was detected using confocal laser scanning microscopy. SU is represented by a pseudo cyan color. Each value represents the mean value ± SE for three independent experiments performed in triplicate. $^*P < 0.05$ vs. untreated control cells. Photographs were captured using a 60× objective lens. Scale bar, 10 μm. This figure is available in black and white in print and in colour at Glycobiology online.

structures consisting of SU fluorescence were observed in SAL-treated cells (Figure 6A). Interestingly, these remarkable vacuole-like structures appeared to "trap" SU and accumulated in HeLa cells; however, they were not observed in SAL-treated Raji cells (Supplementary Figure S5). Although it is still unclear what caused this difference in these cell lines, one possibility might be due to the difference in SAL-induced changes of signal transduction involved in MEK-ERK pathway as described in discussion section, or in the intracellular trafficking mechanisms of SAL. Next, we investigated the mechanism of SAL-induced vacuolation. The vacuoles were formed 9 h after SAL treatment (Figure 6B) and disappeared when SAL was removed from the cell surface by L-rhamnose treatment (Figure 6C). It is known that intracellular SU is sequestered in acidic lysosome compartments of cancer cells (Gotink et al. 2011). We stained various organelles to identify the vacuoles specifically induced by SAL in HeLa cells. As a result, the vacuoles were not stained with Nile Red nor with LysoTracker Green, marker dyes for lipid droplets and acidic organelles such as lysosome, respectively (Supplementary Figures S6 and S7). In addition, the expression of LC3, a marker of the autophagosome, was not observed in the SAL-induced vacuole membrane (Supplementary Figure S8). On the other hand, the vacuoles were stained reddish-brown by Neutral Red, a pH indicator that changes color from red to yellow between pH 6.8 and 8.0, indicating that the pH inside the vacuoles was near neutral (Figure 7A). Lysosomal-associated membrane protein 1 (LAMP1) is a lysosome marker. Although the vacuole might not be a lysosome per its internal pH, we assessed the existence of LAMP1 in the vacuole membrane by constructing HeLa cells transiently expressing a green fluorescence protein (GFP)-tagged LAMP1. As shown in Figure 7B, images similar to that shown in Figure 6A were obtained with the GFP-labeled LAMP1. In SAL-untreated HeLa cells, LAMP1 (lysosomes) was distributed in the cytosol in a "dotted" pattern, whereas characteristic "greenish circles" were observed in SAL-treated cells, indicating that SAL-induced vacuoles could simultaneously contain LAMP1 and SU. To confirm this, the red fluorescence protein (RFP)-labeled LAMP1 was used for double staining with SU. In SAL-treated HeLa cells, SU (cyan) and LAMP1 (magenta) colocalized around the vacuoles (white) (Figure 7C). Lysosomes are known to be derived from the Golgi apparatus (Saftig and Klumperman 2009), and brefeldin A (BFA), an intracellular protein transport inhibitor, was reported to prevent the budding of vesicles from the Golgi complex (Fujiwara et al. 1988; Reaves and Banting 1992). As shown in Figure 7D, BFA inhibited the formation of vacuoles in SAL-treated cells. Furthermore, it was found that the internalized SAL was localized around the vacuoles in the vicinity of nucleus (Figure 7E). From these results, we concluded that the vacuoles formed by SAL in HeLa cells could be lysosome-like organelles derived from the Golgi complex, which contain LAMP1, although their internal environment is not acidic. In addition, the internalized SU molecules are possibly trapped in the SAL-induced vacuole membrane, which is one of the reasons why SAL acts synergistically with SU.

Discussion

In this study, we showed that SAL retards the proliferation of HeLa cells without inducing cell death, but enhances the cytotoxic effect of SU. We proposed a novel function of this lectin involving intracellular vacuolation, which increases SU influx and its retention in the cytosol, where it is sequestered in the vacuole membrane of human cervical carcinoma HeLa cells. This indicates that SAL may be used for combined cancer chemotherapy.

Combination chemotherapy is known to be more effective than monotherapy for treating cancer patients. Usually, two or more drugs elicit different effects due to differences in their target receptors, mechanisms of action and effects on the cell cycle. The benefits of combination therapy include reduction in adverse effects, acquired drug resistance and the dose of each drug used in the treatment. However, it is associated with the potential hazard of drug interactions and certain unexpected side effects. Therefore, lowering the dosage of anticancer drugs via combined therapy is one of the targets of cancer chemotherapy.

In our previous study, we showed that SAL suppresses the proliferation of Gb3-expressing Raji cells and that the molecular mechanism involves an increase in the expression of p21 due to the activation of the mitogen-activated protein/extracellular signal-regulated kinase (ERK) kinase (MEK)-ERK (MEK-ERK) pathway (Sugawara et al. 2017). However, this pathway was not activated in HeLa cells (Supplementary Figure S9). Hence, proliferation of SAL-treated HeLa cells may be suppressed via a mechanism that is different from that of Raji cells. We first suspected that cell membrane collapse may be responsible for the promotion of SU uptake in HeLa cells because PI uptake was increased in SAL-treated cells, which is usually observed in the necrotic or late apoptotic phase of cell death (Figure 1A). However, significant reduction in cell viability and leakage of LDH were not observed in HeLa cells (Figure 1B and D), and hence we concluded that SAL promotes SU uptake without causing cell death or membrane collapse, which is an intriguing observation. CEL-III, a galactose-binding lectin derived from the marine invertebrate *Cucumaria chinate*, binds to sugar chains on the cell surface and causes hemolysis by forming an oligomeric transmembrane pore for the passage of low molecular compounds (Hatakeyama et al. 1995; Hatakeyama et al. 1996; Yamashita et al. 2011; Unno et al. 2014). As SAL is composed of three tandemly repeated carbohydrate recognition domains and forms a trimer in aqueous solution (Murayama et al. 1997), it might possibly form a pore in the cell membrane to promote SU uptake. Furthermore, studies show that the white salmon egg lectin (CSL3) of the RBL family increases the permeability of the fluorescent dye Lucifer Yellow by opening the tight junction of Caco-2 cells (Nemoto et al. 2015). Thus, interaction of lectin with the cell membrane via binding to carbohydrate chains may possibly modify the membrane function. The detailed mechanism of SAL-induced transport will be addressed in the next investigation.

Many cancer cells express adenosine triphosphate (ATP)-binding cassette (ABC) transporters that excrete drugs outside the cells (Domenichini et al. 2019). SAL enhances the cytotoxic effect of antitumor drugs in Raji cells by decreasing the expression of multidrug resistance-associated protein 1 (MRP1), an ABC transporter (Fujii, Sugawara, et al. 2012a). Reports show that P-gp and BCRP are responsible for the efflux of SU in certain tissues (Gotink et al. 2011). In HeLa cells, P-gp and BCRP were expressed in the plasma membrane (Figure 3E), via which the incorporated SU molecules (12.5 μM for 30 min treatment) might be excreted outside within 3 h. However, P-gp and BCRP expression on the membrane increased only slightly after SAL treatment (Figure 3E). In addition, MDR1-P-gp kept its activity after treatment of SAL (Supplementary Figure S3) as described above. Based on these results, we concluded that SU accumulation effect of SAL was at least exerted beyond the capacities of these transporters. Based on these results, we concluded that these transporters may not be involved in regulating the intracellular SU concentration even after 24 h (Figure 3C).

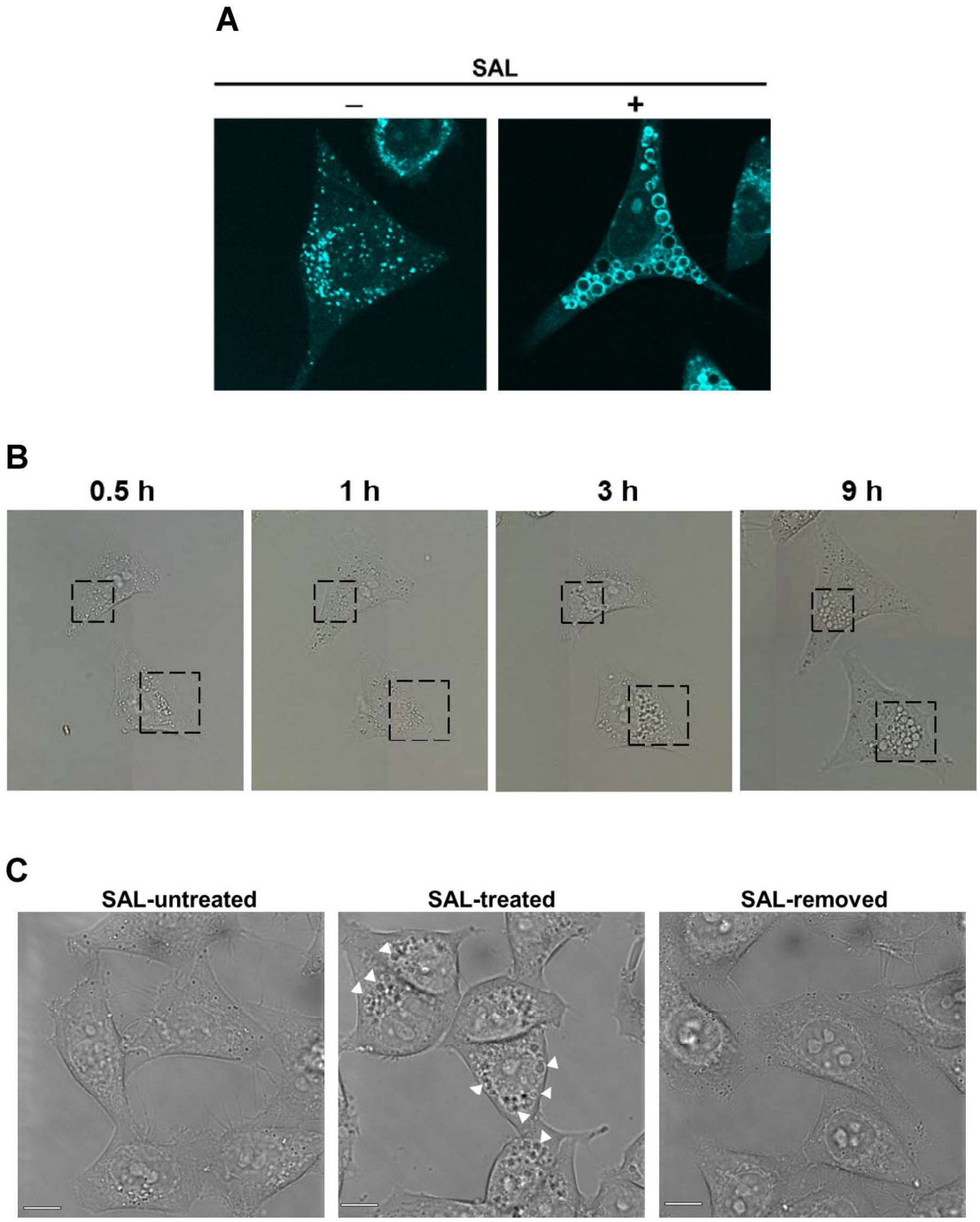

Fig. 6. SAL alters the accumulation profile of SU in HeLa cells. (**A**) Cells (3×10^4) were pretreated with (+) or without (−) SAL (50 μg/mL) for 24 h at 37°C. Thereafter, the cells were treated with SU (12.5 μM) for 30 min at 37°C. The fluorescence of SU was detected using confocal laser scanning microscopy. Photographs were captured using a 60× objective lens with 4× scan zoom. (**B**) Vacuole production was observed between 0.5 and 9 h after treatment with SAL (50 μg/mL). The images are from bright-field microscopy at 60× magnification. (**C**) Cells (5×10^3) were cultured with (SAL-treated) or without (SAL-untreated) SAL (50 μg/mL) for 48 h. Other cells were treated with SAL (50 μg/mL) for 24 h, following which, the SAL bound to the cell membrane was removed with L-rhamnose, and the cells were again cultured in SAL-free medium for 24 h (SAL-removed). Formation of large vacuoles (solid white arrowheads) was detected using an inverted microscope. Photographs were captured using a 100× objective lens. Scale bar, 10 μm. This figure is available in black and white in print and in colour at Glycobiology online.

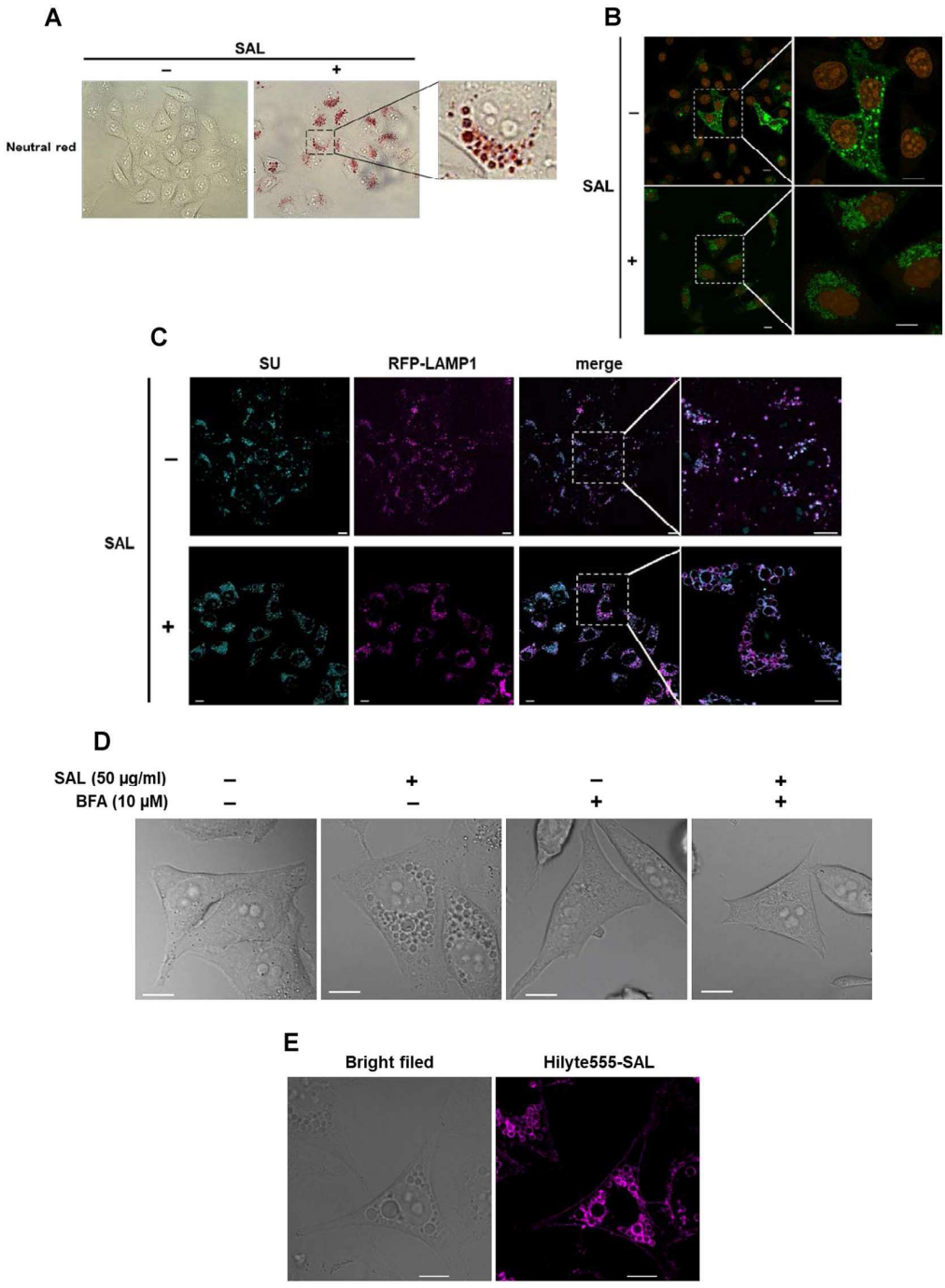

Fig. 7. SAL induces the formation of lysosome-like organelles in HeLa cells. (**A**) Cells (3×10^4) were treated with (+) or without (−) SAL (50 μg/mL) for 24 h at 37°C. Then, cells were exposed to Neutral Red for 30 min. Neutral Red was detected at the same time using the EVOS FL Auto 2 cell imaging system. (**B**) HeLa-LAMP1-GFP cells were pretreated with (+) or without (−) SAL (50 μg/mL) for 24 h at 37°C. Fluorescence of LAMP1-GFP (pseudo green color) was detected using confocal laser scanning microscopy. Nuclei were counterstained with DRAQ5 (pseudo orange color) Scale bar, 10 μm. (**C**) HeLa-LAMP1-RFP cells were pretreated with (+) or without (−) SAL (50 μg/mL) for 24 h at 37°C. Thereafter, the cells were treated with SU (12.5 μM) at 37°C for 30 min. Fluorescence of LAMP1-RFP (pseudo magenta color) and SU (pseudo cyan color) was detected using confocal laser scanning microscopy. Scale bar, 10 μm. (**D**) Cells (1×10^4) were treated with BFA (10 μM) in RPMI-1640 with FBS for 2 h, followed by addition of SAL (50 μg/mL) for 24 h. The images are from bright-field microscopy captured using a 60× objective lens. Scale bar, 10 μm. (**E**) Cells (3×10^4) were treated with HL-SAL (50 μg/mL) for 24 h at 37°C. Then, fluorescence of SAL (magenta) was observed using confocal laser scanning microscopy. Photographs were captured using a 60× objective lens with 3× scan zoom. Scale bar, 10 μm. This figure is available in black and white in print and in colour at Glycobiology online.

Owing to a significant difference in the intracellular distribution pattern of SU in the presence or absence of SAL, we presumed that SU efflux is prevented by the accumulation of SU in unidentified lysosome-like vacuoles formed by the binding of SAL to Gb3. MytiLec isolated from the mussel *Mytilus galloprovincialis* is not RBL but has an affinity for Gb3 as well as SAL (Fujii, Dohmae, et al. 2012). MytiLec significantly decreased the viability of HeLa cells more than 2 μg/mL, unlike in SAL, whereas neither obvious cell death nor vacuole formation was observed less than 2 μg/mL (Supplementary Figure S10). When HeLa cells were treated with 1 μg/mL of MytiLec, a safe concentration for the cells, SU accumulation was not observed. On the other hand, pretreatment of MytiLec clearly inhibited SAL-induced SU accumulation (Supplementary Figure S11). Sorting nexins (SNXs), which belong to a novel family of phox homology (PX) domain-bearing proteins responsible for intracellular transport, are widely conserved across species from yeast to mammals, and at present, 33 mammalian SNXs have been identified (Cullen 2008). SNXs are involved in various cellular functions such as endocytosis, endosome transport and signal transduction and play a fundamental and essential function in the maintenance of intracellular homeostasis. Qin et al. (2006) showed that the overexpression of SNX10 in HeLa cells led to the formation of giant vacuoles (Qin et al. 2006). On the contrary, Xu et al. (2013) reported that SNX11 inhibits SNX10-induced vacuolation (Xu et al. 2013). We reasoned that SAL might induce the formation of vacuoles by changing the expression levels of SNX10 and SNX11; however, expression of neither genes was changed in SAL-treated HeLa cells (Supplementary Figure S12). Therefore, these molecules are not involved in SAL-induced vacuolation.

Furthermore, Lin et al. (2016) have reported that giant vacuoles are formed after yttrium oxide nanoparticles are incorporated into HeLa cells via macropinocytosis (Lin et al. 2016). These vacuoles contain LAMP1 and their internal pH is almost neutral; thus, the properties of these vacuoles are similar to those formed by SAL treatment. It is still unclear if SAL is incorporated into HeLa cells. Further evidence is required to clarify the mechanism underlying SAL-induced vacuole formation.

Reports show that lysosomal sequestration of SU is one of the mechanisms by which tumor cells develop resistance. In fact, significantly more acidic lysosomes sequestering SU in the vacuoles are observed in resistant cells than in nonresistant cells (Gotink et al. 2011). However, SU was trapped "on" the vacuole membrane, i.e. in the cytosol, in the case of nonacidic SAL-induced cytoplasmic vacuoles. On the other hand, Tsai et al. (2017) reported that wheat germ agglutinin (WGA), with affinity for *N*-acetylglucosamine and sialic acid, induces cytoplasmic vacuolation and autophagic or paraptotic cell death in cervical cancer cell lines (Tsai et al. 2017). In addition, Pratt et al. showed that concanavalin-A (ConA) increases autophagic acidic vacuole formation through the intracellular membrane type-1 matrix metalloproteinase (MT1-MMP)-mediated signaling in glioblastoma cells (Pratt et al. 2012). Although such lectin-induced vacuolation may be relevant, it is clearly different from our observation, as SAL did not show any cytotoxicity via apoptotic and nonapoptotic cell death.

Recently, Di Desidero et al. (2017) reported that the combination of SU and CPT-11 showed significant and synergistic antitumor activity in undifferentiated thyroid cancer cells (Di Desidero et al. 2017). However, both drugs can affect normal cells and cause side effects. On the other hand, SAL has the advantage of selectively affecting Gb3-positive cells. It is known that Gb3 is one of the malignant markers overexpressing in the several tumor cells such as breast, ovarian, pancreatic, testicular and colorectal carcinoma (Ohyama et al. 1990; Kovbasnjuk et al. 2005; Wei et al. 2008; Maak et al. 2011; Stimmer et al. 2014). Although some limitations associated with the use of SAL need to be overcome, e.g. immunogenicity of SAL in vivo, as SAL itself is not cytotoxic but only suppresses proliferation, it might be a good candidate for combined cancer chemotherapy.

In conclusion, SAL suppresses cell proliferation, promotes the uptake of SU into cells and suppresses SU excretion in Gb3-positive Hela cells, because of which SU efficiently exerts cytotoxicity on HeLa cells. However, details of the mechanism underlying the formation of the unusual SAL-induced vacuoles remain unknown. Furthermore, the efficacy of SAL is mostly limited to Gb3-expressing cancer cells, which is possibly associated with malignant transformation (Lanne et al. 1996; Stimmer et al. 2014). In the future, SAL may be used for minimally invasive treatments after elucidating its mechanism of action and analyzing the combined effect of SAL and anticancer drugs on various cell types.

Materials and methods

Lectin and cell lines

SAL was purified according to the method described previously (Hosono et al. 1993). MytiLec was kindly gifted by Dr. Y. Ozeki, Yokohama City University, Yokohama, Japan. HeLa, a human cervical carcinoma cell line, obtained from the Cell Resource Center of Biomedical Research, Institute of Development, Aging and Cancer, Tohoku University (Sendai, Japan), was cultured in Roswell Park Memorial Institute (RPMI)-1640 medium (Nissui Pharmaceutical Co., Tokyo, Japan) supplemented with 10% v/v fetal bovine serum (FBS) and antibiotic–antimycotic solution (penicillin [100 IU/mL], streptomycin [100 μg/mL] and amphotericin B [0.25 μg/mL]; Life Technologies, Carlsbad, CA) and maintained at 37°C in a 95% air/5% CO_2 atmosphere.

Incorporation of PI in SAL-treated HeLa

Cells (2×10^5) were treated with or without 100 μL of SAL [50 μg/mL Dulbecco's phosphate-buffered saline (D-PBS)] or rat anti-Gb3 monoclonal antibody (mAb) (clone 38.13; Beckman Coulter, Miami, FL) at a dilution of 1:200 in D-PBS at 4°C for 30 min and washed thrice with D-PBS. Incorporation of PI was detected using the MEBCYTO apoptosis kit (MBL, Nagoya, Japan) and FACSCalibur (BD Biosciences, San Jose, CA).

Cell viability and proliferation assays

Cell viability was determined using the WST-8 assay and the cell counting kit-8 (CCK-8, Dojindo Laboratories, Kumamoto, Japan). After plating the cells into a 96-well flat-bottom plate at 5×10^3 cells/well (90 μL), the cells were treated with SAL (final concentration 50, 100 or 200 μg/mL) or MytiLec (final concentration 0.5, 1, 2, 10, 25 or 50 μg/mL) for 24 h. Next, the WST-8 solution (10 μL) was added into each well, and the cells were incubated for 4 h at 37°C. The absorbance was measured at a wavelength of 450 nm using the GloMax multidetection system (Promega, Madison, WI). Bright-field images were acquired using an inverted microscope (model IX71; Olympus, Osaka, Japan) with a 10 or 100× objective lens. Cell proliferation was determined using a RealTime-Glo^{MT} cell viability assay (Promega). Cells were grown in medium containing the RealTime-Glo^{MT} assay reagent and SAL (50 μg/mL). Proliferation

was monitored every 24 h for 3 d. The luminescence intensity was measured using the GloMax multidetection system (Promega).

Measurement of LDH

The LDH leakage assay was performed using the CytoTox-ONE homogeneous membrane integrity assay Reagent (Promega; Ivanova and Uhlig 2008). Cells (1×10^4) were seeded in a 96-well flat-bottom black plate (Nunc, Roskilde, Denmark) and cultured in serum-free medium for 24 h. Then, the cells were treated with SAL (final concentration 50 μg/mL) at 37°C for 24 h. Subsequently, 100 μL LDH assay reagent was added to each well, and the plates were incubated for 10 min at 22°C. The enzymatic reaction was stopped by adding 50 μL stop solution. LDH released in the extracellular environment was measured using a GloMax multidetection system (Promega) with an excitation wavelength of 525 nm and an emission wavelength of 590 nm. The maximum LDH release control (positive control) was set up by adding 2 μL lysis solution (9% Triton X-100) to control cells before the addition of reagent.

Flow cytometric analysis of Gb3 and ABC subfamily G member 2 (ABCG2)/BCRP expression

Cells (2×10^5) were treated with or without anti-Gb3 monoclonal antibody (mAb) (BGR23, mouse IgG2b; Tokyo Kasei Co. Ltd, Tokyo, Japan) at a dilution of 1:500 or anti-BCRP/ABCG2 mAb (5D3, mouse IgG2b; Santa Cruz Biotechnology, Dallas, TX) at a dilution of 1:200 in D-PBS (100 μL) at 4°C for 30 min and washed thrice with D-PBS. The cells were then treated with Alexa Fluor (AF) 488-conjugated goat anti-mouse IgG (H + L) (Molecular Probes, Invitrogen AG, Basel, Switzerland) at a dilution of 1:2500 in D-PBS (100 μL) at 4°C for 30 min. The degree of Gb3 or ABCG2/BCRP expression on the cell surface was analyzed using FACSCalibur (BD Biosciences).

Thin layer chromatography (TLC) for glycolipid expression analysis

Cells (1×10^6) were suspended in a solution of chloroform–methanol (2:1, v/v) and incubated for 1 h at 37°C, following which they were centrifuged at 1000 × *g* for 10 min. The supernatant was recovered in a glass tube. The pellet was resuspended in a solution of chloroform–methanol–water (1:2:0.8, v/v) and treated for 2 h at 37°C, following which they were then centrifuged at 1000 × *g* for 10 min. The supernatant was collected and evaporated to dryness under nitrogen gas. The residue was dissolved in 20 μL of chloroform–methanol (2:1, v/v), placed on a high-performance TLC (HPTLC) plate (Merck, Darmstadt, Germany) and developed using the solvent system of chloroform–methanol–water (60: 35: 8, v/v). Gb3 was visualized by spraying 0.5% orcinol in 10% sulfuric acid.

Analyzing the effect of the combination of SU and SAL

For determining the effect of SU, cells (5×10^3) were treated with SU (0, 3.12, 6.25, 12.5, 25, 50, and 100 μM) for 24 h at 37°C. For determining the effect of the SU and SAL combination, cells were incubated with SAL (50 μg/mL) in RPMI-1640 with FBS for 24 h, supplemented with SU (0, 12.5, and 25 μM), and incubated for another 24 h at 37°C. Cell viability was determined using the WST-8 assay as described above.

Influx and efflux of SU and Rho123 from SAL-treated HeLa cells

Cells (5×10^5) were cultured for 24 h in RPMI-1640 medium containing SAL (50 μg/mL), SAL (50 μg/mL)/saccharide (20 mM) or without SAL at 37°C in an atmosphere of 95% air/5% CO_2, supplemented with SU (3.12, 6.25 and 12.5 μM) or Rho123 (1 μM) and incubated for another 30 min. Influx of SU and Rho123 was detected using FACSCalibur (BD Biosciences) and an Olympus FV1000 confocal scanning microscope (Olympus). For studying SU and Rho123 efflux, cells (5×10^5) were cultured for 24 h in RPMI-1640 medium containing SAL (50 μg/mL), or without SAL at 37°C in an atmosphere of 95% air/5% CO_2, supplemented with SU (12.5 μM) or Rho123 (1 μM) and incubated for another 30 min. SU was removed from each well at 3 or 6 h intervals for a maximum of 24 h. Rho123 was removed from each well for 30 min. SU and Rho123 efflux was ascertained using FACSCalibur (BD Biosciences) and an Olympus FV1000 confocal scanning microscope (Olympus).

CRISPR/Cas9-mediated knockout of A4GALT

HeLa cells (1×10^6) were centrifuged and resuspended in 100 μL nucleofection V solution (Lonza, Basel, Switzerland) containing pRGEN-Human-A4GALT-U6 sgRNA vector (200 ng) and p3s-Cas9-Ef1a expression vector (200 ng) (ToolGen, Seoul, Korea) and electroporated with a Nucleofector (Lonza) using the I-13 program. After nucleofection, the cells were transferred to a 12-well plate containing 1 mL fresh complete medium (RPMI 1640 containing 10% FBS and antibiotic–antimycotic solution) and incubated at 37°C for 150 h. After incubation, the expression of Gb3 was detected using FACSCalibur (BD Biosciences) and TLC as described above.

Time series measurements of intracellular SU contents

Cells (1×10^4) were seeded in a CellCarrier™-96 microplates (PerkinElmer, Hamburg, Germany) and cultured in RPMI-1640 medium containing SAL (50 μg/mL) or without SAL at 37°C in an atmosphere of 95% air/5% CO_2. Before imaging, the cells were stained with Hoechst33342 (Dojindo Laboratories). The plate was scanned on Perkin Elmer Operetta CLS high-content imager using a 40× objective lens on confocal mode in a prewarmed live cell chamber set at 37°C in an atmosphere of 95% air/5% CO_2. Fluorescent images were captured in the Hoechst33342 channel at 488 nm before and at 3 min intervals after the addition of SU (final concentration 12.5 μM) for a maximum of 30 min. Subsequently, SU was removed from each well at 0.5 or 3 h intervals for a maximum of 24 h. Images were quantified using the Harmony software (PerkinElmer).

Analysis of intracellular accumulation site of SU

HeLa cells (1×10^4) were seeded in a 48-well flat-bottom plate (BD Falcon, Corning Life Sciences, MA) and incubated with SAL (50 μg/mL) for 0.5, 3, 9 or 18 h. Vacuole formation was observed using an EVOS FL Auto 2 cell imaging System (Thermo Fisher) in bright-field mode. For detecting lipid droplets, cells (1×10^4) were seeded in 24-well glass bottom culture plate (Iwaki EZView™, Asahi Techno Glass, Tokyo, Japan), incubated at 37°C in an atmosphere of 5% CO_2 for 24 h and then treated with SAL (50 μg/mL) for 24 h. Then, cells were fixed with 1% paraformaldehyde in D-PBS at 4°C for 15 min and washed thrice with D-PBS. The paraformaldehyde-fixed cells were treated with 0.1% Triton X-100 in D-PBS at 4°C for

15 min to permeabilize the cells. The permeabilized cells were treated with 0.5 μg/mL Nile Red (Wako, Osaka, Japan) at room temperature for 5 min. After washing, the cells were observed using a confocal scanning microscope (model FV1000; Olympus) with a 60× objective lens. For Neutral Red staining and LysoTracker Green DND-26 assay, HeLa cells (1×10^4) were seeded in 48-well flat-bottom culture plate (BD Falcon), incubated at 37°C in the presence of 5% CO_2 for 24 h and then treated with SAL (50 μg/mL) for 24 h and washed twice in D-PBS. These cells were then stained with Neutral Red (100 μg/mL, Wako, Osaka, Japan) and LysotTacker Green DND-26 (500 nM, Thermo Fisher) for 30 min under growth conditions. After washing, the cells were observed under a fluorescence microscope (EVOS FL Auto 2 Cell imaging system; Thermo Fisher). For the establishment of HeLa RFP-LAMP1 and HeLa GFP-LAMP1 cell lines, HeLa cells were treated with CellLight® Lysosome labeling BacMam 2.0-RFP and CellLight® Lysosome labeling BacMam 2.0-GFP (Thermo Fisher), respectively, according to the manufacturer's protocol. Twenty-four hours after treatment, the cells were cultured for 24 h in RPMI-1640 medium containing SAL (50 μg/mL) or without SAL at 37°C in an atmosphere of 95% air/5% CO_2, supplemented with SU (12.5 μM) and incubated for another 30 min. SU and LAMP1 exhibiting green and red fluorescence were acquired using a confocal scanning microscope (model FV1000; Olympus) with a 60× objective lens. Nuclei were counterstained with DRAQ5 (Biostatus Ltd, Leicestershire, UK). BFA (1 μg, Abcam, Cambridge, UK) was dissolved in 247 μL dimethyl sulfoxide to make a 10 mM stock solution. Cells were incubated with BFA (10 μM) in RPMI-1640 with FBS for 2 h, supplemented with SAL (50 μg/mL) and incubated for another 24 h. Bright-field images were acquired using a confocal scanning microscope (model FV1000; Olympus) with a 60× objective lens. For detecting LC3, cells (1×10^4) were seeded in 24-well glass bottom culture plate (Iwaki), incubated at 37°C in an atmosphere of 5% CO_2 for 24 h and then treated with SAL (50 μg/mL) for 24 h. Then, cells were fixed with 4% paraformaldehyde in D-PBS at room temperature for 15 min and washed thrice with D-PBS. The paraformaldehyde-fixed cells were treated with 0.1% Triton X-100 in D-PBS at room temperature for 15 min to permeabilize the cells. The cells were treated with anti-LC3 pAb (rabbit IgG; MBL) at a dilution of 1:500 in D-PBS (200 μL) at room temperature for 2 h and washed thrice with D-PBS. The cells were then treated with AF 546-conjugated goat anti-rabbit IgG (H + L) (Molecular Probes) at a dilution of 1:2000 in D-PBS (200 μL) at room temperature for 1 h. After washing, the cells were observed using a confocal scanning microscope (model FV1000; Olympus) with a 60× objective lens.

mRNA expression analysis

HeLa cells (5×10^5) were cultured for 24 h in RPMI-1640 medium containing SAL (50 μg/mL) or without SAL at 37°C in an atmosphere of 95% air/5% CO_2. Total RNA was extracted from cells using a Direct-zol RNA mini prep kit (Zymo Research Co., CA). cDNA was synthesized from the total RNA (1 μg) using a SuperScript VILO cDNA synthesis kit (Invitrogen, San Diego, CA). Quantitative reverse transcription-polymerase chain reaction (qRT-PCR) assays were performed using a LightCycler 480 system with the LightCycler 480 probes master kit (Roche Diagnostics, Indianapolis, IN). PCR primers for amplification of *SNX10* (forward: 5′-CGAAGAAGATATAGAGAATTCGTGTG-3′, reverse: 5′-GATGGAAGTTCTGGCAGTTGTA-3′) and *SNX11* (forward: 5′-GGAGCTGGTGCTGTTCTCA-3′, reverse: 5′-TCAGCCAATATGTACTGCCAAC-3′) were designed by the Universal Probe Library Assay Design Center (https://www.roche-applied-science.com/sis/rtpcr/upl/acenter.jsp) using a TaqMan/probe library assay. The expression levels of these genes were standardized relatively to the mRNA expression level of *GAPDH* (as a housekeeping gene) based on their average crossing point values.

Western blot analysis

HeLa cells (5×10^4) were cultured for 48 h in RPMI-1640 with (50 μg/mL) or without SAL at 37°C in an atmosphere of 95% air/5% CO_2 and lysed with ice-cold lysis buffer (10 mM Tris buffer [pH 7.5], 150 mM NaCl, 1% w/v TritonX-100, 5 mM ethylenediaminetetraacetic acid and complete protease inhibitor cocktail [Roche, Mannheim, Germany]) for 30 min at 4°C. The cell lysate was separated using sodium dodecyl sulfate-polyacrylamide gel electrophoresis (SDS-PAGE) (12.5% separation gel) and electrotransferred onto a polyvinylidene difluoride (PVDF) membrane (pore size 0.45 μm) (Hybond-P; GE Healthcare BioSciences AB, Uppsala, Sweden). The membrane was treated with blocking buffer (Blocking One; Nacalai Tesque Inc., Kyoto, Japan) for 1 h at room temperature and washed with Tris-buffered saline (TBS) containing 0.05% Tween-20. The primary antibodies used were against phospho-$MEK_{1/2}$ (1:1000, rabbit mAb; Cell Signaling Technology Inc., Danvers, MA [CST]), $MEK_{1/2}$ (1:1000, rabbit mAb; CST), phospho-$ERK_{1/2}$ (1:1000, rabbit mAb; CST), ERK1 (1:5000, mouse mAb; BD Biosciences) and GAPDH (1:20,000, mouse mAb; clone 6C5; Ambion/Invitrogen, Carlsbad, CA). These antibodies were applied in immunoreaction enhancer solution (Can Get Signal Solution 1; Toyobo Co., Osaka, Japan), and the membrane was incubated for 16 h at 4°C. The secondary antibody, horseradish peroxidase (HRP)-conjugated anti-mouse or anti-rabbit IgG (Chemicon International Inc., Temecula, CA), was diluted 1:20,000 in immunoreaction enhancer solution, applied on the membrane and incubated for 1 h at room temperature. The membrane was exposed to X-ray film (Fuji Film Co., Tokyo, Japan) after treatment with enhanced chemiluminescence (ECL) Prime detection reagent (GE Healthcare BioSciences AB).

Internalization of SAL into HeLa

SAL was labeled using HiLyte Fluor™ 555 (HL) labeling kit-NH_2 (Dojindo) according to the instruction manual. HeLa cells (1×10^4) were seeded in 24-well glass bottom culture plate (Iwaki), incubated at 37°C in an atmosphere of 5% CO_2 for 24 h and then treated with HL-SAL (50 μg/mL) for 24 h. After washing, the cells were observed using a confocal scanning microscope (model FV1000; Olympus) with a 60× objective lens.

Statistical analysis

Experimental results are presented as mean ± standard error (SE). Differences in means were evaluated using the two-tailed Student's *t*-test, with P values <0.05 considered statistically significant.

Supplementary data

Supplementary data for this article is available online at http://glycob.oxfordjournals.org/.

Acknowledgments

We thank Editage (www.editage.jp) for English language editing.

Funding

This work was supported by the Ministry of Education, Culture, Sports, Science and Technology (MEXT) of Japan.

Conflict of interest

The authors declare that there are no conflicts of interest regarding the publication of this paper.

Author contributions

S. Sugawara, M. Takayanagi and S. Honda conducted all experiments and analyzed the data. S. Sugawara and M. Takayanagi wrote the manuscript. M. Hosono contributed to manuscript revision. Y. Fujii and Y. Ozeki provided a sample. T. Tatsuta., Y. Ozeki., J. Ito, M. Sato and M. Hosono supervised all experiments. All authors read and approved the final manuscript.

Abbreviations

A4GALT, α1,4-galactosyltransferase; ABC, ATP-binding cassette; ABCG2, ABC subfamily G member 2; AF, Alexa Fluor; ATP, adenosine triphosphate; BCRP, breast cancer resistance protein; BFA, brefeldin A; c-kit, tyrosine protein kinase kit; ConA, concanavalin A; CPT-11, irinotecan; D-PBS, Dulbecco's phosphate-buffered saline; Dox, doxorubicin; ECL, enhanced chemiluminescence; ERK, extracellular signal-regulated kinase; FBS, fetal bovine serum; FITC, fluorescein isothiocyanate; Gb3, globotriaosylceramide; GEM, glycosphingolipid-enriched microdomains; GFP, green fluorescence protein; HPTLC, high-performance TLC; HRP, horseradish peroxidase; LAMP1, lysosomal-associated membrane protein 1; mAb, monoclonal antibody; MEK, mitogen-activated protein/extracellular signal-regulated kinase; mRCC, metastatic renal cell carcinoma; MRP1, multidrug resistance-associated protein 1; MytiLec, mussel *Mytilus galloprovincialis* lectin; PDGFR, platelet-derived growth factor receptor; P-gp, P-glycoprotein; PI, propidium iodide; PVDF, polyvinylidene difluoride; PX, phox homology; pAb, polyclonal antibody; qRT-PCR, quantitative reverse transcription-polymerase chain reaction; RBL, rhamnose-binding lectin; RFP, red fluorescence protein; rhodamine123, Rho123; RPMI, Roswell Park Memorial Institute; SAL, *Silurus asotus* egg lectin; SDS-PAGE, sodium dodecyl sulfate-polyacrylamide gel electrophoresis; SE, standard error; SNX, sorting nexin; SU, sunitinib; TBS, Tris-buffered saline; TK, tyrosine kinase; VEGFR, vascular endothelial growth factor receptor; VBL, vinblastine; WGA, wheat germ agglutinin; LDH, lactate dehydrogenase

References

Abrams TJ, Lee LB, Murray LJ, Pryer NK, Cherrington JM. 2003. SU11248 inhibits KIT and platelet-derived growth factor receptor beta in preclinical models of human small cell lung cancer. *Mol Cancer Ther*. 2:471–478.

Aparicio-Gallego G, Blanco M, Figueroa A, García-Campelo R, Valladares-Ayerbes M, Grande-Pulido E, Antón-Aparicio L. 2011. New insights into molecular mechanisms of sunitinib-associated side effects. *Mol Cancer Ther*. 10:2215–2223.

Boegemann M, Hubbe M, Thomaidou D, Blackburn S, Bent-Ennakhil N, Wood R, Bargo D. 2018. Sunitinib treatment modification in first-line metastatic renal cell carcinoma: Analysis of the STAR-TOR registry. *Anticancer Res*. 38:6413–6422.

Carelle N, Piotto E, Bellanger A, Germanaud J, Thuillier A, Khayat D. 2002. Changing patient perceptions of the side effects of cancer chemotherapy. *Cancer*. 95:155–163.

Croci DO, Cerliani JP, Pinto NA, Morosi LG, Rabinovich GA. 2014. Regulatory role of glycans in the control of hypoxia-driven angiogenesis and sensitivity to anti-angiogenic treatment. *Glycobiology*. 24:1283–1290.

Cullen PJ. 2008. Endosomal sorting and 29chinate29: An emerging role for sorting nexins. *Nat Rev Mol Cell Biol*. 9:574–582.

Demetri GD, van Oosterom AT, Garrett CR, Blackstein ME, Shah MH, Verweij J, McArthur G, Judson IR, Heinrich MC, Morgan JA, et al. 2006. Efficacy and safety of sunitinib in patients with advanced gastrointestinal stromal tumour after failure of imatinib: A randomized controlled trial. *Lancet*. 368:1329–1338.

Di Desidero T, Antonelli A, Orlandi P, Ferrari SM, Fioravanti A, Alì G, Fontanini G, Basolo F, Francia G, Bocci G. 2017. Synergistic efficacy of irinotecan and sunitinib combination in preclinical models of anaplastic thyroid cancer. *Cancer Lett*. 411:35–43.

Domenichini A, Adamska A, Falasca M. 2019. ABC transporters as cancer drivers: Potential functions in cancer development. *Biochim Biophys Acta Gen Subj*. 1863:52–60.

Fujii Y, Sugawara S, Araki D, Kawano T, Tatsuta T, Takahashi K, Kawsar SM, Matsumoto R, Kanaly RA, Yasumitsu H, et al. 2012a. MRP1 expressed on Burkitt's lymphoma cells was depleted by catfish egg lectin through Gb3-glycosphingolipid and enhanced cytotoxic effect of drugs. *Protein J*. 31:15–26.

Fujii Y, Dohmae N, Takio K, Kawsar SM, Matsumoto R, Hasan I, Koide Y, Kanaly RA, Yasumitsu H, Ogawa Y, et al. 2012b. A lectin from the mussel *Mytilus galloprovincialis* has a highly novel primary structure and induces glycan-mediated cytotoxicity of globotriaosylceramide-expressing lymphoma cells. *J Biol Chem*. 287:44772–44783 287(53.

Fujiwara T, Oda K, Yokota S, Takatsuki A, Ikehara Y. 1988. Brefeldin A causes disassembly of the Golgi complex and accumulation of secretory proteins in the endoplasmic reticulum. *J Biol Chem*. 263:18545–18552.

Gotink KJ, Broxterman HJ, Labots M, de Haas RR, Dekker H, Honeywell RJ, Rudek MA, Beerepoot LV, Musters RJ, Jansen G, et al. 2011. Lysosomal sequestration of sunitinib: A novel mechanism of drug resistance. *Clin Cancer Res*. 17:7337–7346.

Hatakeyama T, Nagatomo H, Yamasaki N. 1995. Interaction of the hemolytic lectin CEL-III from the marine invertebrate Cucumaria 31chinate with the erythrocyte membrane. *J Biol Chem*. 270:3560–3564.

Hatakeyama T, Furukawa M, Nagatomo H, Yamasaki N, Mori T. 1996. Oligomerization of the hemolytic lectin CEL-III from the marine invertebrate *Cucumaria 31chinate* induced by the binding of carbohydrate ligands. *J Biol Chem*. 271:16915–16920.

Hosono M, Kawauchi H, Nitta K, Takayanagi Y, Shiokawa H, Mineki R, Murayama K. 1993. Purification and characterization of *Silurus asotus* (catfish) roe lectin. *Biol Pharm Bull*. 16:1–5.

Hosono M, Ishikawa K, Mineki R, Murayama K, Numata C, Ogawa Y, Takayanagi Y, Nitta K. 1999. Tandem repeat structure of rhamnose-binding lectin from catfish (*Silurus asotus*) eggs. *Biochim Biophys Acta Gen Subj*. 1472:668–675.

Hosono M, Sugawara S, Tatsuta T, Hikita T, Kominami J, Nakamura-Tsuruta S, Hirabayashi J, Kawsar SM, Ozeki Y, Hakomori SI, et al. 2013. Domain composition of rhamnose-binding lectin from shishamo smelt eggs and its carbohydrate-binding profiles. *Fish Physiol Biochem*. 39: 1619–1630.

Ivanova L, Uhlig S. 2008. A bioassay for the simultaneous measurement of metabolic activity, membrane integrity, and lysosomal activity in cell cultures. *Anal Biochem*. 379:16–19.

Kawano T, Sugawara S, Hosono M, Tatsuta T, Ogawa Y, Fujimura T, Taka H, Murayama K, Nitta K. 2009. Globotriaosylceramide-expressing Burkitt's lymphoma cells are committed to early apoptotic status by rhamnose-binding lectin from catfish eggs. *Biol Pharm Bull*. 32:345–353.

Kovbasnjuk O, Mourtazina R, Baibakov B, Wang T, Elowsky C, Choti MA, Kane A, Donowitz M. 2005. The glycosphingolipid globotriaosylceramide in the metastatic transformation of colon cancer. *Proc Natl Acad Sci USA*. 102:19087–19092.

Kunimatsu S, Mizuno T, Fukudo M, Katsura T. 2013. Effect of P-glycoprotein and breast cancer resistance protein inhibition on the pharmacokinetics of sunitinib in rats. *Drug Metab Dispos*. 41:1592–1597.

Lanne B, Jondal M, Karlsson KA. 1996. Galα4Gal-binding antibodies: Specificity and use for the mapping of glycolipids of Burkitt lymphoma and other human tumors. *Glycobiology*. 6:423–431.

Lin J, Shi SS, Zhang JQ, Zhang YJ, Zhang L, Liu Y, Jin PP, Wei PF, Shi RH, Zhou W, et al. 2016. Giant cellular vacuoles induced by rare earth oxide nanoparticles are abnormally enlarged endo/lysosomes and promote mTOR-dependent TFEB nucleus translocation. *Small*. 12: 5759–5768.

Maak M, Nitsche U, Keller L, Wolf P, Sarr M, Thiebaud M, Rosenberg R, Langer R, Kleeff J, Friess H, et al. 2011. Tumor-specific targeting of pancreatic cancer with Shiga toxin B-subunit. *Mol Cancer Ther*. 10:1918–1928.

Mendel DB, Laird AD, Xin X, Louie SG, Christensen JG, Li G, Schreck RE, Abrams TJ, Ngai TJ, Lee LB, et al. 2003. In vivo antitumor activity of SU11248, a novel tyrosine kinase inhibitor targeting vascular endothelial growth factor and platelet-derived growth factor receptors: Determination of a pharmacokinetic/pharmacodynamic relationship. *Clin Cancer Res*. 9:327–337.

Murayama K, Taka H, Kaga N, Fujimura T, Mineki R, Shindo N, Morita M, Hosono M, Nitta K. 1997. The structure of *Silurus asotus* (catfish) roe lectin (SAL): Identification of a noncovalent trimer by mass spectrometry and analytical ultracentrifugation. *Anal Biochem*. 247:319–326.

Nemoto R, Yamamoto S, Ogawa T, Naude R, Muramoto K. 2015. Effect of chum salmon egg lectin on tight junctions in Caco-2 cell monolayers. *Molecules*. 20:8094–8106.

Nowak-Sliwinska P, Weiss A, van Beijnum JR, Wong TJ, Kilarski WW, Szewczyk G, Verheul HM, Sarna T, van den Bergh H, Griffioen AW. 2015. Photoactivation of lysosomally sequestered sunitinib after angiostatic treatment causes vascular occlusion and enhances tumor growth inhibition. *Cell Death Dis*. 6:e1641.

Ohyama C, Fukushi Y, Satoh M, Saitoh S, Orikasa S, Nudelman E, Straud M, Hakomori S. 1990. Changes in glycolipid expression in human testicular tumor. *Int J Cancer*. 45:1040–1044.

Pratt J, Roy R, Annabi B. 2012. Concanavalin-A-induced autophagy biomarkers requires membrane type-1 matrix metalloproteinase intracellular signaling in glioblastoma cells. *Glycobiology*. 22:1245–1255.

Qin B, He M, Chen X, Pei D. 2006. Sorting nexin 10 induces giant vacuoles in mammalian cells. *J Biol Chem*. 281:36891–36896.

Raymond E, Dahan L, Raoul JL, Bang YJ, Borbath I, Lombard-Bohas C, Valle J, Metrakos P, Smith D, Vinik A, et al. 2011. Sunitinib malate for the treatment of pancreatic neuroendocrine tumors. *N Engl J Med*. 364:501–513.

Reaves B, Banting G. 1992. Perturbation of the morphology of the trans-Golgi network following brefeldin A treatment: Redistribution of a TGN-specific integral membrane protein, TGN38. *J Cell Biol*. 116: 85–94.

Saftig P, Klumperman J. 2009. Lysosome biogenesis and lysosomal membrane proteins: Trafficking meets function. *Nat Rev Mol Cell Biol*. 10:623–635.

Sawyers C. 2004. Targeted cancer therapy. *Nature*. 432:294–297.

Shin IS, Ishii S, Shin JS, Sung KI, Park BS, Jang HY, Kim BW. 2009. Globotriaosylceramide (Gb3) content in HeLa cells is correlated to Shiga toxin-induced cytotoxicity and Gb3 synthase expression. *BMB Rep*. 42:310–314.

Stimmer L, Dehay S, Nemati F, Massonnet G, Richon S, Decaudin D, Klijanienko J, Johannes L. 2014. Human breast cancer and lymph node metastases express Gb3 and can be targeted by STxB-vectorized chemotherapeutic compounds. *BMC Cancer*. 14:916.

Sugawara S, Hosono M, Ogawa Y, Takayanagi M, Nitta K. 2005a. Catfish egg lectin causes rapid activation of multidrug resistance 1 P-glycoprotein as a lipid translocase. *Biol Pharm Bull*. 28:434–441.

Sugawara S, Sasaki S, Ogawa Y, Hosono M, Nitta K. 2005b. Catfish (Silurus asotus) lectin enhances the cytotoxic effects of doxorubicin. *Yakugaku Zasshi*. 125:327–334.

Sugawara S, Araya K, Hosono M, Tatsuta T, Nitta K. 2011. Combination effect of catfish lectin and anti-cancer drugs on Raji and K562 cells. *J Tohoku Pharm Univ*. 58:41–46.

Sugawara S, Im C, Kawano T, Tatsuta T, Koide Y, Yamamoto D, Ozeki Y, Nitta K, Hosono M. 2017. Catfish rhamnose-binding lectin induces $G_{0/1}$ cell cycle arrest in Burkitt's lymphoma cells via membrane surface Gb3. *Glycoconj J*. 34:127–138.

Tekisogullari K, Topcul M. 2013. The effects of sunitinib malate used in targeted therapy on the proliferation of HeLa cells in vitro. *J BUON*. 18:253–260.

Tsai TL, Wang HC, Hung CH, Lin PC, Lee YS, Chen HHW, Su WC. 2017. Wheat germ agglutinin-induced paraptosis-like cell death and protective autophagy is mediated by autophagy-linked FYVE inhibition. *Oncotarget*. 8:91209–91222.

Tsujimoto Y. 1997. Apoptosis and necrosis: Intracellular ATP level as a determinant for cell death modes. *Cell Death Differ*. 4:429–434.

Unno H, Goda S, Hatakeyama T. 2014. Hemolytic lectin CEL-III heptamerizes via a large structural transition from α-helices to a β-barrel during the transmembrane pore formation process. *J Biol Chem*. 289:12805–12812.

Xu J, Xu T, Wu B, Ye Y, You X, Shu X, Pei D, Liu J. 2013. Structure of sorting nexin 11 (SNX11) reveals a novel extended phox homology (PX) domain critical for inhibition of SNX10-induced vacuolation. *J Biol Chem*. 288:16598–16605.

Yamashita K, Kawai Y, Tanaka Y, Hirano N, Kaneko J, Tomita N, Ohta M, Kamio Y, Yao M, Tanaka I. 2011. Crystal structure of the octameric pore of staphylococcal γ-hemolysin reveals the β-barrel pore formation mechanism by two components. *Proc Natl Acad Sci U S A*. 108: 17314–17319.

Wei F, Cao S, Ren X, Liu H, Yu J, Li H, Hao X. 2008. Efficient antiproliferative and antiangiogenic effects on human ovarian cancer growth by gene transfer of attenuated mutants of Shiga-like toxin I. *Int J Gynecol Cancer*. 18:677–691.

Chapter 35

Bacterial Expression of Rhamnose-Binding Lectin from Catfish Eggs

Shigeki Sugawara, Takeo Tatsuta, and Masahiro Hosono

Abstract

SUEL-like lectins, also termed rhamnose-binding lectins (RBL), are unique in animal lectin families because of their tandemly repeated structure that is characteristic of carbohydrate-recognition domains, as well as their α-galactoside-binding capacity. RBLs are known to be expressed in inclusion bodies in *Escherichia coli*. Here, we describe the methods for the expression and refolding of *Silurus asotus* lectin (SAL) using *E. coli* KRX as the host strain. From our results, highly basic and reduced conditions due to arginine and dithiothreitol, respectively, tend to keep SAL recombinants soluble.

Key words SUEL-like lectin, Rhamnose-binding lectin, Inclusion body, Refolding, Soluble aggregate

1 Introduction

A number of "sea urchin egg lectin (SUEL)-like" family lectins have been found in aquatic animals such as teleosts, echinoderms, and mollusks [1]. Since L-rhamnose was the most potent inhibitory sugar for these lectins, we termed them "rhamnose-binding lectins (RBLs)" [2]. Since L-rhamnose (6-deoxy-L-mannose) is not present in animal tissues, the most likely cell surface ligand of RBL is thought to be globotriaosylceramide (Gb3) because of the α-galactoside-binding capacity of RBLs [1, 3, 4]. SUEL was the first RBL to be sequenced [5]. RBLs mainly consist of two or three tandemly repeated carbohydrate-recognition domains (CRDs), each of which include two characteristic RBL-CRD motifs, ANYGR residues at the *N*-terminus, and DPC-KYL residues at the C-terminus [6]. Interestingly, SUEL is the only RBL that consists of covalently bonded dimeric proteins. Aside from eggs, body fluids such as plasma [7], mucus [8], and venom [9] have gradually become common sources of RBL in the last two decades. Although the biological functions of RBLs are not yet fully understood, they have been presumed to be involved in innate immunity, as well as in certain cellular functions such as cell death [1].

Jun Hirabayashi (ed.), *Lectin Purification and Analysis: Methods and Protocols*, Methods in Molecular Biology, vol. 2132, https://doi.org/10.1007/978-1-0716-0430-4_35,

Silurus asotus lectin (SAL, 32 kDa) isolated from catfish eggs consists of three RBL domains [6]. We have shown that SAL decreases the proliferation of Gb3-expressing Burkitt's lymphoma Raji cells without inducing cell death [10]. SAL also promoted the uptake of doxorubicin (Dox) into Raji cells and consequently enhanced the cytotoxic effect of Dox [11]. The combined effect of SAL and a particular antitumor drug is currently being in studied in our laboratory.

Interestingly, the SUEL homodimer is reported to be inactive during hemagglutination under reducing conditions, whereas it keeps its binding capacity to thiodigalactoside as an affinity ligand [5]. To define the importance of RBL-CRD and the other motifs for lectin activities, we tried to obtain deletion mutants of SAL using bacterial expression system. Up to eight cysteine residues in each CRD, twenty-four residues in a molecule, were major bottleneck in recombinant protein production. Although expression of SUL-1, an RBL from sea urchin venom, in *E. coli* has been reported previously [12], we encountered some problems in the expression of rSAL. To solve these problems, we have made some modifications, and the improved protocol is described in this chapter.

The essential points are

1. *E. coli* KRX strain is used instead of BL21 (*see* **Note 1**).
2. Upon solubilization of inclusion bodies, 0.1 M dithiothreitol (DTT) is added to denaturation buffer (*see* **Note 3**).
3. To avoid forming soluble aggregates, "dilution" step is introduced before dialysis in the refolding process (*see* **Note 4**).
4. To avoid misfolding, highly basic refolding buffer is used with "free" arginine when starting dialysis and then the buffer pH is lowered gradually (*see* **Note 5**).

2 Materials

2.1 Protein Expression in KRX and Isolation of Inclusion Bodies

1. *E. coli* KRX competent cells.
2. Expression plasmids: pET16b.
3. Enzymes: *Nco*I, *Nde*I, *Bam*HI, *Bgl*II, and lysozyme.
4. Growth medium: Luria-Bertani and Terrific broth supplemented with 50 μg/mL carbenicillin.
5. 20% L-rhamnose solution.
6. Sonication buffer (SB): 50 mM Tris–HCl buffer (TB) (pH 8.0) containing 50 mM NaCl.
7. Triton X-100.
8. Equipments: spectrophotometer (GeneQant 100); sonicator (VCX-600).

2.2 Denaturation, Refolding, and Purification

2.2.1 Buffers

1. Denaturation buffer (DB): 0.1 M phosphate buffer (PB) (pH 8.0) containing 6 M guanidine-HCl.
2. 6U50TB10 and 4U50TB10: 50 mM TB (pH 10) containing 6 M or 4 M urea, respectively.
3. 8U100PB8 and 8U100PB6.3: 0.1 M PB (pH 8 and 6.3, respectively) containing 8 M urea.
4. Refolding buffer (RB): 50 mM TB (pH 10) containing 0.3 M arginine, 5% glycerol, 5 mM reduced glutathione, 0.5 mM oxidized glutathione, and 0.3 M NaCl.
5. 50TBS8~10: 50 mM TB (pH 8, 9, and 10, respectively) containing 0.15 M NaCl.
6. DTT.

2.2.2 Affinity Resins and the Others

1. Galactose-Sepharose: galactose affinity resin is prepared by the method of Fornstedt and Porath using divinyl sulfone as a resin activator [13].
2. D-galactose.
3. Ni Sepharose 6 fast flow.
4. Imidazole.
5. Spectra/Por3 MWCO 3500.
6. Centrifugal ultrafiltration device: Vivaspin500 MWCO 3000.

2.3 Protein Detection

1. SDS-polyacrylamide gel electrophoresis (PAGE): Mini-PROTEAN II.
2. DC protein assay kit.

2.4 Hemagglutination and Inhibition Assays

1. Rabbit erythrocytes (Nippon Biotest).
2. 96-well U-plate
3. Phosphate-buffered saline (PBS): 10 mM PB (pH 8.0) containing 0.15 M NaCl.
4. Tuple mixer.

3 Methods

E. coli KRX competent cells (*see* **Note 1**) are transformed with the plasmid (*see* **Note 2** and Fig. 1) of interest according to the manufacturer's protocol.

3.1 Protein Expression in KRX and Isolation of Inclusion Bodies

1. Pre-culture the transformed KRX cells overnight at 37 °C in Luria-Bertani medium with vigorous shaking.
2. Add aliquots (1.0 mL) of culture to 100 mL of Terrific broth medium and shake the flask at 37 °C until the absorbance at 600 nm (A_{600}) reaches 0.8–1.0.

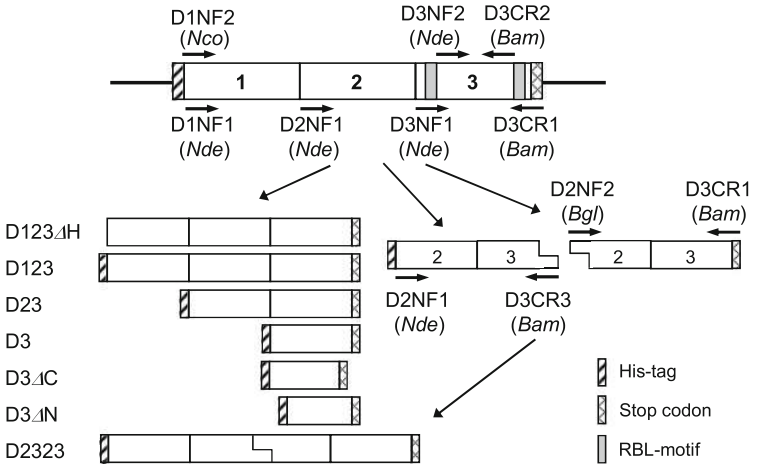

Fig. 1 Construction of expression plasmid for rSAL and its mutants. cDNA of rSAL recombinants were designed by PCR using sequence-specific primers and cloned into the multiple cloning site of pET16b. Primer pairs used: D1NF2 and D3CR1 for D123ΔH; D1NF1 and D3CR1 for D123; D2NF1 and D3CR1 for D23; D3NF1 and D3CR1 for D3; D3NF1 and D3CR2 for D3ΔC; D3NF2 and D3CR1 for D3ΔN; D2NF1 and D3CR3, D2NF2 and D3CR1 for D2323, respectively

3. Transfer the flask to another shaker set at 23 °C and continue shaking until A_{600} reaches 1.2.
4. Add 0.5 mL of 20% L-rhamnose solution and culture for 24 h.
5. Collect cells by centrifugation at 4000 × *g* for 10 min and re-suspend with 5 mL of SB.
6. Lyse the cells by addition of lysozyme (200 μg) with gentle inversion at 4 °C for 30 min. (Reduce the viscosity by sonication with micro probe.)
7. Add 5 mL of SB containing 10% Triton X-100 and incubate at 4 °C for 30 min.
8. Sonicate the suspension for 30 s at 30% of full power of the apparatus. Repeat three times on ice.
9. Remove soluble lysate by centrifugation at 15,000 × *g* for 20 min.
10. Suspend the pellet in 5 mL of SB containing 2% Triton X-100 and repeat 8–9 times until the supernatant becomes colorless.
11. Dispense the suspension into microtubes and wash the pellet four times with cold H_2O by centrifugation at 18,000 × *g* for 20 min. Store at −80 °C until use.

3.2 Denaturation, Refolding, and Purification of Recombinants Except for D3Δ C and D3Δ N (See Note 2)

1. Dissolve washed inclusion bodies (~100 mg) in 1 mL of DB containing 0.1 M DTT (*see* **Note 3**) with mild inversion overnight at 4 °C.
2. Dilute (1:60) the denatured protein solution by dropping into 6U50TB10 on ice (*see* **Note 4**).
3. Dialyze the diluted solution serially against 2 L of 4U50TB10 at 4 °C followed by twofold dilutions of urea from 2 M to 62.5 mM with freshly prepared RB, then 50TBS10 and 50TBS9 (*see* **Note 5**).
4. Centrifuge at 15,000 × *g* for 20 min.
5. Apply the supernatant to the galactose-Sepharose column (1 × 20 cm) equilibrated with 50TBS9 (*see* Subheading 2.2).
6. Washout non-adsorbed proteins with 50TBS9 thoroughly.
7. Elute the adsorbed protein with 50TBS9 containing 0.2 M D-galactose. Combine the fractions containing protein on the basis of A_{280}.
8. Dialyze the lectin fractions against 50TBS9 thoroughly.
9. Concentrate the dialyzed solution and change buffer with a centrifugal ultrafiltration device to give a protein concentration of approx. 1 mg/mL in 50TBS8.

3.3 Denaturation, Purification, and Refolding of D3Δ C and D3Δ N

1. Dissolve the washed inclusion bodies in 0.5 mL of DB with mild inversion overnight at 4 °C.
2. Centrifuge at 15,000 × *g* for 20 min.
3. Apply the supernatant to a Ni-column (1 mL of bed volume) equilibrated with 8U100PB8 at a flow rate of 100 μL/min.
4. Wash the column with 15 mL of 8U100PB6.3 followed by 5 mL of 8U100PB8 containing 10 mM imidazole. Collect the eluate by dispensing 1 mL each in microtubes.
5. Elute adsorbed protein using 8U100PB8 containing 250 mM imidazole (10–20 mL) and measure the A_{280} of each fraction.
6. Collect protein-positive fractions and dialyze against 2 L of 6U50TB10 at 4 °C for 24 h with changing buffer.
7. Add DTT to the dialyzed solution to give a final concentration of 0.1 M and incubate for 1 h at 4 °C.
8. Go to **step 3** in Subheading 3.2.
9. Go to **step 9** in Subheading 3.2.

3.4 Protein Detection

SDS-PAGE and protein assay are carried out based on the Laemmuli and Lowry's methods, respectively (*see* Subheading 2.3 and **Note 6**).

3.5 Hemagglutination and Inhibition Assays

Hemagglutination activity of recombinants and their sugar specificity are measured according to the method of Sano et al., with a little modification [14] (*see* **Note 6**) by using rabbit erythrocytes at room temperature: take **steps 1A**, **4,** and **5** for hemagglutination assay, and **steps 1B** through **5** for inhibition assay:

1. Make the serial twofold dilution of (A) the recombinants (25 μL) or (B) the sugars desired (15 μL) in 50TBS8 in the 96-well U-shape plate.
2. Add the fixed amount of recombinant solution (10 μL) to every well which includes four times the minimum concentration of sample showing obvious hemagglutination, except for control wells.
3. Mix the plate by Tuple mixer for 10 min and then allow to stand for 20 min.
4. Add 2% rabbit erythrocyte suspension (25 μL) in PBS and mix the plate by Tuple mixer for 10 min.
5. Allow the plate to stand for 30 min and then observe hemagglutination or inhibition.

4 Notes

1. In our previous experience, *E. coli* expression systems requiring IPTG as an inducer such as BL21, AD494, and Rosetta-gami, as well as their variants, do not work well. Thus, we tried to express the recombinant proteins in *E. coli* KRX containing the rhamnose operon and consequently succeeded in obtaining all rSAL mutants from inclusion bodies.
2. All recombinants were designed by PCR using sequence-specific primer pairs of interest on SAL cDNA-inserted pET16b expression vector as a template (Fig. 1). First, we generated the D123ΔH construct that included domains 1, 2, and 3 (almost corresponding to SAL) but lacked the N-terminal His-tag sequence using the *Nco*I/*Bam*HI sites of the vector. The other recombinants included an extra sequence containing a His-tag at the N-terminus for purification through a Ni-column because D3ΔC and D3ΔN, which lack C-terminal (DPC-KYL) and N-terminal (ANYGR) RBL-motifs, respectively, were thought to be inactive for affinity purification using galactose-sepharose. Meanwhile, D2323 cDNA was prepared by fragment coupling through *Bgl*II and *Bam*H1 sites between two domains that generate compatible cohesive ends to obtain an uncleavable construct.

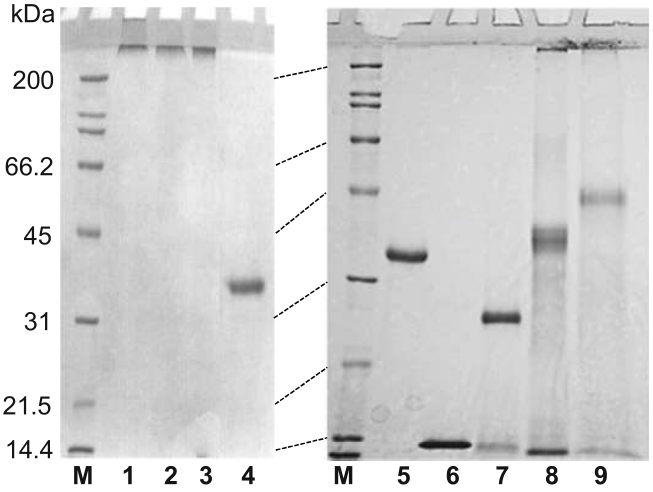

Fig. 2 SDS-PAGE pattern of rSAL recombinants. Samples are subjected to SDS-PAGE on 12.5% separation gels under reducing conditions. Lanes 1–3: D123 obtained by refolding system without dilution (*see* **Note 4**) treated with: lane 1, 5% 2-mercaptoethanol (same as lanes 5–9); lane 2, 25% mercaptoethanol; and lane 3, 0.25 M dithiothreitol, respectively. Lanes 4 and 5, intact SAL. Lane 6, D3. Lane 7, D23. Lane 8, D123. Lane 9, D2323. M, molecular marker

3. Inclusion bodies of rSAL mutants composed of up to two domains are clearly dissolved only in DB, whereas those composed of more than three domains are hardly soluble. These insoluble materials required DB containing more than 0.1 M DTT to be soluble. Since the compatibility of Ni-resin against DTT is guaranteed by the manufacturer to be as low as 5 mM, D123 and D2323 cannot be purified directly through the Ni column unlike the other smaller mutants. Approximately 100 mg of wet weight of inclusion bodies can be obtained from 100 mL of culture.
4. Although the reason is still unclear, recombinants composed of more than three domains form soluble aggregates during dialysis when refolding is performed without dilution. These recombinants do not migrate in an SDS-PAGE under exhaustive reducing conditions (Fig. 2, lanes 1–3). This problem can be solved by performing a dilution step before the beginning of dialysis (Fig. 2, lanes 6–9).
5. Initially, we performed refolding of D123ΔH by this dialyzing system using RB-containing arginine hydrochloride (around pH 8). However, misfolded protein precipitated during dialysis. This problem is solved by using arginine to keep the pH of RB at around 11. The first half of dialysis is for reducing urea, while the latter half is for adapting refolded protein to lower concentrations of reagents, as well as to the pH condition of

Table 1
Hemagglutination activity of SAL and recombinants

Samples	Activity[a] (μg/mL)
SAL	0.1
D3	7.8
D23	0.5
D123	0.4
D123ΔH	0.8
D2323	0.5
D3ΔC	>250
D3ΔN	>250

[a]Hemagglutination activity was represented as a minimum protein concentration (μg/mL) required for complete hemagglutination of rabbit erythrocytes

50TBS9. Resulted protein is adsorbed onto both Ni and galactose-Sepharose columns, indicating that recombinant lectin is successfully obtained as an active form. In fact, the recombinant lectin also possesses hemagglutination activity toward rabbit erythrocytes (Table 1). Approximately 1 mg of recombinant protein is obtained from 100 mg of inclusion bodies.

6. As shown in Table 1, D3ΔC and D3ΔN show no hemagglutination activity, indicating that the two RBL motifs are essential for this lectin. The D3 molecule is capable of binding to galactose-sepharose as it is not found in the flow-through fraction of this column, but it partially behaves like a divalent molecule or with non-covalent association. However, it does not form a huge aggregate unlike the recombinants with more than three domains (Fig.2). D23, D123, and D2323 show comparable hemagglutination activity, suggesting that the number of domains does not affect the activity. Meanwhile, the activity of D123ΔH is slightly lower compared with the His-tagged recombinants, but all of the recombinants are less active than SAL (Table 1). This may be attributed either to the additional amino acid sequence from the plasmid or to partial misfolding. Optimizing for more suitable refolding conditions and understanding the underlying mechanisms are required to overcome these problems.

References

1. Ogawa T, Watanabe M, Naganuma T et al (2011) Diversified carbohydrate-binding lectins from marine resources. J Amino Acids. https://doi.org/10.4061/2011/838914
2. Sakakibara F, Takayanagi G, Kawauchi H (1981) An L-rhamnose-binding lectin in the eggs of *Misgurnus anguillicaudatus*. Yakugaku Zasshi 101(10):918–925
3. Sugawara S, Hosono M, Ogawa Y et al (2005) Catfish egg lectin causes rapid activation of multidrug resistance 1 P-glycoprotein as a lipid translocase. Biol Pharm Bull 28 (3):434–441
4. Watanabe Y, Tateno H, Nakamura-Tsuruta S et al (2009) The function of rhamnose-binding lectin in innate immunity by restricted binding to Gb3. Dev Comp Immunol 33(2):187–197
5. Ozeki Y, Matsui T, Suzuki M et al (1991) Amino acid sequence and molecular characterization of a D-galactoside-specific lectin purified from sea urchin (*Anthocidaris crassispina*) eggs. Biochemistry 30(9):2391–2394
6. Hosono M, Ishikawa K, Mineki R et al (1999) Tandem repeat structure of rhamnose-binding lectin from catfish (*Silurus asotus*) eggs. Biochim Biophys Acta 1472:668–675
7. Okamoto M, Tsutsui S, Tasumi H et al (2005) Tandem repeat L-rhamnose-binding lectin from the skin mucus of ponyfish, *Leiognathus nuchalis*. Biochem Biophys Res Commum 333 (2):463–469
8. Cammarata M, Parisi MG, Benenati G (2014) A rhamnose-binding lectin from sea bass (*Dicentrarchus labrax*) plasma agglutinates and opsonizes pathogenic bacteria. Dev Comp Immunol 44(2):332–340
9. Hatakeyama T, Ichise A, Yonekura T et al (2015) cDNA cloning and characterization of a rhamnose-binding lectin SUL-I from the toxopneustid sea urchin *Toxopneustes pileolus* venom. Toxicon 94:8–15
10. Sugawara S, Im C, Kawano T et al (2017) Catfish rhamnose-binding lectin induces G0/1 cell cycle arrest in Burkitt's lymphoma cells via membrane surface Gb3. Glycoconj J 34:127–138
11. Sugawara S, Sasaki S, Ogawa Y et al (2005) Catfish (*Silurus asotus*) lectin enhances the cytotoxic effects of doxorubicin. Yakugaku Zasshi 125(3):327–334
12. Hatakeyama T, Ichise A, Unno H et al (2017) Carbohydrate recognition by the rhamnose-binding lectin SUL-I with a novel three-domain structure isolated from the venom of globiferous pedicellariae of the flower sea urchin *Toxopneustes pileolus*. Protein Sci 26:1547–1583
13. Fornstedt N, Porath (1975) Characterization studies on a new lectin found in seeds of *Vicia ervilia*. FEBS Lett 57:187–191
14. Sano K, Ogawa H (2014) Hemagglutination (inhibition) assay. In: Hirabayashi J (ed) Lectins. Methods in molecular biology, vol 1200. Springer, Heidelberg, pp 47–52

特集：Human Glycomeがもたらす未来

糖鎖立体構造解析技術の開発要素

山口　芳樹

真の生命像を俯瞰的に捉えるためには，未解明問題が多く残っている糖鎖の研究を積極的に推進することが急務である．糖鎖の生理的機能を解明するためには，生化学的手法（酵素による糖鎖の切断），分子生物学的手法（糖転移酵素のノックアウト）などさまざまな手法が考えられるが，中でも糖鎖の化学構造を決定し，その立体構造・運動性や相互作用様式を調べるアプローチは，糖鎖の機能を視覚的に理解することを促し，説得力がある．いわゆる構造生物学的な考えであるが，糖鎖を対象とする場合は，他の生体高分子と異なる特異な性質を十分理解する必要がある．本稿では糖鎖の立体構造・運動性・相互作用について概説し，糖鎖の立体構造や相互作用について筆者が普段よく質問されることを中心にQ&A形式でまとめ，最後に立体構造解析技術の現状と展望を述べたい．

1.　はじめに―糖鎖の特徴は何か―

生体分子としての糖鎖を核酸やタンパク質など他の生体高分子と比較すると，共通点も存在するが，相違点がきわだっている．核酸もタンパク質も糖鎖も，構成ユニット（ビルディングブロック）がつながって高分子ができ上がっているという点では共通であるが，その構成ユニットとその結合様式を比較すると糖鎖の特徴を理解することができる（**図1**）．核酸の場合は，ヌクレオチドがホスホジエステル結合で，タンパク質の場合はアミノ酸がペプチド結合（アミド結合）でつながっており，結合様式は一義的である．一方で，糖鎖の場合は，構成ユニット（主に単糖）間の水酸基（ヒドロキシ基）どうしが脱水縮合してグリコシド結合を形成しており，その結合様式は立体化学・結合部位の点から実に多様である．まさにこの点が，糖鎖の化学構造の多様性を生み出していることと密接に関係し，糖鎖は多機能な情報分子としての潜在能力を秘めている．別の観点からいえば，核酸やタンパク質はその結合様式の特徴から直鎖構造しか形成することができないが，糖鎖は構成ユニット中に水酸基を複数持つことから，分岐構造（枝分かれ構造）を形成することが可能である．この分岐構造については，糖鎖と糖鎖結合分子（レクチン，抗体など）との相互作用を理解するときに，特に注意を払うべき点である．というのは，複数の分岐はしばしば同じ構造ユニットを有しており，1本の糖鎖あたり複数のタンパク質相互作用部位を有するからである．

糖鎖は遊離の状態，もしくはタンパク質や脂質と結合した状態（複合糖質）として生体内で存在している．タンパク質と糖鎖の結合様式も複数存在すること，また脂質自身も脂質の鎖長の違いなどで構造多様性を有することから，複合糖質としてはいっそう多様性を増すことになる．核酸の場合でもリボースやデオキシリボースといった糖がその構成ユニットとして入り込んでおり，核酸も糖質と無縁ではない．細胞質や核内にもリン酸化と同じように糖修飾が見いだされ，多くは競合する関係にある．このように糖あるいは糖鎖は生体内に広く分布しており，さまざまな形で見いだされる．したがって糖鎖・糖質を対象とする糖鎖生物学は，さまざまな研究分野に浸透するべきものであろう．

2.　糖鎖の立体構造の表現方法

糖鎖に限らず，生体分子の世界を見たいと思う．分子の世界を手に取るように見ることができれば，その分子の働きを容易に理解することができるであろう．しかし，原子レベルの分解能で分子を見るには，特殊な方法を用いる必要がある．その方法については後述するとして，ここでは

東北医科薬科大学（宮城県仙台市青葉区小松島4–4–1）
Techniques for analyzing 3D structure and dynamics of glycan
Yoshiki Yamaguchi (Tohoku Medical and Pharmaceutical University, 4–4–1 Komatsushima, Aoba-ku, Sendai, Miyagi 981–8558, Japan)
DOI: 10.14952/SEIKAGAKU.2020.920369

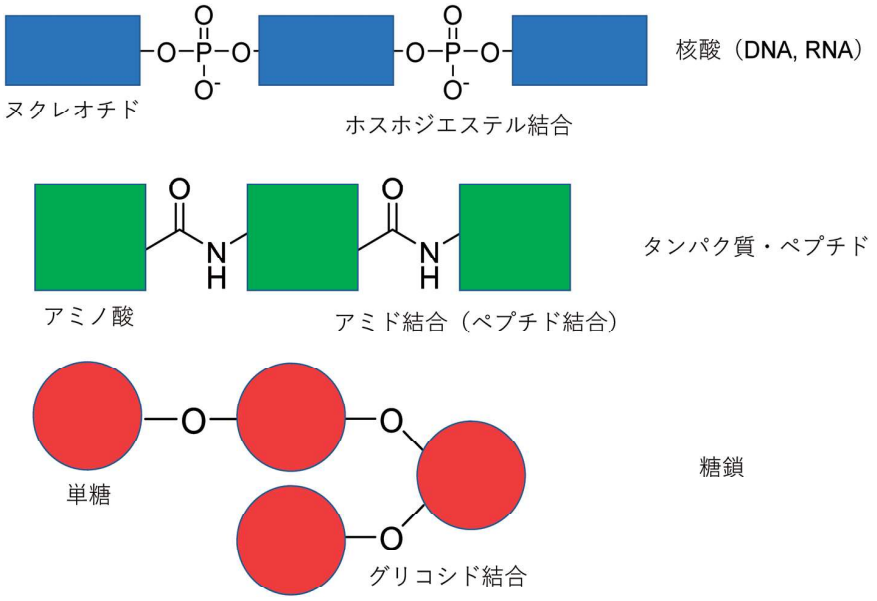

図1　生体高分子（核酸，タンパク質，糖鎖）の構成ユニットと結合様式の模式図
糖鎖は核酸やタンパク質と異なり，分岐構造の形成が可能である．

糖鎖の立体構造の表現方法について述べたい．

糖鎖の立体構造を明らかにするということは，糖鎖を構成する各原子の座標（x, y, z）を明らかにするということと同義である．座標を明らかにすることができれば，適当なソフトウェアを用いることにより，糖鎖を立体構造表示することができ，分子の世界をのぞき込むことが可能になる．一方で，糖鎖の立体構造を比較したり，運動性を評価したりする際に，糖鎖の立体構造を表現するパラメータを定義すると便利である．そのパラメータが，単糖間のグリコシド結合周りの二面角である．都合がよいことに，糖鎖を構成する単糖はほとんどの場合環状構造となっており，その環状構造は通常エネルギー的に安定ないす形構造を占めている．そのため，糖鎖の全体的な立体構造を捉える場合は，環状構造部分は固定して考えてよく，自由度のあるグリコシド結合周りの二面角のみを調べればよいことになる．これはタンパク質主鎖のコンホメーションを考えるときに，主鎖二面角を表示したラマチャンドラン・プロットを用いることと似ている．

糖鎖のグリコシド結合周りの二面角は，二面角を構成する連続した四つの原子の座標から規定される（**図2**）．たとえば六員環の単糖(i)と単糖（i−1）が1–4結合でつながっている場合，以下の二つの二面角φ（ファイ）とψ（プサイ）を用いることがIUPAC-IUB合同委員会により推奨されている[1]．

$$\varphi = \mathrm{O5}(i) - \mathrm{C1}(i) - \mathrm{O4}(i-1) - \mathrm{C4}(i-1)$$

$$\psi = \mathrm{C1}(i) - \mathrm{O4}(i-1) - \mathrm{C4}(i-1) - \mathrm{C3}(i-1)$$

さてNMR法により得られるパラメータ，特に^3Jカップリング定数を用いて糖鎖のグリコシド結合周りの二面角を明らかにすることができる．^3Jカップリング定数は以下のKarplusの式によって二面角の情報に変換できるからである．

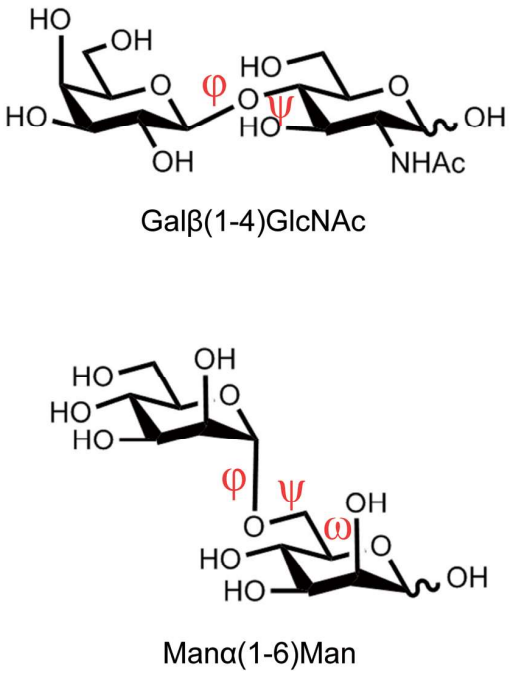

図2　糖鎖のグリコシド結合周りの二面角の定義

$$^3J = A\cos 2\theta + B\cos\theta + C$$

（ただしA, B, Cは経験則から得られる定数）

NMR法では主に水素原子を観測対象とするため，^3Jカップリング定数と二面角を関連づける場合，以下のような水素原子を含めた二面角の定義が用いられることもある．

$$\varphi = \mathrm{H1}(i) - \mathrm{C1}(i) - \mathrm{O4}(i-1) - \mathrm{C4}(i-1)$$

$$\psi = \mathrm{C1}(i) - \mathrm{O4}(i-1) - \mathrm{C4}(i-1) - \mathrm{H4}(i-1)$$

X線結晶構造解析から得られた糖鎖の像は水素原子の情報が含まれていないことが多いので，その場合は前者の水素原子を使わない定義を用いることになる．論文間で二面角の定義が異なることもあり，データを比較して議論する際には二面角の定義を確認する必要がある．

多くの場合，グリコシド結合周りの二つの二面角φとψで糖鎖のコンホメーションを描写することが可能であるが，一部の結合（1-6結合など）についてはφとψに加えて，ω（オメガ）など追加の二面角が必要になる（図2下）．

$$\omega = \mathrm{O6}(i-1) - \mathrm{C6}(i-1) - \mathrm{C5}(i-1) - \mathrm{O5}(i-1)$$

（水素原子を含めない定義）

$$\omega = \mathrm{O6}(i-1) - \mathrm{C6}(i-1) - \mathrm{C5}(i-1) - \mathrm{H5}(i-1)$$

（水素原子を含めた定義）

六員環の環状糖のリング部分は先に述べたようにいす形がエネルギー的に安定であり，多くの場合，環状構造はいす形を占めていると考えてよい．しかし，酵素反応の中間体（遷移状態）としてのリガンド糖鎖，あるいは硫酸化を過度に受けた糖残基などはいす形から逸脱することがあるので注意を促したい[2]．また核酸を構成するリボース，デオキシリボースなど五員環は，六員環よりも環状構造は柔らかい．通常，糖の環状構造（パッカリング）はCremerとPopleによって提案された三つのパラメータによって表現される[3]．六員環の場合，いす形(C)2個に加えて舟形(B)6個，ねじれ舟形(S)6個，封筒形(E)12個，半いす形(H)12個の合計38個に分類される．

パッカリングの重要性を示す一例として，抗インフルエンザウイルス薬をあげることができる．リレンザやタミフルはシアル酸の誘導体であるが，その環状構造内に炭素–炭素間の二重結合が導入されている．これは二重結合の導入によりいす形を崩し，ウイルス由来のノイラミニダーゼ（シアリダーゼ）の基質の遷移状態を模倣している．もう一つの例として細菌のラムノース転移酵素をあげたい．ラムノースを付加する糖転移酵素EarPは，細菌の伸長因子EF-Pの特定のArg残基（Arg32）をラムノース化する[4]．EarPの結晶構造解析からラムノースはいす形で結合していたが[5]，想定されるS_N2反応（立体化学の反転を伴う反応）を進行させるためには，いす形では反応が進まず，ねじれ舟形のようないす形とは異なる形になることが予想された．実際に分子動力学計算を行うと，いす形ではないラムノースの形が安定な形として見いだされた．これらのことから，酵素反応は非いす形を経て反応が進むことが考えられた[5]．他に，ERマンノシダーゼにおいてもその結晶構造からリガンド糖鎖の非いす形のコンホメーションが議論されている[6]．

最近になり，環状構造を持たない直鎖状のユニット（リビトール）が哺乳動物の糖鎖に存在することも見いだされた[7,8]．このリビトール内および連結部分のコンホメーションを表現する場合には通常より多くの二面角が必要になる．新しいメンバーであるリビトールの安定なコンホメーションを実験および計算の両面から調べることは今後の課題である[9,10]．

3. 糖鎖の立体構造と相互作用について

さて糖鎖の立体構造と相互作用については，タンパク質や核酸の場合と比較して圧倒的に情報量が少ないことから，統計的に調べることが困難な状況である．たとえばPDBを用いて糖鎖の像が得られている糖タンパク質の立体構造を調べた場合，その数は2015年6月の時点で重複を除くと100を超えていない[11]．限られた例数で我々の糖鎖の立体構造・相互作用についての理解は十分ではないが，それでも糖鎖を対象とした先駆的な研究報告も多数存在する．そこで本節では，筆者がこれまで糖鎖の立体構造や相互作用に関して受けた質問を中心に疑問点をあげて，過去の論文を参照しつつQ&A形式で回答してみたい．

1） X線結晶構造で糖鎖の像が見えないのはなぜか？

糖タンパク質を結晶化しているにもかかわらず，糖鎖の像が得られていない場合がある．これは大きく分けて二つの場合が考えられる．一つは，結晶化の効率を上げるために，何らかの方法で糖タンパク質の糖鎖をあらかじめ取り除いている場合である．糖鎖をグリコシダーゼで除く，あるいは糖鎖付加がそもそもできない大腸菌で糖タンパク質を発現している場合などがある．もう一つは，糖鎖が結合しているにもかかわらず電子密度像として得られていない場合である．これは主に糖鎖のグリコシド結合周りの二面角の自由度に由来すると考えられる．タンパク質の結晶構造解析において，N末端やC末端，あるいはループ部分など比較的運動性の高いと思われる領域の電子密度像が得られない事象と似ている．このような場合，糖鎖の全体像はわからないが，糖鎖が部分的に像を与えることもしばしばみられる．Asnに結合している*N*-アセチルグルコサミン1〜2残基はよく観測されるものの，それ以降の電子密度像が得られていないケースである．これはAsnに結合している糖鎖の根本付近は比較的堅く，自由度が比較的乏しいことに対応していると考えられる．糖鎖を切断しているからその像が見えないのか，それとも糖鎖は存在するけれど，その自由度が高いために像が得られていないのかは，立体構造のデータだけからは判断できない場合が多く，元の論文をひもとく必要がある．

一方で，例外的にほとんど完全に糖鎖の電子密度像が得られることがある．代表的な例として，抗体のFc領域に結合している糖鎖があげられる[12]．1対の二本鎖複合型糖鎖が結合しているが，一部の糖残基を除き，全体像を観察することができる．これは糖鎖がFc分子の比較的内部に埋もれており，糖鎖とポリペプチド鎖が広範囲で分子内相

互作用しており，糖鎖の運動性が比較的抑制されていることと関係している[13, 14]．

2） 糖鎖の立体構造を決めるのはなぜ難しいのか？

糖鎖の立体構造を知ることは，その機能をよく理解するための大事なステップである．たとえば，糖タンパク質糖鎖の立体構造を知るためには，糖タンパク質のままで結晶構造解析を行えばよいことになる．しかしながら，結晶が得られたとしても，先に述べた理由により糖鎖の電子密度像を得られない場合が多い．その場合は，糖鎖の立体構造に関する情報を積極的に得るためには他の手法に依存することになる．ありうる方法の中で溶液NMR法は，水溶液中における生体分子の立体構造・運動性・相互作用に関する情報を原子レベルで提供する方法である．これまで糖鎖・糖タンパク質のNMR解析がなされてきたが，立体構造を決定した報告は多くなく，その背景には糖鎖のNMR解析の難しさがある．これにはいくつか理由がある．第一に糖鎖の立体構造を規定するために利用できるNMRパラメータの少なさである．立体構造を制限するための十分な情報が得られないため，立体構造を一義的に規定するに至らない場合が多い．距離情報を提供する水素原子数が少ないこととも関係する．第二に本質的な問題として，糖鎖は一つの形をとっているのではなく，多くの場合複数のコンホマー間をすばやく遷移していることがあげられる．立体構造を規定する情報が少ない上に，1形でないとすると，その立体構造の描写は著しく困難になる．複数の安定構造からなる糖鎖の立体構造の描写を行うためには，(準)安定コンホマーを一つ一つ明らかにするとともに，その占有数（エネルギー差）や遷移速度を明らかにする必要がある．筆者らは，複数のレクチンを使って一つの共通の糖鎖と結合させ，各糖鎖-レクチン複合体の結晶構造解析を行うことにより，糖鎖の一つ一つのコンホマーを明らかにすることを試みた．その方法により，これまで一過的にしか捉えることのできなかった糖鎖の折れ曲がり構造が実験的に可視化された[15]．

3） 計算によって得られる糖鎖の立体構造はどの程度正しいのか？

糖鎖の立体構造を実験的に決定することが難しいため，分子動力学計算などの計算化学的な手法による糖鎖の立体構造の解明は重要な位置を占めている．分子動力学計算によって明らかにされた糖鎖の動的振る舞いをながめていると，静的なスナップショットをながめていただけでは出てこないような新しいインスピレーションも湧いてくる．ただ，実験を行う立場から気になる点は，計算によって得られた立体構造やダイナミクスは，どの程度本来の水溶液中の状態を反映しているのか，言葉を変えると計算結果はどの程度信頼できるか，である．この問いに答えるのは容易ではない．その理由として，実験的に得られた糖鎖の立体構造やダイナミクスの情報がそもそも多くないことがあげられる．それでも，これまでの先駆的な研究において計算データとNMRデータの比較がなされており，報告によると(準)安定構造と各構造の占有数は計算化学によっておおよそ再現することができるという[16, 17]．しかし，現状でも，どの力場を用いるか，水分子をどう扱うか，計算時間は十分か，実験結果と計算結果が対応しているかなど常に注意を払う必要がある．筆者の経験から，(*N*-アセチル基のない）グルコサミンやリビトールリン酸，硫酸化を受けた糖鎖などに対して力場のパラメータが設定されているかどうかを計算時に確認する必要がある[2]．

4） 糖鎖はタンパク質と相互作用するときにコンホメーションが変化するか？

糖鎖は柔軟な構造をしているため，複数の安定な構造をすばやく遷移しているが，タンパク質と相互作用する際に，その中のどのコンホマーが結合時に選択されるかは，糖鎖構造生物学の関心事の一つである．複数のコンホマーの存在と各コンホマーの占有率は通常，分子動力学計算などの手法により明らかにされるが，興味深いことにその占有数比はPDB中のリガンド糖鎖の各立体構造の出現頻度とよく一致する．すなわち，1分子を対象とした計算により得られたエネルギー的に安定なコンホメーションは，タンパク質と糖鎖の複合体の結晶構造中で統計的に頻度高くみられるコンホメーションと一致する[18]．したがって，「糖鎖はタンパク質と相互作用するときにコンホメーションが変化するか？」の質問に対する答えとしては，「糖鎖のコンホメーションは変化しない」が最も妥当な答えになる．もちろん，糖鎖のタンパク質結合部分は運動性の低下を伴うので，そのイメージを持ちながらの答えであり，例外も存在する．筆者らのグループが最近行った糖鎖とタンパク質の相互作用の例では，タンパク質の結合に伴い，遊離の糖鎖では観測されなかったコンホメーションでタンパク質と結合することが計算化学により示された[19]．

5） 糖鎖とタンパク質（レクチン）との親和性はなぜ一般に弱いのか？

通常単糖とタンパク質の一価（1対1）の相互作用は弱く，解離定数にしておおよそmM程度である場合が多い．なぜ相互作用が弱いのか．それは，結合自由エネルギーの内訳にヒントが隠されている．解離定数K_d（結合定数K）は結合自由エネルギーΔGと関係し，結合自由エネルギーはエンタルピー項ΔHとエントロピー項$T\Delta S$に分けることができる．

$$\Delta G = -RT\ln K$$

$$\Delta G = \Delta H - T\Delta S$$

ここでRは気体定数，Tは絶対温度である．糖鎖とタンパク質の相互作用の多くの場合，ΔHがΔGに大きく寄与しており，$T\Delta S$は通常結合に不利に働いている．このΔHと$T\Delta S$がほぼ相殺し，そのわずかな差がΔGとなってい

る．せっかくΔHで相互作用に貢献してもΔSが大きく足を引っ張っているのである．一例として，抗糖鎖抗体と糖鎖（ポリシアル酸DP～100）との相互作用の場合，ΔH＝−80.1 kcal/mol, $T\Delta S$＝−72.7 kcal/molであり，ΔHと$T\Delta S$がほぼ相殺してΔG＝−7.4 kcal/mol（K_d＝3.5 μM）となっている[20]．

ΔSの解釈は単純ではないが，水分子の再配置[21]や糖鎖のコンホメーションの柔軟性の喪失[22]によるものと考えられている．ΔSを人為的に小さくすることができれば，高親和性の糖鎖リガンドも原理的に開発することが可能である．自然界では，その弱い相互作用を克服するために多価での相互作用が利用されているようである．IgG抗体が二価で働いているように，糖鎖側およびタンパク質（レクチン）側も多価になっている場合が多く，みかけの親和性（avidity）は一価の相互作用の場合の親和性と比べて格段に強くなる．一般にその見かけの親和性は，それぞれ一価の結合定数の掛け算に匹敵する．

$$K_d^{avidity} = K_{d1} \times K_{d2}$$

こうして多価の相互作用が実現されたときにはμM程度の親和性となり，実効的には問題のない結合力となる．

6） 糖鎖はタンパク質の立体構造にどの程度影響を与えるか？

タンパク質の半数以上は糖鎖修飾を受けているという見積もりがあり，その糖鎖の役割は何なのか，タンパク質の立体構造に与える影響はどの程度なのか，糖鎖生物学の課題の一つである．タンパク質に結合している糖鎖の機能を大きく二つに分けると，糖鎖そのものがレクチンで認識されてシグナルとして働く場合（分子間相互作用）と，糖鎖がタンパク質の安定化に寄与している場合（分子内相互作用）になる[23]．ここで問題としたいのは，糖鎖とタンパク質の分子内相互作用がタンパク質の立体構造に及ぼす影響である．糖タンパク質から糖鎖を取り除くと，そのタンパク質は細胞外へ分泌されなくなる，溶解度が減少する，立体構造形成がうまくいかなくなる，生理活性が喪失・低下するなどの報告がある．このことから糖鎖はタンパク質の立体構造や物理化学的性質に影響を与えているといえる．具体的に糖鎖がタンパク質の立体構造にどのような影響を及ぼすかは，タンパク質ごと，糖鎖修飾部位ごとで議論することが必要になるが，Asnに糖鎖修飾を受けたタンパク質とそうでないタンパク質を統計的に比較すると，糖鎖修飾によりAsnの側鎖コンホメーションの自由度が制限される傾向にあるという[23–25]．また糖鎖の欠損により，一般的にタンパク質の運動性（揺らぎ）が増す傾向にあるようである[26, 27]．ただ現状では報告例が多くなく，今後のさらなる解析が必要になる．

4. 糖鎖の立体構造解析手法

糖鎖を含めた生体分子の立体構造解析を行う場合には，構造生物学的な手法が必要になる．原子レベルの分解能を提供する手法といえばX線結晶構造解析が王道であるが，溶液NMR法，固体NMR法に加えて最近では電子顕微鏡による解析が雑誌を賑わす存在になった．現在PDB中には約159,000個の立体構造情報が登録されており（2019年12月15日現在），そのうちX線は141,000個と圧倒的に多く，次にNMRの13,000個，次に電子顕微鏡の4,000個である．電子顕微鏡により決定された立体構造数の伸びは著しい（**図3**）．ここでは各手法の特徴と糖鎖に関連する最

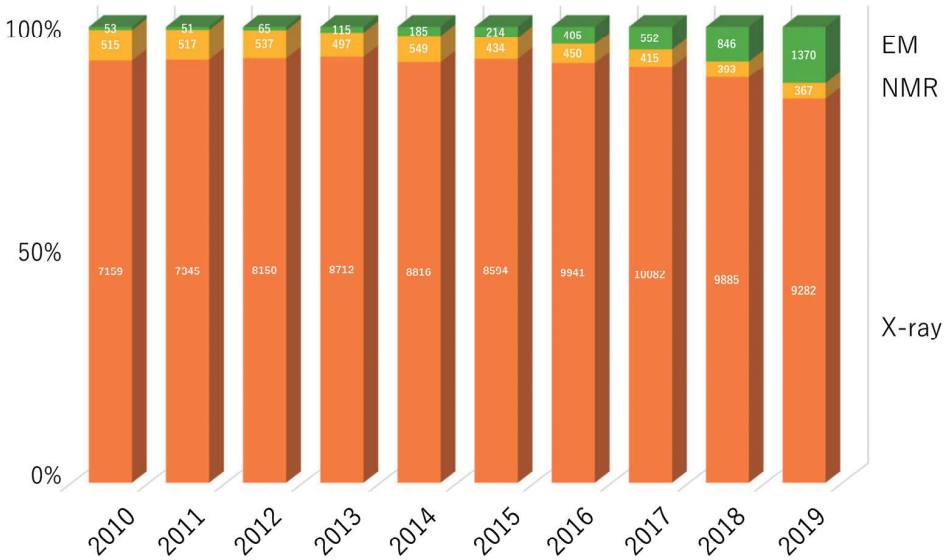

図3 各年にPDBに登録された生体高分子の解析手法の内訳
各年に登録された立体構造全体をそれぞれ100％とし，各解析手法［X線結晶構造解析（X-ray），NMR，電子顕微鏡（EM）］の割合を示した．棒グラフ中に示している数字は実際の立体構造数である．近年，電子顕微鏡によって解析された立体構造の割合が増加している．

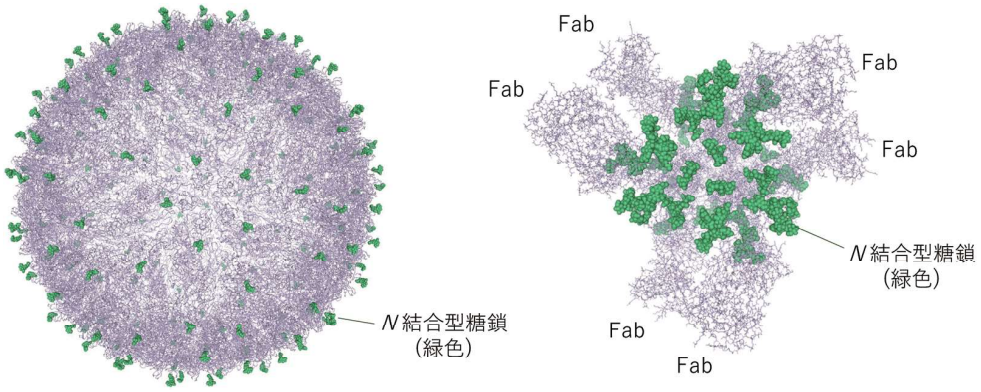

図4　ジカウイルスのクライオ電顕像(左)[28]とHIV-1エンベロープ糖タンパク質のX線結晶構造(右)[35]
いずれの図においても*N*結合型糖鎖を緑で示している．ジカウイルスのAsn154に結合している*N*結合型糖鎖の像は部分的に観測されている（GlcNAcβ1-4GlcNAcβ1-Asn）．エンベロープ糖タンパク質（三量体）には2種類のFab（合計六つ）が結合している．立体構造表示はNGL viewerにて行った[46]．

近の進展をまとめたい．

1）　クライオ電子顕微鏡

最近になり，生体高分子のクライオ電子顕微鏡（以下クライオ電顕）による観察例は増加の一途をたどっている．膜タンパク質やタンパク質線維，ウイルス，細胞など適用範囲はさまざまである．試料の調製の改善が進んだこともあるが，コンピュータに制御されたデータの取得とデータ処理の進展によるところが大きい．古典的な電子顕微鏡では，固定化や染色などが必要であり，そのステップで生体試料にダメージを与えることもしばしばであったが，クライオ電顕では薄い氷の中に閉じ込められた試料を可視化するため，生理的条件下により近い条件で測定することが可能である．ランダムに配向した分子の単粒子解析を行うことにより，3次元構造をおおよそ原子レベルの分解能で構築することができる．対称性の高い球状のウイルスなどは，電顕による構造解析に適した試料といえる．

糖タンパク質を対象とする場合，クライオ電顕は魅力的である．結晶化の必要がなく，糖鎖の不均一性や柔軟性は深刻な問題にはならない．仮に糖鎖が複数のコンホメーションからなっていたとしても，適切な分類により解決できるかもしれない．

糖鎖の像が得られている例をいくつか紹介する．ジカウイルスのクライオ電顕像が3.8Åの分解能で2016年に報告されたが，大変興味深いことに，Asn154に結合している糖鎖の像が部分的ではあるものの観測されている（**図4**左）[28]．その糖鎖は，宿主側のC型レクチン受容体DC-SIGNとの結合を介しているということが想定されている．実際デングウイルスの糖鎖とDC-SIGNの相互作用のようすが低分解能ながらクライオ電顕により調べられており，糖鎖のオリエンテーションや立体構造の重要性を示している[29]．同様に糖鎖の重要性が指摘されているウイルスがHIVである．これまでいくつかの報告がなされているが，Bjorkmanらの論文では詳細にエンベロープ糖タンパク質の糖鎖の構造について述べており，結晶構造とクライオ電顕から得られた糖鎖の像を比較している[30]．残念ながらクライオ電顕像の結果からは，その分解能の低さから糖鎖全体のコンホメーションを議論することは妨げられたが，高分解能の結晶構造のデータを用いて，低分解能の電子密度像への当てはめを行って議論することが可能であった．

またクライオ電顕像に限ったことではないが，結晶構造解析も含めて低分解能の糖鎖密度像を用いた解析の場合，糖鎖の立体化学の間違えや，環の不自然なゆがみなどを生み出すことがしばしばある[31]．実際PDB中の糖鎖構造には多くのエラーが存在しており，そのデータを用いた統計的な解析には注意を要する．コンホメーションや立体化学のエラーの検出や修正を行う方法も報告されており[32–34]，クライオ電顕により得られた低分解能の電子密度に正しく糖鎖を当てはめて構造精密化がなされている．

2）　X線結晶構造解析

構造生物学的手法の中で最も実績があるのがX線結晶構造解析であり，高分解能の情報を提供する．これまで多くの糖タンパク質や糖鎖-タンパク質複合体などが原子レベルで解明されてきた．他の手法を用いる場合でも同様であるが，試料の調製が鍵となる．いかに良質な試料を調製できるかが結晶化・構造解析の成否を決めるといってもよい．

糖タンパク質の場合，多くの場合は糖鎖の像が得られないが，しばしば電子密度像が得られることがある．糖鎖とタンパク質が分子内で広範に相互作用している場合は，先に述べたようにほぼ完全な状態で糖鎖の電子密度像を得られることがある．たとえば極端な例として，HIV-1のエンベロープ糖タンパク質は高マンノース型糖鎖や複合型糖鎖が高密度で結合しているにもかかわらず，2種類のFabを結合させることによって結晶構造が得られている[35]（**図4**

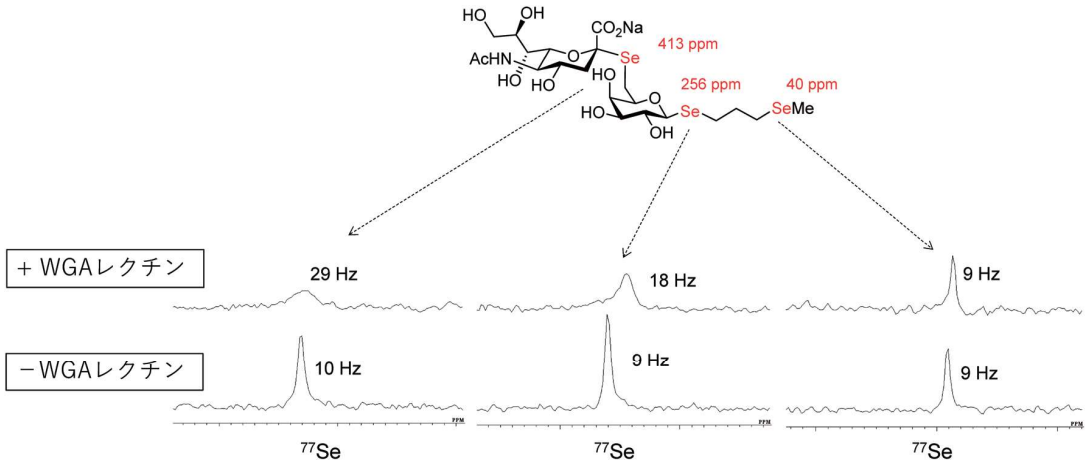

図5　合成セレン含有糖鎖とレクチンの相互作用の^{77}Se-NMR解析[45]
各NMRシグナルの線幅（半値幅）をHz単位で図中に示している．WGAレクチンの添加により，特定のセレンシグナルの線幅の広幅化が観測されている．一方でWGAレクチンの結合に関与していない部分に由来するセレンシグナルの線幅はほとんど変化していない．このことから，WGAレクチンの相互作用部位を同定することができる．

右）．通常であれば糖鎖を均一にするなどの方策をとるのが一般的であるが，これは糖鎖をnativeな状態で結晶化することに成功しており大変意義深い．一方で，糖タンパク質の結晶構造解析で注意しなければならないことは，結晶中では分子がパッキングされているため，生理的には観測されないような相互作用が強いられている可能性もあることである．糖分解酵素や糖転移酵素の結晶化を行ったところ，自身のAsnに結合している糖鎖が隣接分子の基質結合部位に収まって，基質を模倣している場合があった[36, 37]．その相互作用により結晶化が促進されている面もあるが，結晶中における糖鎖のコンホメーションや相互作用を議論するときは，それが生理的条件下・水溶液中でも起こるかどうかを常に意識しなければならない．

3）　NMR

NMR法，特に溶液NMR法は，水溶液中における原子レベルの情報を提供する唯一の方法である．溶液NMR法は糖鎖の運動性を調べるのに特に適した方法である．運動性はNMRパラメータのうちの緩和時間が適しており，緩和時間を用いた糖鎖のダイナミクス研究も報告例が多数存在する[13, 38, 39]．一方で，糖鎖の立体構造を調べるためには，立体構造を規定するためのNMRパラメータとしてNOE（核オーバーハウザー効果）と^{3}Jカップリング定数があげられるが，糖鎖は水素の密度が少ないこともあり，この二つだけでは不十分な場合が多い．そのため，追加で立体構造を規定するようなパラメータが必要になり，RDC（残余双極子カップリング）やPCS（擬コンタクトシフト）などを利用した糖鎖のコンホメーション解析が進んでいる[40]．特に多分岐糖鎖において，PCSなどを利用することにより，各分枝に由来する信号を区別して議論できるようになったことは大きなブレークスルーである[41–43]．筆者らも糖鎖のコンホメーションを解析するための新たなNMRパラメータとして，糖残基間の^{1}H-^{13}C異核NOEやグリコシド酸素をセレンに置換したセレン含有糖鎖における^{77}Seカップリング定数の利用[44]などを検討している．セレンに由来するNMR信号は化学シフトの範囲が広く，かつレクチンとの結合を鋭敏に反映するため（**図5**），生体溶液中（血清中など）での相互作用の特異的検出など今後の応用が期待される[45]．

5.　今後の課題と展望

糖鎖の立体構造からその機能を理解する「糖鎖構造生物学」は，これからより普及していく必要がある．主役はタンパク質であることは間違いないが，その機能調節をドラスティックに行っているのは脇役の糖鎖である．受容体の機能を糖鎖に着目すると，新しい側面が見えてくることもある．そのためには，糖鎖を対象とした構造生物学的手法の開発が必要であり，一つの方法だけではなく，計算化学的手法も含めた複数の手法の組合わせが必要になる．今後異分野のますますの連携が必要になる．また新しい技術開発は新しい知見をもたらすのが常であり，構造生物学分野のさらなる技術開発も必要である．糖鎖の立体構造・運動性・相互作用をより理解することができれば，医薬品の開発につながることも期待される．いままでにない視点からのアプローチも可能になるため，筆者も医薬品の開発において「糖鎖構造生物学分野」から貢献することを意識している．

文　　献

1) IUPAC-IUB Joint Commission on Biochemical Nomenclature (JCBN). (1983) Symbols for Specifying the Conformation of Polysaccharide Chains Recommendations 1981. *Eur. J. Biochem.*, **131**, 5–7.

2) Singh, A., Tessier, M.B., Pederson, K., Wang, X., Venot, A.P., Boons, G.J., Prestegard, J.H., & Woods, R.J. (2016) Extension and validation of the GLYCAM force field parameters for modeling glycosaminoglycans. *Can. J. Chem.*, **94**, 927–935.
3) Cremer, D. & Pople, J.A. (1975) General definition of ring puckering coordinates. *J. Am. Chem. Soc.*, **97**, 1354–1358.
4) Lassak, J., Keilhauer, E.C., Furst, M., Wuichet, K., Godeke, J., Starosta, A.L., Chen, J.M., Sogaard-Andersen, L., Rohr, J., Wilson, D.N., et al. (2015) Arginine-rhamnosylation as new strategy to activate translation elongation factor P. *Nat. Chem. Biol.*, **11**, 266–270.
5) Sengoku, T., Suzuki, T., Dohmae, N., Watanabe, C., Honma, T., Hikida, Y., Yamaguchi, Y., Takahashi, H., Yokoyama, S., & Yanagisawa, T. (2018) Structural basis of protein arginine rhamnosylation by glycosyltransferase EarP. *Nat. Chem. Biol.*, **14**, 368–374.
6) Karaveg, K., Siriwardena, A., Tempel, W., Liu, Z.J., Glushka, J., Wang, B.C., & Moremen, K.W. (2005) Mechanism of class 1 (glycosylhydrolase family 47) alpha-mannosidases involved in N-glycan processing and endoplasmic reticulum quality control. *J. Biol. Chem.*, **280**, 16197–16207.
7) Manya, H., Yamaguchi, Y., Kanagawa, M., Kobayashi, K., Tajiri, M., Akasaka-Manya, K., Kawakami, H., Mizuno, M., Wada, Y., Toda, T., et al. (2016) The Muscular Dystrophy Gene TMEM5 Encodes a Ribitol β1,4-Xylosyltransferase Required for the Functional Glycosylation of Dystroglycan. *J. Biol. Chem.*, **291**, 24618–24627.
8) Kanagawa, M., Kobayashi, K., Tajiri, M., Manya, H., Kuga, A., Yamaguchi, Y., Akasaka-Manya, K., Furukawa, J.I., Mizuno, M., Kawakami, H., et al. (2016) Identification of a Post-translational Modification with Ribitol-Phosphate and Its Defect in Muscular Dystrophy. *Cell Rep.*, **14**, 2209–2223.
9) Klein, R.A., Hartmann, R., Egge, H., Behr, T., & Fischer, W. (1994) The aqueous solution structure of the tetrasaccharide-ribitol repeat-unit from the lipoteichoic acid of Streptococcus pneumoniae strain R6 determined using a combination of NMR spectroscopy and computer calculations. *Carbohydr. Res.*, **256**, 189–222.
10) Hatcher, E., Guvench, O., & Mackerell, A.D. Jr. (2009) CHARMM Additive All-Atom Force Field for Acyclic Polyalcohols, Acyclic Carbohydrates and Inositol. *J. Chem. Theory Comput.*, **5**, 1315–1327.
11) Suga, A., Nagae, M., & Yamaguchi, Y. (2018) Analysis of protein landscapes around N-glycosylation sites from the PDB repository for understanding the structural basis of N-glycoprotein processing and maturation. *Glycobiology*, **28**, 774–785.
12) Deisenhofer, J. (1981) Crystallographic refinement and atomic models of a human Fc fragment and its complex with fragment B of protein A from Staphylococcus aureus at 2.9- and 2.8-A resolution. *Biochemistry*, **20**, 2361–2370.
13) Yamaguchi, Y., Kato, K., Shindo, M., Aoki, S., Furusho, K., Koga, K., Takahashi, N., Arata, Y., & Shimada, I. (1998) Dynamics of the carbohydrate chains attached to the Fc portion of immunoglobulin G as studied by NMR spectroscopy assisted by selective 13C labeling of the glycans. *J. Biomol. NMR*, **12**, 385–394.
14) Yamaguchi, Y. & Barb, A.W. (2019). *Glycobiology*.
15) Nagae, M., Kanagawa, M., Morita-Matsumoto, K., Hanashima, S., Kizuka, Y., Taniguchi, N., & Yamaguchi, Y. (2016) Atomic visualization of a flipped-back conformation of bisected glycans bound to specific lectins. *Sci. Rep.*, **6**, 22973.
16) Nishima, W., Miyashita, N., Yamaguchi, Y., Sugita, Y., & Re, S. (2012) Effect of bisecting GlcNAc and core fucosylation on conformational properties of biantennary complex-type *N*-glycans in solution. *J. Phys. Chem. B*, **116**, 8504–8512.
17) Re, S., Miyashita, N., Yamaguchi, Y., & Sugita, Y. (2011) Structural diversity and changes in conformational equilibria of biantennary complex-type *N*-glycans in water revealed by replica-exchange molecular dynamics simulation. *Biophys. J.*, **101**, L44–L46.
18) Imberty, A. (1997) Oligosaccharide structures: theory versus experiment. *Curr. Opin. Struct. Biol.*, **7**, 617–623.
19) Nagae, M., Mishra, S.K., Neyazaki, M., Oi, R., Ikeda, A., Matsugaki, N., Akashi, S., Manya, H., Mizuno, M., Yagi, H., et al. (2017) 3D structural analysis of protein O-mannosyl kinase, POMK, a causative gene product of dystroglycanopathy. *Genes Cells*, **22**, 348–359.
20) Nagae, M., Ikeda, A., Hane, M., Hanashima, S., Kitajima, K., Sato, C., & Yamaguchi, Y. (2013) Crystal structure of anti-polysialic acid antibody single chain Fv fragment complexed with octasialic acid: insight into the binding preference for polysialic acid. *J. Biol. Chem.*, **288**, 33784–33796.
21) Lemieux, R.U., Delbaere, L.T., Beierbeck, H., & Spohr, U. (1991) Involvement of water in host-guest interactions. *Ciba Found. Symp.*, **158**, 231–245, discussion, 245–238.
22) Carver, J.P. (1993) Oligosaccharides: How can flexible molecules act as signals? *Pure Appl. Chem.*, **65**, 763–770.
23) Nagae, M. & Yamaguchi, Y. (2012) Function and 3D structure of the N-glycans on glycoproteins. *Int. J. Mol. Sci.*, **13**, 8398–8429.
24) Lütteke, T. (2009) Analysis and validation of carbohydrate three-dimensional structures. *Acta Crystallogr. D Biol. Crystallogr.*, **65**, 156–168.
25) Petrescu, A.J., Milac, A.L., Petrescu, S.M., Dwek, R.A., & Wormald, M.R. (2004) Statistical analysis of the protein environment of N-glycosylation sites: implications for occupancy, structure, and folding. *Glycobiology*, **14**, 103–114.
26) Lee, H.S., Qi, Y., & Im, W. (2015) Effects of *N*-glycosylation on protein conformation and dynamics: Protein Data Bank analysis and molecular dynamics simulation study. *Sci. Rep.*, **5**, 8926.
27) Joao, H.C., Scragg, I.G., & Dwek, R.A. (1992) Effects of glycosylation on protein conformation and amide proton exchange rates in RNase B. *FEBS Lett.*, **307**, 343–346.
28) Sirohi, D., Chen, Z., Sun, L., Klose, T., Pierson, T.C., Rossmann, M.G., & Kuhn, R.J. (2016) The 3.8 Å resolution cryo-EM structure of Zika virus. *Science*, **352**, 467–470.
29) Pokidysheva, E., Zhang, Y., Battisti, A.J., Bator-Kelly, C.M., Chipman, P.R., Xiao, C., Gregorio, G.G., Hendrickson, W.A., Kuhn, R.J., & Rossmann, M.G. (2006) Cryo-EM reconstruction of dengue virus in complex with the carbohydrate recognition domain of DC-SIGN. *Cell*, **124**, 485–493.
30) Gristick, H.B., Wang, H., & Bjorkman, P.J. (2017) X-ray and EM structures of a natively glycosylated HIV-1 envelope trimer. *Acta Crystallogr. D Struct. Biol.*, **73**, 822–828.
31) Agirre, J., Davies, G.J., Wilson, K.S., & Cowtan, K.D. (2017) Carbohydrate structure: the rocky road to automation. *Curr. Opin. Struct. Biol.*, **44**, 39–47.
32) Frenz, B., Ramisch, S., Borst, A.J., Walls, A.C., Adolf-Bryfogle, J., Schief, W.R., Veesler, D., & DiMaio, F. (2019) Automatically Fixing Errors in Glycoprotein Structures with Rosetta. *Structure*, **27**, 134–139.
33) Agirre, J., Iglesias-Fernandez, J., Rovira, C., Davies, G.J., Wilson, K.S., & Cowtan, K.D. (2015) Privateer: software for the conformational validation of carbohydrate structures. *Nat. Struct. Mol. Biol.*, **22**, 833–834.

34) Lutteke, T. & von der Lieth, C.W. (2004) pdb-care (PDB carbohydrate residue check): a program to support annotation of complex carbohydrate structures in PDB files. *BMC Bioinformatics*, **5**, 69.
35) Gristick, H.B., von Boehmer, L., West, A.P. Jr., Schamber, M., Gazumyan, A., Golijanin, J., Seaman, M.S., Fatkenheuer, G., Klein, F., Nussenzweig, M.C., et al. (2016) Natively glycosylated HIV-1 Env structure reveals new mode for antibody recognition of the CD4-binding site. *Nat. Struct. Mol. Biol.*, **23**, 906–915.
36) Kuhn, B., Benz, J., Greif, M., Engel, A.M., Sobek, H., & Rudolph, M.G. (2013) The structure of human α-2,6-sialyltransferase reveals the binding mode of complex glycans. *Acta Crystallogr. D Biol. Crystallogr.*, **69**, 1826–1838.
37) Tempel, W., Karaveg, K., Liu, Z.J., Rose, J., Wang, B.C., & Moremen, K.W. (2004) Structure of mouse Golgi alpha-mannosidase IA reveals the molecular basis for substrate specificity among class 1 (family 47 glycosylhydrolase) alpha1,2-mannosidases. *J. Biol. Chem.*, **279**, 29774–29786.
38) Berman, E., Walters, D.E., & Allerhand, A. (1981) Structure and dynamic behavior of the oligosaccharide side chain of bovine pancreatic ribonuclease B. Application of carbon 13 nuclear magnetic resonance spectroscopy. *J. Biol. Chem.*, **256**, 3853–3857.
39) Wyss, D.F., Choi, J.S., Li, J., Knoppers, M.H., Willis, K.J., Arulanandam, A.R., Smolyar, A., Reinherz, E.L., & Wagner, G. (1995) Conformation and function of the N-linked glycan in the adhesion domain of human CD2. *Science*, **269**, 1273–1278.
40) Kato, K. & Yamaguchi, T. (2015) Paramagnetic NMR probes for characterization of the dynamic conformations and interactions of oligosaccharides. *Glycoconj. J.*, **32**, 505–513.
41) Usachev, K., Yamaguchi, Y., Takamatsu, M., Pavlova, N., Klochkov, V., Kurbangalieva, A., Murase, T., Shimoda, T., & Tanaka, K. (2017) Simple Gd^{3+}-Neu5NAc complexation results in NMR chemical shift asymmetries of structurally equivalent complex-type N-glycan branches. *Analyst (Lond.)*, **142**, 2897–2900.
42) Canales, A., Boos, I., Perkams, L., Karst, L., Luber, T., Karagiannis, T., Dominguez, G., Canada, F.J., Perez-Castells, J., Haussinger, D., et al. (2017) Breaking the Limits in Analyzing Carbohydrate Recognition by NMR Spectroscopy: Resolving Branch-Selective Interaction of a Tetra-Antennary N-Glycan with Lectins. *Angew. Chem. Int. Ed. Engl.*, **56**, 14987–14991.
43) Fernandez de Toro, B., Peng, W., Thompson, A.J., Dominguez, G., Canada, F.J., Perez-Castells, J., Paulson, J.C., Jimenez-Barbero, J., & Canales, A. (2018) Avenues to Characterize the Interactions of Extended N-Glycans with Proteins by NMR Spectroscopy: The Influenza Hemagglutinin Case. *Angew. Chem. Int. Ed. Engl.*, **57**, 15051–15055.
44) Uzawa, J., Shimabukuro, J., Suzuki, T., Imamura, A., Ishida, H., Ando, H., & Yamaguchi, Y. (2018) J(^{77}Se,^{1}H) and J(^{77}Se,^{13}C) couplings of seleno-carbohydrates obtained by ^{77}Se satellite 1D ^{13}C spectroscopy and ^{77}Se selective HR-HMBC spectroscopy. *Magn. Reson. Chem.*, **56**, 836–846.
45) Suzuki, T., Hayashi, C., Komura, N., Tamai, R., Uzawa, J., Ogawa, J., Tanaka, H.N., Imamura, A., Ishida, H., Kiso, M., et al. (2019) Synthesis and Glycan-Protein Interaction Studies of *Se*-Sialosides by ^{77}Se NMR. *Org. Lett.*, **21**, 6393–6396.
46) Rose, A.S., Bradley, A.R., Valasatava, Y., Duarte, J.M., Prlic, A., & Rose, P.W. (2018) NGL viewer: web-based molecular graphics for large complexes. *Bioinformatics*, **34**, 3755–3758.

著者寸描

●山口　芳樹（やまぐち　よしき）

東北医科薬科大学．博士（薬学）．

■略歴　1993年東京大学薬学部卒業．98年同大学院薬学研究科博士課程修了．98～2001年日本学術振興会特別研究員．01年東京大学薬学部助手．01～07年名古屋市立大学大学院薬学研究科講師．07～18年理化学研究所チームリーダー．19年同研究所研究員．19年4月より現職．

■研究テーマと抱負　構造に不均一性（曖昧さ）をもつ糖鎖が時に厳密に制御され機能している，そのギャップに生命の不思議さを感じつつ，糖鎖の機能を一つでも多く明らかにし，得られた知識を医薬品開発につなげることができればこの上ない喜びです．

■趣味　習い始めの合気道，年に1, 2回のゴルフ，車の運転練習を兼ねた日帰り温泉の旅．

International Journal of
Molecular Sciences

MDPI

Review

3D Structural Insights into β-Glucans and Their Binding Proteins

Noriyoshi Manabe and Yoshiki Yamaguchi *

Division of Pharmaceutical Physical Chemistry, Tohoku Medical and Pharmaceutical University, 4-4-1 Komatsushima, Aoba-ku, Sendai, Miyagi 981-8558, Japan; manabe@tohoku-mpu.ac.jp
* Correspondence: yyoshiki@tohoku-mpu.ac.jp; Tel.: +81-22-727-0208

Abstract: β(1,3)-glucans are a component of fungal and plant cell walls. The β-glucan of pathogens is recognized as a non-self-component in the host defense system. Long β-glucan chains are capable of forming a triple helix structure, and the tertiary structure may profoundly affect the interaction with β-glucan-binding proteins. Although the atomic details of β-glucan binding and signaling of cognate receptors remain mostly unclear, X-ray crystallography and NMR analyses have revealed some aspects of β-glucan structure and interaction. Here, we will review three-dimensional (3D) structural characteristics of β-glucans and the modes of interaction with β-glucan-binding proteins.

Keywords: β-glucan; 3D structure; triple helix; X-ray crystallography; NMR; βGRP/GNBP3; Dectin-1; endoglucanase

Citation: Manabe, N.; Yamaguchi, Y. 3D Structural Insights into β-Glucans and Their Binding Proteins. *Int. J. Mol. Sci.* **2021**, *22*, 1578. https://doi.org/10.3390/ijms22041578

Academic Editor: Hiroshi Tamura
Received: 14 January 2021
Accepted: 30 January 2021
Published: 4 February 2021

1. Introduction—Variation of β-Glucan Primary Structures

β-glucan is widely distributed in bacteria, fungi, algae and plants. β-glucan can be utilized as a "recognition pattern" in host defense systems. To understand the system recognizing β-glucan, the primary and tertiary structures of β-glucan need to be elucidated as well as the cognate receptors identified. β(1,3)-glucan is a polymer with the main chain composed of β(1,3)-linked D-glucose and often branched with side chains, starting with a β(1,6)-linked D-glucose residue. The length of the main chain, the interval between branching and the side chain length (structure) are characteristic of each β-glucan from different sources (Figure 1). Curdran, which was isolated from an *Agrobacterium* species, is a linear β(1,3)-glucan essentially free from β(1,6) branching, with its degree of polymerization (DP) approximately 135 glucose units [1–3]. Curdran is water-insoluble and tends to form a gel upon heating. By contrast, schizophyllan, which is produced by *Schizophyllum commune*, is a β(1,3)-glucan modified with β(1,6)-linked monoglucose residues every three β(1,3)-linked glucose residues and has a molecular weight of 4.3×10^6 Da [4]. Unlike curdran, schizophyllan is water-soluble, suggesting a role for β(1,6)-linked monoglucose residues in defining the solubility of β-glucan. Scleroglucan, produced by *Sclerotium* species, is very similar to schizophyllan in having β(1,6)-linked monoglucose residues at about every three β(1,3)-linked glucose residues [5]. Lentinan, from *Lentinus edodes*, is a β-glucan having two β(1,6) glucopyranoside branches for every five β(1,3)-glucose residues [6]. A few internal β(1,6) linkages may be present as β(1,6)-linked side chains. Overall, the chemical structure of lentinan is similar to that of schizophyllan and scleroglucan. Laminarin, which was isolated from *Laminaria digitata*, is a water-soluble, small β-glucan with DP of 20~30. Like schizophyllan, laminarin has an average 1.3 β(1,6)-linked monoglucose residues per molecule (one branched glucose residue is covalently attached every seven β(1,3)-linked glucose residues). The reducing end of laminarin is capped with reducing D-glucose (G-series) or non-reducing D-mannitol (M-series) in a ratio of 1:3 [7]. Yeast cell wall β-glucans show different branching structures. A soluble *Candida* species β(1,3)-glucan (CSBG), a dimethyl sulfoxide-soluble fraction extracted from the NaClO-oxidized cell wall, is modified with long β(1,6)-linked glucosyl side chains [8]. The ratio of β(1,3):β(1,6)

glucosyl linkages varies according to the *Candida* species, ranging from 1:0.2 to 1:0.7, and the DP of the side chains may be as few as 10 to over 50. Many other β-glucans are known with differences in backbone chain length, branching interval and side-chain structures. It should be emphasized that differences in chemical structure of the β-glucans likely define tertiary structure and hence affect biological activities [9].

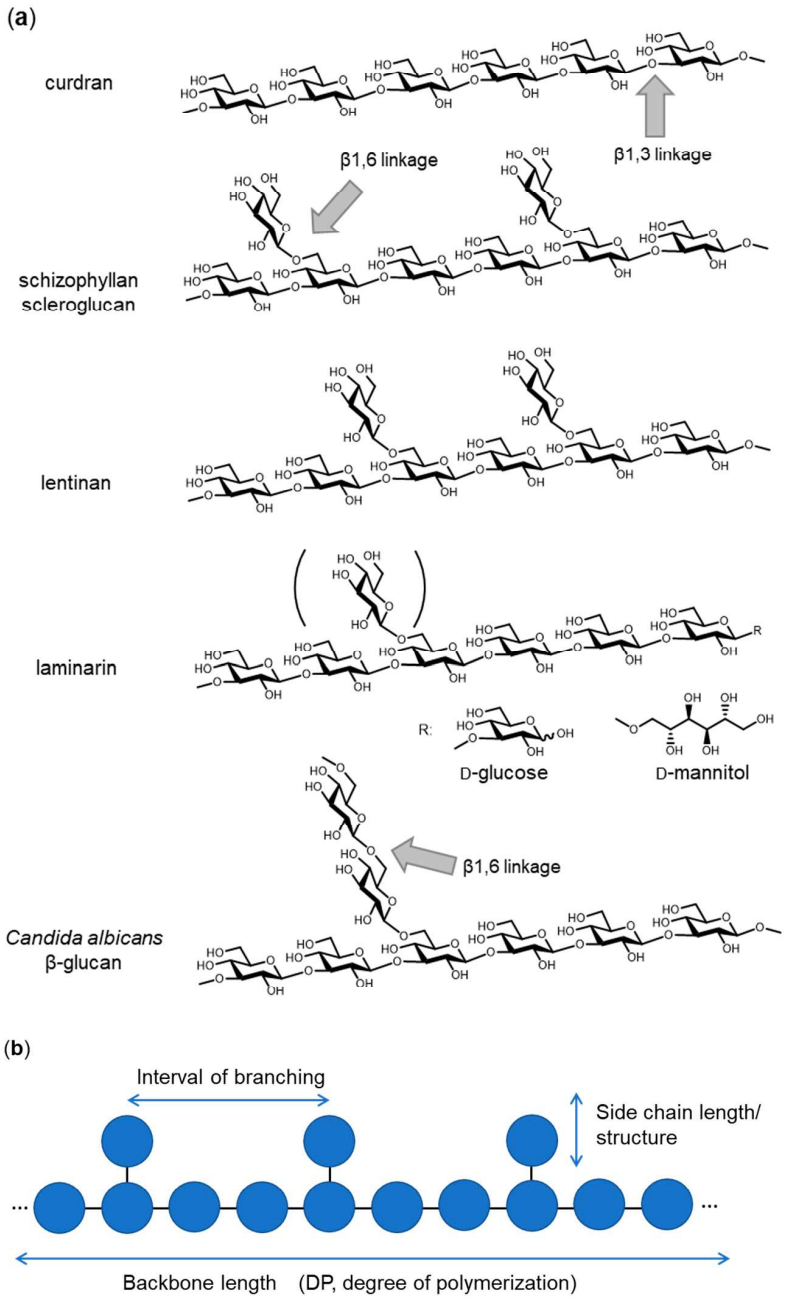

Figure 1. Chemical structure of representative β(1,3)-glucans. (**a**) Curdran from *Agrobacterium* species, schizophyllan from *Schizophyllum commune*, scleroglucan from *Sclerotium* species, lentinan from *Lentinula edodes*, laminarin from *Laminaria digitata* and *Candida albicans* β-glucan. (**b**) A schematic drawing of β-glucan with the key parameters (backbone length, interval of branching and side chain length/structure) that define the primary structure.

2. 3D Structure of β-Glucan—What Does β-Glucan Look Like?

Accumulating evidence suggests that long-chain β-glucan forms a triple helix structure similar to that of collagen. X-ray diffraction studies of several β(1,3)-glucans reveal a triple helical backbone structure. Probable models of lentinan have been proposed from X-ray fiber diffraction and theoretical conformational analysis [10]. Five models have been proposed, one is a single helix, two are double helices and two are triple helices (right-handed or left-handed). Of these, the most probable is the right-handed triple helix, by analogy with the determined structure of β(1,3)-xylan. Hydrated curdran is a triplex of right-handed, six-fold helical chains [11]. The individual chains of curdran are composed of a six-glucose unit per turn. Water molecules are clustered near the O4 and O5 oxygen atoms of the glucose residues in curdran, and this may indicate the presence of water-mediated hydrogen bonds between the two glucose residues. X-ray diffraction experiments on curdran and scleroglucan show the diameter of the triplex to be 14.3 Å and 17.3 Å, respectively [12]. Each chain is composed of six glucose residues per turn, yielding a pitch of 2.9–3.0 Å per residue. These parameters indicate that the backbone conformation of scleroglucan is similar to that of curdran. It is therefore likely that the β(1,6)-linked side chain of scleroglucan is outside of the triple helix, such that it does not significantly disturb the backbone conformation.

From these diffraction data, atomic models of triplex β-glucan have been proposed. In a widely accepted model, the hydroxy group at position 2 (2-OH) of each glucose residue forms interchain hydrogen bonds with the 2-OH groups in the other two strands (Figure 2). These are formed perpendicular to the axis of the triple helix. The 2-OH groups of the glucose residues lie inside the hydrophobic core. In contrast, the hydroxy groups at position 6 (6-OH) of the glucose residues face towards the hydrophilic solvent. Thus, it follows that β-glucan branching occurs at the 6-position of a main-chain glucose residue.

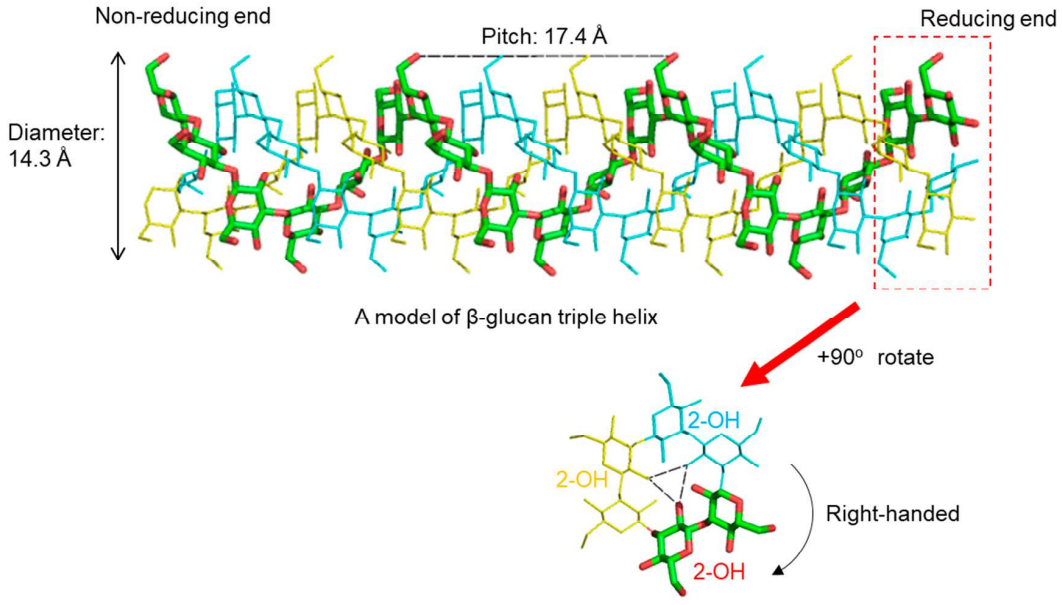

Figure 2. A model of right-handed triple helical β(1,3)-glucan based on X-ray diffraction data [11]. A pitch of helix is estimated as 17.4 Å and the diameter as 14.3 Å. Inter-strand hydrogen bonds are formed between 2-OH of glucose residues, which are perpendicular to the helix axis.

In addition to X-ray fiber diffraction analysis, several methods have been applied to probe the structure of triple helical β-glucans. Solid-state ^{13}C-NMR spectroscopy has been applied to conformational analysis of β-glucans. It has been shown that ^{13}C chemical shifts readily distinguish three conformations, single chain, single helix and triple helix. The triple helix has also been characterized in solution state. Solution studies of shizophyllan

by light scattering and viscosity measurement suggest a semi-flexible, rod-like structure with the pitch per glucose residue and the persistence length of the triple helix of 3.0 A and 18 Å, respectively [13].

What is the required length of β-glucan for formation of a triple helix? To answer this question, β-glucans with different chain length were obtained from partial hydrolysis of curdran and examined by optical rotatory dispersion [14]. A β-glucan chain with DP more than 200 (molecular mass of 32,000 Da per chain) was found to be necessary to form an ordered structure. β-glucans with DPs below 25 are soluble and assume a disordered structure in water. For schizophyllan, a molecular mass of higher than 50,000 Da (as a triplex) is required for the formation of a triple helix [15]. Laminarin from *Laminaria digitata*, whose molecular mass is around 5000 Da, is present mostly in a monomeric form with triplex structures a minor population (5%) [16,17]. According to these studies, it can be seen that a molecular weight of more than several tens of thousands per one β-glucan chain is necessary to form a stable triple helix.

Triple helices of β-glucan denature into random coils when dissolved in an alkaline solution (pH > 12) [12], in dimethyl sulfoxide (DMSO) [18] or when the temperature is increased above the melting temperature (~135 °C) [19]. The mechanisms are different in each case. It is likely that in an alkaline condition, hydroxyl groups will be negatively charged, which would lead to electrostatic charge repulsion between the strands [9]. DMSO will destabilize hydrogen bonds and high temperatures are expected to destabilize strands [9]. Renaturation of β-glucans from the denatured state has also been examined. Denatured schizophyllan dissolved in DMSO and dialyzed against water renatures to a mixture of circular, linear and aggregated structures [20]. Denatured lentinan can be renatured by dialysis against water after denaturation in 0.15 M NaOH [21]. From AFM observations, renatured lentinan consists of linear, circular and branched species of triple helix.

3. Dectin-1–β Glucan Interaction

Dectin-1 is the most studied of the β-glucan receptors from vertebrates [22]. It is mainly expressed on myeloid cells such as macrophages, dendritic cells and neutrophils. Dectin-1 is a type II membrane protein composed of an extracellular lectin domain, a transmembrane domain and a cytosolic region with an immunoreceptor tyrosine-based activation motif called ITAM. The lectin domain is responsible for Ca^{2+}-independent β-glucan binding, and binding depends on chain length. The minimum length required for detectable binding is a 10- or 11-mer, as determined by glycan microarray experiments [23]. In these experiments, there was no binding of glycans other than β-glucan, indicating high specificity. An NMR interaction study determined that Dectin-1 binds weakly with laminarihexaose (degree of polymerization, DP = 6), moderately with a chemically synthesized β-glucan chain (DP = 16) and strongly with laminarin (average DP = 25) [16]. STD-NMR analysis using β-glucan chains (DP = 6, 16 and 25) revealed that only the middle part of the β-glucan chain is recognized, not the reducing/non-reducing ends [16,24]. The mechanism of the chain-length-dependent interaction is unclear. NMR data suggest that increasing β-glucan chain length correlates with increasing secondary structure formation. In general, a polymer such as a polypeptide can form secondary structures anywhere along its length, except at the termini where there is no hydrogen-bonding partner. Certainly, laminarin, with an average DP of 25, does have secondary structure, as evidenced by deuterium-induced ^{13}C-NMR isotope shifts [16]. The evidence then points to chain-length-dependent interaction being explained by the presence of helical structures, which are expected to snugly fit into the ligand-binding site of the Dectin-1 lectin domain.

In addition to the backbone chain-length of β-glucan, β(1,6)-branching affects binding to Dectin-1. Adams et al. investigated the interaction of Dectin-1 with a library of natural and synthetic β-glucans [25]. Dectin-1 differentially interacted with β-glucans over a wide range of affinities. The range of IC_{50} is from 2.6 mM for nonbranched, linear octasaccharide glucan, to an astounding 2.2 pM for glucan phosphate. This is likely the highest affinity interaction reported for a C-type lectin-like receptor. Importantly, the branched nonasac-

charide (ID_{50} = 2.9 μM) is 1000-fold stronger than linear nonasaccharide (ID_{50} = 2.6 mM). There was a ~270-fold increase in affinity between the branched nonasaccharide and linear decasaccharide (0.7 mM versus 2.9 μM). It remains to be seen how the Dectin-1 lectin domain preferentially interacts with branched β-glucan.

A crystal structure of the murine Dectin-1 lectin domain has been reported in the ligand-free form (Figure 3) [26]. The lectin domain shows a typical C-type lectin fold composed of two anti-parallel β-sheets and two α-helices, with two coordinated Ca^{2+} ions. The bound Ca^{2+} ions are not required for ligand-binding but stabilize the structure of the domain. There is a dimeric arrangement in the crystal lattice, which trapped a short β-glucan ligand at the interface. The site is far from the putative ligand binding site previously defined by Trp221 and His223 [27]. The dimer found in the crystal will not be formed under physiological conditions because Asn185 is normally N-glycosylated [28] and located in the dimer interface. Currently, a three-dimensional (3D) structure of a β-glucan–Dectin-1 complex is not available, and therefore neither is the β-glucan structure nor binding mode at the atomic level.

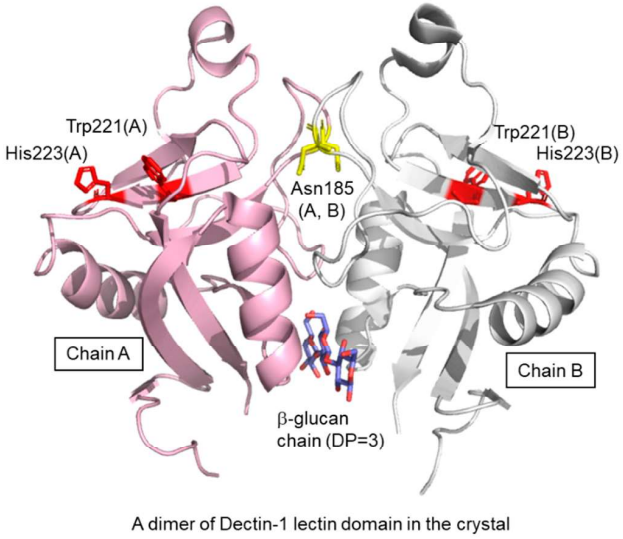

Figure 3. Crystal structure of dimeric Dectin-1 lectin domain trapping laminaritriose. Proteins are shown in ribbon model and chain A and chain B are colored in pink and white, respectively. Trapped laminaritriose, Trp221, His223 and Asn185 are in stick representation.

The lectin domain of Dectin-1 forms higher-order oligomers when bound to laminarin [26]. Oligomer formation is cooperative, with a Hill coefficient of ~3 [29]. How the β-glucan directs the cooperative oligomer formation is not known and awaits future study. The ligand-induced oligomer formation of Dectin-1 may occur at the cell surface in the physiological situation, and the oligomerization may enhance the signaling through the cytosolic region. A recent preprint shows that full-length Dectin-1 on the cell surface forms a dimer/oligomer upon binding to structured β-glucans [30].

Dectin-1 has always been considered a β-glucan receptor participating in the innate immune self-defense system, but recent reports suggest other functional aspects. Dectin-1 apparently binds to the conserved core domain of annexins (annexin A1, A4 and A13) expressed on apoptotic cells and induces immune tolerance [31]. The binding is very strong at nanomolar affinity via a site distinct from the β-glucan interaction site. As expected, Dectin-1-deficent mice generate a stronger immune response against apoptotic cells and develop autoimmunity. Another study suggests that Dectin-1 recognizes the N-terminal asparagine at the glycosylation site as well as the core fucose on the N-glycan of the IgG-Fc region [32]. Dectin-1 also appears to be involved in the recognition of characteristic N-

glycans on antibodies, although its biological significance remains unclear. Further study will likely show that Dectin-1 has a whole range of functions in vivo.

4. Complement Receptor 3(CR3)–β-Glucan Interaction

Complement receptor 3 (CR3, Mac-1, $\alpha_m\beta_2$ integrin, CD11b/CD18) is a heterodimeric complex composed of α_m integrin (CD11b, 165 kDa) and β_2 integrin (CD18, 95 kDa), expressed on mature myeloid cells, NK cells and minor subsets of B and T cells. CR3 binds to complement component iC3b and is responsible for phagocytosis of complement-opsonized particles. Both chains of CR3 are multi-domain proteins and several studies have reported on the lectin domain and sugar-binding specificity. Several lines of evidence suggest that a carbohydrate binding site is likely located in the C-terminus of CD11b [33,34]. CR3 binds a variety of carbohydrate ligands, including β-glucans but not α-mannan [33]. The 3D structure of the lectin domain and the binding mode is currently not known, precluding the understanding of its physiological function.

5. βGRP/GNBP3–β-Glucan Interaction

β1,3-Glucan recognition protein (βGRP)/Gram-negative bacteria-binding protein 3(GNBP3) is a soluble pattern recognition receptor found in the hemolymph of invertebrates such as silkworm and Drosophila. βGRP/GNBP3 is one of the best characterized families of pattern recognition receptors in invertebrates [35]. βGRP/GNBP3 binds to long, structured β(1,3)-glucan [36,37]. βGRP/GNBP3 consists of two domains: a well-conserved N-terminal domain and a C-terminal glucanase-like domain which does not have glucanase activity. The N-terminal domain consists of about 100 amino acid residues and binds β(1,3)-glucan. Binding of βGRP/GNBP3 to β(1,3)-glucan through its N-terminal domain triggers an innate immune response by activation of the Toll pathway.

In 2009, pioneering structural work revealed the 3D structures of the ligand-free βGRP/GNBP3 N-terminal domain by X-ray crystallography [37] and solution NMR spectroscopy [36]. The crystal structure of the Drosophila βGRP/GNBP3 N-terminal domain shows an immunoglobulin fold. The β-glucan binding site was predicted to be the hydrophobic surface which is masked by a C-C′ loop. A ligand-binding mechanism was proposed, in which long-chain structured β-glucan binds to the hydrophobic surface with displacement of the occluding C-C′ loop. At about the same time, the solution structure of the silkworm βGRP/GNBP3 N-terminal domain also showed the same β sandwich fold. The NMR titration experiments and mutational analysis suggested that β-glucan preferentially binds to the non-aromatic concave surface. Further studies then described crystal structures of the N-terminal β(1,3)-glucan recognition domain of βGRP/GNBP3 from *Plodia interpunctella* and *Bombyx mori* in complex with β(1,3)-linked glucose hexamer (laminarihexaose) (Figure 4). In both complexes, the laminarihexaoses are spatially arranged to form pseudo-quadruplex structures, which well mimics the triplex of β-glucan. These 3D structures can be utilized for understanding the β-glucan triplex and its interaction with protein receptors. The laminarihexaoses form inter-strand hydrogen bonds between 2-OH groups. The observed hydrogen-bonding pattern is very similar to that in models of triple helical β-glucan. In addition, the helical structure of the laminarihexaoses is stabilized by intra-strand and inter-residue hydrogen bonds between their OH-4 (i-1) and O5(i), which is also found in the triplex model. Furthermore, water-mediated hydrogen bonds are common between OH-4 (i-1) and O6(i). The binding site of laminarihexaoses is on the convex surface, which is different from previously proposed sites [36,37]. The reason for the discrepancy is not known, but one possibility may be differences in chemical structures of the β-glucans used in the various experiments. Another possible reason may stem from site-directed mutagenesis affecting the local structure of the protein.

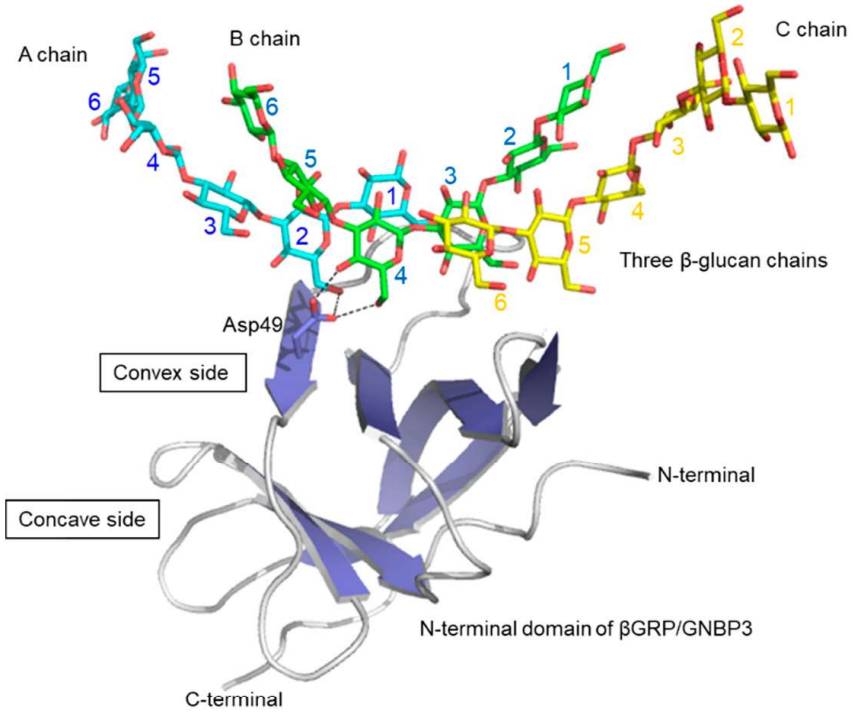

Figure 4. Crystal structure of *Bombyx mori* βGRP/GNBP3 N-terminal domain bound to three β-glucan chains [38]. Proteins are shown in the surface model and three laminarihexaose chains are in stick representation. As an example of β-glucan-interacting residues, Asp49 side chain is shown in stick representation, interacting with A and B chains.

The interaction mode of laminarihexaoses with βGRP/GNBP3 is characteristic: one βGRP/GNBP3 interacts with three laminarihexaoses, which are spatially arranged like a triple helix. This interaction mode well explains the previous observations that βGRP/GNBP3 binds triple-helical β-glucan strongly but has little affinity for denatured β-glucan or shorter β(1,3)-linked glucan chains [36,37]. This is the first example that provides a structural basis for how triple helical β(1,3)-glucan is recognized by a protein receptor at the atomic level.

βGRP/GNBP3 is widely distributed among species and forms a large family [39]. A recent study reports on the ligand binding characteristics of βGRP/GNBP3 from four insects (*Bombyx mori*, *Plodia interpunctera*, *Tribolium castaneum* and *Tenebrio molita*) [40]. From the solid-phase ELISA assays, the binding specificities were found to be categorized into two groups. One group (*Bombyx mori* and *Plodia interpunctera*) tend to bind to triple-helical native β-glucans, while the other group (*Tribolium castaneum* and *Tenebrio molita*) prefer alkaline-treated β-glucans. These results suggest that the preferred β-glucan conformation is different for individual βGRP/GNBP3. The difference will be clarified through 3D structural analysis of each βGRP/GNBP3.

βGRP/GNBP3 binding to triplex β-glucan activates the prophenoloxidase cascade [41,42] and antifungal Toll pathway [43]. The mechanism is not fully understood. Interaction of β-glucan laminarin (~6 kDa) with βGRP/GNBP3 N-terminal domain (15 kDa) has been analyzed by solution NMR and analytical ultracentrifugation [44]. The N-terminal domain of *Plodia interpunctella* βGRP GNBP3 is sufficient to activate the prophenoloxidase pathway, resulting in melanin formation. The N-terminal domain forms a stable complex with laminarin (~102 kDa) and is possibly composed of six proteins and three laminarins. The ligand-induced self-association of βGRP/GNBP3 may provide a platform for recruitment of downstream proteases. Similarly, the βGRP/GNBP3 N-terminal domain of *Manduca sexta* also provokes oligomer formation. When the laminarin/protein ratio is low (ca. 1), an insoluble aggregate forms, when high (>5), a soluble complex containing at least five protein molecules results. It appears from these reports that ligand-induced oligomer

formation of βGRP/GNBP3 is the initial event that then triggers the downstream pathway. The triple helix structure of β-glucan likely plays a key role in the oligomer formation, but this needs further structural analysis.

6. Factor G–β-Glucan Interaction

Horseshoe crab Factor G is a non-covalent heterodimer composed of anα-subunit (72 kDa) and a β-subunit (37 kDa). The α-subunit is responsible for the recognition of β-glucan, while the β-subunit is a serine protease which becomes activated when factor G binds to β-glucan. The α-subunit comprises three kinds of modules: a single β-glucanase A1-like module, three tandem xylanase A-like modules and two tandem xylanase Z-like modules (Z1 and Z2). Z1 and Z2 modules have independent β-glucan-binding sites and cooperatively enhance avidity toward β-glucan-containing pathogens [45]. A chemical shift preservation experiment has helped map the laminaripentaose-binding site to a cleft on a β-sheet in the predicted 3D model [46]. Activation of Factor G increases over 100-fold on treatment of β-glucan with 0.3 M NaOH, which converts a triple helix to a single helix [47]. The binding specificity and activity of Factor G has led to its clinical application as a diagnostic reagent for the detection of fungal infections in humans [48].

7. Other β-Glucan–Protein Interactions

In addition to these β-glucan receptors, some other related proteins are known to bind structured β-glucan. In the CAZy database (Carbohydrate Active Enzymes database), carbohydrate-binding module (CBM) families 4, 6, 13, 32, 39, 43, 52, 54, 56, 65, 72, 76, 79, 80, 81 and 85 have an ability to interact with β-glucans [49,50]. Some 3D structural information is available on how CBM binds to β-glucan chains. A good example is the β(1,3)-glucanase BH0236 from *Bacillus halodurans*, which is a multidomain protein composed of three parts: a N-terminal family 81 glycosyl hydrolase (GH81) catalytic module [51], an internal CBM6 that binds to the non-reducing end of β(1,3)-glucan chains [52] and a C-terminal CBM56 that binds to β(1,3)-glucan chains [53] (Figure 5). There are crystal structures of a *Bacillus halodurans* endo β-glucanase (GH family 81) catalytic domain in complex with β-glucan chains [51]. Soaking crystals with laminarin resulted in three β-glucan chains binding to the protein. A large oligosaccharide was found in the active site that was modelled as laminaridecaose (10-mer). In addition to this, two other β-glucan chains (DP = 2 and 3) were detected close to the bound laminaridecaose. Interestingly, the structure of laminaridecaose and other shorter oligosaccharides roughly mimic the triple helical β-glucan. The architecture of the catalytic site in this enzyme seems structured to accommodate the double and/or triple helical quaternary structures of β-glucan chains. The crystal structure of C-terminal CBM56 is similar to the N-terminal domain of *Plodia interpunctella* GNBP3, with RMSD of 1.9 Å using Cα atoms. The NMR-mapped laminarin-binding site of this C-terminal CBM56 corresponds to the surface of the laminarihexaose-binding site in *Plodia interpunctella* GNBP3 [38]. They may share a common β(1,3)-glucan binding mode.

Another endo β-glucanase (GH64), from *Paenibacillus barengoltzii*, is also capable of recognizing triplex β-glucan. This β-glucanase is composed of two regions: a N-terminal CBM56 with β-glucan binding ability, and a C-terminal region corresponding to a β-glucanase domain (GH64). A crystal structure of this full-length enzyme (inactive mutant) in complex with laminarihexaose [54] shows, similar to the previous example, that two β-glucan chains bind within the single groove of the catalytic site, with four glucose units in one chain and five glucose units in the other chain. The two oligosaccharide chains are slightly twisted together and hence could essentially be part of a triple-helical β-1,3-glucan.

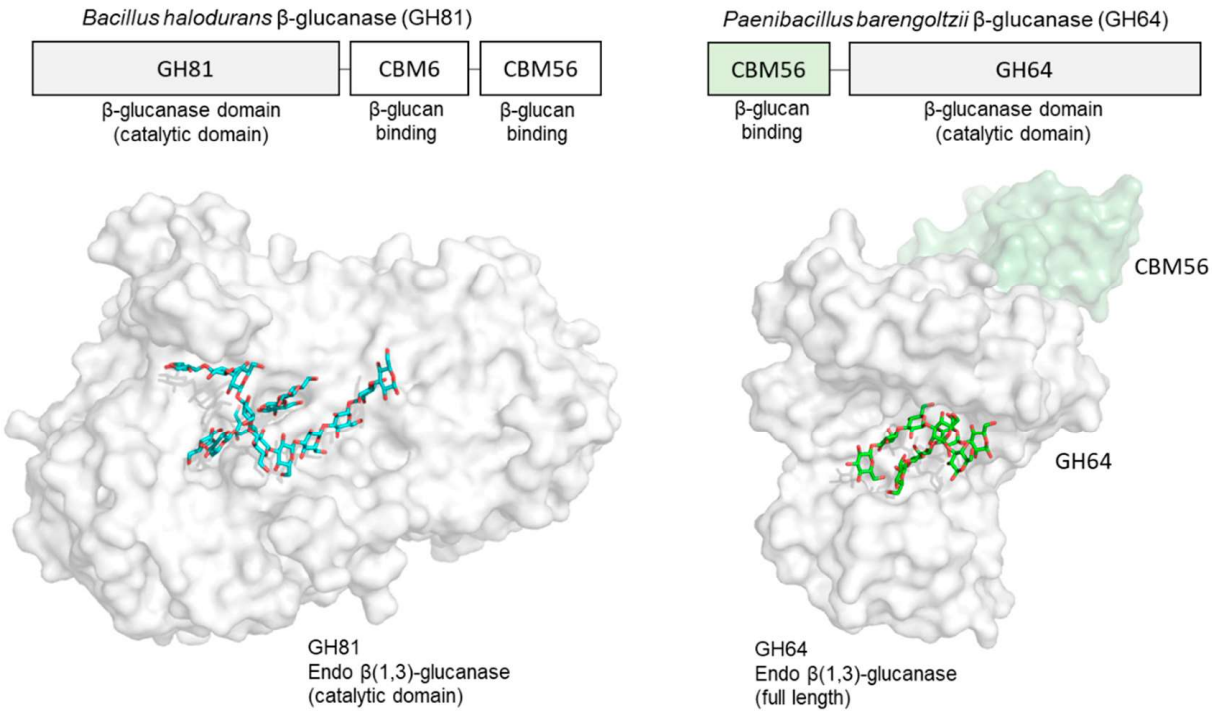

Figure 5. Crystal structure of endoglucanases bound to β-glucan chains. GH81 endo β-1,3-glucanase in complex with three β-glucan chains (DP = 10, 3, 2) derived from laminarin (PDB ID: 5T4G) (left) and GH64 endo β-1,3-glucanase in complex with two laminarihexaose chains (PDB ID: 5H9Y) (right). Proteins are shown in surface model and β-glucan chains in stick representation.

Anti-β-glucan antibody may also recognize structured β(1,3)-glucans. Antibody JoJ48C11 was generated against schizophyllan by an antibody phage display system. A crystal structure of this Fab fragment in complex with unbranched laminarihexaose yielded a partial electron density of the ligand [55]. If schizophyllan is assumed to have a triple helix, the coordinates fit well in the observed density. A β(1,6)-linked glucose residue is very important for antibody binding and the model of the complex does indeed suggest the involvement of a β(1,6)-linked glucose residue in the interaction.

8. Effect of β(1,6)-Branching on β-Glucan Conformation

The effect of β1,6 branching on β-glucan conformation is of interest, because β(1,6)-branching significantly affects the biological activity of β-glucan [25]. Curdran has no side chain branching and assumes an insoluble triple helix in water. Schizophyllan, in contrast, is soluble in water. Hence, modification with a β(1,6)-linked glucose residue on every third β(1,3)-linked glucose residue increases the solubility. Hydrogen bonding and surrounding water molecules may play their roles in defining such behavior. The molecular dynamics study of Okobira et al., of triple helical β-glucan with and without β(1,6)-branching, shows that β(1,6)-branching affects several conformational properties [56]. As the population of side chains increases, the helical pitch decreases. The average pitch of curdran is 20.6 Å, while that of schizophyllan is 18.8 Å. Two types of hydrogen bonding exist for branched β-glucan: side chain–main chain and side chain–side chain. A small cavity with a diameter of 3.5 Å occurs within the triple helix of schizophyllan but not in curdran. Furthermore, β(1,6)-branching causes a tilt of the main-chain glucose residue with respect to the helix.

There is a paucity of experimental results that shed light on the conformation of branched β-glucans at the atomic level. One example is found in a crystallographic analysis of GH16 1,3(4)-β-glucanase (*Phanerochaete chrysosporium* laminarinase 16A), complexed with a β-glucan product of laminarin hydrolysis, i.e., Glcβ(1,6)-Glcβ(1,3)-Glcβ(1,3)-Glc [57].

In the crystal structure, two ligands are found: In the acceptor site is the tetrasaccharide, including a β(1,6)-linked side chain, while in the donor site are three β(1,3)-linked glucose residues (Figure 6). The β(1,6)-glucose residue in the acceptor site lies deep within the cleft and interacts with a main-chain glucose residue (+2 position) via a hydrogen bond. Experimental observations such as these, coupled with theoretical studies, will help to gain understanding of structure–function relationships of branched β-glucans, and the role of branching.

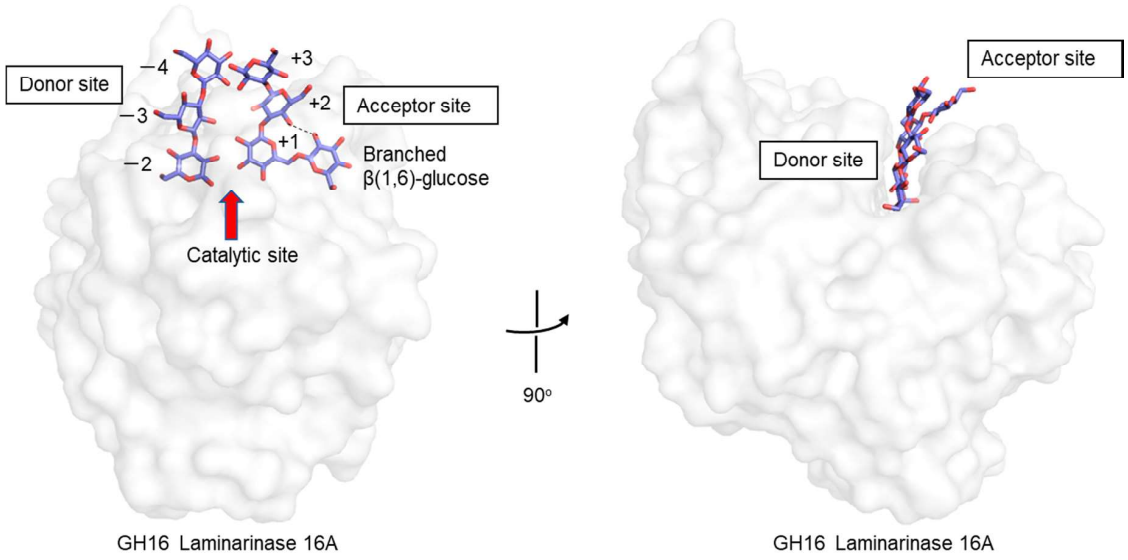

Figure 6. Crystal structure of a GH16 laminarinase in complex with products of laminarin. Proteins are shown in the surface model and β-glucan chains in stick representation. A hydrogen bond between β(1,6)-side chain and main chain glucose residue (+2 position) is shown as a dashed line.

9. Summary and Future Perspectives

The triple helix structure of β-glucan was initially proposed from X-ray fiber diffraction studies and the atomic structure is now well-supported by several X-ray crystallographic analyses of short β(1,3)-glucan chains in complex with β-glucan chain binding proteins. These examples point to the importance of higher-order structures of β-glucan in the associated biological phenomena. However, several reports suggest that triple helical or higher-ordered structures are not essential or advantageous for the expression of certain biological activities [40,58,59]. Detailed information of how β-glucan is recognized and how downstream signaling occurs is still lacking. One difficulty in the study of structure–function relationships of β-glucans is because β-glucan from natural sources is chemically heterogeneous, e.g., in terms of chain length and branching. Also, determination of 3D structures of β-glucan remains challenging. Likely, advances will be greatest using chemically and conformationally defined β-glucan chains. These would be easier to obtain and analyze and should provide clearer structure–function relationships of β-glucan and the binding proteins. These are also expected to provide important clues to the development of β-glucan assay technology, covering a variety of structural characteristics, and that of new therapeutic drug treatment and monitoring of invasive fungal infections which can lead to sepsis.

Author Contributions: Writing—Original draft preparation, Y.Y.; writing—Review and editing, Y.Y. and N.M. All authors have read and agreed to the published version of the manuscript.

Funding: This work was supported in part by Grants-in-And for Scientific Research (B) (16H04758 and 19H03362 to Y.Y.).

Acknowledgments: Our studies on Dectin-1 and βGRP/GNBP3 were performed by Mayumi Kanagawa, Tadashi Satoh, Shinya Hanashima, Hari P. Dulal, and Sushil K. Mishra in collaboration with Profs. Naohito Ohno, Yoshiyuki Adachi, and Hiroshi Tanaka.

Conflicts of Interest: The authors declare no conflict of interest.

References

1. Harada, T.; Masuda, M.; Fujimori, K.; Maeda, I. Production of a firm, resilient gel-forming polysaccharide by a mutant of Alcaligenes faecalis var. myxogenes 10C3. *Agric. Biol. Chem.* **1966**, *30*, 196–198.
2. Saito, H.; Misaki, A.; Harada, T. A comparison of strucure of curdlan and pachyman. *Agric. Biol. Chem.* **1968**, *32*, 1261–1269. [CrossRef]
3. Harada, T.; Misaki, A.; Saito, H. Curdlan: A bacterial gel-forming beta-1,3-glucan. *Arch. Biochem. Biophys.* **1968**, *124*, 292–298. [CrossRef]
4. Tabata, K.; Ito, W.; Kojima, T.; Kawabata, S.; Misaki, A. Ultrasonic degradation of schizophyllan, an antitumor polysaccharide produced by Schizophyllum commune Fries. *Carbohydr. Res.* **1981**, *89*, 121–135. [CrossRef]
5. Rinaudo, M.; Vincendon, M. ^{13}C NMR structural investigation of scleroglucan. *Carbohydr. Polym.* **1982**, *2*, 135–144. [CrossRef]
6. Sasaki, T.; Takasuka, N. Further study of the structure of lentinan, an anti-tumor polysaccharide from Lentinus edodes. *Carbohydr. Res.* **1976**, *47*, 99–104. [CrossRef]
7. Read, S.M.; Currie, G.; Bacic, A. Analysis of the structural heterogeneity of laminarin by electrospray-ionisation-mass spectrometry. *Carbohydr. Res.* **1996**, *281*, 187–201. [CrossRef]
8. Ohno, N.; Uchiyama, M.; Tsuzuki, A.; Tokunaka, K.; Miura, N.N.; Adachi, Y.; Aizawa, M.W.; Tamura, H.; Tanaka, S.; Yadomae, T. Solubilization of yeast cell-wall beta-(1–>3)-D-glucan by sodium hypochlorite oxidation and dimethyl sulfoxide extraction. *Carbohydr. Res.* **1999**, *316*, 161–172. [CrossRef]
9. Sletmoen, M.; Stokke, B.T. Higher order structure of (1,3)-β-D-glucans and its influence on their biological activities and complexation abilities. *Biopolymers* **2008**, *89*, 310–321. [CrossRef]
10. Bluhm, T.L.; Sarko, A. The triple helical structure of lentinan, a linear β-(1→3)-D-glucan. *Can. J. Chem.* **1977**, *55*, 293–299. [CrossRef]
11. Chuah, C.T.; Sarko, A.; Deslandes, Y.; Marchessault, R.H. Packing analysis of carbohydrates and polysaccharides. Part 14. Triple-helical crystalline-structure of curdlan and paramylon hydrates. *Macromolecules* **1983**, *16*, 1375–1382. [CrossRef]
12. Bluhm, T.L.; Deslandes, Y.; Marchessault, R.H.; Perez, S.; Rinaudo, M. Solid-state and solution conformation of scleroglucan. *Carbohydr. Res.* **1982**, *100*, 117–130. [CrossRef]
13. Kashiwagi, Y.; Norisuye, T.; Fujita, H. Triple helix of *Schizophyllum commune* polysaccharide in dilute solution. 4. Light scattering and viscosity in dilute aqueous sodium hydroxide. *Macromolecules* **1981**, *14*, 1220–1225. [CrossRef]
14. Ogawa, K.; Tsurugi, J.; Watanabe, T. The dependence of the conformation of a (1→3)-β-D-glucan on chain-length in alkaline solution. *Carbohydr. Res.* **1973**, *29*, 397–403. [CrossRef]
15. Kojima, T.; Tabata, K.; Itoh, W.; Yanaki, T. Molecular-weight dependence of the antitumor-activity of schizophyllan. *Agric. Biol. Chem.* **1986**, *50*, 231–232.
16. Hanashima, S.; Ikeda, A.; Tanaka, H.; Adachi, Y.; Ohno, N.; Takahashi, T.; Yamaguchi, Y. NMR study of short β(1-3)-glucans provides insights into the structure and interaction with Dectin-1. *Glycoconj. J.* **2014**, *31*, 199–207. [CrossRef]
17. Oda, M.; Tanabe, Y.; Noda, M.; Inaba, S.; Krayukhina, E.; Fukada, H.; Uchiyama, S. Structural and binding properties of laminarin revealed by analytical ultracentrifugation and calorimetric analyses. *Carbohydr. Res.* **2016**, *431*, 33–38. [CrossRef]
18. Norisuye, T.; Yanaki, T.; Fujita, H. Triple helix of a schizophyllum-commune polysaccharide in aqueous-solution. *J. Polym. Sci. Part B Polym. Phys.* **1980**, *18*, 547–558. [CrossRef]
19. Yanaki, T.; Tabata, K.; Kojima, T. Melting behavior of a triple helical polysaccharide schizophyllan in aqueous-solution. *Carbohyd. Polym.* **1985**, *5*, 275–283. [CrossRef]
20. Stokke, B.T.; Elgsaeter, A.; Brant, D.A.; Kuge, T.; Kitamura, S. Macromolecular cyclization of (1–>6)-branched-(1–>3)-beta-D-glucans observed after denaturation-renaturation of the triple-helical structure. *Biopolymers* **1993**, *33*, 193–198. [CrossRef] [PubMed]
21. Zhang, X.; Zhang, L.; Xu, X. Morphologies and conformation transition of *Lentinan* in aqueous NaOH solution. *Biopolymers* **2004**, *75*, 187–195. [CrossRef] [PubMed]
22. Brown, G.D. Dectin-1: A signalling non-TLR pattern-recognition receptor. *Nat. Rev. Immunol.* **2006**, *6*, 33–43. [CrossRef] [PubMed]
23. Palma, A.S.; Feizi, T.; Zhang, Y.; Stoll, M.S.; Lawson, A.M.; Díaz-Rodríguez, E.; Campanero-Rhodes, M.A.; Costa, J.; Gordon, S.; Brown, G.D.; et al. Ligands for the β-glucan receptor, Dectin-1, assigned using "designer" microarrays of oligosaccharide probes (neoglycolipids) generated from glucan polysaccharides. *J. Biol. Chem.* **2006**, *281*, 5771–5779. [CrossRef]
24. Tanaka, H.; Kawai, T.; Adachi, Y.; Hanashima, S.; Yamaguchi, Y.; Ohno, N.; Takahashi, T. Synthesis of β(1,3) oligoglucans exhibiting a Dectin-1 binding affinity and their biological evaluation. *Bioorg. Med. Chem.* **2012**, *20*, 3898–3914. [CrossRef]
25. Adams, E.L.; Rice, P.J.; Graves, B.; Ensley, H.E.; Yu, H.; Brown, G.D.; Gordon, S.; Monteiro, M.A.; Papp-Szabo, E.; Lowman, D.W.; et al. Differential high-affinity interaction of dectin-1 with natural or synthetic glucans is dependent upon primary structure and is influenced by polymer chain length and side-chain branching. *J. Pharmacol. Exp. Ther.* **2008**, *325*, 115–123. [CrossRef] [PubMed]

26. Brown, J.; O'Callaghan, C.A.; Marshall, A.S.; Gilbert, R.J.; Siebold, C.; Gordon, S.; Brown, G.D.; Jones, E.Y. Structure of the fungal β-glucan-binding immune receptor dectin-1: Implications for function. *Protein Sci.* **2007**, *16*, 1042–1052. [CrossRef]
27. Adachi, Y.; Ishii, T.; Ikeda, Y.; Hoshino, A.; Tamura, H.; Aketagawa, J.; Tanaka, S.; Ohno, N. Characterization of β-glucan recognition site on C-type lectin, dectin 1. *Infect. Immun.* **2004**, *72*, 4159–4171. [CrossRef]
28. Kato, Y.; Adachi, Y.; Ohno, N. Contribution of N-linked oligosaccharides to the expression and functions of β-glucan receptor, Dectin-1. *Biol. Pharm. Bull.* **2006**, *29*, 1580–1586. [CrossRef]
29. Dulal, H.P.; Adachi, Y.; Ohno, N.; Yamaguchi, Y. β-Glucan-induced cooperative oligomerization of Dectin-1 C-type lectin like domain. *Glycobiology* **2018**, in press. [CrossRef]
30. Anaya, E.U.; Amin, A.E.; Danielson, M.; Michel, K.; Neumann, A.K. Innate antifungal immune receptor, Dectin-1, undergoes ligand-induced oligomerization with highly structured β-glucans and at fungal cell contact sites. *bioRxiv* **2019**. [CrossRef]
31. Bode, K.; Bujupi, F.; Link, C.; Hein, T.; Zimmermann, S.; Peiris, D.; Jaquet, V.; Lepenies, B.; Weyd, H.; Krammer, P.H. Dectin-1 binding to annexins on apoptotic cells induces peripheral immune tolerance via NADPH oxidase-2. *Cell Rep.* **2019**, *29*, 4435–4446.e4439. [CrossRef]
32. Manabe, Y.; Marchetti, R.; Takakura, Y.; Nagasaki, M.; Nihei, W.; Takebe, T.; Tanaka, K.; Kabayama, K.; Chiodo, F.; Hanashima, S.; et al. The core fucose on an IgG antibody is an endogenous ligand of Dectin-1. *Angew. Chem. Int. Ed. Engl.* **2019**, *58*, 18697–18702. [CrossRef]
33. Thornton, B.P.; Vetvicka, V.; Pitman, M.; Goldman, R.C.; Ross, G.D. Analysis of the sugar specificity and molecular location of the beta-glucan-binding lectin site of complement receptor type 3 (CD11b/CD18). *J. Immunol.* **1996**, *156*, 1235–1246.
34. Xia, Y.; Ross, G.D. Generation of recombinant fragments of CD11b expressing the functional beta-glucan-binding lectin site of CR3 (CD11b/CD18). *J. Immunol.* **1999**, *162*, 7285–7293.
35. Brown, G.D.; Gordon, S. Immune recognition of fungal β-glucans. *Cell Microbiol.* **2005**, *7*, 471–479. [CrossRef]
36. Takahasi, K.; Ochiai, M.; Horiuchi, M.; Kumeta, H.; Ogura, K.; Ashida, M.; Inagaki, F. Solution structure of the silkworm betaGRP/GNBP3 N-terminal domain reveals the mechanism for beta-1,3-glucan-specific recognition. *Proc. Natl. Acad. Sci. USA* **2009**, *106*, 11679–11684. [CrossRef]
37. Mishima, Y.; Quintin, J.; Aimanianda, V.; Kellenberger, C.; Coste, F.; Clavaud, C.; Hetru, C.; Hoffmann, J.A.; Latge, J.P.; Ferrandon, D.; et al. The N-terminal domain of *Drosophila* Gram-negative binding protein 3 (GNBP3) defines a novel family of fungal pattern recognition receptors. *J. Biol. Chem.* **2009**, *284*, 28687–28697. [CrossRef]
38. Kanagawa, M.; Satoh, T.; Ikeda, A.; Adachi, Y.; Ohno, N.; Yamaguchi, Y. Structural insights into recognition of triple-helical β-glucans by an insect fungal receptor. *J. Biol. Chem.* **2011**, *286*, 29158–29165. [CrossRef]
39. Rao, X.J.; Zhan, M.Y.; Pan, Y.M.; Liu, S.; Yang, P.J.; Yang, L.L.; Yu, X.Q. Immune functions of insect betaGRPs and their potential application. *Dev. Comp. Immunol.* **2018**, *83*, 80–88. [CrossRef]
40. Adachi, Y.; Ishii, M.; Kanno, T.; Tetsui, J.; Ishibashi, K.I.; Yamanaka, D.; Miura, N.; Ohno, N. N-Terminal (1–>3)-beta-d-glucan recognition proteins from insects recognize the difference in ultra-structures of (1–>3)-beta-d-glucan. *Int. J. Mol. Sci.* **2019**, *20*, 3498. [CrossRef]
41. Ochiai, M.; Ashida, M. A pattern-recognition protein for β-1,3-glucan. The binding domain and the cDNA cloning of β-1,3-glucan recognition protein from the silkworm, *Bombyx mori*. *J. Biol. Chem.* **2000**, *275*, 4995–5002. [CrossRef]
42. Ma, C.; Kanost, M.R. A β1,3-glucan recognition protein from an insect, *Manduca sexta*, agglutinates microorganisms and activates the phenoloxidase cascade. *J. Biol. Chem.* **2000**, *275*, 7505–7514. [CrossRef]
43. Gottar, M.; Gobert, V.; Matskevich, A.A.; Reichhart, J.M.; Wang, C.; Butt, T.M.; Belvin, M.; Hoffmann, J.A.; Ferrandon, D. Dual detection of fungal infections in *Drosophila* via recognition of glucans and sensing of virulence factors. *Cell* **2006**, *127*, 1425–1437. [CrossRef] [PubMed]
44. Dai, H.; Hiromasa, Y.; Takahashi, D.; VanderVelde, D.; Fabrick, J.A.; Kanost, M.R.; Krishnamoorthi, R. An initial event in the insect innate immune response: Structural and biological studies of interactions between beta-1,3-glucan and the N-terminal domain of beta-1,3-glucan recognition protein. *Biochemistry* **2013**, *52*, 161–170. [CrossRef]
45. Takaki, Y.; Seki, N.; Kawabata Si, S.; Iwanaga, S.; Muta, T. Duplicated binding sites for (1–>3)-beta-D-glucan in the horseshoe crab coagulation factor G: Implications for a molecular basis of the pattern recognition in innate immunity. *J. Biol. Chem.* **2002**, *277*, 14281–14287. [CrossRef]
46. Ueda, Y.; Ohwada, S.; Abe, Y.; Shibata, T.; Iijima, M.; Yoshimitsu, Y.; Koshiba, T.; Nakata, M.; Ueda, T.; Kawabata, S. Factor G utilizes a carbohydrate-binding cleft that is conserved between horseshoe crab and bacteria for the recognition of beta-1,3-D-glucans. *J. Immunol.* **2009**, *183*, 3810–3818. [CrossRef] [PubMed]
47. Saito, H.; Yoshioka, Y.; Uehara, N.; Aketagawa, J.; Tanaka, S.; Shibata, Y. Relationship between conformation and biological response for (1—-3)-beta-D-glucans in the activation of coagulation factor G from limulus amebocyte lysate and host-mediated antitumor activity. Demonstration of single-helix conformation as a stimulant. *Carbohydr. Res.* **1991**, *217*, 181–190. [CrossRef]
48. Theel, E.S.; Doern, C.D. beta-D-glucan testing is important for diagnosis of invasive fungal infections. *J. Clin. Microbiol.* **2013**, *51*, 3478–3483. [CrossRef] [PubMed]
49. Boraston, A.B.; Bolam, D.N.; Gilbert, H.J.; Davies, G.J. Carbohydrate-binding modules: Fine-tuning polysaccharide recognition. *Biochem. J.* **2004**, *382*, 769–781. [CrossRef]
50. Lombard, V.; Golaconda Ramulu, H.; Drula, E.; Coutinho, P.M.; Henrissat, B. The carbohydrate-active enzymes database (CAZy) in 2013. *Nucleic Acids Res.* **2014**, *42*, D490–D495. [CrossRef]

51. Pluvinage, B.; Fillo, A.; Massel, P.; Boraston, A.B. Structural analysis of a family 81 glycoside hydrolase implicates its recognition of β-1,3-glucan quaternary structure. *Structure* **2017**, *25*, 1348–1359.e3. [CrossRef]
52. van Bueren, A.L.; Morland, C.; Gilbert, H.J.; Boraston, A.B. Family 6 carbohydrate binding modules recognize the non-reducing end of beta-1,3-linked glucans by presenting a unique ligand binding surface. *J. Biol. Chem.* **2005**, *280*, 530–537. [CrossRef]
53. Hettle, A.; Fillo, A.; Abe, K.; Massel, P.; Pluvinage, B.; Langelaan, D.N.; Smith, S.P.; Boraston, A.B. Properties of a family 56 carbohydrate-binding module and its role in the recognition and hydrolysis of beta-1,3-glucan. *J. Biol. Chem.* **2017**, *292*, 16955–16968. [CrossRef]
54. Qin, Z.; Yang, D.; You, X.; Liu, Y.; Hu, S.; Yan, Q.; Yang, S.; Jiang, Z. The recognition mechanism of triple-helical β-1,3-glucan by a β-1,3-glucanase. *Chem. Commun.* **2017**, *53*, 9368–9371. [CrossRef] [PubMed]
55. Sung, K.H.; Josewski, J.; Dubel, S.; Blankenfeldt, W.; Rau, U. Structural insights into antigen recognition of an anti-β-(1,6)-β-(1,3)-D-glucan antibody. *Sci. Rep.* **2018**, *8*, 13652. [CrossRef]
56. Okobira, T.; Miyoshi, K.; Uezu, K.; Sakurai, K.; Shinkai, S. Molecular dynamics studies of side chain effect on the β-1,3-D-glucan triple helix in aqueous solution. *Biomacromolecules* **2008**, *9*, 783–788. [CrossRef] [PubMed]
57. Vasur, J.; Kawai, R.; Andersson, E.; Igarashi, K.; Sandgren, M.; Samejima, M.; Stahlberg, J. X-ray crystal structures of Phanerochaete chrysosporium Laminarinase 16A in complex with products from lichenin and laminarin hydrolysis. *FEBS J.* **2009**, *276*, 3858–3869. [CrossRef] [PubMed]
58. Yoshioka, Y.; Uehara, N.; Saito, H. Conformation-dependent change in antitumor activity of linear and branched (1–>3)-β-D-glucans on the basis of conformational elucidation by carbon-13 nuclear magnetic resonance spectroscopy. *Chem. Pharm. Bull.* **1992**, *40*, 1221–1226. [CrossRef] [PubMed]
59. Kulicke, W.M.; Lettau, A.I.; Thielking, H. Correlation between immunological activity, molar mass, and molecular structure of different (1–>3)-beta-D-glucans. *Carbohydr. Res.* **1997**, *297*, 135–143. [CrossRef]